Thèse de doctorat

Université de Limoges

Université de Limoges

École Doctorale Sciences et Ingénierie pour l'Information, Mathématiques (ED 521)

Institute de recherche XLIM, UMR CNRS 7252, Limoges

Thèse pour obtenir le grade de

Docteur de l'Université de Limoges

Electronique des Hautes Fréquences, Photoniques et Systèmes

Présentée et soutenue par

M. Ximeng ZHENG

Le 18 juillet 2017

Fiber post-processing and atomic spectroscopy for the development of atomic-vapour photonic microcell

Thèse dirigée par Pr. Fetah BENABID et Dr. Frédéric GEROME

JURY :

Président du jury :

Mr. Philippe Thomas, Directeur de recherche, SPCTS, Centre Européen de la Céramique, Université de Limoges

Rapporteurs:

Mr. Patrick Windpassinger, Professeur, Universität Mainz

Mr. Daniel Bloch, Directeur de recherche CNRS, Laboratoire de Physique des Lasers, Université Paris13

Examinateurs :

Mr. Luca Vincetti, Professeur associé, Université de Modena

Mr. Simon Bernon, Maitre de conférence, Laboratoire Photonique, Numérique et Nanosciences, Institut d'Optique d'Aquitaine – Université Bordeaux 1

Mr. Fetah Benabid, Directeur de Recherche CNRS, XLIM, Université de Limoges

Mr. Frédéric Gérôme, Chargé de Recherche CNRS, XLIM, Université de Limoges

Acknowledgement

I would like to thank my supervisor Pr. Fetah Benabid for give me the opportunity to complete my Ph.D research. Thank his expertise, support and guidance through these years. Without him, this wide topic thesis would not be accomplished. I would also like to thank my wife Sixia Liu, who gave me strong support in mental part during my hard Ph.D life.

I would like to thank the past and present members of the Gas Phase Photonics and Microwave Materials Group. Specially thank Dr. Frédéric Gérôme for teach me the basic knowledge in these years and give me all neccesairy help. His kindness and French elegance will accompany me in my future research life. I would also like to thank Benoît Debord for the Kagome HC-PCF samples fabrication. Thank Jenny Juin and Thomas Philippe in laboratory SPCTS for the help of inner wall surface anti-relaxation material coating. Thank Luca Vincetti for the guidance simulation part. Thank kind Sébastien Rougier for teach me the fiber drawing and the SEM characterization. Additionally I would like to achnowledge our lab crews in Limoges: Benoît Beaudou, Assaad Baz, Meshaal Alharbi, Muhammed Adnan, Ekaterina Ilinova, Abhilash Amsanpally, Madhoussoudhana Dontabactouny, Aurélien Benoît, Katell Gadonna, Debashri Ghosh, Florien Vial, Amrani Foued, Matthieu Chafer, Maurel Martin, Kergoustin David, Delahaye Frederic.

Finally I would like to thanks my family and friends for your support during my Ph.D life.

Un peuple malheureux fait les grands artistes. - Alfred de MUSSET

à mon grand-père

Abstract

Atom optics in confined in nano- and micro-structured devices geometry is becoming a timely topic. The pursuit of miniaturizing atom based functionalities such as frequency references, atomic clocks and quantum sensors is motivated by transferring the outstanding performances in frequency control and coherent optics achieved in laboratory environments to a broader community of users through the development a compact, friendly-user and stand-alone atom devices. Moreover, atomic-vapor micro-confinement implies innovative technological solutions and platform to explore new fundamental phenomena.

Among the atom devices that have been or are being developed, we cite hollow-core photonic crystal fiber (HC-PCF) and its gas-filled form the photonic microcell (PMC). The latter outstands with its long interaction length and small modal area, making it thus an efficient platform to enhance gas-laser nonlinear interaction and/or absorption contrast by several orders of magnitude relative to free-space configurations. However, the micrometric scale of the fiber core harboring the atoms raises several technical and scientific challenges. Among the technical challenges, we list the development of efficient process for atom loading inside very long hollow channels with small core diameter, the suppression or mitigation of physio-chemical reactivity of the confined atoms (*i.e.* Rubidium, Caecium) with the fiber core inner-surface silica etc. In parallel, once the atoms are successfully confined, the large surface-to-volume ratio of the atom-harboring fiber-core raises questions like the coherence relaxation dynamics and the nature and effect of the atom-surface interaction. Within this context, the work presented in this thesis builds up on previous work in my research group GPPMM to address some of the above-mentioned challenges. In particular, the thesis reports on fiber-core inner surface coating with different materials as an effort to mitigate

the physio-chemical reactions of the confined atoms with the surface, on tapering large outer-diameter and core-diameter inhibited coupling guiding Kagome HC-PCF, and splicing technique that ensures low splice loss and no atomic reactivity during the splicing process. In parallel, the thesis reports on a set of spectroscopy experiments to assess the relaxation dynamics of atoms inside HC-PCF and to report on novel sub-Doppler transparencies.

The manuscript is structured as follows. Chapter 1 introduces the context of atom optics in micro-structured systems, the scientific and technological motivations behind this theme and review the different development and results achieved in the last two decades.

Chapter 2 details the description of guidance mechanism of the HC-PCF. We draw the main differences between photonic bandgap guiding HC-PCF and Inhibited-Coupling guiding HC-PCF. We list the main modal properties of IC guiding HC-PCF, which is used along this thesis, and the rationale behind the choice of this type of fibers for our atom-optics experiments and aim to develop all-fiber Rb-PMC. We then show the optical and physical properties of Kagome HC-PCF that are purposely fabricated to operate near 780 nm, and which will be used throughout my doctoral wotk.

In Chapter 3, we introduce the different processes in post-processing HC-PCF before, during and after the atom loading inside the fiber. This process chain is required in making what would be the first all-fiber alkali-vapor photonic microcell (PMC). It comprises HC-PCF tapering, splicing, in-fiber gas handling, fiber core inner-wall coating and of course vapor loading. The chapter stresses on techniques of tapering HC-PCF with hypocycloid core-contour with no structural distortion and splicing them to an all-solid optical fiber. The chapter presents also alternative ways to splice HC-PCF to solid fiber using sleeving techniques. Finally, we report on the coating material synthesis and on the process of the fiber core

inner-wall coating. Several HC-PCFs with ceramic and PDMS coated core along with uncoated HC-PCF have been put in a high vacuum system for rubidium loading, lifetime assessment and for spectroscopy experiments. The results show that all the coated HC-PCF kept their optical performances. As expected, the ceramic coated HC-PCFs exhibit much longer Rb life time inside the fiber which is paramount for stand-alone PMC applications.

Chapter 4 deals with investigating the atom dephasing dynamics inside the core with an emphasis on the effect of the surface. In this chapter, we present experimental results on the relaxation dynamic of rubidium ground state polarization relaxation. The experimental protocol relies on monitoring the magneto-optical rotation of the atoms in the dark. Based on this technique, relaxation time of Rb inside HC-PCF with different core inner-wall surfaces and under different magnetic field amplitude, pump power levels have been measured. The results demonstrate that the measured polarization relaxation is dominant by the dwell time of the adsorbed atoms and that the polarized atoms are primarily formed by slow atoms. Finally, we used this technique to deduce the dwell time for bare silica surface, ceramic coating and PDMS coating.

Chapter 5 introduces Rb-surface interaction induced sub-Doppler transparencies observed in the absorption spectrum of Rb-confined vapor inside a Kagome HC-PCF. Unlike with saturated absorption or electromagnetically induced transparency, the sub-Doppler lines are generated with a single forward propagating laser beam. The chapter reports on how these sub-Doppler transparencies change with magnetic field, laser power and polarization for three different core inner-wall surfaces. Then, the results are compared with those of a theoretical model, which considers the adsorbed atom trapped in a Van-der-Waal potential, and shows that sub-Doppler transparencies can occurs via optical pumping between the translational energy levels of the adatoms inside the potential. The comparison between the theoretical model and the experimental

results show a qualitative consistency and paves the way for a novel spectroscopy based on atoms in HC-PCF.

Table of contents

List of figures

List of tables

Abbreviations

ARROW	Anti-resonant reflecting optical waveguide
CMOS	Complementary metal-oxide-semiconductor
CPT	Coherent population trapping
CQED	Cavity quantum electrodynamics
CSAC	Chip Scale Atomic Clock
CSAM	Chip scale atomic magnetometer
CW	Continuous wave
DOPS	Density of photonic state
DR	Down-ratio
DSC	Differential scanning calorimetery
ECDL	External cavity diode laser
EIT	Electromagnetically induced transparency
FEM	Finite element method
FM	Fundamental mode
FOM	Figure of merit
FOR	Fire of ring
FWHM	Full width at half maximum
HC-PCF	Hollow-core photonic crystal fiber
HHG	High harmonic generation
HOM	Higher order mode
HWP	Half wave plate
IC	Inhibited coupling
ID	Inner diamter
IR	Infrared
ISO	Isolator
LIAD	Light induced atomic desorption
LID	Light induced drift
LJ	Lennard-Jones
MAC	Miniature atomic clock
MEMS	Micro-electronic mechanical systems
MFD	Mode field diameter
MFP	Mean free path
MOS	Magneto-optical spectroscopy

NEP	Noise equivalent power
NF	Near field
NIR	Near-Infrared
NPBS	Non-polarizing beam splitter
OD	Optical density
ODMS	Octadecyldimethylmethoxysilane
OSA	Optical spectrum analyzer
OSCC	Optical space Cs clock
OTS	Octdecyltrichlorosilane
PBG	Photonic bandgap
PBS	Polarizing beam splitter
PD	Photodetector
PDMS	Polydimethylsiloxane
PMC	Photonic Microcell
PML	Perfectly matched layer
PTBM	Photonic tight binding model
QWP	Quarter waveplate
Rb	Rubidium
SAS	Saturated absorption spectroscopy
SDL	Sub-Doppler lines
SEM	Scanning electron microscope
SMF	Single mode fiber
SNOM	Near field optical microscopy
SNR	Signal to noise ratio
SRS	Stimulated raman scattering
TBM	Tight binding model
TEOS	Tetraethoxysilane
TG	Thermos-gravimetry
TIR	Total internal reflection
TL	Transition length
UHV	Ultra-high vacuum
UV	Ultra-violet
VdW	Van der Waals
XRD	X-Ray diffraction

Chapter 1

Atom optics in gas confined hollow-core photonic microstructures

This chapter introduces the physics background of atom optics confined in dielectric micro-structures such as hollow-core photonic crystal fibers and the different efforts being recently undertaken world-wide along with their underpinning motivations. We list the different atom confining geometries that have been explored with a discussion on their respective advantages and disadvantages. Finally, we finish with describing the layout of the thesis chapters.

1.1 Introduction

Atomic or molecular transitions are widely applied in laser frequency metrology and spectroscopy as a frequency reference for its very weak sensitivity to environmental changes such as pressure or mechanical vibrations [1]. This feature is also explored in other fields such as quantum optics, quantum sensors or quantum information. For example, optical magnetometers in which a magnetic field is probed by observing changes in the properties of light-matter interaction can achieve extremely high sensitivity [2]. Rydberg transitions based on single photon interactions are currently explored for quantum information and computing applications to develop functionalities such as controlled-NOT quantum gate based on Rydberg blockade interactions [3]. Moreover, quantum memory [4], slow light [5], cavity quantum electrodynamics (CQED) [6] are other demonstrations illustrating the impact of atom-laser interaction.

In addition to the above, when laser cooling techniques [7][8][9] are deployed to cool the atoms, one can achieve an extremely high frequency stability level, which is now illustrated in microwave and optical atomic clocks with frequency instability reaching 1 part in 10^{14} and 1 part in 10^{17} respectively [10][11][12]. Furthermore, ultra-low temperature cold atoms (*i.e.* Bose-Einstein Condensates) represent a novel matter phase [13] that led to the emergence of the field of matter wave, and which is used to develop next generation gravimeters [14], gyroscopes [15] based on atomic interference techniques [14].

In parallel to the impressive progress made in the physics and technology of atom optics mentioned above, another pursuit emerged in the last decade which consists in miniaturizing the atom optical systems. Indeed, so far all the best performances of atomic clocks and quantum sensors were achieved in laboratory environment using highly complex set-ups and requiring highly qualified scientists. The motivations of miniaturizing atom optic devices such as atomic clocks or magnetometers are justified by the huge impact such these outstanding laboratory performances would have in both a technological and scientific stand point if delivered in stable and compact devices. An illustration of the impact of the availability of such devices to industry and the world outside specialised

laboratories is given by the Chip-Scale-Atomic-Clock (CSAC), developed in NIST in the last decade [16], and which is now industrialized in several applications such telecommunications and sub-marine geophysical explorations.

The miniaturization of atom optics systems entails first a drastic size-reduction of the host structure containing atomic and molecular gases. In addition to the technological challenges that this aim implies, reducing the dimensions of the gas host structure could reduce the signal to noise ratio (SNR) of any probed transition if the interaction length with the medium is not appropriately addressed. Secondly smaller gas host systems result in increased level of interactions with the walls of the container, and subsequently in undesired spectral broadening and shifting of atomic and molecular transitions spectral lines. Thirdly, the vicinity of atoms to the host wall surface poses problems in the atoms' lifetime in such microstructures via the physio-chemical reaction between the atoms and surface. In this chapter we list the different routes explored to develop miniature atom cells and how the above-mentioned challenges are addressed.

Below, we start with a brief overview of the basic physics underlining the key principles of atom-laser interactions and highlighting their relevance to the work presented later. In the following sections of the chapter a review of the work to date on reducing the physical dimensions of the gas host container will be presented. Different methods have been used for reducing the physical dimensions of the gas host, varying from micro-electronic-mechanical systems (MEMS) technology to dielectric waveguide technologies. The use of dielectric waveguiding geometries such as hollow-core photonic crystal fibers (HC-PCF) for hosting gas phase atomic and/or molecular media offers several benefits. It particularly includes a very long interaction length which is possible due to low loss propagation in such waveguide, tight transverse mode confinement and easy integration with existing fiber optic systems. These features mitigate some of the problems involved with reducing the transverse dimensions of the gas host container such as increased atom wall collisions. Miniaturisation of the gas host has become a pressing need to deliver the outstanding performance of atomic vapours to industry and the world outside the laboratory.

1.2 Basics of atom-light interaction

If we have to single out one key performance indicator to define the performance of an atom-optic device such a frequency reference and subsequently atomic clocks or magnetometers, it would be the magnitude ratio between the quality factor of the transition spectral and the SNR; Q/SNR. Indeed, the larger this ratio is the more stable the frequency reference is. This means that the linewidth of the transition spectral line must be as small as possible.

Whilst atomic and molecular transitions have an intrinsic fundamental linewidth set by the Heisenberg uncertainty principle, their lines are typically Doppler broadened to hundreds of megahertz by the Maxwell-Boltzmann velocity distribution of the atoms or molecules. This is why several experimental techniques for generating sub-Doppler transparency features in atomic and molecular have been developed and atom/molecule based frequency references. Examples of these techniques are saturated absorption spectroscopy (SAS) [17], electromagnetically induced transparency (EIT) [18][19], coherent population trapping (CPT) [20] and Ramsey interference [21][22]. Such methods are commonly used to generate extremely narrow sub Doppler transparency features for laser frequency stabilisation, atomic clocks and quantum sensors. The generation of such sub-Doppler spectral lines result from either velocity selective transition saturation or setting the atom in a coherent superposition state. Below, after listing the different mechanisms of line spectral broadening, we review the basic physics behind the generation of these sub-Doppler spectral lines.

1.2.1 Spectral line shapes

Atom absorbs photons appear optical absorption and optical lines shape are required resonant or near-resonant to the atomic transition. The experimentally observed linewidth of optical absorption is typically combined and broadened by four main mechanisms named Natural Broadening, Doppler Broadening, Power Broadening and Pressure Broadening. Atomic and molecular transitions are often formed as a Lorentzian oscillator.

The essential characteristics of the features of the atomic transition includes the quality factor (Q-factor) and signal-to-noise ratio (SNR) accompany with spectral broadening mechanisms which relate to atom or gas medium. These mechanisms limit the minimum linewidth of a spectral feature due to the Doppler broadening. The Lorentzian oscillators can be characterized by using the resonance Q-factor, which is expressed as the ratio of the average energy stored in the resonance and the dissipation rate of the energy.

$$Q = \frac{\omega_0}{\Delta\omega}, \tag{1-1}$$

here ω_0 is the frequency of the atomic transition and $\Delta\omega$ is the linewidth of the transition. Another characteristic employed in frequency standards and laser metrology is signal-noise-ratio which is combined with Q-factor as the fractional frequency deviations [23][24] and are described as following:

$$\frac{\Delta f}{f} \propto \frac{1}{SNR*Q}, \tag{1-2}$$

To minimize the fractional frequency deviation, a high Q-factor or high SNR are preferred. A high SNR can be required by optimizing the atom-light interaction (discussed in section 1.5). Extremely high Q factors have been achieved by laser cooling and trapping [8] ($Q \sim 9.8 \times 10^9$) and by using metastable optical transitions [10] ($Q \sim 1.6 \times 10^{13}$). Generally, a high Q-factor is obtained by minimizing the linewidth of the resonance. The following section will describes the main broadening mechanisms in the spectral features.

The absorption line shape is typically broadened by several processes, including Doppler, collisional, power and transit time. These mechanisms can be broken down into two categories, homogeneous [25, 26], acting on all the atoms in the same manner and inhomogeneous [25–27], a perturbation that depends on the energy state of each atom (*e.g.* atom velocity). Power and collisional broadening are examples of homogeneous broadening while transit time and Doppler broadening are examples of inhomogeneous broadening because of the dependence on the individual atomic velocities.

A. Natural Broadening

Natural broadening is the reason of quantum uncertainty in spontaneous emission of energy level. The interval energy level ΔE, in the form of the Heisenberg uncertainty principle is

$$\Delta E \Delta t \geq \hbar. \tag{1-3}$$

The uncertainty in time is the natural lifetime, $\Delta t = \tau_{nat}$. The uncertainty in frequency is $\Delta\nu = \Delta E/2\pi\hbar$, giving the natural linewidth $\Gamma_{nat} = \Delta\nu = 1/2\pi\tau_{nat}$. The excited states for example for Rb atom, $^2P_{1/2}$ and $^2P_{3/2}$ states, have natural lifetime τ_{nat} around 25 -35 ns. For the D1 and D2 transitions of alkali atoms, the natural linewidth is about 4-6 MHz. This magnitude of broadening mechanism is much smaller than other contributions which presents Lorentzian distribution. Ultimately the linewidth of an atomic transition can be reduced to this quantum limit.

B. Doppler Broadening

Doppler Broadening of atomic resonance lines is caused by the Doppler Effect, which the motional atom or molecular defined by temperature cause the absorbed light frequency shift from the resonance frequency as:

$$\nu = \nu_0 \left(1 - \frac{\upsilon_z}{c}\right), \tag{1-4}$$

Thus, the atomic population absorbs the off-resonance light. The probability $P(\upsilon_z)d\upsilon_z$ of an atom having a velocity in the range from υ_z to $\upsilon_z + d\upsilon_z$ is given by the Maxwellian distribution

$$P(v_z)dv_z = \left(\frac{m}{2\pi k_B T}\right)^{\frac{1}{2}} e^{-mv_z^2/2k_B T} dv_z, \tag{1-5}$$

resulting in the full width at half maximum (FWHM),

$$\Gamma_G = 2\frac{v_0}{c}\sqrt{\frac{2k_B T}{m} ln2}, \tag{1-6}$$

Doppler broadened linewidth of the D1 transition for ^{85}Rb and ^{87}Rb atom at room temperature is about 480 MHz [28]. The FWHM temperature dependency can be decreased by limiting the atom motion such as laser cooling [29][30].

C. Power Broadening

The power broadening is the dependence of the light intensity appeared on the spectral linewidth broadening. Typically, power broadening is observed as a Lorentzian profile when continuously monitored. For example, the excited state population in a two level system are interacted with a CW laser. The increase of laser intensity for any detuning causes more population to go to the excited state, so the signal is enhanced. The transition linewidth is the range of detuning for which the excited state acquires considerable transient population during the transit process. The range is broadened when the laser intensity increases, therefore power broadening is observed. As the host of quantum sensor, the operated light intensity in HC-PCF should be as low as possible to limit the power broadening and the stack shift from light [31].

D. Collisional Broadening

Atom-atom collisions and atom-wall collisions perturb the atoms with reduced lifetime in the excited state. This pressure dependent mechanism results in both a shift and broadening of the optical absorption line. The magnitudes of these phenomena are proportional to the number of perturbing atoms or gas molecules which are referred to the pressure shift and pressure broadening. This contribution of spectral broadening is a homogeneous effect therefore a Lorentzian distribution. Otherwise, the magnitude of collisional shift is much lower than the collisional broadening. The atom-wall collision in HC-PCF is enhanced due to the micro-meter geometric core size.

1.2.2 Coherence

According to quantum mechanics principles, the state of a quantum system such as an atom can be either in one of its eigenstates or in a superposition of these eigenstates. In this case, the latter exhibits a phase relationship between them and the resulting state is coined a coherent state. In practice, the coherent state is generated by one or more laser field resonant with atomic transition states. The stimulated electric dipole oscillations are strongly enhanced when the laser frequency is detuning close to the resonant frequency which is the phase relation between the field-induced coupled-states. The simplest coherence effect can be observed in a 2-level system driven by a laser frequency ω. The population of the ground state in such a system can be depleted to minimize spontaneous emission. Therefore, stimulated absorption and stimulated emission processes repeatedly oscillates between the ground state and the excited state. This process is known as Rabi oscillations and the coupling between the two states occurs at the oscillation frequency, called the Rabi frequency and given by

$$\Omega_R = \sqrt[2]{\Omega_0^2 + \Delta^2}, \tag{1-7}$$

where Δ is the detuning frequency from the resonance and

$$\Omega_0 = \frac{\mu \cdot E_0}{\hbar}. \tag{1-8}$$

E_0 is the amplitude of the electric field, μ is the transition electric dipole moment and ħ is reduced Planck constant. The Rabi frequency is generally used to take into account both the transition strength and the laser intensity thereby characterizing the light-matter interaction.

Figure 1-1 (b) shows the Rabi oscillations in two level system for different detuning frequency from resonance, $\Delta = 0$, Ω_0, $2\Omega_0$ (color curves respectively). In fact, the population in higher energy level has natural limited life time and decays at a rate given by spontaneous emission γ_{sp}. Such decay rate is strongly enhanced by external physical mechanisms which called dephasing mechanisms.

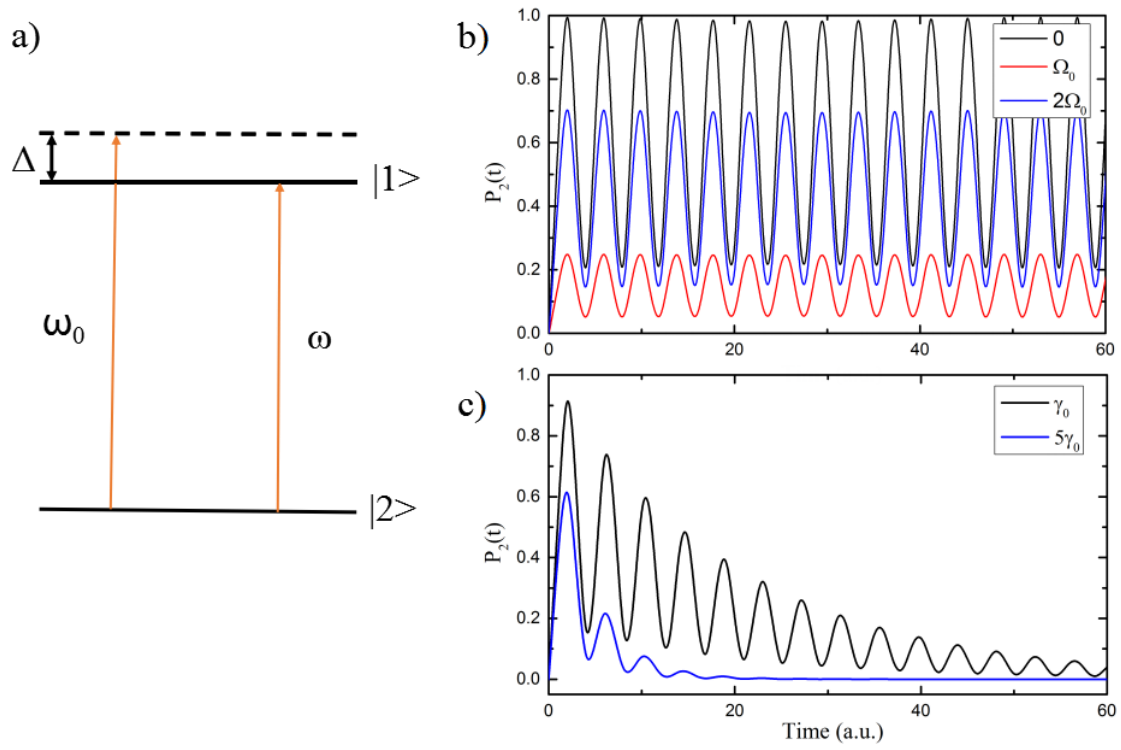

Figure 1-1: (a) 2-level atomic system resonant with frequency ω_0 interacted by laser field frequency ω. (b) Rabi oscillations of a 2-level atomic system with different detuning frequencies, $\Delta=0$ (black line), $\Delta=\Omega_0$ (blue line), $\Delta=2\Omega_0$ (red line). c) Rabi oscillations of a 2-level atomic system including dephasing. Dephasing rate = γ_o (black line) and $5\gamma_o$ (blue line).

The dephasing mechanisms could originate from any of the line broadening effects mentioned above. These dephasing strongly attenuate such an oscillation (coherence). If we limit these mechanism to those of collisional origin, then the coherence decay takes the following form given by $\frac{\gamma_{sp}}{2}+\gamma_{coll}$. Here, γ_{coll} is the collision induced coherence decay. Figure 1-1 (c) shows Rabi oscillations with different dephasing rates (γ_o-black curve and $5\gamma_o$-blue curve) resulting in damping of the oscillation as the relative phase relation between the levels is disrupted. Given that often the dephasing rate is always greater than the spontaneous emission limit, engineering coherence is extremely challenging and any resulting coherence is fragile and sensitive to perturbations.

1.2.3 Sub-Doppler transparencies generated techniques

A. Saturated Absorption Spectroscopy (SAS)

One of generating sub-Doppler features technique is saturated absorption spectroscopy (SAS), which does not depend on the coherence effect between atomic states but rely on the thermal atom velocity selection through optical pump process. The experimental configuration consists on using counter-propagate scheme through the atom medium which includes a single laser beam derived into one higher pump beam and one weak probe beam. This is described by using the population rate equations and can be realized by using only one single laser source. In the case of one single laser source, an individual atom at a velocity v cannot be resonant with the two fields (the same frequency) at the same time for a given transition. Once the atom is on resonance with pump beam, the atomic population of the ground state are fully pumped to the excited state and become saturated so that the counter-propagating weak probe beam will not interact with this atomic transition and appear transparent on the absorption lines. The sub-Doppler transparencies are recorded with the Doppler broadened absorption lines due to the Doppler effect of the thermal atom across the resonant transition. SAS was firstly and experimentally demonstrated in acetylene medium by Labachelerie *et al.* [32], by using a high finesse Fabry-Perot cavity in order to provide a sufficient interaction length for the laser-matter interaction. A linewidth of ~ 2 MHz is reported in this reference which feature linewidth can be as narrow as the power broadened linewidth and SAS have been extensively used in laser stabilization schemes.

B. Coherent Population Trapping

Coherent population trapping (CPT) was first demonstrated by Alzetta *et al.* in 1976 [33], and this was very shortly reviewed by Arimondo *et al.* [34] which is considered as coherent effect in a Lambda type 3-level systems. It was understood that the atoms were optical pumped into a dark state by two excitation beams. When the detuning between these two excitation beams is equal to the detuning of the two states, it will form a non-

dipole allowed transition whereby the state cannot spontaneously decay hence the atoms are trapped.

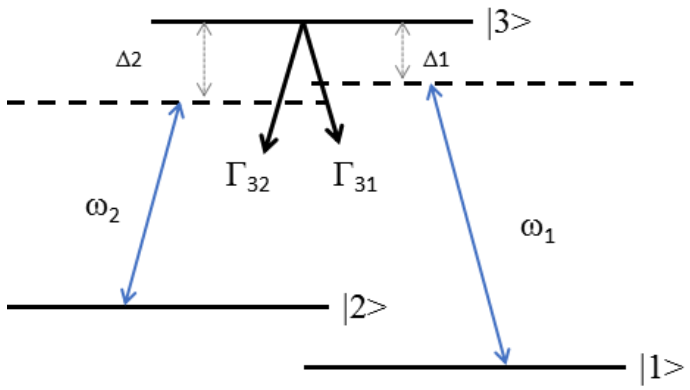

Figure 1-2: Schematic of three level system with related parameters: Δ_1 and Δ_2 are the detuning frequency from the resonance of each laser field which $\Delta_1=\omega_{31}-\omega_1$ and $\Delta_2=\omega_{32}-\omega_2$ respectively. Γ_{31} and Γ_{32} are the decay terms from the excited state to the two ground states.

The dark state was created by the interferences between two excitation levels from two ground states to a common excited state. This required Λ-type 3-levels system shown in fig. 1-2. Customarily, the laser resonating with the |1> ↔ |2> transition is called the probe laser, and the beam driving the |2> ↔ |3> transition is called the control laser. Both transitions are electric-dipole allowed transitions. Δ_1 and Δ_2 are the detuning frequency from the resonance of each laser field which $\Delta_1=\omega_{31}-\omega_1$ and $\Delta_2=\omega_{32}-\omega_2$ respectively. Γ_{31} and Γ_{32} are the spontaneous decay rates from the excited state to the two ground states, are about 1- 10 MHz.

In the experimental conditions, the presence of the laser fields changes the eigenstates of the Hamiltonian of atom-laser system thus the atom eigenstates are linear overlapped:

$$|\alpha^+\rangle = \sin\theta \sin\Phi\,|2\rangle + \cos\Phi\,|3\rangle + \cos\theta \sin\Phi\,|1\rangle$$

$$|\alpha^0\rangle = \sin\theta|1\rangle + \cos\theta\,|2\rangle, \qquad (1\text{-}9)$$

$$|\alpha^-\rangle = \sin\theta \cos\Phi\,|2\rangle + \sin\Phi\,|3\rangle + \cos\theta \cos\Phi\,|1\rangle$$

where θ and Φ are the 'mixing angles' which are expressed as [35]:

$$\tan\theta = \frac{\Omega_p}{\Omega_c}, \tag{1-10}$$

and

$$\tan 2\theta = \frac{\sqrt{\Omega_p^2+\Omega_c^2}}{\Delta}, \tag{1-11}$$

The detuning of the probe laser formed as the dressed states and the second formula in Eq. 1-11 indicates the formation of dark state $|\alpha^0\rangle$ when no decoupling from $|3\rangle$ state, any population spontaneous decay to the $|\alpha^0\rangle$ state becomes population trapped here. Thus two lasers are required to be phase coherent hence the dark overlap state can be formed.

C. Electromagnetically Induced Transparency (EIT)

Electromagnetically induced transparency (EIT) is a coherent effect but works on a slightly different principle compare to CPT, which phenomenon usually appears in the regime where the control laser is much stronger than the probe laser, *i.e.* $\Omega_p \ll \Omega_c$, and only the population of the state $|1\rangle$ has considered to be pumped completely. EIT phenomenon was first experimental observed by Harris *et al.* in strontium vapor cell [36]. Under the condition of $\Omega_p \ll \Omega_c$, the strong control laser shifts the energy levels away from the resonant center via AC stack effect, which can be understood as the creation of dressed states in atom-light system [37]. When the stack shift is equal to the Rabi frequency of the control laser, the absorption of the probe laser splits into a classic Autler-Townes doublet which splitting frequency is equivalent to the control laser Rabi frequency, and results an enhanced transparency at the resonant center-electromagnetically induced transparency.

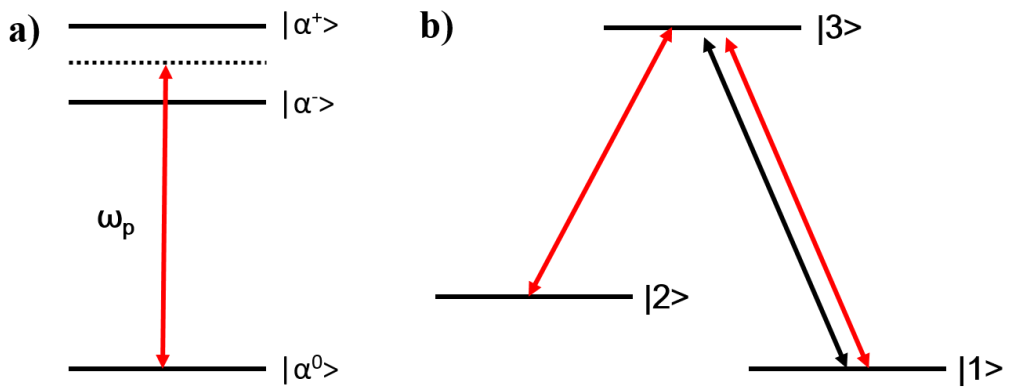

Figure 1-3: (a) Dressed states in atom-light system (b) Λ-type of 3-level system includes two coherent pathways |1>-|3> (black line) and |1>-|3>-|2>-|3> (red line).

In the case of $\Omega_p \ll \Omega_c$, the three dressed states can be simplified to give in the following equations:

$$|\alpha^+\rangle = \frac{1}{\sqrt{2}}(|2\rangle + |3\rangle)$$

$$|\alpha^0\rangle = |1\rangle, \qquad (1\text{-}12)$$

$$|\alpha^-\rangle = \frac{1}{\sqrt{2}}(|2\rangle - |3\rangle)$$

The schematic of dressed states is shown in fig. 1-3 (a). When a probe laser is applied to scanning across the bare states |2> and |3>, a modified absorption profile for these two dressed states is recorded. And the ground state is unmodified in the second equation. Considering interference pathways in a Λ-type 3-level system, the coupling laser which couples the states |2> and |3> through the available pathways to the excited state (|1>- |3> or |1>- |3>- |2>- |3>) has much higher Rabi frequency than the probe laser. Therefore the transit probability for these two pathways are quite similar and coherent, which lead to the absorption cancellation [38].

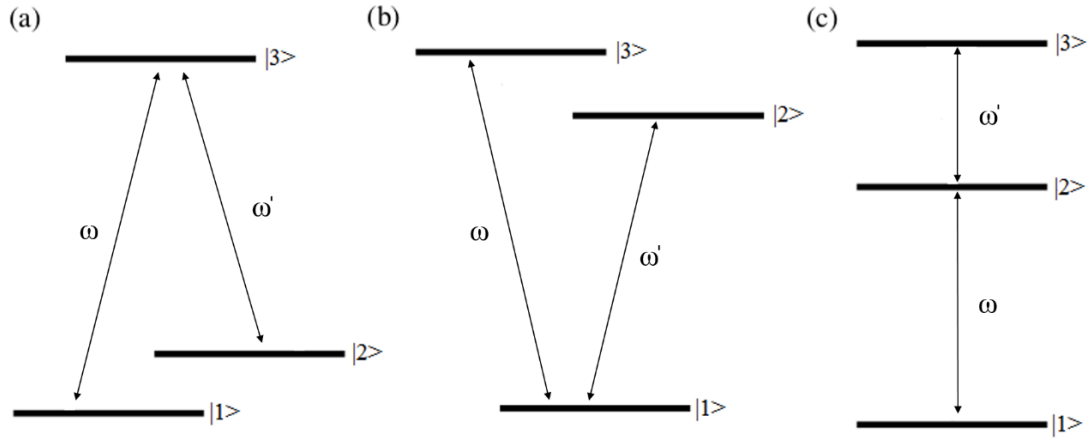

Figure 1-4: 3-level atom-light interaction system. a) Lambda (Λ) system, b) Vee (V) system, c) ladder system.

In EIT, there also exists quantum interference but mainly when the control laser Rabi frequency is in the order of the excited state linewidth. The destructive interference between the transit pathways of ground state to the induced dressed states is important in Λ-type systems [39], shown in fig. 1-4 (a). The interference results in the probe absorption being zero at the resonant center. Furthermore, the dressed state interference is not the main role in V-type (fig. 1-4 (b)) and ladder systems (fig.1-4 (c)) [40].

1.3 Compact host for atomic optics

The effort in miniaturizing atom or molecular cells for atom-optic related devices started in the 2000s. Two main classes of integrated or compact technologies have since been developed by several research groups. These are summarized in fig. 1-5. The first class to confine the atoms is a solution based on Micro-electronic-mechanical systems (MEMS) technology, and where by the atoms cell is sandwiched in layered architecture between integrated laser source and photodetector. The second class is based on dielectric waveguides where the gas cell acts as a harboring platform for the atoms and a light guidance. The first of these components is hollow-core photonic crystal fibers (HC-PCF), which has been transformed into a photonic microcell (PMC) by filling the fiber core with a given gas [41][42]. The most elaborate form of PMC consists of a gas filled HC-PCF that

is hermetically sealed by splicing its both ends to solid fibers. However, so far this all-fiber PMC has been limited to molecular gases, and atom vapor PMC is still to be developed. In parallel to HC-PCF, CMOS compatible resonant reflecting optical waveguides (ARROW's) have also been developed as atom cells [43][44].

Below a briefly overview on these atom-optic components. It is noteworthy that other schemes have or are being pursued, such as tapered nano-fiber, however, we limit our survey to those which acts as atom cells.

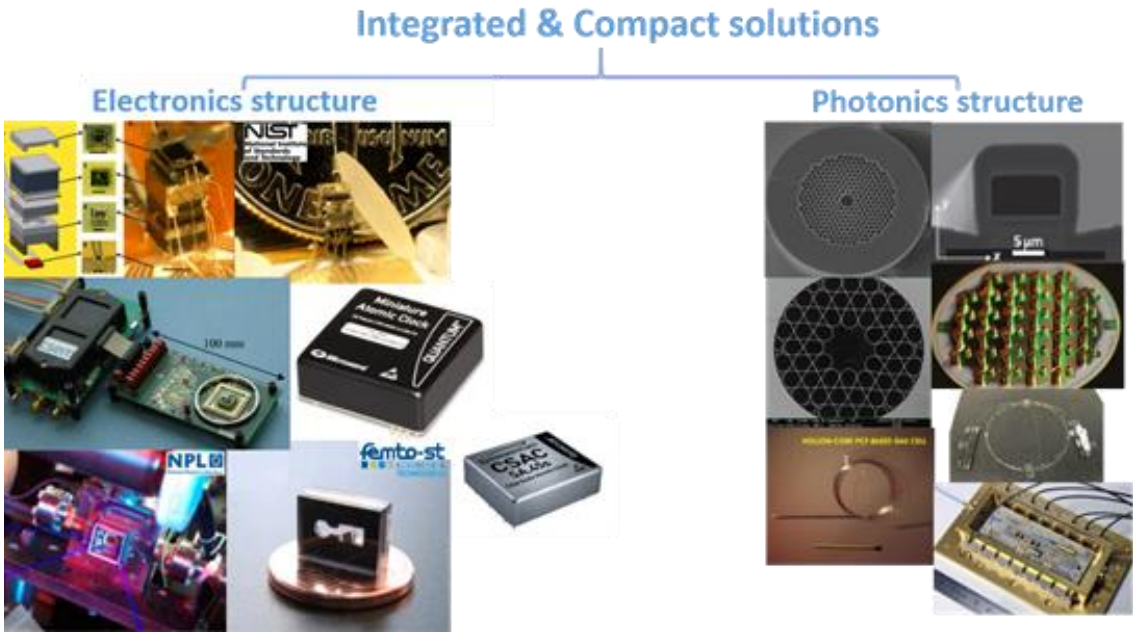

Figure 1-5: Illustrations of two compact solutions for atom and gas confined host. Left images are exciting electronics structure based on MEMS technology, right images are developing miniaturization solution based on photonics structure.

1.3.1 Compact quantum sensors in electronic structure: Chip Scale Atomic Clock (CSAC) and Chip Scale Atomic Magnetometer (CSAM)

The Chip Scale Atomic Clock (CSAC) program was initiated by DARPA in 2002. And very soon later, a micro fabricated atomic clock was reported by Knappe *et al*. in 2004 [16]. A MEMS-based atomic clock [16] and atomic magnetometer [45] was then reported by S. Knappe *et al.* in 2004 and become commercial device available now. This

miniaturization units are low cost repeatable manufactured and stable. For such a MEMS-based atomic clock, a volume of 10 mm^3 of this device could have a fractional frequency stability of 2.5×10^{-10} s^{-1}, and is featured with 7.1 kHz linewidth of Cesium atom sub-Doppler feature.

This device fulfils many of the requirements for a compact frequency standard such as reasonable short term stability, compact size and low power consumption. However the device requires external temperature and current control which adds to the size. Also the interaction length with the Cs vapour is extremely short because of the compact size as such the contrast of the frequency reference is extremely small, 0.91% of the total absorption line strength. For compact magnetometer, a chip-scale atomic magnetometer [46] has been implemented at NIST which is based on the D1 absorption line of ^{87}Rb atoms. The active interaction volume of this magnetometer is 1 mm^3 and can measure the magnetic fields with a sensitivity of 50 pT $Hz^{-1/2}$ over a frequency range of 10-100 Hz. It is the first chip-scale magnetometer based on an MEMS atomic vapor cell with comparable sensitivity to cost magneto-resistive sensors. New generation of Miniature Atomic Clock (MAC) SA.35m was released in 2012 by Microsemi *et al.* and could have a frequency accuracy of $3*10^{-11}$ per second with Rubidium, operation beam power is 12 mW and the weight is less than 100 g. In Parallel, some European projects such as MUSO project and CSEM project in Swiss, Optical space Cs clock (OSCC) project in France for Galileo system, have been established to develop miniature atomic clocks.

Finally, while the design is fully integrated it relies upon traditional free space propagation scaled down to the device size opposed to the following devices which are all waveguiding based designs, hence do not suffer from misalignment of optics.

1.3.2 Atom cell based on Hollow-core Anti Resonant Reflecting Optical Waveguide (ARROW)

Monolithically integrated rubidium vapor cell using hollow-core antiresonant reflecting optical waveguides (ARROWs) on a silicon chip has been reported in [43]. The Rb contained volume of ARROW is orders of magnitude less than bulk cells which enables high intensity light-atom interaction. And the saturation absorption spectroscopy (SAS) was demonstrated in Rb-filled ARROW waveguide with optical density (OD) > 2. Soon afterwards, the same group reported the reduced decoherence from atom-wall collision in octadecyldimethylmethoxysilane (ODMS) coated hollow-core ARROW [47]. A transparency feature of EIT has been observed in Rb vapor confined by using a pump beam of 18.2 mW and probe beam of 3.6 mW. The linewidth of EIT feature is ~ 50 MHz and the dephasing rate of 33MHz is much smaller than the expected in micrometric core size hollow-core waveguide which points to the efficiency of the ODMS coating and a loss of coherence after an average of 10.5 wall bounces. This is the first compact Rb confined photonics cell without bulk vacuum system. The absorption line contrast and the compactness of the cell is comparable to the bulk reference cell and MEMS device.

1.3.3 Gas-cell based on Hollow-core Photonic Crystal Fiber

The first reported works related to Rb vapor confined HC-PCF were reported by Gaeta group from Cornel university in 2006 [48] and the GPPMM, when located in the University of Bath, in 2007 [49]. In both works, the fiber core inner walls were coated with anti-relaxation material. In [48], the coating was organosilane, and which have later used as light-induced atomic desorption to release Rb atoms into the core, while in [49], the Rb was confined in polydimethylsiloxane (PDMS) coated Kagome HC-PCF.

In these seminal works, EIT generation has been demonstrated with a light-level as low as nanowatt power, which represents more than a 1000-fold reduction from the power required in bulk cell. Following on from this pioneering work demonstrating loading of Rb vapour into hollow-core photonic bandgap (PBG) fibers, a large body of work using these fibers has been demonstrated. Examples of such work includes spectroscopy of Rb atoms

loaded in hollow-core PBG fibers characterising the Stark and power shifts of Rb atoms confined within the hollow core [50]. Other work has involved loading cold trapped atoms either from magneto optical traps or Bose-Einstein condensates into the core of PBG fibers [51], [52]. Additionally the optical guidance of Rb atoms through a hollow-core PBG fiber [53], [54] has been demonstrated for potential applications in matter wave interferometry. More recently, cold Sr inside Kagome HC-PCF and trapped in 1D optical lattice has been successfully demonstrated [55]. Remarkably, the measured absorption linewidth of less than 10 kHz is limited by the excited state lifetime rather than the collision with the wall.

However all the atom filled HC-PCF systems so far reported are still connected to a bulk vacuum pump as maintaining the vacuum at 10^{-7} Torr level. And the atom loading time is still long in such a large core size hollow-core fiber.

1.3.4 Comparison of atom-confined photonic structures

The comparison of each photonic structures in different parameters are shown in Table (1-1). It is very clear shown the advantages and disadvantages for each structure. Mention here, the operating powers are required to observe sub-Doppler transparencies with confined optical mode field.

In ARROW, the operating power is extremely high because of the inefficient coupling in the waveguides and high losses [44]. There are two main drawbacks in atomic vapor applications, they are firstly long atom vapor loading time in small geometric core and secondly pressure broadening due to the wall-collision. Moreover, longer interaction length provides higher SNR. For PBG and Kagome HC-PCFs, it is possible to have hundreds of meters of interaction length with literally no propagation loss. Furthermore, the large core Kagome HC-PCF has the narrowest linewidth compare to other photonic waveguide.

Table 1-1: Comparison of atom-confined photonic structures.

PLATFORM	OPERATING POWER	MODE AREA (μM^2)	INTERACTION LENGTH (MM)	FWHM (MHZ)
ARROW	mW	8.8	50	50
PBG HC-PCF	nW	28	>1000	60
KAGOME HC-PCF	µW	95	>1000	6

1.4 Atom-Laser interaction enhancement in HC-PCF

Conventional experiments of matter-laser interaction is focusing laser beam to increase the intensity over a limited short interaction distance, which is Rayleigh length ($z_R = w_0^2/\lambda$) related to the Gaussian beam properties. The effective interaction volume $V = \pi w_0^2 z_R$ rapidly decreases with the waist radius w_0^4. Typically, this length is around 2 mm long for 30 µm waist beam. The comparison between the intensity and interaction length give a trade-off to increase the interaction efficiency which is expressed by a figure of merit [56]:

$$f_{om} = \frac{L_{int}\lambda}{A_{eff}}, \tag{1-13}$$

where L_{int} is the effective interaction length, λ is the wavelength, and A_{eff} is the cross-section area. The figure of merits for different guidance are plotted in the following figure. For a core radius of 10 µm HC-PCF with 0.07 dB/m attenuation, FOM is ~ 10^5 times higher than the FOM in capillary and thus prominently reduce the operated power for quantum sensor applications. Lower operated power has less stack shift and power broadening from the light.

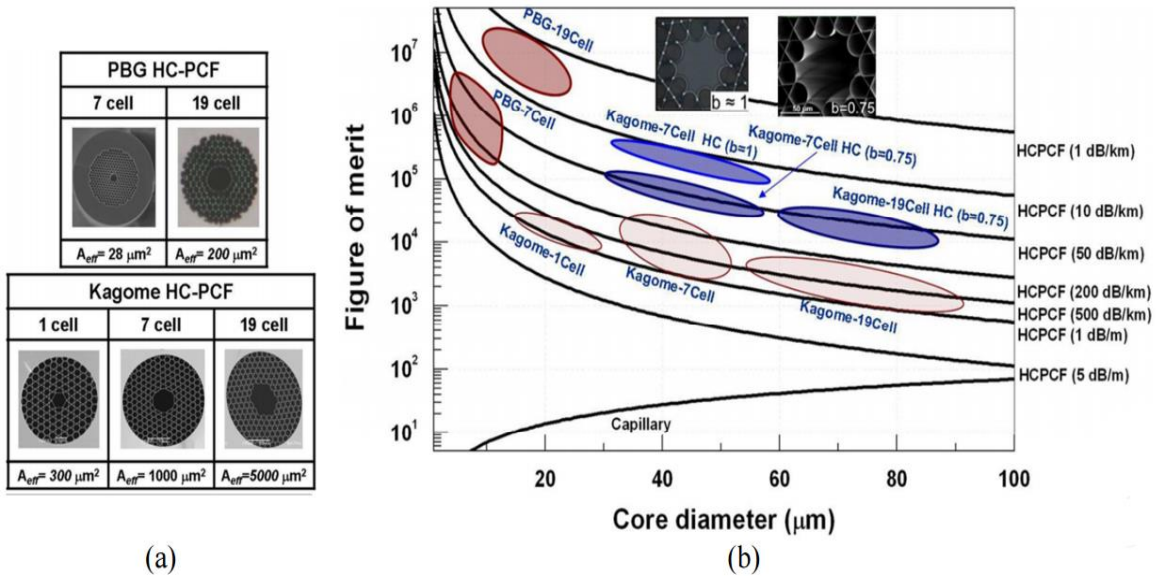

Figure 1-6: Comparisons of figure of merit (FOM) for capillary (black line), and different transmission loss HC-PCF [57].

Meanwhile, quantum sensor's performance is estimated the ultimate frequency stability of a frequency standard by [56]:

$$\sigma(\tau) = \frac{1}{K}\frac{1}{Q}\frac{1}{SNR}\frac{1}{\sqrt{\tau/s}}, \tag{1-14}$$

where $Q = v_0/\Delta v$ is the quality of factor, K is a constant of the order unity which depends on $I(\nu)$. The quantity Δv is the linewidth of the probed spectral signal, and thus is directly proportional to the total dephasing rate $\Delta v \propto \gamma_{tot}$. In the case of HC-PCF is often dominated by the collision with the wall which is above 1 MHz (see below). However, because of the strong increase in FOM mentioned above, the SNR is expected to be increased compared to bulk cells by as much as the order ~10^5 of FOM. Consequently, the degradation of Q in HC-PCF due to atom-wall collisions is strongly mitigated by the increase in SNR. Furthermore, such high SNR enables the observation of resonances with ultra-weak transition dipole moments, and that cannot be observed otherwise.

1.5 Progress in Gas Filled HC-PCF

The development on HC-PCF guidance has opened up vast possibilities for new gas or molecular filled optical sensing applications [41]. Below an impressive list of works reported: Mid-IR tunable laser based CO2 confined hollow-core fiber [58], Mid-IR laser emission from a C2H2 gas filled hollow-core fiber [59], hermetic Iodine hollow guidance frequency standard for telecommunication [60], resonant fiber optic gyroscope for rotational sensing application [61], acetylene filled hollow-core fiber optical frequency standard for telecommunication [62][63], nonlinear optics [64], efficient 1.9 μm emission in H2-filled hollow-core fiber [65], comb stabilization to an acetylene-filled HC-PCF [66], high power delivery and pulse compression [67], self-phase modulation in Xe-filled hollow-core PCF [68][69], near infrared C2H2 and HCN prototype hollow-core optical fiber gas laser [70], characterization of mid-infrared emissions from C2H2, CO, CO2, and HCN-filled hollow fiber lasers [71][72]. Also we count, several experiments demonstrate the possibilities of applications such as quantum memory[73], Raman comb generation in hollow-core PCF [74][75], ignition of an UV microwave Microplasma in Ar-filled HC-PCF [76], hollow-waveguide gas correlation radiometer for ultra-precise column measurements of formaldehyde (H_2CO on Mars environment [77]. In laser metrology applications such as EIT in acetylene filled HC-PCF [78][79][80], in Rb-filled HC-PCF [49][48] and in H2-filled HC-PCF [81], UV & Visible Raman laser in hydrogen (H2)-filled HC-PCF [82], 10 kHz accuracy of an optical frequency reference based on $^{12}C_2H_2$-filled large-core Kagome photonic crystal fibers [83], High harmonic generation (HHG) in a gas-filled HC-PCF [84], FM saturation spectroscopy on near infrared of ammonia (14NH3) in a HC-PBF [85], CW Raman Fiber-Gas-Laser based on H_2-filled HC-PCF [81], Saturated absorption (SAS) is studied in overtone transitions of C2H2 and H13CN molecules confined in the hollow-core of a photonic bandgap fiber [86] and Stimulated Raman Scattering (SRS) in Hydrogen-Filled Hollow-Core Photonic Crystal Fiber [56] have been demonstrated.

1.6 The dephasing effects in HC-PCF

The micro-confined geometric of HC-PCF cause disadvantages of increasing of atom-wall collision because of the mean free path of thermal atom or molecular is much larger than the core diameter. Generally, the time of fly between two walls collision is shorter than 100 ns for a core diameter of 50 μm. This phenomenon causes dephasing effects of atom-wall collision which is a significant limiting factor in the linewidth broadening. The transit time broadening and atom wall broadening are given by the following [87] [48]:

$$\gamma_{TT} = \frac{0.58}{\pi R_{MFD}} \sqrt{\frac{2K_B T}{m}}, \tag{1-15}$$

and,

$$\gamma_{wall} = \frac{2.405^2 D}{R_{core}^2} \left(\frac{1}{1+cK_n} \right), \tag{1-16}$$

where k_B is the Boltzmann constant, T is ambient temperature, m is the atomic mass, c is 6.8 in the limit of the hard-sphere model, K_n is the Knudsen number and D is the self-diffusion coefficient given by [26]

$$D = \frac{1.86\times10^{-22}\, T^{3/2}}{P\sigma^2\sqrt{m}}, \tag{1-17}$$

where P is the atom or molecular gas pressure and σ is the atomic collisional cross section [28] which equals 2.9×10^{-9} cm^2 for ^{85}Rb.

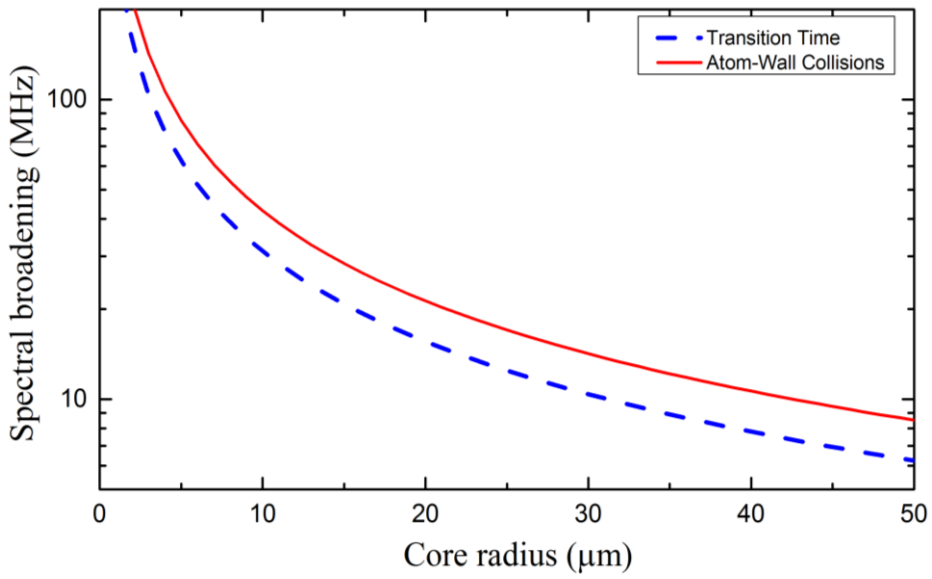

Figure 1-7: Spectral broadening from the transit time (dash line) and atom-wall collisions of core radius (solid line) dependency.

Figure 1-7 shows the spectral broadening due to the transit time and the atom-wall collision for different fiber core radii. The curve clearly shows the advantage of using HC-PCF with larger core diameter. From the stand point, Kagome fibers offers the advantage of exhibiting broadband transmission but also has reduced dephasing rate compared to PBG guiding HC-PCF. This broadening contribution from both transit time and atom-wall collision are much larger than the linewidth of sub-Doppler features. For example, the pressure broadening from transit time and atom-wall collision are γ_{TT} ~ 4 MHz andγ_{wall} ~ 5 MHz for a core size of 15 μm Kagome HC-PCF. Furthermore, the small difference between the two dephasing mechanisms makes it challenging to distinguish the transit time from the wall collision rate in HC-PCF's sub-Doppler transparencies which is difficulty to investigate the performance of antirelaxtion coating material for quantum sensor applications. In fact, antirelaxation material coating performance has been studied in macroscopic Alkali atom vapor cells by Balabas and Budker [88][89][90][91][92][93][94][95] with outstanding performance of ultra-long transverse relaxation times coating. However, previous method to know the coating performance in HC-PCF is estimated from the measurement of the FWHM of sub-Doppler features. In this thesis, investigation on the longitudinal relaxation time of coating which is distinguished

from transit time to understand the anti-relaxation material coating performance have been reported (Chapter 4). Sub-Doppler features are also observed in such coated Kagome HC-PCF (Chapter 5).

1.7 Atom loading in HC-PCF

The Alkali atom loading into micron geometric HC-PCF is a conspicuously challenge over past decades because of the ultra-low vacuum confinement pressure of Alkali atom. One way to overcome this challenge is to heating the ultra-high vacuum (UHV) host to increase the contained pressure.

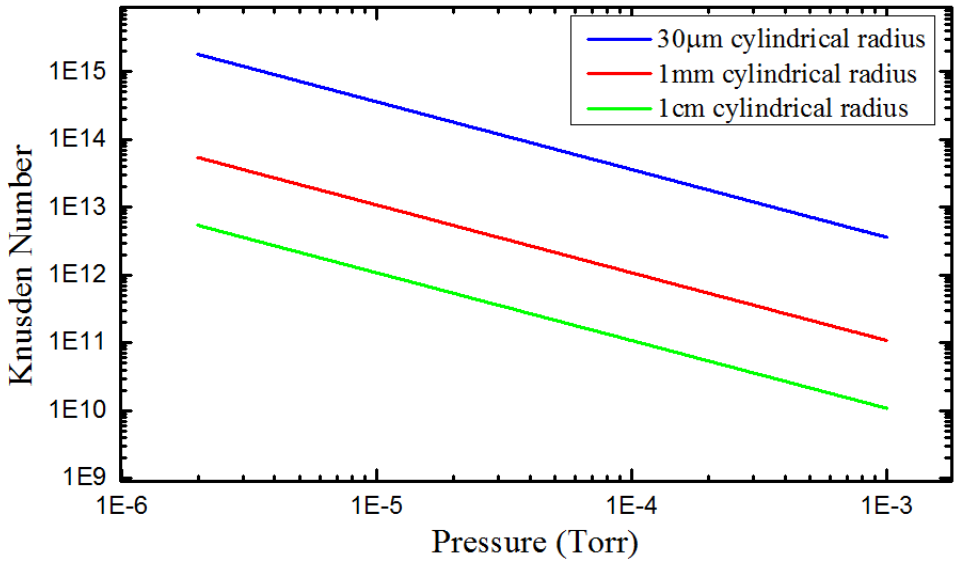

Figure 1-8: Knudsen numbers for Rb atom at different pressures with different host cylindrical radius, 30 μm (blue line), 1 mm (red), 1 cm (green).

Secondly consideration of the problem is the mean free path much larger than the fiber geometric core size which relate by considering the Knudsen number with different gaseous flow regimes [96][97].

$$K_n = \frac{\lambda_{MFP}}{d}, \tag{1-18}$$

where d is the radius of hollow host to diffused in, λ_{MFP} is the mean free path of Rb atom given by [97]

$$\lambda_{MFP} = \frac{\sqrt{\pi}\mu}{2P}\left(\frac{2k_BT}{m}\right)^{1/2}, \tag{1-19}$$

where μ the viscosity coefficient, k_B is the Boltzmann constant, m is the atomic mass, T is the ambient temperature, and P is the gas pressure. When the atoms or molecules follow a molecular-free flow regime, the low ambient pressure offer atoms' mean free paths on the order of 10s' meters. In this regime, atom-atom collisions is much less than atom-wall collisions, thus only atom-wall collision could change the atomic velocity. The Knudsen number is plotted in fig.1-8 for different host radius as a function of Rb atom vacuum pressure. One can direct see that the higher gas pressure (10^{-3} Torr) with large core diameter 1 cm, the Knudsen number is quite large ($K_n > 10^8$) corresponding to the regime of molecular free flow. In the typical experimental parameters where the Rb atom pressure is < 10^{-4} Torr and the host core radius is ~ 30 μm, the Knudsen number is extremely large, which $K_n > 10^{12}$. When consider the large aspect ratio of HC-PCF of fiber length >> inner core diameter with Knudsen numbers, the loading process of the Rb atom into the hollow-core will become extremely slow. The pressure evolution of atom medium in HC-PCF is given by [98]

$$\frac{P(t)}{P_0} = 1 - \frac{8}{\pi}\sum_{j=1,3,5}^{\infty}\frac{1}{j}\exp\left[-\left(\frac{j\pi}{\xi L}\right)Dt\right], \tag{1-20}$$

where P(t) is the temporal pressure in HC-PCF, P_0 is the initial ambient pressure out of the HC-PCF, ξ is a geometric factor, ξ = 1 for both fiber ends loading, ξ = 2 for one single open loading, L is the fiber length, t is the loading time and D is the diffusion constant of gas flow rate. This diffusion constant in free flow regime is given by:

$$D = \frac{2}{3}av, \tag{1-21}$$

where a is core radius, and v is the thermal atom velocity. In the viscous flow regime the diffusion constant is given by

$$D = \frac{a^2 P_0}{8\eta}, \tag{1-22}$$

where P_0 is the ambient pressure out of the fiber andη is the gas viscosity. The equation (1-20) is plotted in fig. 1-9 (a) for molecular free flow and viscous flow regimes. Clearly to see the loading time for molecular is much shorter compare to Rb atom loading.

The estimation of loading time into the 80 mm HC-PCF at P_0 = 1 bar for Rb atoms is around 60 days. The loading time estimation is given by,

$$t_{fill} = \frac{(\xi L)^2}{\pi^2 D} \ln\left[\frac{\pi}{8} \times \frac{P_0}{P_0 - P}\right], \tag{1-22}$$

where P is 85% of P_0 are given above. The estimated ^{85}Rb atom loading time decreases as a function of the hollow-core size plotted in fig. 1-9 (b). For a typical Kagome hollow-core size of 10 ~ 50 µm, the loading time varies between 20 ~ 80 days.

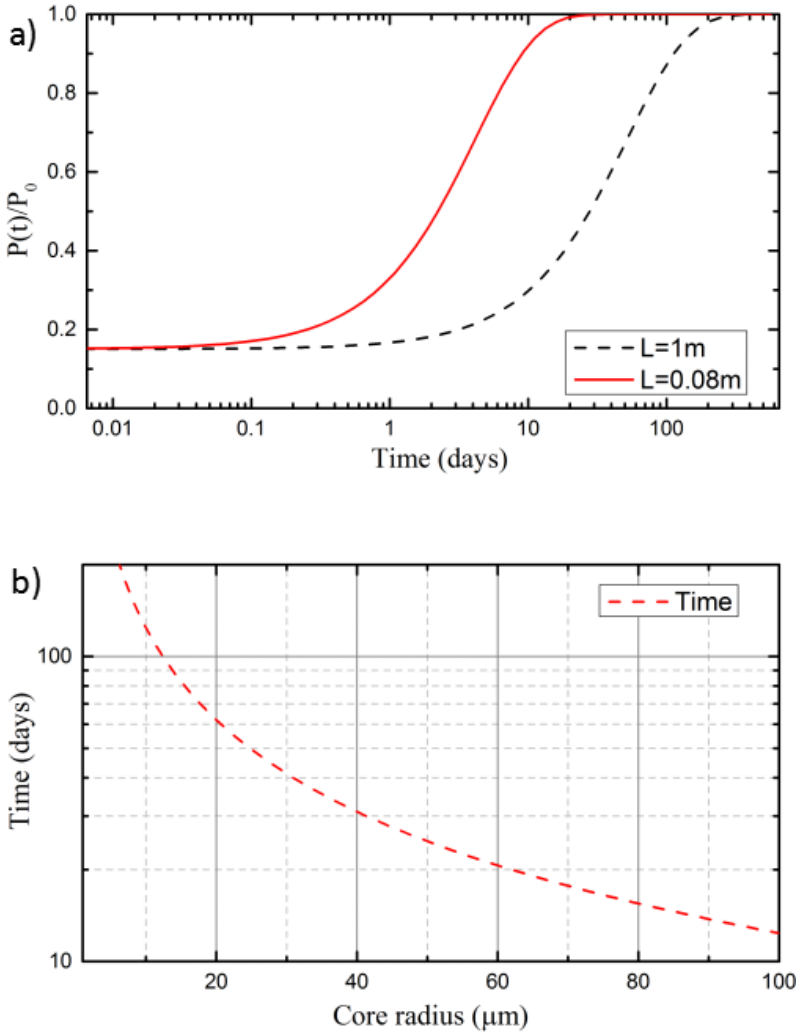

Figure 1-9: (a) Molecular (dashed black) loading in 1 m length of HC-PCF with core diameter of 30 µm and atomic Rb vapour (solid black) loading dynamics in 80 mm length of Kagome HC-PCF with 30 µm diameter hollow-core, (b) Characteristic Rb vapour loading time as a function of hollow-core radius.

1.8 Summary and thesis outline

In this chapter, the physics of atomic optics and the technique to generate sub-Doppler spectral lines were introduced. The motivations in developing miniature atom cell and atom-optics devices were delineated. Two main routes in compact atom cell are now emerging. The one which is pursued in this thesis relates to HC-PCF based atom cells. We have seen that while HC-PCF provides strong enhancement in SNR and fulfills the compactness requirements, this solution show challenges to be address from a technological and performance point of view.

The work presented in this thesis is related to the development of atom vapor PMC. This means the development of a stand-alone fiber component that acts also as highly compact and integrable vapor-cell. The thesis presents the different processes in the Rb loading HC-PCF. This process chain comprises fiber definition and characterization, fiber post-processing, which spans from fiber wall-coating to tapering and HC-PCF end-splicing. The thesis also presents the different spectroscopy experiments that have been set-up to assess the dominant relaxation effects that affect coherent optical phenomena in atom filled HC-PCF. An emphasis is put on the role of the atom-surface interactions, and whereby atom-surface induced sub-Doppler transparencies are reported. The thesis in outlined as follows:

In Chapter 2 we review the optical guidance principles in HC-PCF. An emphasis is drawn on Inhibited-Coupling (IC) guiding HC-PCF, developed in the GPPMM, and whose properties are very promising for atom-optics application. We also present the different fibers that were selected for atom loading and characterize their optical properties. These fibers exhibits different core diameter and ranges from ~ 30 to 80 µm to assess in a systematic manner the effect of the core size on the atom dynamics inside the fiber.

In Chapter 3, we list the different processes that have been used in post-processing the HC-PCF before and during the rubidium loading. This post-processing chain will be used for alkali vapor PMC assembly. It comprises HC-PCF specific tapering and splicing techniques. In the post-processing, the HC-PCF can be coated with different coating materials, and in our case we use PDMS and ceramic coating to assess the atom-surface

dynamics and to reduce the physio-chemical adsorption effects respectively. We also describe the HC-PCF setting inside high vacuum systems and present the different coated and uncoated HC-PCF that have been loaded with the Rb. We have then assessed the atom life time inside the HC-PCF.

Chapter 4 and 5 covers spectroscopy experimental work. In Chapter 4, we describe a magneto-optical spectroscopy set-up to measure the Rb ground state polarization relaxation rate. Using this protocol backed with Monte-Carlo simulations we deduce the relaxation rate of different mechanisms. The results show that the dwell time of the atom of the surface play a dominant role along with the transit time, which because of it short duration, slow atoms are preferred in optical pumping or quantum state preparation. Finally the measured relaxation rate for different core surface is shown.

In the last Chapter 5, we report on a new mechanism of sub-Doppler transparency generation. Unlike SAS or EIT, the experimental configuration to generate these sub-Doppler lines requires only one single forward propagating laser beam. Systematic experimental and theoretical analysis of these transparencies indicate that the results from the vibrational levels of the atoms trapped in the fiber core surface potential. These results are further insight to the results of chapter in hgihlighting the original dynamic of the atoms inside the core of HC-PCF. These results would certainly be very useful in anticipating and designing quantum devices based on alkali vapor PMC.

1.9 References

[1] Townes, Charles H. "Production of coherent radiation by atoms and molecules." (1964): 30-43. N. Lecture

[2] D.Budker, *Optical Magnetometry*. 2013.

[3] Holloway, Christopher L., Josh A. Gordon, Matt T. Simons, David A. Anderson, Andrew Schwarzkopf, Stephanie A. Miller, Nithiwadee Thaicharoen, and Georg Raithel. "Atom-based RF field probe: From self-calibrated measurements to sub-wavelength imaging." In *Nanotechnology (IEEE-NANO), 2015 IEEE 15th International Conference on*, pp. 789-791. IEEE, 2015.

[4] Heshami, Khabat, Duncan G. England, Peter C. Humphreys, Philip J. Bustard, Victor M. Acosta, Joshua Nunn, and Benjamin J. Sussman. "Quantum memories: emerging applications and recent advances." *Journal of Modern Optics* 63, no. 20 (2016): 2005-2028.

[5] Khurgin, Jacob B. "Slow light in various media: a tutorial." *Advances in Optics and Photonics* 2, no. 3 (2010): 287-318.

[6] S. Haroche and D. Kleppner, “Cavity quantum electrodynamics,” *Phys. Today*, vol. 42, no. 1, pp. 24–30, 1989.

[7] Phillips, William D. "Nobel Lecture: Laser cooling and trapping of neutral atoms." *Reviews of Modern Physics* 70, no. 3 (1998): 721.

[8] Hall, John L., and NIST JILA. "Defining and Measuring Optical Frequencies: The Optical Clock Opportunity–and More." *Nobel Lecture, December* 8 (2005): 7.

[9] Anderson, Brian P., and M. A. Kasevich. "Loading a vapor-cell magneto-optic trap using light-induced atom desorption." *Physical Review A* 63, no. 2 (2001): 023404.

[10] Takamoto, Masao, Feng-Lei Hong, Ryoichi Higashi, and Hidetoshi Katori. "An optical lattice clock." *Nature* 435, no. 7040 (2005): 321-324.

[11] R. Le Targat, L. Lorini, Y. Le Coq, M. Zawada, J. Guéna, M. Abgrall, M. Gurov, P. Rosenbusch, D. G. Rovera, B. Nagórny, R. Gartman, P. G. Westergaard, M. E. Tobar, M. Lours, G. Santarelli, A. Clairon, S. Bize, P. Laurent, P. Lemonde, and J. Lodewyck, "Experimental realization of an optical second with strontium lattice clocks.," *Nat. Commun.*, vol. 4, p. 2109, 2013.

[12] Hänsch, Theodor W. "Nobel lecture: passion for precision." *Reviews of Modern Physics* 78, no. 4 (2006): 1297.

[13] Anderson, Mike H., Jason R. Ensher, Michael R. Matthews, Carl E. Wieman, and Eric A. Cornell. "Observation of Bose-Einstein condensation in a dilute atomic vapor." *science* 269, no. 5221 (1995): 198.

[14] J. Fixler, "Atom interferometer-based gravity gradiometer measurements (Thesis: PhD)," *Thesis*, p. 138 pp., 2003.

[15] Gustavson, T. L., P. Bouyer, and M. A. Kasevich. "Precision rotation measurements with an atom interferometer gyroscope." *Physical Review Letters* 78, no. 11 (1997): 2046.

[16] S. Knappe, V. Shah, P. D. D. Schwindt, L. Hollberg, J. Kitching, L. A. Liew, and J. Moreland, "A microfabricated atomic clock," *Appl. Phys. Lett.*, vol. 85, no. 9, pp. 1460–1462, 2004.

[17] Akulshin, A. M., V. A. Sautenkov, V. L. Velichansky, A. S. Zibrov, and M. V. Zverkov. "Power broadening of saturation absorption resonance on the D2 line of rubidium." *Optics Communications* 77, no. 4 (1990): 295-298.

[18] S. E. Harris, "Lasers without Inversion: Interference of Lifetime-Broadened Resonances," *Phys. Rev. Lett.*, vol. 62, no. 9, pp. 1033–1036, 1989.

[19] K. J. Boller, A. Imamoglu, and S. E. Harris, "Observation of Electromagnetically Induced Transparency," *Phys. Rev. Lett.*, vol. 66, no. 20, pp. 2593–2596, 1991.

[20] Arimondo, Ennio. "V coherent population trapping in laser spectroscopy." *Progress in optics* 35 (1996): 257-354.

[21] Ramsey, Norman F. "A molecular beam resonance method with separated oscillating fields." *Physical Review* 78, no. 6 (1950): 695.

[22] Ramsey, Norman F. "Experiments with separated oscillatory fields and hydrogen masers." Reviews of modern physics 62, no. 3 (1990): 541.

[23] D. W. Allan, "Statistics of Atomic Frequency Standards," *Proc. IEEE*, vol. 54, no. 2, pp. 221–230, 1966.

[24] Cutler, Leonard S., and Campbell L. Searle. "Some aspects of the theory and measurement of frequency fluctuations in frequency standards." *Proceedings of the IEEE* 54, no. 2 (1966): 136-154.

[25] Demtröder, Wolfgang. "Widths and Profiles of Spectral Lines." In *Laser Spectroscopy*, pp. 57-98. Springer Berlin Heidelberg, 1996.

[26] Shimoda, K. O. I. C. H. I. "Line broadening and narrowing effects." *High-Resolution Laser Spectroscopy* (1976): 11-49.

[27] Rautian, Sergei G., and Igor I. Sobel'man. "The effect of collisions on the Doppler broadening of spectral lines." *Soviet Physics Uspekhi* 9, no. 5 (1967): 701.

[28] S. J. Seltzer, "Developments in Alkali-Metal Atomic Magnetometry," *Dissertation*, 2008.

[29] Okaba, Shoichi, Tetsushi Takano, Fetah Benabid, Tom Bradley, Luca Vincetti, Zakhar Maizelis, Valery Yampol'Skii, Franco Nori, and Hidetoshi Katori. "Lamb-Dicke spectroscopy of atoms in a hollow-core photonic crystal fibre." *Nature communications* 5 (2014).

[30] Alharbi, Meshaal, Anton Husakou, M. Chafer, Benoît Debord, Frédéric Gérome, and F. Benabid. "Sub-recoil linewidth and high power CW stimulated Raman scattering in the Lamb-Dicke regime." In *Lasers and Electro-Optics (CLEO), 2016 Conference on*, pp. 1-2. IEEE, 2016.

[31] Vitanov, N. V., B. W. Shore, L. Yatsenko, K. Böhmer, T. Halfmann, T. Rickes, and K. Bergmann. "Power broadening revisited: theory and experiment." *Optics communications* 199, no. 1 (2001): 117-126.

[32] M. De Labachelerie, K. Nakagawa, and M. Ohtsu, "Ultranarrow 13C2H2 saturated-absorption lines at 1.5 μm," *Opt. Lett.*, vol. 19, no. 11, pp. 840–842, 1994.

[33] Alzetta, G. A. M. L., A. Gozzini, L. Moi, and G. Orriols. "An experimental method for the observation of rf transitions and laser beat resonances in oriented Na vapour." *Il Nuovo Cimento B (1971-1996)* 36, no. 1 (1976): 5-20.

[34] Arimondo, Ennio. "V coherent population trapping in laser spectroscopy." *Progress in optics* 35 (1996): 257-354.

[35] J. P. Marangos, "Topical review Electromagnetically induced transparency," *J. Mod. Phys.*, vol. 45, no. 3, pp. 471–503, 1998.

[36] J. E. Field, K. H. Hahn, and S. E. Harris, "Observation of Electromagnetically Induced Transparency in CoIlisionally Broadened Lead Vapor," *Physical Review Letters*, vol. 67. p. 3062, 1991.

[37] Cohen-Tannoudji, Claude, and Serge Reynaud. "Modification of resonance Raman scattering in very intense laser fields." *Journal of Physics B: Atomic and Molecular Physics* 10, no. 3 (1977): 365.

[38] M. Fleischhauer and J. P. Marangos, "Electromagnetically induced transparency: Optics in coherent media," *Rev Mod Phys*, vol. 77, no. 2, pp. 633–673, 2005.

[39] Li, Yong-qing, and Min Xiao. "Observation of quantum interference between dressed states in an electromagnetically induced transparency." *Physical Review A* 51, no. 6 (1995): 4959.

[40] Khan, Sumanta, Vineet Bharti, and Vasant Natarajan. "Role of dressed-state interference in electromagnetically induced transparency." *Physics Letters A* 380, no. 48 (2016): 4100-4104.

[41] F. Benabid, F. Couny, J. C. Knight, T. a Birks, and P. S. J. Russell, “Compact, stable and efficient all-fibre gas cells using hollow-core photonic crystal fibres.,” *Nature*, vol. 434, no. 7032, pp. 488–491, 2005.

[42] F. Benabid, J. C. Knight, G. Antonopoulos, and P. S. J. Russell, “Stimulated Raman scattering in hydrogen-filled hollow-core photonic crystal fiber.,” *Science*, vol. 298, no. August 2016, pp. 399–402, 2002.

[43] W. Yang, D. B. Conkey, B. Wu, D. Yin, A. R. Hawkins, and H. Schmidt, “Atomic spectroscopy on a chip,” *Nat. Photonics*, vol. 1, no. 6, pp. 331–335, 2007.

[44] B. Wu, J. F. Hulbert, A. R. Hawkins, and H. Schmidt, “Planar hollow-core waveguide technology for atomic spectroscopy and quantum interference in alkali vapors,” *J. Light. Technol.*, vol. 26, no. 23, pp. 3727–3733, 2008.

[45] S. Knappe, P. D. D. Schwindt, V. Gerginov, V. Shah, L. Liew, J. Moreland, H. G. Robinson, L. Hollberg, and J. Kitching, “Microfabricated atomic clocks and magnetometers,” *IEEE/LEOS Opt. MEMS 2005 Int. Conf. Opt. MEMS Their Appl.*, vol. 8, pp. 193–194, 2005.

[46] P. D. D. Schwindt, S. Knappe, V. Shah, L. Hollberg, J. Kitching, L. A. Liew, and J. Moreland, “Chip-scale atomic magnetometer,” *Appl. Phys. Lett.*, vol. 85, no. 26, pp. 6409–6411, 2004.

[47] Wu, Bin, John F. Hulbert, Evan J. Lunt, Katie Hurd, Aaron R. Hawkins, and Holger Schmidt. "Slow light on a chip via atomic quantum state control." *Nature Photonics* 4, no. 11 (2010): 776-779.

[48] Ghosh, Saikat, Amar R. Bhagwat, C. Kyle Renshaw, Shireen Goh, Alexander L. Gaeta, and Brian J. Kirby. "Low-light-level optical interactions with rubidium vapor in a photonic band-gap fiber." *Physical review letters* 97, no. 2 (2006): 023603.

[49] Light, P. S., Fetah Benabid, F. Couny, M. Maric, and A. N. Luiten. "Electromagnetically induced transparency in Rb-filled coated hollow-core photonic crystal fiber." *Optics letters* 32, no. 10 (2007): 1323-1325.

[50] A. D. Slepkov, A. R. Bhagwat, V. Venkataraman, P. Londero, and A. L. Gaeta, "Spectroscopy of Rb atoms in hollow-core fibers," *Phys. Rev. A - At. Mol. Opt. Phys.*, vol. 81, no. 5, 2010.

[51] M. Bajcsy, S. Hofferberth, T. Peyronel, V. Balic, Q. Liang, A. S. Zibrov, V. Vuletic, and M. D. Lukin, "Laser-cooled atoms inside a hollow-core photonic-crystal fiber," *Phys. Rev. A - At. Mol. Opt. Phys.*, vol. 83, no. 6, 2011.

[52] C. Christensen, S. Will, M. Saba, G.-B. Jo, Y.-I. Shin, W. Ketterle, and D. Pritchard, "Trapping of ultracold atoms in a hollow-core photonic crystal fiber," *Phys. Rev. A*, vol. 78, no. 3, p. 33429, Sep. 2008.

[53] T. Takekoshi and R. J. Knize, "Optical Guiding of Atoms through a Hollow-Core Photonic Band-Gap Fiber," *Phys. Rev. Lett.*, vol. 98, no. 21, p. 210404, 2007.

[54] S. Vorrath, S. a. Möller, P. Windpassinger, K. Bongs, and K. Sengstock, "Efficient guiding of cold atoms through a photonic band gap fiber," *New J. Phys.*, vol. 12, 2010.

[55] S. Okaba, T. Takano, F. Benabid, T. Bradley, L. Vincetti, Z. Maizelis, V. Yampol'skii, F. Nori, and H. Katori, "Lamb-Dicke spectroscopy of atoms in a hollow-core photonic crystal fibre," *Nat Commun*, vol. 5, Jun. 2014.

[56] F. Benabid, J. C. Knight, G. Antonopoulos, and P. S. J. Russell, "Stimulated Raman Scattering in Photonic Crystal Fiber," *October*, vol. 298, no. October, pp. 2000–2003, 2002.

[57] Benoit, Aurélien. "Sources laser fibrées hybrides de haute puissance: Amplification et conversion de fréquences." PhD diss., Université de Limoges, 2015.

[58] P. G. Westergaard, J. W. Thomsen, M. R. Henriksen, M. Michieletto, M. Triches, J. K. Lyngsø, and J. Hald, "Compact, CO_2-stabilized tuneable laser at 205 microns," *Opt. Express*, vol. 24, no. 5, p. 4872, 2016.

[59] Fujii, Toshihiro. "Analysis of products from a C 2 H 2/N 2 microwave discharge: new nitrile species." *Chemical physics letters* 313, no. 5 (1999): 733-740.

[60] P. S. Light, J. D. Anstie, F. Benabid, and A. N. Luiten, “Hermetic optical-fiber iodine frequency standard,” *Opt. Lett.*, vol. 40, no. 12, pp. 2703–2706, 2015.

[61] Fsaifes, I., Gilles Feugnet, S. Schwartz, Benoît Debord, Frédéric Gerôme, Georges Humbert, F. Benabid, and Fabien Bretenaker. "Kagome hollow-core photonic crystal fiber resonator for rotation sensing." In *The European Conference on Lasers and Electro-Optics*, p. CH_5_1. Optical Society of America, 2015.

[62] Triches, Marco, Anders Brusch, Jan Hald, Jesper Lægsgaard, and Ole Bang. "Fiber-based portable optical frequency standard for telecommunication." In *Lasers and Electro-Optics (CLEO), 2015 Conference on*, pp. 1-2. IEEE, 2015.

[63] C. Wang, N. V Wheeler, C. Fourcade-Dutin, M. Grogan, T. D. Bradley, B. R. Washburn, F. Benabid, and K. L. Corwin, “Acetylene frequency references in gas-filled hollow optical fiber and photonic microcells.,” *Appl. Opt.*, vol. 52, no. 22, pp. 5430–9, 2013.

[64] P. S. J. Russell, P. Hölzer, W. Chang, A. Abdolvand, and J. C. Travers, “Hollow-core photonic crystal fibres for gas-based nonlinear optics,” *Nat. Photonics*, vol. 8, no. 4, pp. 278–286, 2014.

[65] Z. Wang, F. Yu, W. J. Wadsworth, and J. C. Knight, “Efficient 1.9 μ m emission in H 2 -filled hollow core fiber by pure stimulated vibrational Raman scattering,” *Laser Phys. Lett.*, vol. 11, no. 10, p. 105807, 2014.

[66] S. Wu, C. Wang, C. Fourcade-Dutin, B. R. Washburn, F. Benabid, and K. L. Corwin, “Direct fiber comb stabilization to a gas-filled hollow-core photonic crystal fiber,” *Opt. Express*, vol. 22, no. 19, pp. 23704–23715, 2014.

[67] F. Emaury, C. F. Dutin, C. J. Saraceno, M. Trant, O. H. Heckl, Y. Y. Wang, C. Schriber, F. Gerome, T. Südmeyer, F. Benabid, and U. Keller, “Beam delivery and pulse compression to sub-50 fs of a modelocked thin-disk laser in a gas-filled Kagome-type HC-PCF fiber,” *Opt. Express*, vol. 21, no. 4, pp. 4986–4994, 2013.

[68] M. Azhar, N. Y. Joly, J. C. Travers, and P. S. J. Russell, "Nonlinear optics in Xe-filled hollow-core PCF in high pressure and supercritical regimes," *Appl. Phys. B Lasers Opt.*, vol. 112, no. 4, pp. 457–460, 2013.

[69] Lynch-Klarup, Kyle E., Erin Mondloch, Michael G. Raymer, Fetah Benabid, Frederic Gerome, and Damien Arrestier. "Supercritical-xenon-filled photonic crystal fiber as a Raman-free nonlinear optical medium." In *Frontiers in Optics*, pp. FM4I-2. Optical Society of America, 2012.

[70] A. V. V. Nampoothiri, A. M. Jones, C. Fourcade Dutin, C. Mao, N. Dadashzadeh, B. Baumgart, Y. Wang, M. Alharbi, T. Bradley, N. Campbell, F. Benabid, B. R. Washburn, K. L. Corwin, and W. Rudolph, "Hollow-core Optical Fiber Gas Lasers (HOFGLAS): a review [Invited]," *Opt. Mater. Express*, vol. 2, no. 7, pp. 948–961, 2012.

[71] Jones, A. M., C. Fourcade-Dutin, C. Mao, Bastian Baumgart, V. A. V. Nampoothiri, N. Campbell, Y. Y. Wang et al. "Characterization of mid-infrared emissions from C2H2, CO, CO2, and HCN-filled hollow fiber lasers." In *SPIE LASE*, pp. 82373Y-82373Y. International Society for Optics and Photonics, 2012.

[72] P. S. Light, F. Couny, and F. Benabid, "Low insertion-loss (1.8 dB) and vacuum-pressure all-fiber acetylene cell based on hollow-core PCF," *Conf. Lasers Electro-Optics, 2007, CLEO 2007*, vol. 2, no. C, pp. 4–5, 2007.

[73] Sprague, Michael R., Duncan G. England, Amir Abdolvand, Joshua Nunn, Xian-Min Jin, W. Steven Kolthammer, Marco Barbieri et al. "Efficient optical pumping and high optical depth in a hollow-core photonic-crystal fibre for a broadband quantum memory." *New Journal of Physics* 15, no. 5 (2013): 055013.

[74] F. Benabid and P. J. Roberts, "Linear and nonlinear optical properties of hollow core photonic crystal fiber," *J. Mod. Opt.*, vol. 58, no. 2, pp. 87–124, 2011.

[75] F. Couny, F. Benabid, P. J. Roberts, P. S. Light, and M. G. Raymer, "Generation and photonic guidance of multi-octave optical-frequency combs," *Science (80-.).*, vol. 318, no. 2007, pp. 1118–1121, 2007.

[76] B. Debord, F. Gérôme, R. Jamier, C. Boisse-Laporte, P. Leprince, O. Leroy, J.-M. Blondy, and F. Benabid, "First Ignition of an UV Microwave Microplasma in Ar-filled Hollow-Core Photonic Crystal Fibers - OSA Technical Digest (CD)," *37th Eur. Conf. Expo. Opt. Commun.*, p. Mo.2.LeCervin.5, 2011.

[77] Wilson, Emily L., Marc Neveu, Haris Riris, Elena M. Georgieva, and William S. Heaps. "A hollow-waveguide gas correlation radiometer for ultra-precise column measurements of formaldehyde on Mars." *Measurement Science and Technology* 22, no. 8 (2011): 085902.

[78] N. V Wheeler, P. S. Light, F. Couny, and F. Benabid, "Slow and Superluminal Light Pulses in an Acetylene Filled Photonic Mircocell," *J. Light. Technol.*, vol. 28, no. 6, pp. 870–875, 2010.

[79] F. Couny, P. S. Light, F. Benabid, and P. S. J. Russell, "Electromagnetically induced transparency and saturable absorption in all-fiber devices based on 12C2H2-filled hollow-core photonic crystal fiber," *Opt. Commun.*, vol. 263, no. 1, pp. 28–31, 2006.

[80] F. Benabid, P. Light, F. Couny, and P. Russell, "Electromagnetically-induced transparency grid in acetylene-filled hollow-core PCF.," *Opt. Express*, vol. 13, no. 15, pp. 5694–5703, 2005.

[81] F. Couny, F. Benabid, and P. S. Light, "Subwatt Threshold cw Raman Fiber-Gas Laser Based on H[sub 2]-Filled Hollow-Core Photonic Crystal Fiber," *Phys. Rev. Lett.*, vol. 99, no. October, p. 143903, 2007.

[82] Y. Y. Wang, F. Couny, P. S. Light, B. J. Mangan, and F. Benabid, "Compact and portable multiline UV and visible Raman lasers in hydrogen-filled HC-PCF," *Opt. Lett.*, vol. 35, no. 8, pp. 1127–1129, 2010.

[83] K. Knabe, S. Wu, J. Lim, K. a Tillman, P. S. Light, F. Couny, N. Wheeler, R. Thapa, A. M. Jones, J. W. Nicholson, B. R. Washburn, F. Benabid, and K. L. Corwin, "10 kHz accuracy of an optical frequency reference based on (12)C2H2-filled large-core kagome photonic crystal fibers.," *Opt. Express*, vol. 17, no. 18, pp. 16017–16026, 2009.

[84] O. H. Heckl, C. R. E. Baer, C. Kränkel, S. V. Marchese, F. Schapper, M. Holler, T. Südmeyer, J. S. Robinson, J. W. G. Tisch, F. Couny, P. Light, F. Benabid, and U. Keller, "High harmonic generation in a gas-filled hollow-core photonic crystal fiber," *Appl. Phys. B Lasers Opt.*, vol. 97, no. 2, pp. 369–373, 2009.

[85] A. M. Cubillas, J. Hald, and J. C. Petersen, "High resolution spectroscopy of ammonia in a hollow-core fiber.," *Opt. Express*, vol. 16, no. 6, pp. 3976–3985, 2008.

[86] J. Henningsen, J. Hald, and J. C. Peterson, "Saturated absorption in acetylene and hydrogen cyanide in hollow-core photonic bandgap fibers.," *Opt. Express*, vol. 13, no. 26, pp. 10475–10482, 2005.

[87] Bhagwat, Amar Ramdas. Low-light-level nonlinear optics with rubidium atoms in hollow-core photonic band-gap fibers. Cornell University, 2010.

[88] Budker, D., D. F. Kimball, S. M. Rochester, V. V. Yashchuk, and M. Zolotorev. "Sensitive magnetometry based on nonlinear magneto-optical rotation." *Physical Review A* 62, no. 4 (2000): 043403.

[89] Yi, Y. W., H. G. Robinson, S. Knappe, J. E. Maclennan, C. D. Jones, Chengjie Zhu, N. A. Clark, and J. Kitching. "Method for characterizing self-assembled monolayers as antirelaxation wall coatings for alkali vapor cells." *Journal of Applied Physics* 104, no. 2 (2008): 023534.

[90] M. V. Balabas, D. Budker, J. Kitching, P. D. D. Schwindt, and J. E. Stalnaker, "Magnetometry with millimeter-scale anti-relaxation-coated alkali-metal vapor cells," *J. Opt. Soc. Am. B*, vol. 23, no. 6, p. 7, 2005.

[91] S. J. Seltzer, D. J. Michalak, M. H. Donaldson, M. V. Balabas, S. K. Barber, S. L. Bernasek, M. a. Bouchiat, a. Hexemer, a. M. Hibberd, D. F. J. Kimball, C. Jaye, T. Karaulanov, F. a. Narducci, S. a. Rangwala, H. G. Robinson, a. K. Shmakov, D. L. Voronov, V. V. Yashchuk, a. Pines, and D. Budker, "Investigation of antirelaxation coatings for alkali-metal vapor cells using surface science techniques," *J. Chem. Phys.*, vol. 133, pp. 1–11, 2010.

[92] Budker, Dmitry, Leo Hollberg, Derek F. Kimball, J. Kitching, Szymon Pustelny, and Valeriy V. Yashchuk. "Microwave transitions and nonlinear magneto-optical rotation in anti-relaxation-coated cells." *Physical Review A* 71, no. 1 (2005): 012903

[93] M. T. Graf, D. F. Kimball, S. M. Rochester, K. Kerner, C. Wong, D. Budker, E. B. Alexandrov, M. V. Balabas, and V. V. Yashchuk, "Relaxation of atomic polarization in paraffin-coated cesium vapor cells," *Phys. Rev. A - At. Mol. Opt. Phys.*, vol. 72, no. 2, 2005.

[94] S. J. Seltzer, D. M. Rampulla, S. Rivillon-Amy, Y. J. Chabal, S. L. Bernasek, and M. V. Romalis, "Testing the effect of surface coatings on alkali atom polarization lifetimes," *J. Appl. Phys.*, vol. 104, no. 10, pp. 1–7, 2008.

[95] E. P. Corsini, T. Karaulanov, M. Balabas, and D. Budker, "Hyperfine frequency shift and Zeeman relaxation in alkali-metal-vapor cells with antirelaxation alkene coating," *Phys. Rev. A*, vol. 87, no. 2, p. 22901, 2013.

[96] C. Weng, W. Li, and C. Hwang, "Gaseous flow in microtubes at arbitrary Knudsen numbers," *Nanotechnology*, vol. 10, pp. 373–379, 1999.

[97] Weng, Cheng-I., Wang-Long Li, and Chi-Chuan Hwang. "Gaseous flow in microtubes at arbitrary Knudsen numbers." *Nanotechnology* 10, no. 4 (1999): 373.

[98] I. Dicaire, J.-C. Beugnot, and L. Thévenaz, "Analytical modeling of the gas-filling dynamics in photonic crystal fibers.," *Appl. Opt.*, vol. 49, pp. 4604–4609, 2010.

Chapter 2

Hollow-core photonic crystal fiber guidance

The performance of alkali-vapor photonic microcell (PMC) is chiefly determined by the hollow-core photonic crystal fiber (HC-PCF) choice and its characteristics. Among the relevant fiber properties, we can mention a few as its transmission loss, core size, birefringence properties or modal content. In this chapter we review the fundamental principles behind the light guidance in HC-PCF, and the subsequent optical properties that has an effect on atom-optics applications, and to identify the most suitable HC-PCF. Furthermore, the chapter covers the characterization and presentation of different hypocycloidal core shape inhibited-coupling Kagome lattice HC-PCFs that will be used for the experiments operating around 780 nm region.

2.1 Introduction

The miniaturization of the structure confining atomic vapours became today essential and will be beneficial for various applications such as laser frequency stabilization, laser cooling and frequency standards for both industry and fundamental works. Hollow-core waveguides technology provides several advantages to confine light and atomic vapours for strong interactions. Beyond these advantages, the reduction of transverse dimensions of the gas container is restrictive because implying the increase of atom wall collisions and consequently dephasing of the excited state. This crucial point has to be taken into account for development of efficient systems based on miniaturized scheme. Before to investigate post-processing solution in the core surface of such waveguides through different anti-relaxation coatings (see next chapter), the geometrical parameters of these waveguides as to be studied and decision made.

Guidance within an air or vacuum core has outstanding properties and offers broad potential applications. There are several reasons why this kind of guidance is desired. Firstly, the guidance in air or vacuum has no optical transparent window limitation compare to the conventional absorption wavelength from 0.4 to 4 μm for silica material. This guidance can then enable light guidance in UV and mid- to far-IR with low loss transmission. Secondly, the damaged threshold of laser intensity guiding is increased which enables confinement and guidance of high power laser suitable for nonlinear effects and plasma applications to mention a few. Moreover, hollow-core fiber filled with gases or liquids offer a novel standard for matter-light interactions along meters even kilometers length could be attractive for fiber sensing or optical fundamental experiments. Through these advantages, atom- or molecular-filled hollow-core guidance could also benefit of such new potentialities and will be investigated in this thesis.

The history of attempts on development of air-guidance is introduced in the following. A hollow circular waveguide made of dielectric material or metal is the earliest work for application as an optical waveguide [1], proposed by E. A. J. Marcatili *et al.* in 1964. This dielectric hollow waveguide had strong losses of 1.85 dB/m at 1 μm for a 1 mm core diameter. In addition, the loss is double simply for a bending radius of R~10 cm,

explaining its non-implementation in commercial applications. In 1978, Yariv and Yeh [3] proposed the concept of one dimensional hollow Bragg waveguide with periodic alternative layers of higher refractive index. Next, with the advent of hollow guidance within photonic bandgap (PBG) concept, a very late design permits omnidirectional reflectivity for all polarizations of coupling light over a wide desired range of wavelengths reported by Fink *et al.* in 1998 [4]. The reflector was simply constructed as a stack of nine alternating micro thick layers of polystyrene and tellurium over the range from 10 to 15 μm [5]. The low loss record of this fiber is 1 dB/m for fundamental bandgap at 10.6 μm [6] and such a fiber has been used for CO_2 laser beam delivery in micro-laryngoscopy for benign lesions removal and early-stage laryngeal cancer [7]. However, the bending loss sensitivity is still quite high for such fiber design.

A HC-PCF provides a periodic arrangement of air holes as two-dimensional photonic crystal cladding with an air-core and was first proposed by Russell in 1995 [8]. This concept of out-of-plan PBG in photonic crystal structures was further investigated in the reference [9]. Then, several PCF were made. In 1996, Knight *et al.* [11] fabricated a first solid core photonic crystal fiber which guidance based on total internal reflection (TIR). In 1998, Knight *et al.* fabricated a first solid core PBG guidance fiber [12] composed by a periodic honeycomb cladding structure surrounding the core defect. One year later, the first true meaning HC-PCF was fabricated by Cregan *et al.* in 1999 [10] based on a triangular lattice cladding. After this point, several HC-PCF fabrications were reported by many groups with the aim of decreasing loss level. These HC-PCFs can be classified by their guidance mechanism into two main families. The first design class is based on PBG guidance mechanism, and whose experimental demonstration was reported in 2002 by Corning. The second design class is based on the Inhibited Coupling (IC) guidance mechanism with large pitch Kagome lattice cladding structure, which was first reported by Benabid *et al.* in 2002 [13]. The guidance mechanism was then elucidated by Benabid and co-workers in 2007 [14]. Consequently, this chapter will be composed as the following. The first part will describe the guidance mechanism of these two classes of HC-PCFs. The well-established PBG will be presented in details and its formation described through photonic tight binding model [16]. Potential offered by this concept for dual wavelengths

guidance with double PBG HC-PCF and especially for doublet 780 and 794 nm will be also presented. Then the more recent IC will be developed and in particular the recent enhancement of its optical performances by the introduction of hypocycloidal core shape. After a comparative table to highlight the better potential of IC HC-PCF type for our aim of alkali-vapor PMC development, fabrication of different IC Kagome fibers dedicated to this work will be reported. Excellent guidance around 780 nm will be demonstrated including state-of-the-art loss figure, large core diameter, high mode quality and large optical bandwidth.

2.2 Photonic Bandgap guidance HC-PCF

The PBG guidance HC-PCF could confine light in a core defect by a 2D- out of plane PBG cladding, which is usually composed by several layers of periodic silica triangular lattice of air holes [9]. In other words, coupling of the core mode to the cladding is disallowed by micro-engineering the structure of the cladding such that its modal spectrum is void from any propagation modes at the core guided mode effective index frequency space (n_{eff}-ω). This describes for a given propagation constant $\beta = n_{eff}\,k$, where neff is the effective index and k is the vacuum wave-vector. One explanation for the out of plane configuration is the transverse effective index step, $n_{gl,\perp}/n_{air,\perp} = k_{gl,\perp}/k_{air,\perp}$ can present very large values compare to the low constant value of n_{gl}/n_{air} = 1.46. The different of silica/air refractive index is not sufficient for the light scattering from any geometric structure which is strong enough to construct a bandgap for in-plan propagation. The following figure illustrates the usual plot of density of photonic states (DOPS) for a PBG.

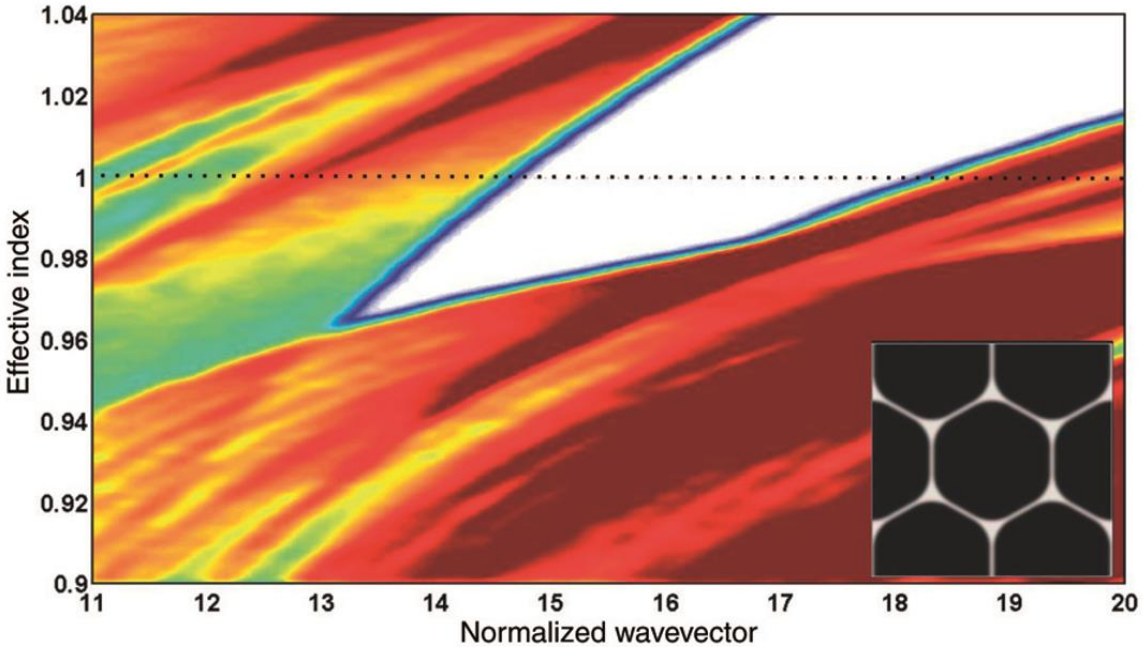

Figure 2-1: Density of photonic states (DOPS) of a triangular lattice photonic bandgap with a given silica/air fraction [15].

The DOPS is mapped by numerically solving the Maxwell Helmholtz equation by plane wave analysis or finite element method and is plotted as effective index n_{eff} versus the normalized frequency. The colored regions present the supported guiding modes by the photonic crystal cladding, and the white region illustrates the unsupported guiding modes, constituting PBG in the space (k, n_{eff}), where the density of states is null. The darker red in the gradient color depicts more supported guiding modes and the lighter color indicates less supported guiding modes. The absence of photonic states below the air line (effective index = 1) permits a selected guiding mode with specific propagation constant (β) guiding through the hollow-core defect. In an effort to provide an intuitive tool, a model based on the analogue of the photonic tight binding model (PTBM) which is used in solid state physics has been proposed by Couny *et al.* [16]. In the next section, PTBM is reviewed.

2.3 Photonic Tight Binding Model

Several prior models were proposed to depict DOPS as an intuitive tool. For example, we can mention “cellular method” proposed by Birks *et al.* [17] and the anti-resonant reflective optical waveguide (ARROW) model [18][20]. The ‘cellular method’ provides useful insights for all-solid PBG photonic crystal fibers guidance mechanism which cladding structure contain ranges of separated high index layers within a lower index outer surround as the bandgap formation. The ARROW model describes the guiding spectral properties which are mainly determined by the thickness and the refractive index of the high index inclusions which form as optical resonators of bandgaps guidance. However, none of these models elucidate the PBG guidance mechanism and consider the role of complicated cladding structure of HC-PCF.

The tight binding model which is used in solid state physics gives a description of allowed and forbidden electronic bands (solid state physics). When identical and isolated atoms are jointed proximately closer in a crystal lattice, this leads the electron wave function (orbitals) amalgamation to form a band of energy levels with delocalized wave functions (Bloch functions) [19]. The higher energy band is anti-symmetric formed and the lower energy band is formed as symmetric which show same sign oscillations of a more tightly-bonded state. One can transfer the TBM concept in solid state physic to elucidate the role of optical resonators of the HC-PCF photonic cladding structure. In PTBM, the individual atoms are replaced by silica rods which act as the optical resonators.

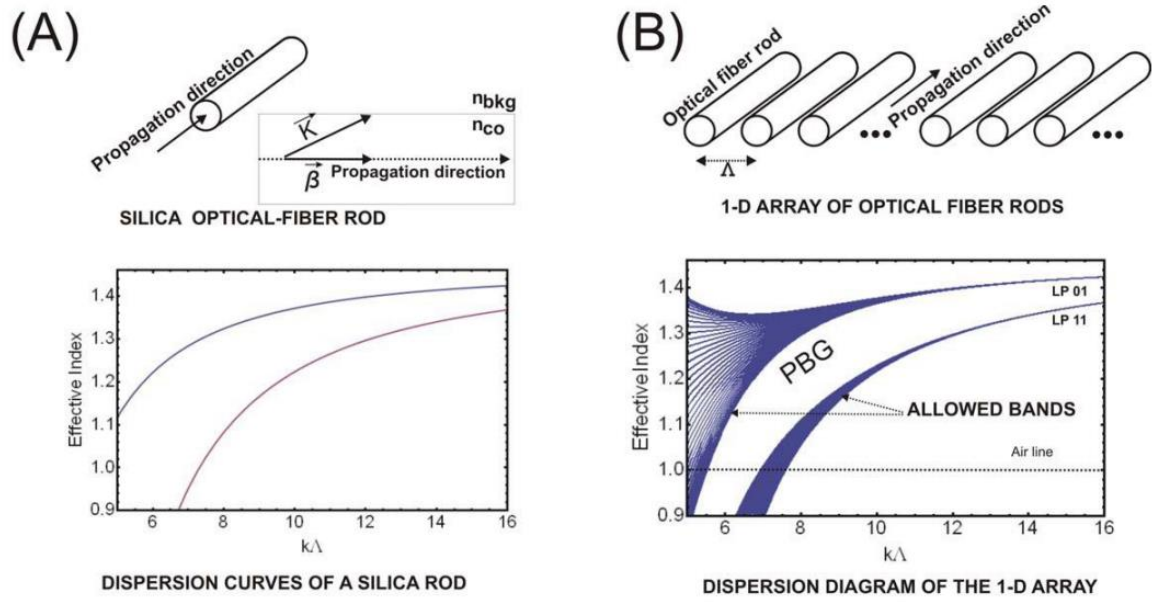

Figure 2-2: Principle of PTBM. (a) Dispersion curve of fundamental and second higher-order modes of a silica rod and (b) Dispersion diagram of an array of silica rods spatially jointed [15, 21].

Figure 2-2 (a) shows the dispersion of the fundamental and second order modes in a single silica rod which can be considered as an individual atom in crystal lattice. Figure 2-2 (b) shows the dispersion diagram when considering an array of silica rod spatially jointed by Λ (fiber pitch). One can see when the pitch decreases (*i.e.* when the rods are closer), the coupling and hybridization appear between degenerated modes, spreading the effective index range of "allowed" photonic bands.

We develop below the nature of the main different modes constituting a DOPS and delimiting the bandgap of a PBG fiber. Figure 2-3 (d) shows the DOPS mapping of a triangular lattice cladding fiber through effective index and normalized frequency space. For this, the elementary cell shown in fig. 2-3 (b) has been considered. The black region defines the bandgap with unsupported guiding modes confined in the core defect. This region is delimited by the trajectory of different cladding modes that can be divided into three: the modes propagating in the silica apexes, the others in silica struts and those propagating in air holes. The low frequency edge of the PBG region (figure 2-3 (d)) is essentially delimited by modes propagating in the interstitial apexes which is defined as apex modes (figure 2-3 (e)). The silica struts (figure 2-3(f)) and air holes modes (figure 2-3

(g)) superimpose to delimit both high frequency edge of the fiber transmission and depth of the PBG. The apex modes, strut modes and airy modes identified in fig. 2-3 (d) have been experimentally demonstrated by Couny *et al.* [16], observed through scanning near field optical microscopy (SNOM).

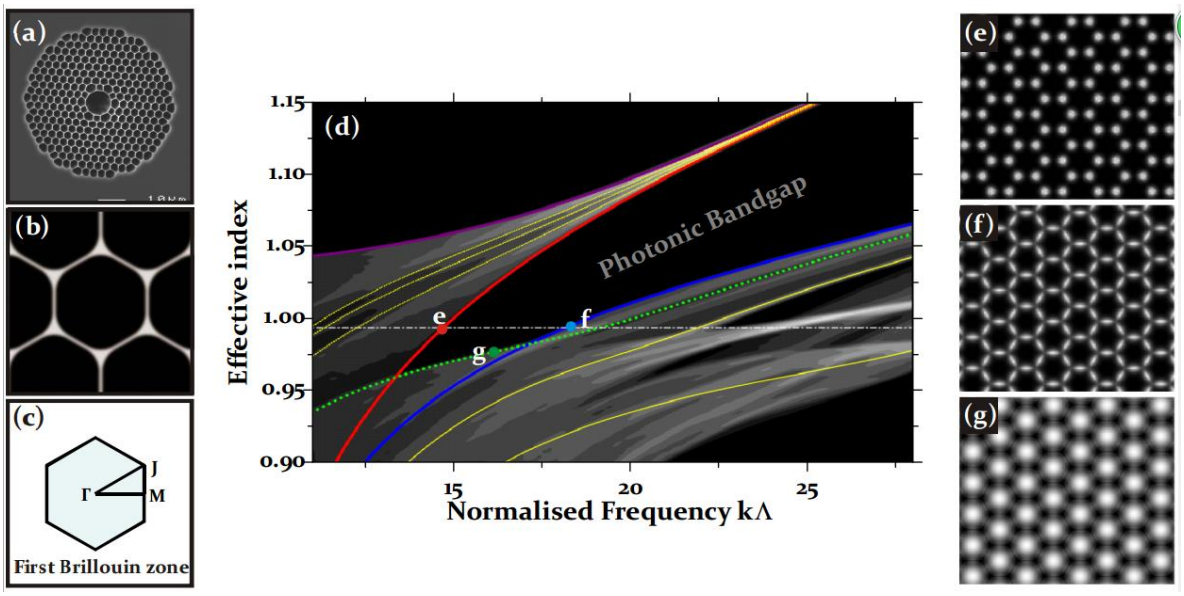

Figure 2-3: (a) SEM image of PBG HC-PCF, (b) SEM image of cladding structure of PBG HC-PCF, (c) model of unit cell in cladding structure, (d) DOPS for PBG HC-PCF, observed modes by scanning near field optical microscopy (SNOM) (e) silica apex mode, (f) silica strut mode, (g) cladding air hole mode [15,21].

2.4 Double Photonic Bandgap guidance mechanism

Figure 2-4 indicates the possibility of higher order guidance at the normalized frequency kΛ ~ 22 just above the air line. In this present section, the modifications on the exact size and diameter of the three resonators (apex, strut, airy) of the triangular lattice PBG cladding design enable to allow the opening of a second PBG below the air line at higher normalized frequency [22]. The fiber fabrication procedure allows independently to control the strut thickness and the apex size to suit the higher order bandgap design of cladding structure. The DOPS for different struts thickness and apex sizes are plotted in fig. 2-4. In the left column, the apex radius r is varied from 0.10Λ (top) to 0.20Λ (bottom) with constant strut thickness t= 0.05Λ. In the right column, the strut thickness is increased from 0.005Λ (top) to 0.015Λ (bottom) with constant apex radius r = 0.15Λ. The results show

that the fundamental bandgap is broaden with thinner struts and larger apexes. The second bandgap is deepening as the width of fundamental bandgap decreases. For higher order bandgap, the spectral width was concluded independent to the strut thickness but sensitive to small apexes. Therefore, a second bandgap at higher normalized frequency become possible by optimizing the apex size and strut thickness simultaneously. However, this fabrication has different challenges to require all exact draw parameters for short wavelengths guidance that will be expressed in section 2.7.

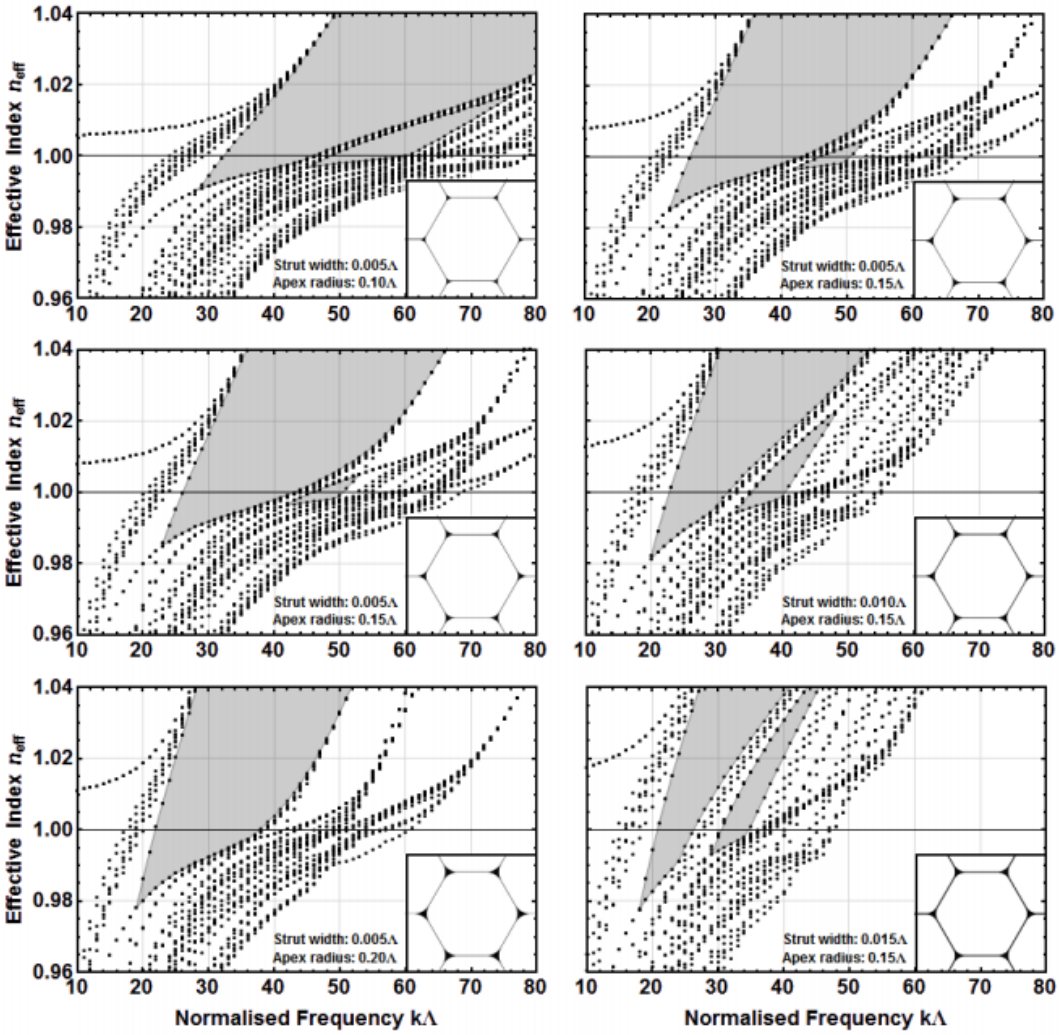

Figure 2-4: Effective indices of cladding modes calculated at high normalized frequency for six different cladding structures. Left column: varying apex radius r (top) $r = 0.10\Lambda$, (middle) $r_c = 0.15\Lambda$ and (bottom) $r = 0.20\Lambda$ with constant strut thickness $t = 0.05\Lambda$. Right column: varying strut thickness t (top) $t = 0.005\Lambda$, (middle) $t = 0.010\Lambda$ and (bottom) $t = 0.015\Lambda$ with constant apex radius $r = 0.15\Lambda$ [22].

2.5 Inhibited Coupling Kagome lattice HC-PCF

PBG guidance mechanism with triangular lattice cladding structure enables low transmission loss for few guiding modes in the core defect (figure 2-5 (a)). However the transmission bandwidth is limited by the spectral width of the bandgap, typically to 70 THz. To overcome this drawback, large pitch Kagome lattice HC-PCF, based on a star David pattern, was proposed by Benabid *et al.* in 2002 [2]. The ratio between the cladding pitch Λ and the central guiding wavelength λ can be ~8 even ~30 for large pitch Kagome lattice HC-PCF [23], which is significant much larger than the ratio of ~2 for triangular lattice PBG HC-PCF. Figure 2-5 (b) presents a comparison between PBG and IC Kagomé lattice fibers in term of fibers cross section structure and DOPS. As previously mentioned, a Kagome lattice HC-PCF does not exhibits a PBG in the guiding modes of the cladding structure but a continuum of modes. Three regions of photonic states could be identified which are two low density of states curtained off by high density of states region which correspond to high loss core guiding modes.

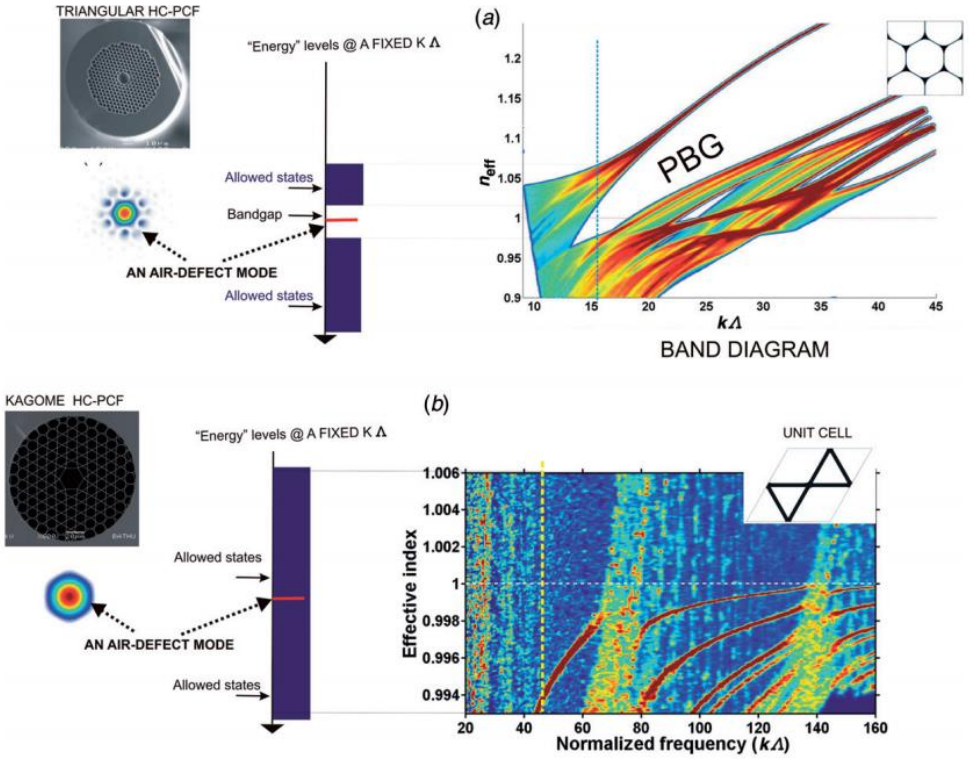

Figure 2-5: (a) Top left: SEM image of a triangular-lattice PBG HC-PCF. Bottom left: near field profile of the fundamental core mode. Right: DOPS diagram of a PBG HC-PCF and for Kagome-lattice HC-PCF. (b) Same representation for the case of IC HC-PCF [13].

The physics of the Kagome lattice guidance mechanism has been elucidated by Couny *et al.* in 2007 [14]. It relies on 'Inhibited Coupling' mechanism that can be explained by analogy to the Von Neumann Wigner electronic state in quantum physics where a core guided-mode and cladding modes can have the same effective index, and yet propagate without strongly interaction. In IC HC-PCF a core guided-mode is inhibited to leak through the cladding by a strong reduction of the coupling between the continuum of cladding modes and a core mode. This can be summarized by considering the dot product between core mode and cladding mode fields that is reduced strongly, by a small field spatial intersection or by a strong mismatch in their transverse phase.

The transverse spatial overlap between core mode and cladding modes is very small where less than 0.05% of the maximum intensity of silica guiding light (figure 2-6 (a)). The very large transverse phase mismatch between the slowly oscillating core modes and the fast oscillating cladding modes (figure 2-6 (b)) causes diminution of overlap integral between these two modes and enable low loss guidance through a broadband spectral range giving strength to the IC guidance mechanism.

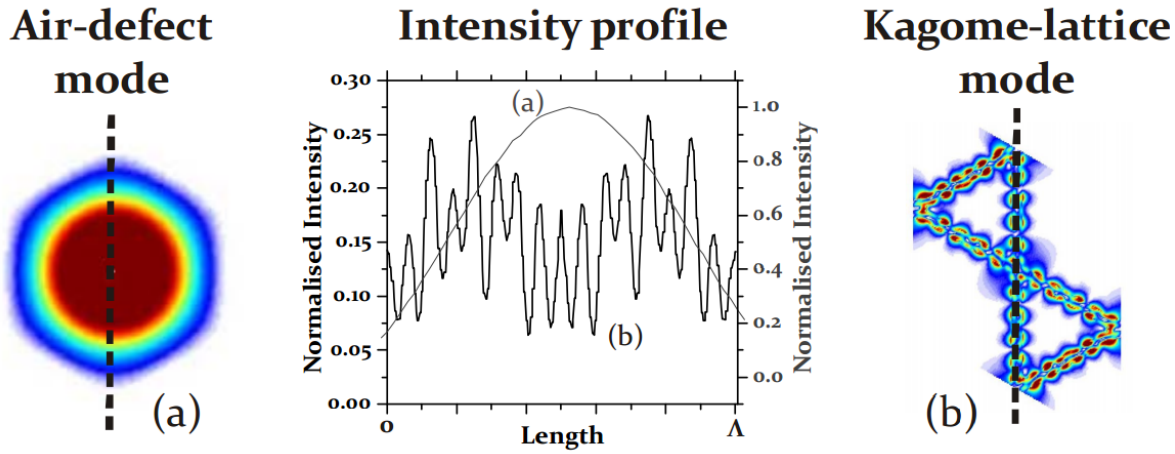

Figure 2-6: (a) Core guiding mode of Kagome lattice HC-PCF, (b) Fast oscillating cladding mode of Kagome HC-PCF. Middle image is the intensity plot of (a) core mode (b) cladding modes [22] along length Λ identified by dashed line.

In figure 2-5 (b) we can see a high density of states region which corresponds to the resonance with cladding structure causes increase of the transmission losses. These low transmission losses ranges are predicted at cut-off wavelengths, λm, by

$$\lambda m = \frac{2t}{m}(n_g^2 - n_{air}^2)^{1/2}, \quad (2\text{-}1)$$

where n_g is the silica glass refractive index, n_{air} is the refractive index in air, m is the mode order and t the strut thickness. Despite the effort in optimizing the cladding structure to reduce the cladding modes and core mode interaction, the loss figures remained at relatively high level (> 0.5 dB/m).

2.6 Enhanced Inhibited coupling hypocycloid core shape Kagome HC-PCF

In 2010, a new attempt to enhance IC Kagome HC-PCF was reported by Wang *et al.* [25] which consists of core shape optimization of Kagome HC-PCF altered from the circular shape to a hypocycloid shape (*i.e.* core contour with negative curvature) [25][26]. As discussed in section 2.5 the IC guidance offers large transverse phase mismatch between the bound state of core mode and the continuum of cladding mode [14]. The cladding modes of the core contour situated in the cladding struts correspond to a higher effective azimuthal number, thus leading to the minimized overlap with the slow oscillating core mode distribution [31]. Figure 2-7 illustrates mode field nature and distribution in a circular core shape and a hypocycloid core shape of Kagome HC-PCF. The fast oscillating strut modes are indicated by the red dots localized in the silica core contour. Meanwhile, the core fundamental mode field profile is a zero order Bessel function.

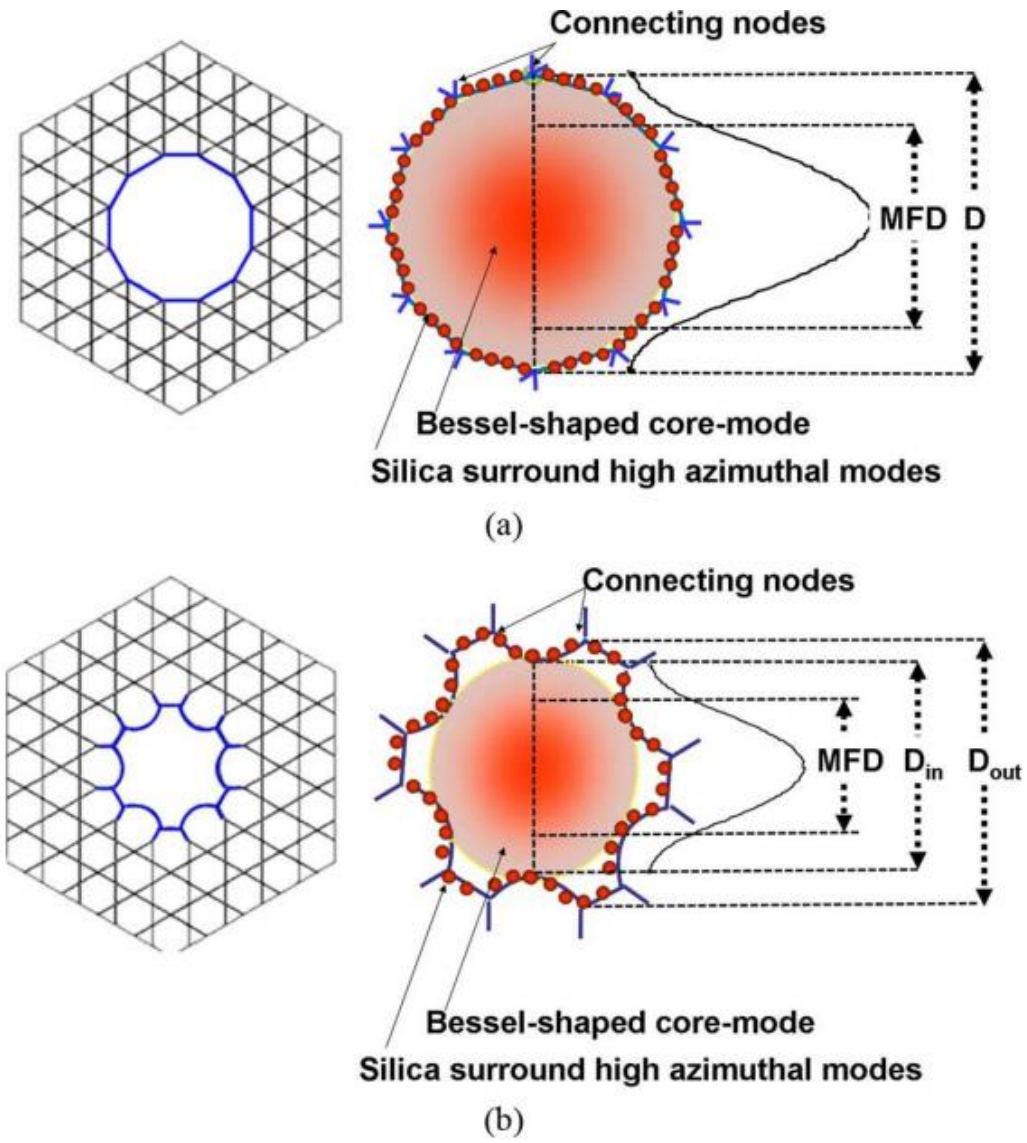

Figure 2-7: Illustration of the enhanced IC guidance by using hypocycloid core contour. (a) Idealized traditional Kagome HC-PCF, core mode overlap with low azimuthal number cladding modes, and 2D profile distribution of core mode field which diameter is related to core boundary .(b) The same for a hypocycloidal Kagome HC-PCF [24].

We can see that the hypocycloidal core shape brings two advantages. Firstly, by considering the virtue of elongation of the core contour path, the azimuthal like number of the silica core contour mode increases and consequently implies reduction of the core mode coupling to cladding. Secondly, the silica nodes of the core contour, linked to low azimuthal number are pushed away from the confined core mode. The mode field diameter in circular core shape is related to the fiber core diameter D by MFD ~ $(\pi/4)D$ with the

entire core surround. For the hypocycloid core shape, the Bessel shape core mode is strict related to the curvature parameter b and the inward cusps diameter D_{in}. This is demonstrated that low loss guidance can be obtained by simply modifying the shape of the core curvature [27][28][29][30]. The effect of arc negative curvature of the hypocycloid core accompany with the confinement loss has been theoretically and experimentally demonstrated by Debord *et al.* [31]. In the following section, we give a summary of this study of the influence of the arc curvature of the core contour on the attenuation figure and its modal contents.

2.6.1 Loss figure dependency of arc curvature

A typical design of hypocycloid core shape Kagome HC-PCF is shown in fig. 2-8 (a). Here, the core defect is composed of 7 missing circular capillaries arranged in triangular manner. The degree of curvature of the hypocycloid core shape is defined as a dimensionless parameter b. This parameter (see in Fig. 2-8 (b)) is quantified as $b = d/r$, where d is the distance from the top of the arc to the connecting chord of two neighboring cells and r is half length of the chord. Therefore, the circular core shape of classical Kagome fiber corresponds to $b = 0$, and a core contour with circular shaped arcs corresponds to $b = 1$. For $0 < b < 1$ and $b > 1$, it corresponds to an elliptical shape of core contour. The core diameter consequently is defined by two different parts, one is the small circle radius R_{in} that is formed by the 6 main inward arcs, and the larger circle radius R_{out} which is constructed by the 6 most outward arcs.

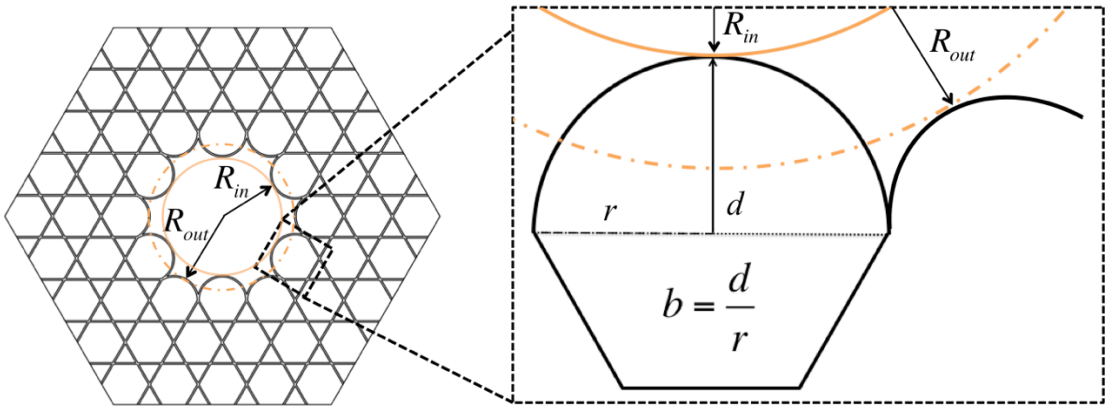

Figure 2-8: (a) Illustration of hypocycloidal core shape Kagome HC-PCF; (b) Definition of the negative curvature parameter *b* [38].

Figure 2-9 (a) summaries the simulation of loss figures evolution of the fundamental core mode for hypocycloid core shape with different arcs curvatures solved by finite-element method with an optimized anisotropic perfectly matched layer (PML) [33][35]. The simulation has been carried out considering HC-PCFs with 7 cells defect and a 3 rings cladding structure, and the strut thickness t = 350 nm. The curvature parameter b varies from b = 0 to b = 1.5 and the core diameters are kept constant at 60 µm (see Fig. 2-9 (b)).

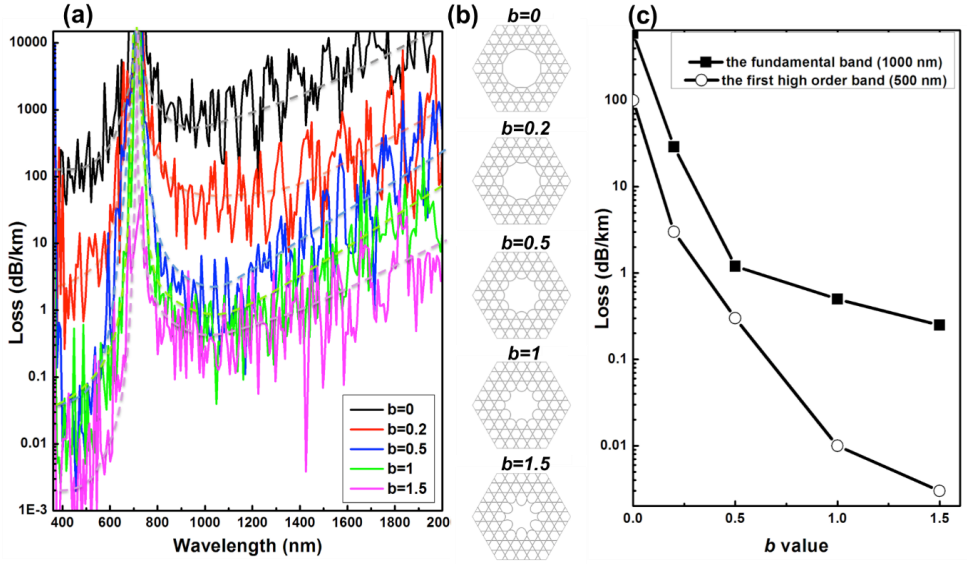

Figure 2-9: (a) Numerical simulations of confinement loss spectrum of hypocycloidal curvature dependency. (b) Fiber model with different curvature *b* parameters. c) Confinement loss evolution with *b* for the fundamental band (1000 nm) and the first high order band (500 nm) [38].

The results show clearly a strong dependence on the core curvature when the loss drops from ~ 1000 dB/km for an approach circular core (*i.e. b = 0*) to below 0.1 dB/km for hypocycloid core with *b* = 1.5 in the IR region. Notice that very strong oscillations in the simulated confinement loss figure are observed which correspond to the resonant cladding features such as corners [14] and Fano resonances [36]. Also, high loss transmission spectra appears in the region around 700 m which corresponds to the resonance of the fundamental mode with the glass struts at wavelength λ_m given by equation (2.1).

Figure 2-9 (c) illustrates the trend of the confinement loss as the curvature parameter *b* increased for wavelengths λ_m = 1000 nm and λ_m = 500 nm, which correspond respectively to the minimum of the fundamental transmission band and the first high order band. Finally, this attenuation reduction with the increasing of curvature parameter *b* has been experimentally confirmed with different fabrication of Kagome HC-PCFs.

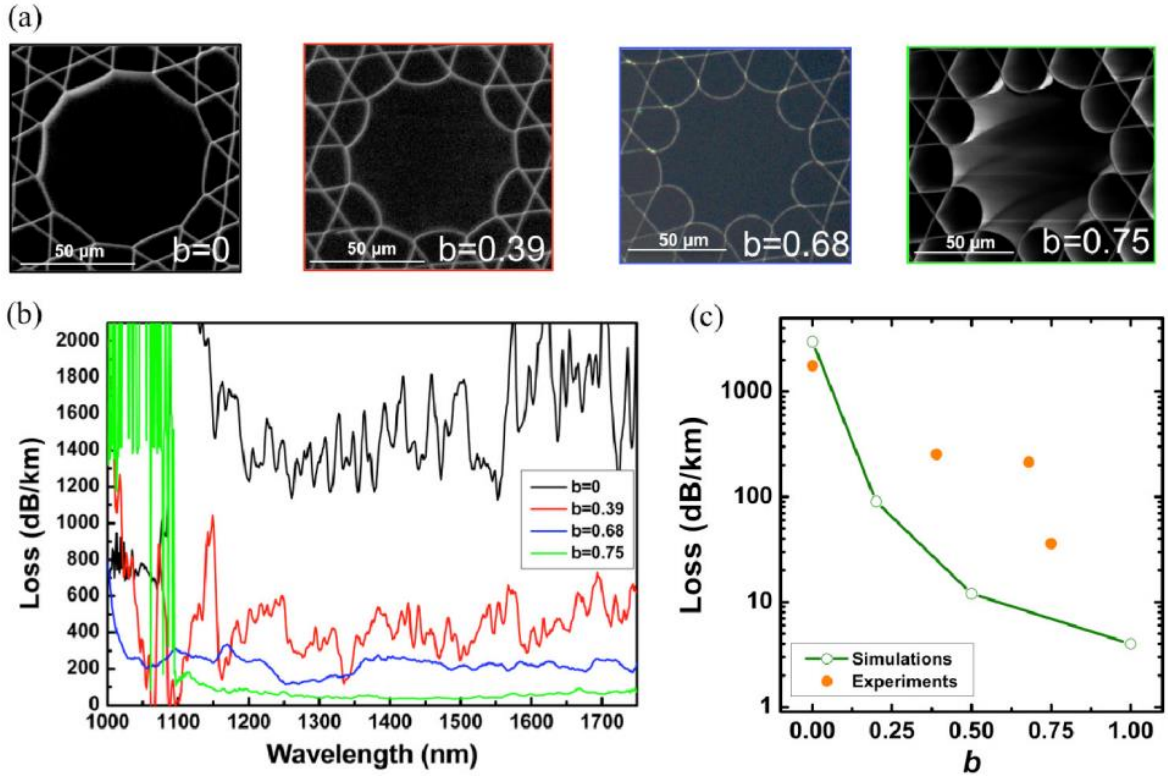

Figure 2-10: (a) SEM images for different core contours Kagome HC-PCFs, (b) Measured transmission loss spectrum for different *b* curvature parameter Kagome HC-PCFs, (c) Experimental and simulated transmission loss at 1500 nm [38].

Figure 2-10 (a) shows SEM images of those fabricated Kagome HC-PCFs with different core contours. The measured transmission loss spectrum are reported in fig. 2-10 (b) for the fundamental band. That is clearly shown that the loss is reduced from ~1300 dB/km with b = 0 to ~ 40 dB/km with b = 0.75, which is in good agreement with expected calculations. Indeed, the transmission loss at a given wavelength of 1500 nm for both simulated and measured are compared in fig. 2-10 (c) as *b* increases.

2.7 PBG vs IC HC-PCFs for atomic applications at 780 nm

We have seen in the previous section the two major mechanisms governing guidance in HC-PCFs. During the last years, many hollow-core fiber fabrications have been carried out associated with different record transmission loss. In particular, for atomic vapour applications that are at the heart of this doctoral work, efforts have been led to reach high performances around 800 nm spectral range both for PBG and IC fibers. Table 2-1 summarizes the different state-of-the-art fibers that have been reported.

Table 2-1: Developed state-of-the-art fibers for atomic applications.

HC-PCF design	Loss (dB/km)	Bandwidth (nm)	MFD (µm)
PBG 7 cell	230 at 780 nm [34]	~100	3.9
PBG 19 cell	107 at 780 nm [41]	~60	5.9
Double PBG	2000 at 780 nm 90 at 1050 nm	~50 at 780 nm 100 at 1050 nm	8.9
IC HC-PCF	30 at 780 nm[42]	~1050	23.6

The small core size of PBG fibers (resulting in mode field diameters (MFD) between 3.9 and 8.9 µm) combined with acceptable low loss figure (between 100 and 250 dB/km) make this fiber family as good candidate for single particle interaction in atomic vapours. However, as previously explained, this kind of fiber supports surfaces modes contamination, small MFD and a limited bandwidth. For applications which require guidance, for off resonance manipulation of atoms and on resonance probing of atomic transitions in a single fiber, of two laser beams usually operating at 1064 and 780 nm,

double PBG fibers have been developed. Unfortunately, whereas a first bandgap has been well opened at 1050 nm with 90 dB/km, the second one is difficult to manage with loss below 2000 dB/km at 780 nm. The difficulty of such fabrication relies on getting the optimized air-filling fraction to open the second PBG.

On the other hand, one can see in the table that IC fibers optimized around 780 nm have been recently fabricated and reported by Debord *et al.* [42] demonstrating a record propagation loss of 30 dB/km combined with a much larger bandwidth. This fiber presents also the advantage of a large core but combined with a quasi-single mode propagation for good beam coupling conditions. Furthermore, surfaces modes in IC guidance are not anymore existing. Consequenlty, for all these reasons, the IC fibers has been chosen to carry out the different experiments in this thesis.

2.8 Properties of the HC-PCFs under test

In this section, properties of the HC-PCFs which have been fabricated and used as experimental samples in this thesis are detailed. The properties include physical structure, transmission and loss spectrum, modal content and MFD. Table 2-2 lists in details these geometrical parameters of the different fiber samples used for the post-porcessing experiments (Chapter 3), the ground state atomic polarization relaxation time measurement in Rb-loaded Kagome HC-PCF (Chapter 4) and single laser beam generated sub-Doppler transparencies in Rb-loaded Kagome HC-PCF (Chapter 5).

Table 2-2 Physical integrities of experimental fiber samples in this thesis.

Experiment	Core defects	Curvature parameter *b*	R_{in} (*μm*)	R_{out} (*μm*)	Mode field diameter (*MFD*)(*μm*)
HC-PCF tapering	*7 cells*	*0.66*	*31.7*	*37.5*	*43.1*
Ground state relaxation time measurement					
#1	*19 cells*	*0.95*	*48.2*	*57.9*	*65.8*
#2	*19 cells*	*1.02*	*37.8*	*46.2*	*51.7*
#3	*7 cells*	*0.82*	*31.7*	*37.6*	*43.4*
#4	*7 cells*	*0.87*	*30.25*	*35.7*	*41.3*
Sub-Doppler transparencies					
#1	*7 cells*	*0.82*	*31.8*	*37.6*	*43.4*

2.8.1 Fiber selection for the post-processing work

Here, the sample used for IC HC-PCF tapering and splicing post-processing test is a hypocycloid-core shape Kagome HC-PCF which presents a 7 cells core defect with core size D_{in}/D_{out} = 63.4/75 μm and curvature *b* parameter is 0.66 (Figure 2-11 top left). The near field mode profile (bottom left Fig 2-11) is recorded at 1550 nm when an external cavity diode laser (ECDL) is coupled through a 5 m length of HC-PCF. The transmission spectrum (Fig. 2-11 right) is measured directly by using a homemade super-continuum source and optical spectrum analyzer (OSA), and the loss spectrum is tested by cutback method. The corresponding optical loss reaches ~ 180 dB/km at 780 nm.

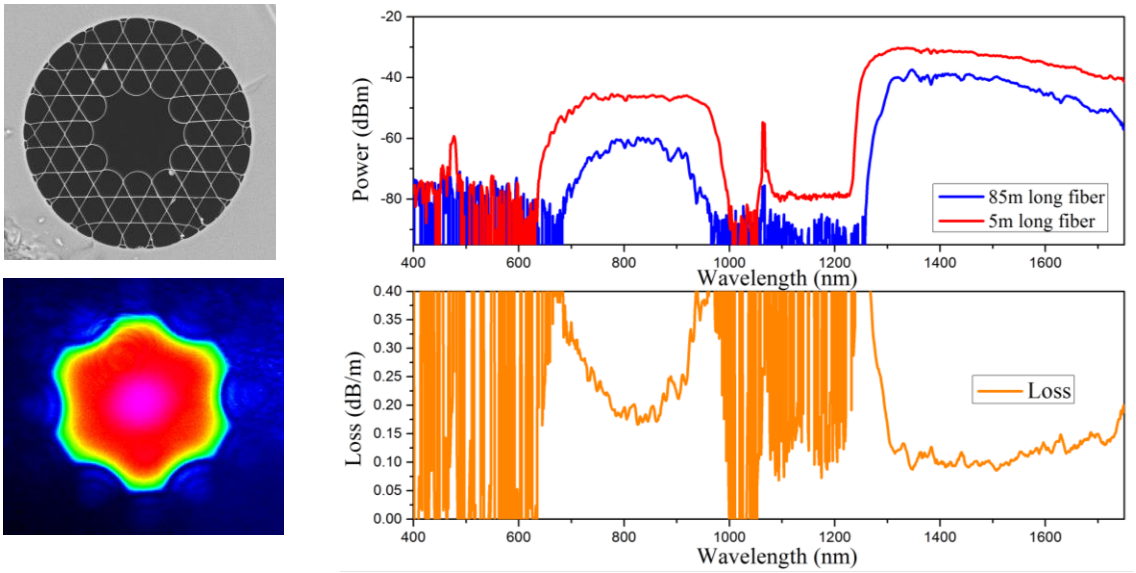

Figure 2-11: SEM image (left top), modal content (left bottom), transmission spectrum and loss spectrum (right) of the fabricated fiber for post-processing.

2.8.2 Fiber selection for ground state atomic polarization relaxation time work

The fiber samples used for the ground state atomic polarization relaxation time measurement are 7 cells or 19 cells core defect hypocycloid-core shape Kagome HC-PCF which provide large inner core > 60 μm. The transverse structure of HC-PCFs are illustrated in sections left top of Fig.2-12 for 4 different samples. All HC-PCFs own curvature *b* parameter > 0.8. The measured transmission and loss spectrum plus the modal contents are recorded. All fibers are designed to present loss as low as possible and quasi single mode guidance.

1

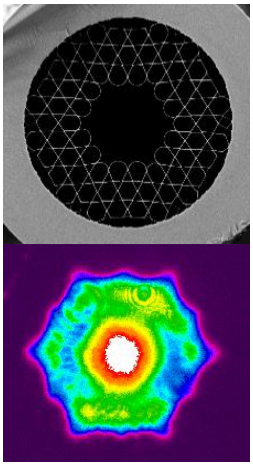

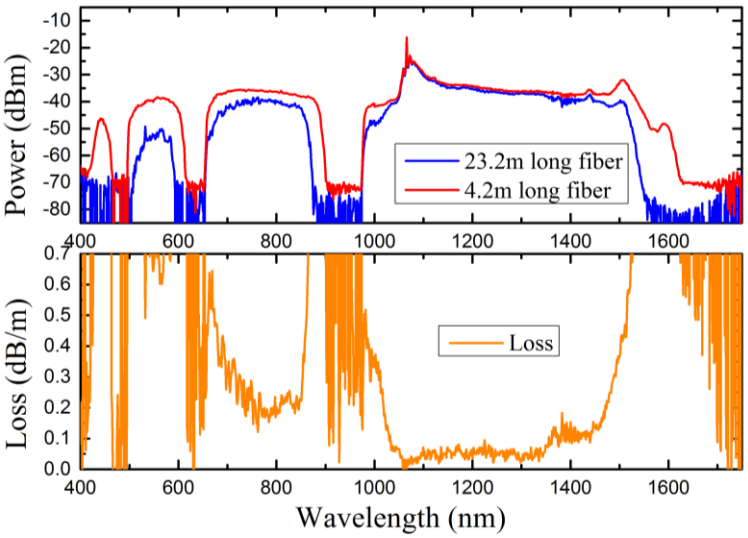
Power (dBm)
23.2m long fiber
4.2m long fiber
Loss (dB/m)
Loss
Wavelength (nm)

2

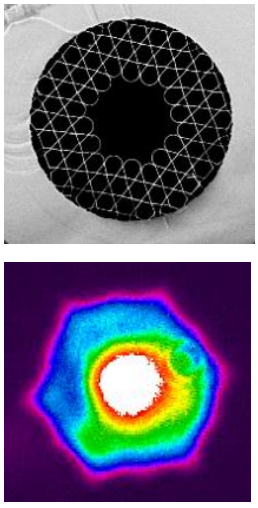

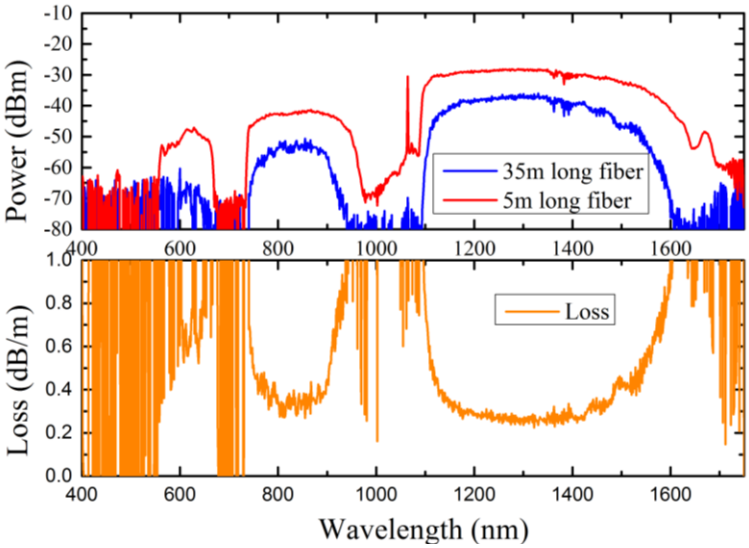
Power (dBm)
35m long fiber
5m long fiber
Loss (dB/m)
Loss
Wavelength (nm)

3

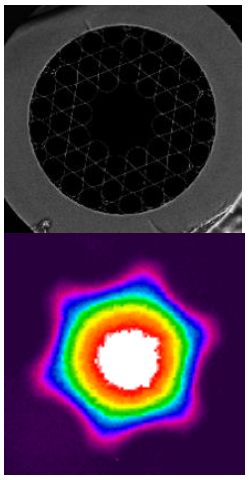

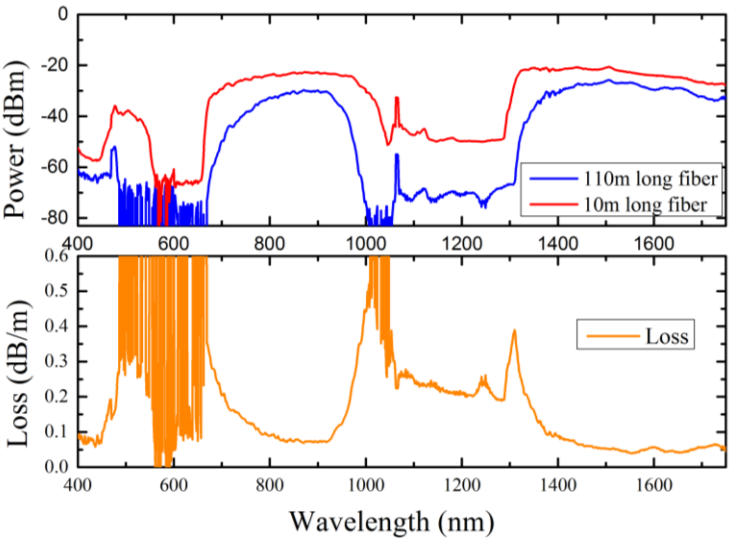
Power (dBm)
110m long fiber
10m long fiber
Loss (dB/m)
Loss
Wavelength (nm)

4

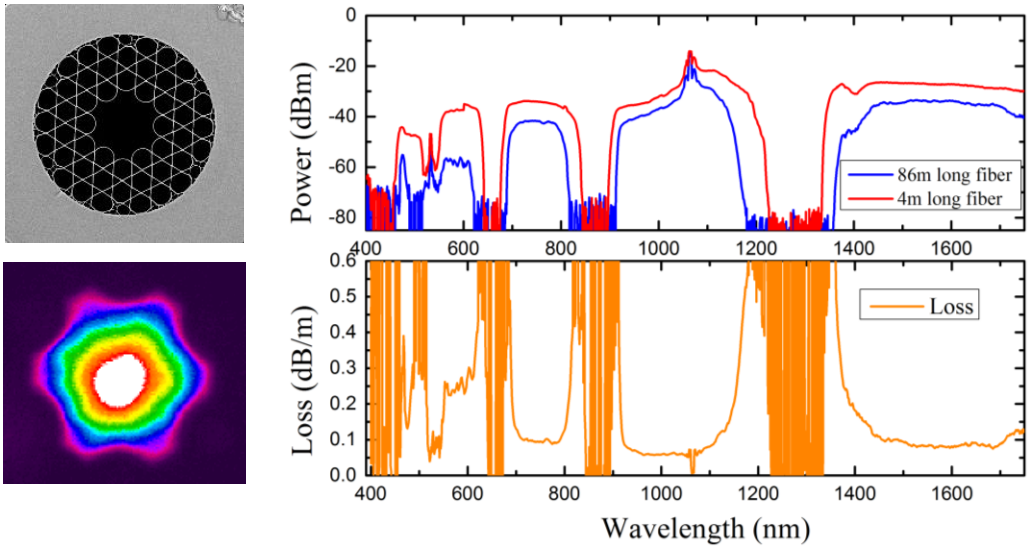

Figure 2-12: SEM image (left top), modal content (left bottom), transmission spectrum and loss spectrum (right) of the four fabricated fiber selected for relaxation measurement.

2.8.3 Fiber selection for Sub-Doppler transparencies work

For single laser beam generated sub-Doppler transparencies in Rb-loaded HC-PCF experiments, we used a fiber sample which presents 7 cells core defect hypocycloid-core shape Kagome HC-PCF. The core size is D_{in}/D_{out} = 63.5/75.5 μm and the curvature parameter *b* is 0.83. The measured loss at 780 nm for this fiber is ~ 100 dB/km with quasi single guiding mode.

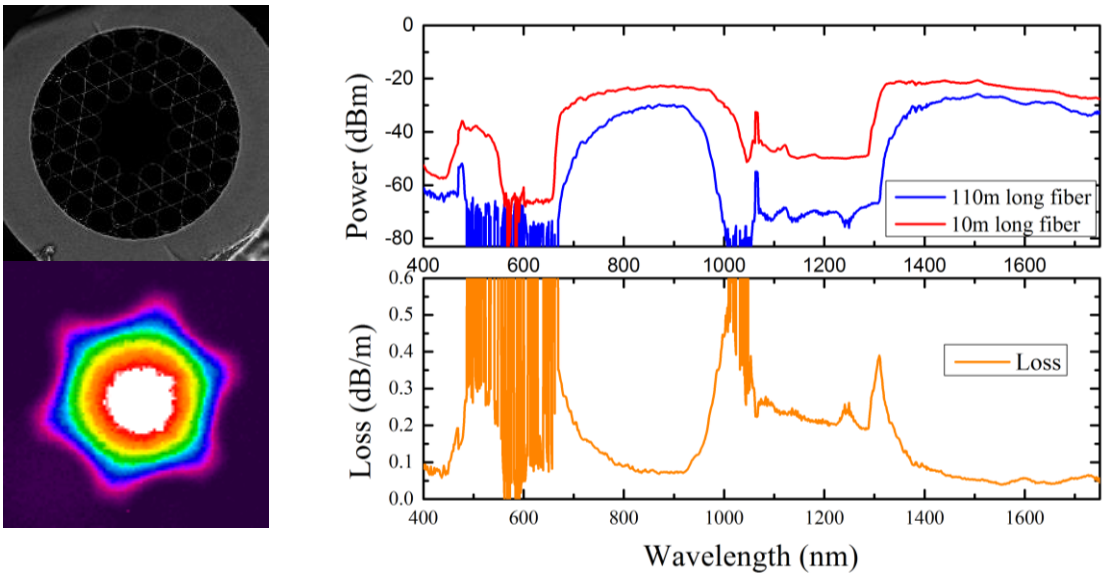

Figure 2-13: SEM image (left top), modal content (left bottom), transmission spectrum and loss spectrum (right) of the fabricated fiber for sub-Doppler transparencies experiment.

2.9 Summary

This chapter reports on the two main families of HC-PCFs named photonic bandgap and inhibited coupling. After a detailed review of their guidance properties, the IC HC-PCF appears as the most suitable for the atomic vapour applications. Indeed, IC HC-PCF can be designed to present both low attenuation and broadband guidance for the classical spectral region of the spectroscopy. In addition, IC HC-PCF can provide a much larger core geometry than the PBG while maintaining a quasi-single mode operation and with the absence of the parasitic surface mode. Consequently, in the last section of this chapter, the fabrications of several IC hypocycloid-core shape HC-PCFs optimized for this thesis are detailed. In the next chapters, investigations based on these fibers such as post-processing techniques, relaxation time measurement and in-fiber single laser generated sub-Doppler transparencies are reported.

2.10 References

[1] Marcatili, Enrique AJ, and R. A. Schmeltzer. "Hollow metallic and dielectric waveguides for long distance optical transmission and lasers." Bell Labs Technical Journal 43, no. 4 (1964): 1783-1809.

[2] Benabid, Fetah, Jonathan C. Knight, G. Antonopoulos, and P. St J. Russell. "Stimulated Raman scattering in hydrogen-filled hollow-core photonic crystal fiber." *Science* 298, no. 5592 (2002): 399-402.

[3] P. Yeh, A. Yariv, and E. Marom, “Theory of Bragg fiber,” J. Opt. Soc. Am., vol. 68, no. 9, p. 1196, 1978.

[4] Fink, Yoel, Joshua N. Winn, Shanhui Fan, Chiping Chen, Jurgen Michel, John D. Joannopoulos, and Edwin L. Thomas. "A dielectric omnidirectional reflector." *Science* 282, no. 5394 (1998): 1679-1682.

[5] S. Johnson, M. Ibanescu, M. Skorobogatiy, O. Weisberg, T. Engeness, M. Soljacic, S. Jacobs, J. Joannopoulos, and Y. Fink, “Low-loss asymptotically single-mode propagation in large-core OmniGuide fibers.,” Opt. Express, vol. 9, no. 13, pp. 748–779, 2001.

[6] B. Temelkuran, S. D. Hart, G. Benoit, J. D. Joannopoulos, and Y. Fink, “Wavelength-scalable hollow optical fibres with large photonic bandgaps for CO2 laser transmission.,” Nature, vol. 420, no. 6916, pp. 650–653, 2002.

[7] Torres, David, Ori Weisberg, Gil Shapira, Charalambos Anastassiou, Burak Temelkuran, Max Shurgalin, Steven A. Jacobs et al. "OmniGuide photonic bandgap fibers for flexible delivery of CO2 laser energy for laryngeal and airway surgery." *In Biomedical Optics 2005*, pp. 310-321. International Society for Optics and Photonics, 2005.

[8] P. Russell, “Photonic crystal fibers.,” Science, vol. 299, no. 5605, pp. 358–62, 2003.

[9] T. A. Birks, “Full 2D photonic band gaps in silica/air structures,” Electon. Lett., vol. 31, no. 22. pp. 1941–1943, 1995.

[10] R. F. Cregan, B. J. Mangan, J. C. Knight, T. A. Birks, P. S. Russell, P. J. Roberts, and D. C. Allan, “Single-mode photonic band gap guidance of light in air,” Science (80-.)., vol. 285, no. 5433, pp. 1537–1539, 1999.

[11] T. A. Birks, J. C. Knight, and P. St. J. Russell, "Endlessly single-mode photonic crystal fiber," Opt. Lett. 22, 961-963, 1997.

[12] Knight, Jonathan C., Jes Broeng, Tim A. Birks, and P. St J. Russell. "Photonic band gap guidance in optical fibers." *Science* 282, no. 5393 (1998): 1476-1478.

[13] F. Benabid, J. C. Knight, G. Antonopoulos, and P. S. J. Russell, “Stimulated Raman scattering in hydrogen-filled hollow-core photonic crystal fiber.,” Science, vol. 298, no. August 2016, pp. 399–402, 2002.

[14] F. Couny, F. Benabid, P. J. Roberts, P. S. Light, and M. G. Raymer, “Generation and photonic guidance of multi-octave optical-frequency combs,” Science, vol. 318, no. 2007, pp. 1118–1121, 2007.

[15] F. Benabid and P. J. Roberts, “Linear and nonlinear optical properties of hollow core photonic crystal fiber,” J. Mod. Opt., vol. 58, no. 2, pp. 87–124, 2011.

[16] F. Couny, F. Benabid, P. J. Roberts, M. T. Burnett, and S. a Maier, “Identification of Bloch-modes in hollow-core photonic crystal fiber cladding.” Opt. Express, vol. 15, no. 2, pp. 325–338, 2007.

[17] T. a Birks, G. J. Pearce, and D. M. Bird, “Approximate band structure calculation for photonic bandgap fibres.,” Opt. Express, vol. 14, no. 20, pp. 9483–9490, 2006.

[18] N. M. Litchinitser, a K. Abeeluck, C. Headley, and B. J. Eggleton, “Antiresonant reflecting photonic crystal optical waveguides.,” Opt. Lett., vol. 27, no. 18, pp. 1592–1594, 2002.

[19] J. R. Hook, and H. E. Hall, Solid State Physics, Great Britain, 2004

[20] T. P. White, R. C. McPhedran, C. Martijnde Sterke, N. M. Litchinitser, and B. J. Eggleton, “Resonance and scattering in microstructured optical fibers,” Opt. Lett., vol. 27, no. 22, p. 1977, 2002.

[21] M. Klein, M. Hohensee, D. F. Phillips, and R. L. Walsworth, “Electromagnetically induced transparency in paraffin-coated vapor cells,” Phys. Rev. A, vol. 83, no. 1, p. 13826, Jan. 2011.

[22] P. Light, F. Couny, Y. Wang, N. Wheeler, P. Roberts, and F. Benabid, “Double photonic bandgap hollow-core photonic crystal fiber.,” Opt. Express, vol. 17, no. 18, pp. 16238–43, 2009.

[23] F. Couny, F. Benabid, and P. S. Light, “Large pitch kagome-structured hollow-core PCF,” Conf. Lasers Electro-Optics, 2007, CLEO 2007, no. August, pp. 3–5, 2007.

[24] Benoît Debord, ‘Génération et micro-confinement de plasmas microondes dans des fibres optiques creuses microstructurées’, thesis 2013.

[25] Y. Y. Wang, F. Couny, P. J. Roberts, and F. Benabid, “Low loss broadband transmission in optimized core-shape Kagome Hollow-Core PCF,” Lasers Electro-Optics Quantum Electron. Laser Sci. Conf. (QELS), 2010 Conf., p. CPDB4, 2010.

[26] Y. Y. Wang, N. V. Wheeler, F. Couny, P. J. Roberts, and F. Benabid, "Low loss broadband transmission in hypocycloid-core Kagome hollow-core photonic crystal fiber," Opt. Lett. 36, 669-671, 2011.

[27] F. Yu, W. J. Wadsworth, and J. C. Knight, “Low loss silica hollow core fibers for 3–4 μm spectral region,” Opt. Express, vol. 20, no. 10, pp. 11153–11158, 2012.

[28] F. Yu and J. C. Knight, “Spectral attenuation limits of silica hollow core negative curvature fiber.,” Opt. Express, vol. 21, no. 18, pp. 21466–71, 2013.

[29] B. Julsgaard, J. Sherson, J. I. Cirac, J. Fiurásek, E. S. Polzik, J. Fiurášek, and E. S. Polzik, “Experimental demonstration of quantum memory for light,” Nature, vol. 432, no. 7016, pp. 482–486, 2004.

[30] Andrey D. Pryamikov, Alexander S. Biriukov, Alexey F. Kosolapov, Victor G. Plotnichenko, Sergei L. Semjonov, and Evgeny M. Dianov, "Demonstration of a waveguide regime for a silica hollow - core microstructured optical fiber with a negative curvature of the core boundary in the spectral region > 3.5 μm," Opt. Express 19, 1441-1448, 2011.

[31] B. Debord, M. Alharbi, T. Bradley, C. Fourcade-Dutin, Y. Wang, L. Vincetti, F. Gérôme, and F. Benabid, "Cups curvature effect on confinement loss in hypocycloid-core Kagome HC-PCF," Cleo 2013, p. CTu2K.4, 2013.

[32] Bradley, Thomas D., et al. "Optical properties of low loss (70dB/km) hypocycloid-core Kagome hollow core photonic crystal fiber for Rb and Cs based optical applications." Journal of Lightwave Technology 31.16 (2013): 2752-2755.

[33] S. Selleri, L. Vincetti, A. Cucinotta, and M. Zoboli, "Complex FEM modal solver of optical waveguides with PML boundary conditions," Opt. Quantum Electron. 33(4/5), 359–371, 2001.

[34] Amezcua-Correa, Rodrigo, N. G. R. Broderick, M. N. Petrovich, F. Poletti, and D. J. Richardson. "Optimizing the usable bandwidth and loss through core design in realistic hollow-core photonic bandgap fibers." Optics Express 14, no. 17 (2006): 7974-7985.

[35] L. Vincetti and V. Setti, "Confinement loss in kagome and tube lattice fibers: Comparison and analysis," J. Light. Technol., vol. 30, no. 10, pp. 1470–1474, 2012.

[36] Vincetti, L., and V. Setti. "Extra loss due to Fano resonances in inhibited coupling fibers based on a lattice of tubes." *Optics express* 20, no. 13 (2012): 14350-14361.

[37] F. Benabid, P. J. Roberts, F. Couny, and P. S. Light, "Light and gas confinement in hollow-core photonic crystal fibre based photonic microcells," J. Eur. Opt. Soc., vol. 4, no. c, pp. 1–9, 2009.

[38] Debord, Benoît, Meshaal Alharbi, Tom Bradley, C. Fourcade-Dutin, Y. Y. Wang, Luca Vincetti, Frédéric Gérôme, and F. Benabid. "Hypocycloid-shaped hollow-core

photonic crystal fiber Part I: Arc curvature effect on confinement loss." Optics Express 21, no. 23 (2013): 28597-c.

[39] Bradley, Thomas David. “Atomic Vapours Filled Hollow Core Photonic Crystal Fibre for Magneto-Optical Spectroscopy University of Bath.” University of Bath.. 2013

[40] Roberts P, Couny F, Sabert H, Mangan B, Williams D, Farr L, et al. Ultimate low loss of hollow-core photonic crystal fibres. Optics express. 2005 Jan 10; 13(1):236–44.

[41] Bradley TD, Wang YY, M A, Fourcade Dutin C, Mangan BJ, Wheeler N V, et al. Progress in hollow core photonic crystal fiber for atomic vapour based coherent optics. Proc. SPIE 8273, Advances in Slow and Fast Light V, 82730. 2012.

[42] B. Debord, A. Amsanpally, J. Blondy, F. Gérôme, and F. Benabid, "Low loss Inhibited coupling Hollow-core photonic crystal fiber with ultrabroad Fundamental Band," in Conference on Lasers and Electro-Optics, OSA Technical Digest (2016) (Optical Society of America, 2016), paper STu4P.2.

Chapter 3

Post-processing of hollow-core photonic crystal fiber

This chapter introduces the different processes in post-processing HC-PCF before, during and after the atom loading inside the fiber. This process chain is required in making what would be the first all-fiber alkali-vapor photonic microcell (PMC). It comprises HC-PCF tapering, splicing, in-fiber gas handling, fiber core inner-wall coating and of course vapor loading. The chapter stresses on techniques of tapering HC-PCF with hypocycloid core-contour with no structural distortion and splicing them to an all-solid optical fiber. The chapter presents also alternative ways to splice HC-PCF to solid fiber using sleeving techniques. Finally, we report on the coating material synthesis and on the process of the fiber core inner-wall coating. Several HC-PCFs with ceramic and PDMS coated core along with uncoated HC-PCF have been put in a high vacuum system for rubidium loading, lifetime assessment and for spectroscopy experiments. The results show that all the coated HC-PCF kept their optical performances. As expected, the ceramic coated HC-PCFs exhibit much longer Rb life time inside the fiber which is paramount for stand-alone PMC applications.

3.1 Photonic microcells (PMCs)

A photonic microcells (PMCs) is an integrated optical component consisting of a length of hollow-core photonic crystal fiber (HC-PCF) which is filled with an active atom or molecular media, and hermetically sealed to solid optical fibers [1]. Process either based on ferrule technique or based on direct integrated technique (*e.g.* splicing or fiber collapsing) [2] are currently used to make these PMC. Also, the development and the optimization on HC-PCF guidance has opened up vast and new possibilities for gases or atoms confined optical applications [3]. Today, we can list several gases such as CO, CO2, C2H2, CH4, H2, H2S, HCN, I2, HF, Xe, Ar already used in HC-PCF to target applications as varied as Near-IR and Mid-IR tunable laser [4,16, 17,30], frequency references for telecommunication [5,6,28], rotational sensing [7-9], nonlinear optics [10,29], Raman comb [11,26], pulse compression [13], self-phase modulation [14,15], Quantum memory [18], Plasma [21], coherent optics [23-26, 31-34] etc. However, the Alkali atom (*e.g.* Rb, Cs) confined PMC is not yet succeed to be fabricated due to the challenge of its high reactivity which requires a strict vacuum environment ($< 10^{-8}$ Torr). To confine such active Rb atom into the hollow-core fiber, we develop a novel sleeve splicing techniques. Additionally, the small hollow-core dimension will cause a substantial increase of the atom-surface interaction resulting in physio-chemical absorption. All these issues will be studied in this chapter.

3.2 IC-PMC vs PBG-PMC

As introduced in the previous chapter, two significant designs of HC-PCF have been developed over the last decade and classified by their guidance mechanism named as Photonic Bandgap (PBG) and Inhibited Coupling (IC). PMCs based on these two common types of HC-PCFs are compared on fig. 3-1 by modal content, collisional dephasing related to the core size and inner wall surface material, transmission loss and insertion loss.

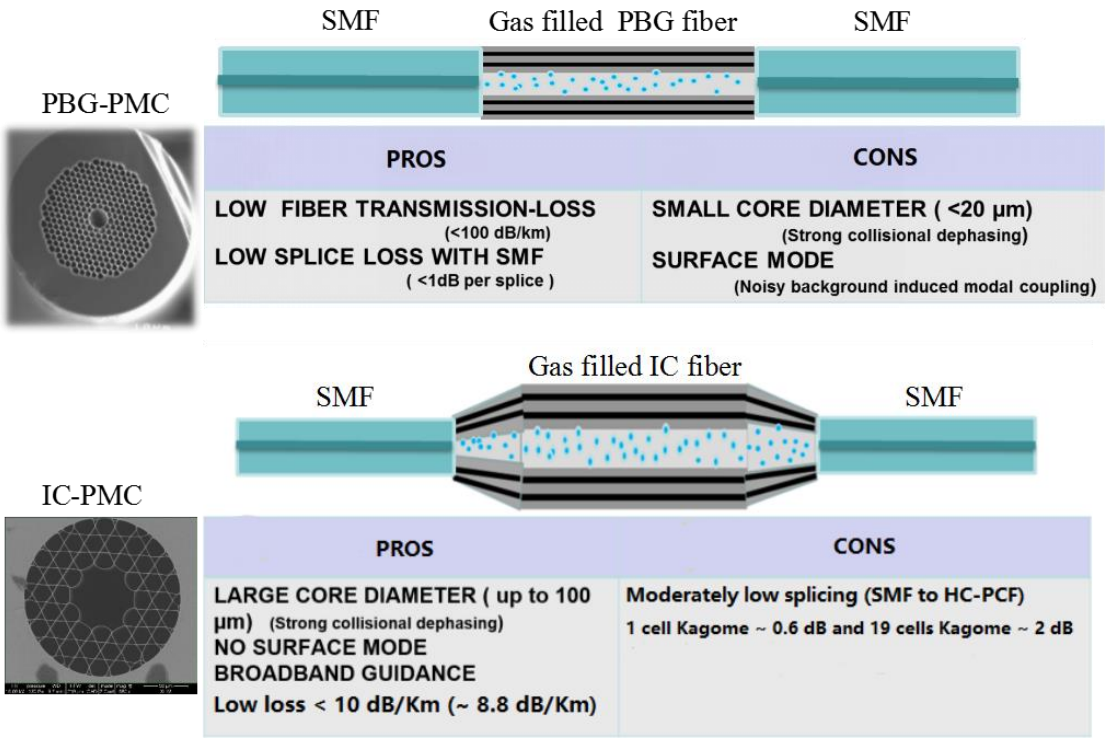

Figure 3-1: Comparison between the IC-PMC and PBG-PMC.

Based on the current PBG fiber fabrication, PBG-PMC has advantages on the single mode guiding modal content, low transmission loss and the comparable core size to SMF inducing splice loss inferior to 1 dB [20]. However, several drawbacks exit regarding our application. First, the core size of such fiber is limited by the PBG mechanism resulting in core diameter around 7-10 µm for a 7-cell design working at 700 - 800 nm. This would affect the linewidth of spectral feature which is related to the dephasing effects corresponding to the collision rate between atoms/molecular and the inner core wall. For example, an acetylene-filled PBG-PMC with 10 µm core diameter provides a FWHM of spectral feature ~ 26 MHz which FWHM is much larger than the one in large core acetylene-filled Kagome HC-PCF [28]. Second, the PBG guidance induces the presence of modes at the interface between the core and cladding named “surface modes”. This results in strong modal beating which degrades the visibility of the absorption features. Finally, the transmission bandwidth is limited to 70 THz which can have drawbacks for several spectroscopy applications. In contrast, the IC mechanism allows fibers with much larger core diameter up to 100 µm [22], broader bandwidth of more than one octave combined

with low loss (current record of 30 dB/km at 780 nm) [12]. These unusual optical performances can reduce the linewidth of spectral feature due to the dephasing effects of atom-wall collisions by ~ 8 times compared to a conventional 10 μm core size. For example, an acetylene-filled Kagome HC-PCF shows a FWHM of ~ 8 MHz for saturable absorption features reported by Knabe *et al.* [28]. We remember that the unwanted surface modes are here completely removed and the transmission band fit perfectly for the broadband spectroscopy applications. However, the integration of such large core size IC HC-PCF to all-fiber systems is not trivial. A direct splice with a standard SMF will induce high insertion loss due to the one order magnitude difference of mode-field mismatch (MFM) between the two fibers but also will present a delicate mechanical joint due to air-cladding structure. In the next section, we address these challenges by tapering the IC HC-PCF to demonstrate low loss splice with SMF.

3.3 Inhibited Coupling hypocycloid core Kagome fiber tapering

This problem of MFM has previously been addressed by tapering down such Kagome fibers and then splicing to SMF [39]. The results obtained show insertion loss figures as low as 0.6 dB for a hexagonal core-shape 1-cell Kagome fiber (core size of 45 μm) and 2 dB for a circular core-shape 19-cell Kagome fiber (core size of 65 μm) [19]. Using this tapering technique for hypocycloid-core Kagome HC-PCF would make sense only if the delicate core-shaping is preserved during the post-processing process.

Indeed, our recent research on core shaping revealed the advantages of increasing the negative curvature parameter at the interface between core/clad, as detailed in the previous chapter. Especially, a strong loss decreases was theoretically and experimentally demonstrated to reach few tens of dB/km loss level [37], [38]. Consequently, integrating such new IC hypocycloid-core fiber would be very attractive in order to propose efficient photonic microcells (PMCs) [39]. For that, we need during the post-processing of fusion splice and tapered the hypocycloid-core Kagome HC-PCF to preserve the delicate negative contour at the fiber-core interface and the aspect ratios of transverse cladding structure. In

this context, a tapering technique by using core vacuum compensation method is applied and presented.

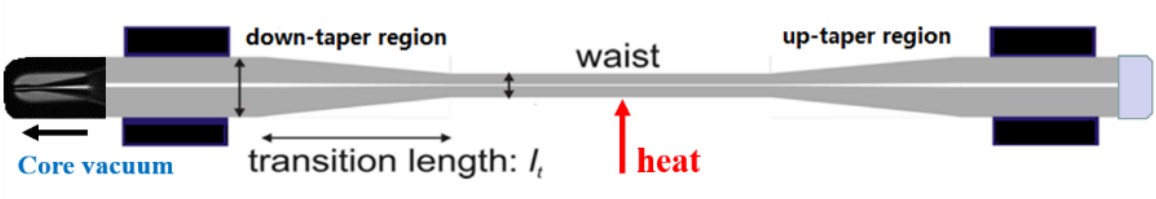

Figure 3-2: Illustration of the fiber tapering procedure using core vacuum method with the referred sections.

Firstly, the cladding at one of the fiber-ends is collapsed while keeping the hypocycloid-core opened by heating the fiber-tip using a commercial filament fusion splicer (Vytran GPX3000). The second fiber-end is completely sealed. The fiber-end with the collapsed cladding is then inserted into mechanical chamber, which is connected to a vacuum pump (10^{-1} mbar maximum) and a pressure gauge. This allows applying a controllable vacuum pressure to the HC-PCF and thus compensating the inner wall surface-tension induced collapse during the tapering process. The last step of the tapering process is achieved by using the function of bi-directional tapering available on the 3SAE LDS plasma fire of ring (FOR) splicer. For that, a fiber section is heated and stretched to form the tapered section. The taper section comprises two regions, one descending in diameter and one ascending in diameter, separated by a section with uniform transverse dimensions. Notice that the descending and ascending sections are referred as the “down-taper” and “up-taper” respectively as shown in Fig. 3-2. The middle section with uniform diameter is referred to the taper “waist”.

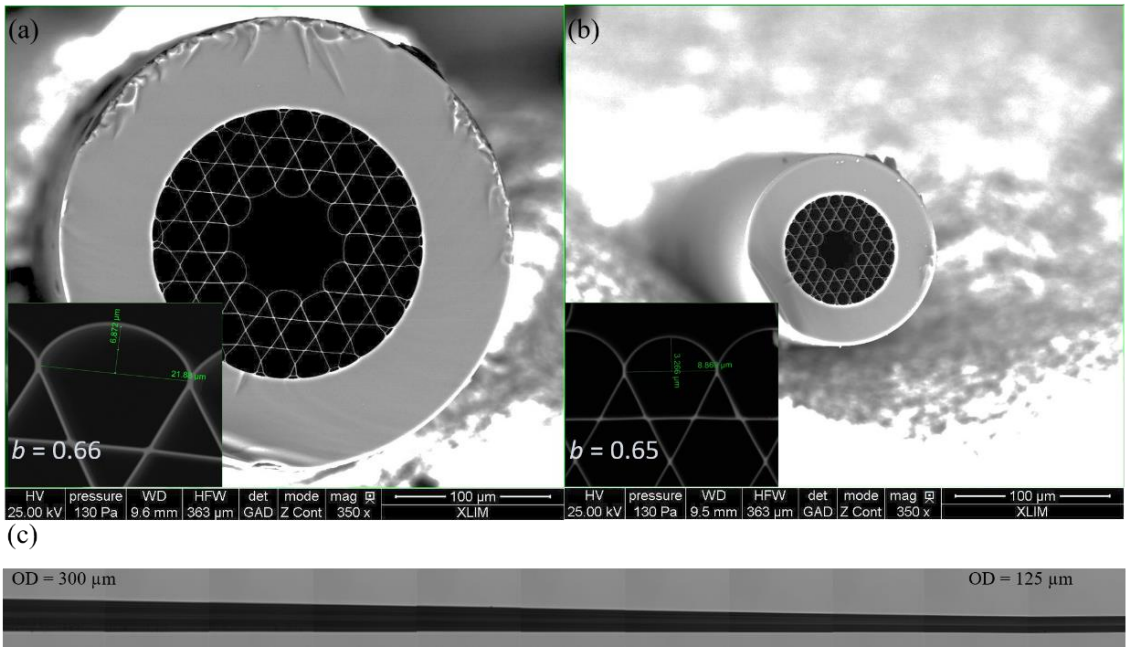

Figure 3-3: (a) Cross section of un-tapered and (b) tapered IC Kagome HC-PCF fiber at the waist region with an outer diameter respectively of 300 µm and 125 µm. In inset: zoom in of the core-contour showing the preservation of the curvature shape before and after the tapering. (c) Evolution of the down-taper region of fiber with length [40].

The fiber sample used for experimental post-processing of fiber tapering was based on a hypocycloid core-shape 7-cell core defect, with 3 rings of Kagome-latticed cladding (see the section 2.8.1 of Chapter 2 for more details of the fiber properties). The strut thickness is equal to t = 550 nm and the curvature parameter b is 0.66 ± 0.02. We remind that b parameter is defined as d/r, where d is the distance between the top of the cups and the chord, r is the radius of the semicircle [37]. The inner and outer core diameter is 63.4 µm and 75 µm respectively. Finally, the fiber presents a fundamental guidance band with a cut-off wavelength at 1100 nm with losses ranging between 90 - 170 dB/km in the analyzed infrared windows.

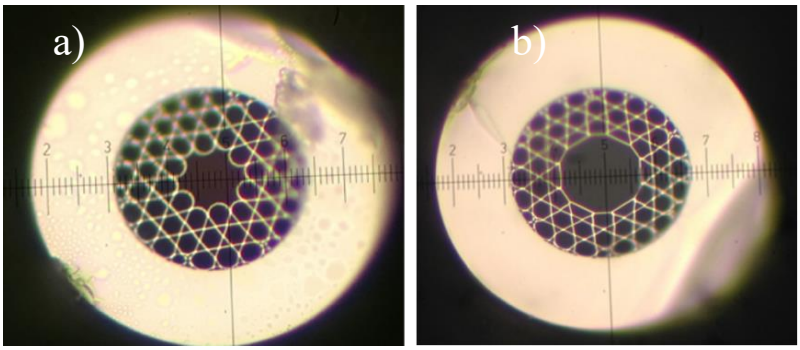

Figure 3-4: IC fiber tapering images with (a) and (b) without core vacuum resulting in the hypocycloid core shape

.

Figures 3-3 (a) and (b) show two scanning electron micrographs (SEM) pictures of the un-tapered and tapered inhibited coupling hypocycloid core shape Kagome fiber. The IC fiber is core vacuumed and outer diameter is fusing stretched from 300 µm down to 125 µm over few tens of mm. The inserted pictures clearly show the curvature of the core contour has been respectively conserved as well as the ratios of the fiber transverse structure. Meanwhile, the strut thickness was reduced as the same ratios from 550 nm to 220 nm. Consequently, the physical integrity of the IC fiber with hypocycloid core shape has been completely preserved during the tapering procedure with a down ratio as large as 2.4. The repeatability of IC fiber tapering is found pretty well with a typical deviation of < 3% on the physical properties, even in the case of further OD reduction down to 80 µm. Figure 3-4 corresponds to the microscopy pics of tapered fiber with core vacuum (Fig. 3-4 (a)) and without core vacuum (Fig. 3-4 (b)) that clearly illustrates that the impact of the vacuum method applied.

In the following step, a systematic study on the impact of the transition length (TL) and down-ratio (DR) of the taper performances made is carried out. A typical transmission and loss spectra of the whole tapered fiber transmission and loss spectrum is shown in fig. 3-5, with down-taper and up-taper TL of 15 mm and DR of 300/200. Notice that the waist length is kept constant to 1 cm. The loss spectrum is characterized by using cut-back technique and by coupling a homemade supercontinuum source. The single mode guiding is confirmed by monitoring the near field of output by an InGaAs IR camera. The transmission spectrum shows a taper loss ranging between 0.2 dB to 0.5 dB in the analyzed IR range < 1680 nm. The recorded fluctuations in the loss spectrum are attributed to the

power noise of the white light source and the limited resolution of the optical spectrum analyzer.

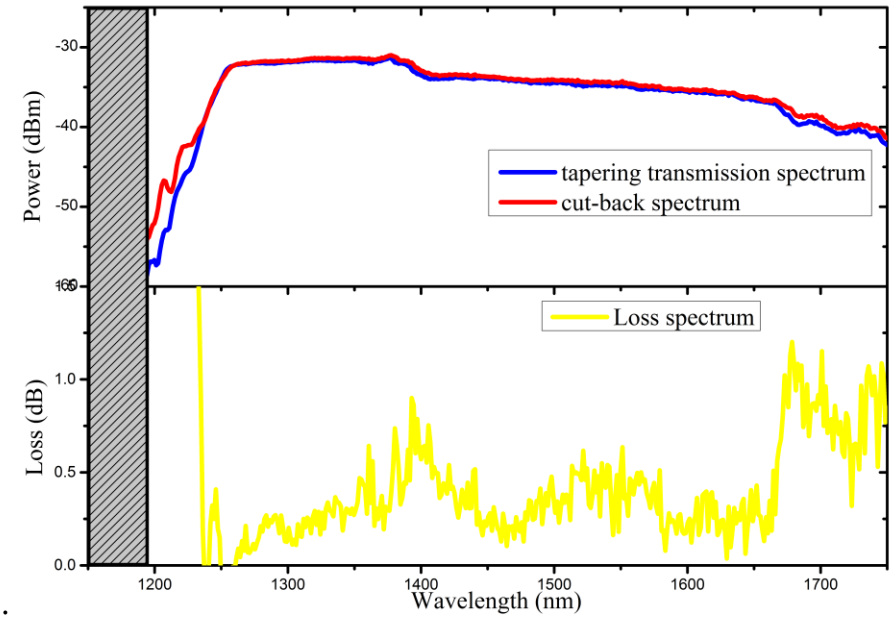

Figure 3-5: Measured transmission spectra of 3 m long HC-PCF with a tapered section from an OD of 300 µm to 200 µm with a full length of 4 cm (TL = 15 mm and waist section length of 10 mm) (blue curve) and of the cut-back at the start of the tapered section (red curve). Full taper loss spectrum (yellow curve).

To get more accurate figures, the loss is measured by launching single wavelength laser operating at 1550 nm. The transmission losses measured at 1550 nm for both full taper and down-taper region with different TL and DR are shown in Fig. 3-6. Notice here, the transmission losses are taken the average of 10 repeating fiber tapering losses for each tapered fiber with fixed TL and DR. The whole taper loss is cut back at the start of the full taper region shown in Fig. 3-6 (a), and the down-taper loss is cut back at the middle of the taper waist region shown in Fig. 3-6 (b). In figure, the error bar corresponds to the standard deviation of the repeated measurements. The first view in the figures shows that the whole taper loss drops 8 folds from 1.6 dB down to 0.14 dB when DR is decreasing from 300/125 to 300/200 for fixed TL of 5 mm. Also, the whole taper loss is dropping from 1.6 dB to 0.4 dB when the TL is tapered more than 20 mm for a fixed DR of 300/125. A further investigation on the propagation loss dynamics along the taper was carried out by

performing loss measurement for the up-taper section by cutting the fiber at the middle of the taper waist. This would be of interest for integrating future PMC. By cutting the tapered fiber at the middle of the taper waist (see Fig. 3-6 (b)), the minimum down-taper loss is found to be 0.07 dB for a TL of 20 mm and DR of 300/125. As expected, for both the whole taper loss and the down-taper loss we found such low tapering loss for IC fiber is induced when the TL is increasing and inversely proportional to the DR. The asymmetry between the down-taper loss and up-taper loss is likely due to excitation of higher order modes in the up-taper region, which means an un-adiabatic taper. However, this asymmetry is improved by increasing the TL, and the up-taper loss/down-taper loss become symmetry when the TL > 20 mm, resulting for the whole taper loss of 0.14 dB. Furthermore, for the taper with the lowest DR, the loss varies little. This evolution reveals that an adiabatic transition [41][42].

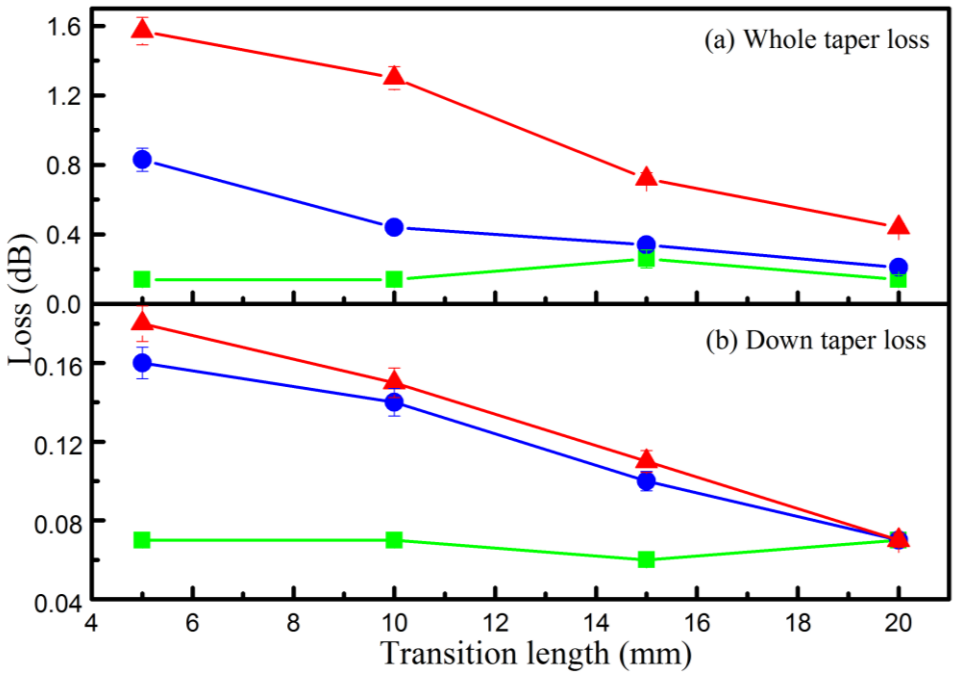

Figure 3-6: (a) Evolution of the loss at 1550 nm of several independent whole tapered fibers for three different DR (300 µm to 200 µm: green line, 300 µm to 150 µm: blue line and 300 µm to 125 µm: red line) and for different TL (5 mm, 10 mm, 15 mm and 20 mm) and (b) for only the down-tapered fiber section.

This conclusion is also confirmed by recording the near field at the tapered IC fiber output (see Fig. 3-7). The figures clearly show that the single mode guiding at the beginning of taper region become multi-mode when the the taper region is reached when TL is 5 mm. For higher TL (*i.e.* 20 mm), the single mode is adiabatic guided through the tapered region with 98.4% light transmission.

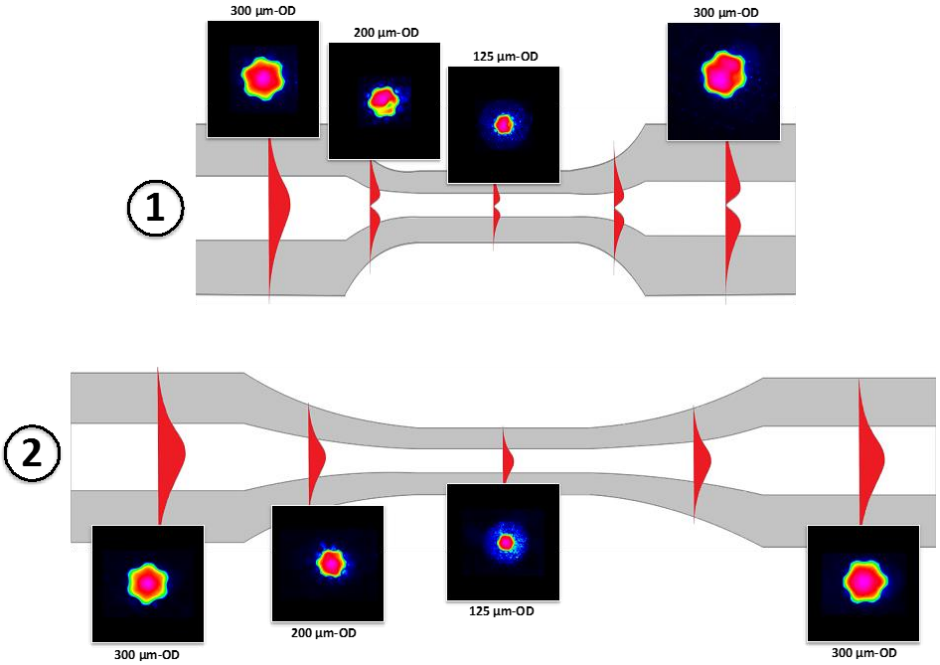

Figure 3-7: Evolution of the near field for two tapers differentiated by different TL, referred by 1 (TL = 5 mm and DR = 300/125) and 2 (TL = 20 mm and DR = 300/125) recorded by launching 1550 nm laser source.

3.4 Inhibited Coupling hypocycloid core Kagome fiber splicing

Low taper loss for IC fiber has been achieved as demonstrated above. Then, investigation on the IC fiber splicing would be of interest for further integrated application. In this context, we propose in this section to study the splice of half taper IC Kagome fiber (down-taper) to a standard SMF. The chosen tapered Kagome fiber presents a transition length of 20 mm and a down ratio of 300/125. The IC fiber splicing is obtained by using the same core vacuum method as previously described. The IC fiber splicing procedure is discussed as following steps. Firstly, the down-taper IC fiber is prepared by cleaving at the

middle of the taper waist. Then the second fiber-end with cladding collapsed is core vacuuming. After few seconds, we start the fusion splicing by normalized fusion power and pushing velocity. As the result, the splicing loss for IC fiber is strongly improved as detailed in the following. Also the mechanical joint at the splicing region of core vacuum splicing (mechanical strength ~ 320 grams) is much stronger than the splicing without core vacuum (mechanical strength ~ 80 grams). This is found mechanically robust as typical PBG-SMF fusion joint. Figure 3-8 shows the transmission spectrum and loss spectrum of both light propagation direction Kagome fiber-to-SMF, and SMF-to-Kagome fiber. Notice here, the total insertion loss spectrum of fiber section is composed of 1.2 m long piece of OD = 300µm Kagome fiber, a tapered region (TL of 20 mm, waist length of 5 mm) and a splice to a 3m long piece of SMF. The light coupling is monitored through an InGaAs IR camera at the output of the 300 µm-OD Kagome fiber to preferentially select the fundamental mode (FM) of core mode.

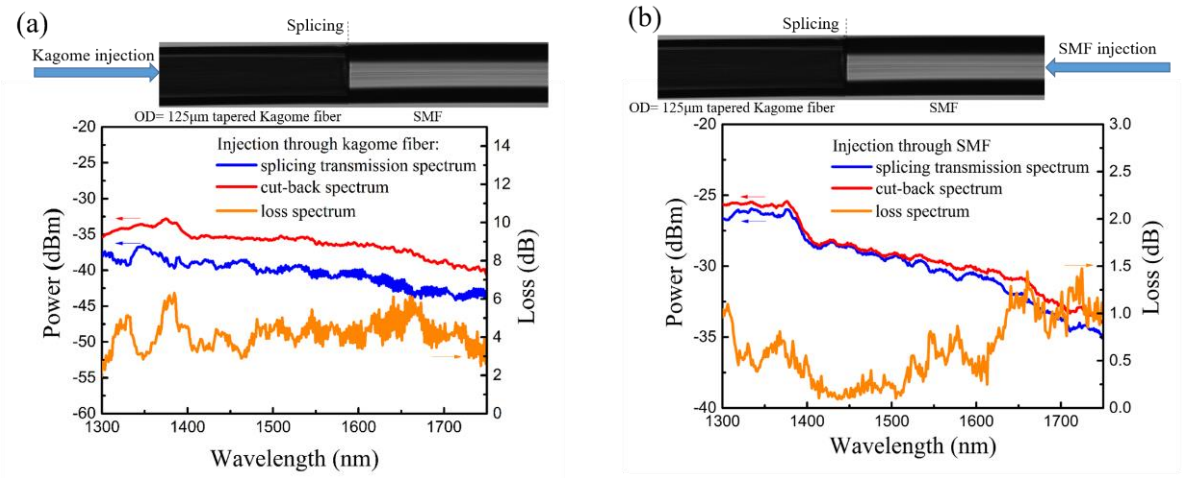

Figure 3-8: Measured splicing transmission spectrum of tapered Kagome-SMF (blue line) the cutback (red line) and the insertion loss spectrum (black line) for the two sides launching. (a) Light is injected from 300 µm-OD Kagome section by a SMF; (b) Light is injected from SMF to the 125 µm-OD Kagomé section. In inset the images of the splice are shown.

For the case of SMF-to-Kagome configuration, the splice loss adding to the previous 0.45 dB of the taper transition is measured to 0.48 dB at 1550 nm. This loss figure presents average of ten splices with a standard deviation of few percent. In order to corroborate and understand this number, the transition loss and modes power modal in-fiber coupling have then been numerically simulated by computing the overlap integrals [43]. This

experimental value is found to be in very good agreement in comparison with the theoretical loss prediction of 98.3% light coupling, *i.e.* an 0.07 dB increased of the total loss, due to the MFM. In more detail, this corresponds to 76.7% of the power coupled to being in the fundamental mode, and 21.6% in the first higher order mode (HOM) which can be excited in case of zero axis offset between the two fibers (here HE_{12}). For the reverse case, *i.e.* light is firstly injected through the 300 µm-OD Kagome fiber, the experimental loss figure increases to 3.5 dB at 1550 nm. This result is found much higher than the MFM theoretical limit of 1.15 dB when only the FM is excited in the Kagome fiber. The difference is thus likely due non-negligible guided power in HOM present at the tapered section. Consequently, in the case where the Kagome fiber modal content is limited to FM and HE_{12}, and in the absence of any other loss source apart from those of MFM, the measured 3.5 dB is found very closed to the following calculated power distribution in the HC-PCF: 18.7% in the foundamental mode and 30.3% in the high order mode HE_{12} (49% total light coupling, *i.e.* 3.1 dB). Notice here that this splicing loss due to the MFM between two fibers could be improved by using, in place of standard SMF, larger single mode fiber as Bragg fiber.

In conclusion, the splicing result obtained is the first step toward integrated IC HC-PCF to all fiber systems. The physical integrity of IC HC-PCF has been completely preserved during the tapering process and the splicing process. Such techniques allow IC-PMCs provide low insertion loss, robust mechanical joint and maintained IC proprieties. In next section, a novel PMC tailoring technique sleeve splice will be introduced in order to address the challenge of confining reactive atom into the HC-PCF.

3.5 Inhibited coupling hypocycloid core Kagome fiber sleeve

In order to confine Rb atom into hollow-core fiber, pioneer work proposed a tailoring process by thermal clamping the helium diffusion [2]. However, using this technique presents several challenges in our case. Indeed, making a fusion splice under such conditions will cause cracks of the fibers very easily due to the low thermal conductivity of

silicate material. Also, helium diffusion method has limited splicing time and became very delicate to manage in the case of our Kagome fibers which present large core diameter susceptive to be quickly contaminated. To solve this problem, a sleeve splicing technique based on surround borosilicate capillary is proposed and developed. The main reason to choice borosilicate glass as the role of host is referred to its lower softening temperature compared to silicate material, allowing better splicing management. Table 3-1 shows the silicate and borosilicate material properties.

Table 3-1: Silicate and Borosilicate glass properties.

	Annealing points	**Softening points**	**Thermal conductivity**	**Thermal expansion**
Borosilicate glass (Schott 8330)	*560 ºC*	*820 ºC*	*1.2 $W.m^{-1}.K^{-1}$*	*3.3×10^{-6} K^{-1}*
Silicate glass (Schott BK7)	*1080 ºC*	*1600 ºC*	*1.114 $W.m^{-1}.K^{-1}$*	*7.1×10^{-6} K^{-1}*

The following introduce the sleeve splice procedures. As the chemical reactive atom or gas' host, both Kagome fiber and borosilicate capillary must be flushing and baking to remove any residential contamination. The ID of sleeve capillary is then chosen to present an optimized fitting with the OD of Kagome fiber in order to limit misalignment problem (angle splicing) during the fusion. The ideal ID of borosilicate capillary is generally ~5 μm to 10 μm larger than the OD of spliced Kagome fiber. Once Kagome fiber is inserted into the sleeve, the borosilicate capillary is fused to clamp the fiber. The fusion power should be optimized to avoid additional losses which are caused by structure deformations and fragility of the sleeve due to the thermal conductivity difference. To protect this fused joint, the section is glued to create a soft layer. The hermetic seal of sleeve splice is then tested under flowing a pressure of 10 bar Helium gas. Figure 3-9 presents examples of two types of sleeve made. The first scheme (Fig. 3-9 (a)) uses in reality two sleeves. The first one matches the OD of SMF and the ID of the second sleeve. This second sleeve hermetically seals the Kagome fiber to the SMF. The second type uses only a single sleeve to splice a tapered Kagome fiber with a SMF (Fig. 3-9 (b)).

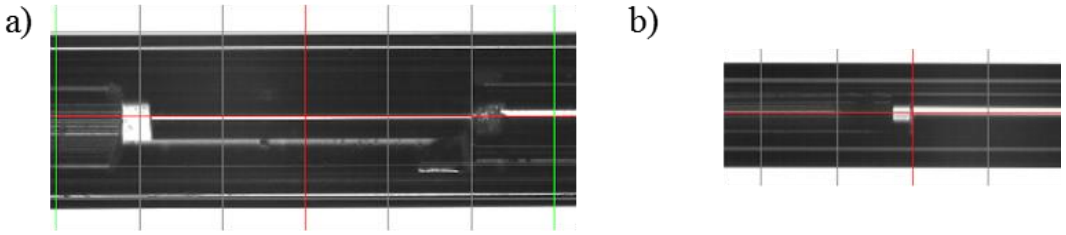

Figure 3-9: Images of two types of sleeve splicing by using (a) a dual or(b) a single sleeve scheme.

In both cases, the insertion loss have been investigated and are summarized in the Table 3-2 as a function of the air gap.

Table 3-2: Single and dual sleeve splicing loss.

Air-cap		10 µm	50 µm	100 µm	150 µm	200 µm
Single sleeve	**SMF to tapered Kago insertion**	*0.58 dB*	*0.93 dB*	*1.12 dB*	*1.34 dB*	*1.51 dB*
	Tapered Kago to SMF insertion	*1.27 dB*	*1.3 dB*	*1.63 dB*	*2.71 dB*	*3.55 dB*
Dual sleeve	**SMF to Untapered Kago insertion**	*2.51 dB*	*2.67 dB*	*2.53 dB*	*2.7 dB*	*2.6 dB*
	Untapered Kago to SMF insertion	*9.7 dB*	*12.9 dB*	*16 dB*	*17.5 dB*	*20.2 dB*

As expected, misalignment causes strong attenuation for the final sleeve splice loss. The optimized single sleeve splicing provides loss ~ 0.58 dB for an air-cap of 10 µm between SMF and tapered Kagome HC-PCF which is acceptable for our applications. For the case of the dual sleeve splicing, losses are found higher as ~ 2.51 dB for an air-cap of 10 µm. Notice that to further reduce the impact of the air-gap, so the Fresnel reflections, the splice could to be angle cleaved as reported in ref [44].

In the following section, anti-relaxation material HC-PCF inner wall coating procedure will be introduced as a very important topic along this thesis. Especially, the characterization of coating quality and the inner wall coating optimization will be developped.

3.6 Anti-relaxation material inner wall surface coating

A last part concerns the challenge of the reactivity of the alkali-materials. Indeed, the micrometer geometric of our hollow-core fiber enhances atom-surface interaction resulting in dephasing problem due to physio-chemical adsorption. Coating the inner wall surface with anti-relaxation material through a chemical deposition could solve this problem which limit the high performance optical spectroscopy applications. Also, the coating materials used on the inner core wall should be transparence at our spectral range operation. Finally, the coating deposition thickness should not be exceeding 100 nm to not affect the optical guidance properties.

In this section two anti-relaxation coating materials are investigated, one is Polydimethylsiloxane (PDMS) and the other is Aluminosilicated sol-gel. This work is done in collaboration with laboratory SPCTS of European ceramic center at Limoges.

3.6.1 Polydimethylsiloxane (PDMS) solution synthesis

For PDMS solution synthesis, a 0.5% volume of silicon oil is diluted into diethyl ether. Practically, as silicon oil is too viscous to measure a volume, we have to weight a small mass of it, then calculate its equivalent volume by dividing the mass by 0.98 which is its volume mass. At this point, add diethyl ether to the solution until a 0.5% ratio is achieved. All of this must be done under controlled temperature to avoid the boiling point of the solution at 35 °C. Continuous stirring during 24 hours is done to ensure the PDMS is uniformly distributed in the diethyl ether solvent. One the solution is ready, the process to fill the HC-PCF is applied by following the method described below (section 3.6.3). Then the samples are just dried at 80°C for 24h, no need for a further thermal treatment. PDMS is characterized as one kind of anti-relaxation material [47], and its LIAD [48] properties determined. The benefits of such materials in HC-PCF on transit time and dwell time will be quantified through a magneto-optical rotation spectroscopic technique in Chapter 4.

3.6.2 Aluminosilicate Sol-Gel solution synthesis

For the second solution, Aluminosilicate sol-gel is synthesized by dissolute Aluminum nitrate hexahydrate ($Al(NO_3)_3$, ^9H_2O) in ethanol at room temperature. Stirring is then applied during half a day to get a uniform dissolution. Then slowly, we add 1.49 mL of tetraethoxysilane (TEOS) in the transparent solution [27][35] which storage solution contain Al/Si ratio = 2 and the metal concentration 0.8 $mol.L^{-1}$. The final solution is diluted in a 2% molar concentration of ethanol to metal concentration of 0.1 $mol.L^{-1}$ to reduce the viscosity. Similarly, pumping this solution into the hollow-core fiber is followed. The motivation of using this material is its high corrosion resistance and low outgassing rate. Also, the possibility of deposition on stainless steel surface has been demonstrated where an increase of corrosion potential with higher heating temperature was reported in [19]. Practically, our vacuum chamber was coated by Aluminosilicate sol-gel synthesis to limit the outgassing rate of vacuum chamber wall surface.

3.6.3 HC-PCF preparation and coating procedure

In order to obtain an uniform coating layer deposition on the inner core wall surface into the HC-PCF, the following procedure is done (Fig. 3-10).

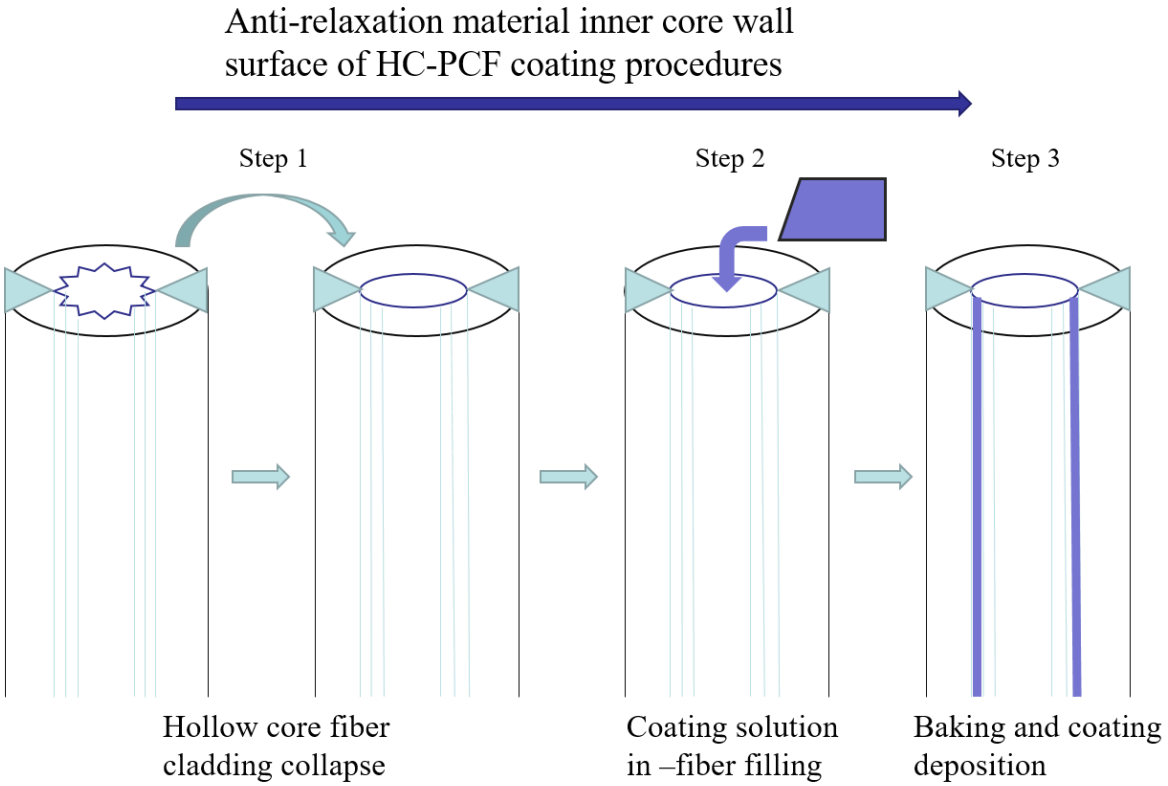

Figure 3-10: Illustrations of the coating procedures of hollow-core PCF cladding collapse, coating solution filling and coating deposition.

Firstly, HC-PCF's cladding structure is cladding collapsed by using filament fusion splicer (Model: Vytran GPX3000) but the hollow-core is remained open. This will allow to fill only the hollow-core region by the coating solution (Fig. 3-11). Then, the fiber is baked at 135 ˚C in vacuum oven for 4 hours to outgas the in-fiber potential contaminations. At the meantime, synthesized coating solution is prepared according to the procedures described in the section 3.6.1 and 3.6.2. The second step consists of chemical deposition of anti-relaxation material on the inner core wall surface (interface between core/clad). The end of the cladding collapsed fiber initially prepared is inserted in a vacuum chamber which is connected with a rough pump and pressure gauge. The second fiber end is

inserted into the coating solution as shown in fig. 3-10. Then switch on the rough pump with a pressure of 10^{-1} mbar (indicated by the pressure gauge) which allow to fill the coating solution inside the hollow-core of the fiber. After 2-5 minutes the hollow-core is complement filled with the coating solution which is indicated by a liquid droplet coming out at the fiber end (viewed through the window of vacuum chamber). Therefore, the liquid-filled fiber is ready. Notice that this coating deposition method is vast applicable to multi-types of anti-relaxation material which could be of interest for other HC-PCF applications. Also, the final coating step depends of the coating properties and may varied slightly on the baking temperature and baking time.

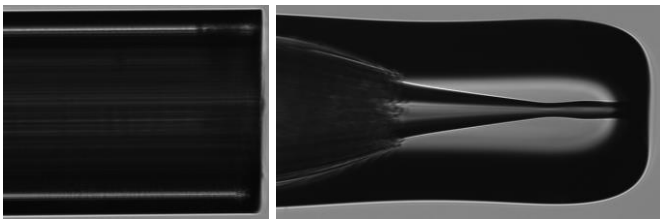

Figure 3-11: Images showing the HC-PCF fiber-tips: before (left side) and after (right side) the cladding collapse

Then, for the PDMS solution, the filled fiber is placed in an air ambient oven heating at 80 ˚C during 24 hours. This process evaporates the diethyl ether from the diluted PDMS solution with chemical reaction in order to get an uniform layer of PDMS on the inner core wall surface. The deposition thickness is characterized by SEM (Fig. 3-15) which show a typical 30 nm thickness. This value is found in good agreement with the calculation of the percentage of PDMS in the liquid volume respect to the fiber core volume. For the deposition of Aluminosilicate sol-gel, a more delicate process is used during the baking part. Indeed, the sol-gel liquid filled HC-PCF is maintaining at 80 ˚C in air ambient oven during 24 hours to remove the ethanol and dry the sol-gel solution. Then the fiber sample is baked at 600 ˚C during 5 hours with a heating ramp of 1 °C.min^{-1} and finally stop heatingfor a natural cooling down. By this process, a thin sol-gel layer can be deposited on the inner core wall surface.

3.6.4 Optimization of the Aluminosilicate Sol-Gel coating

In order to optimize the Aluminosilicate sol-gel coating, characterizations before insertion into the fiber are necessary to especially optimize the coating concentration. The Al2O3 coating material will be characterized on thermal measurement by NETZSCH instrument which is based on the heat-flux differential scanning calorimetery (DSC) principle. A DSC measuring cell consists of a furnace and an integrated sensor with designated positions for the sample and reference container. The sensor is connected to thermocouples. This allows for recording both the temperature difference between the sample and reference container, and the absolute temperature of the sample or reference part. The DSC allows for the determination of caloric values such as the heating fusion or heating crystallization. Then the kinetic analysis of thermal measurement is done by the software Thermokinetics.

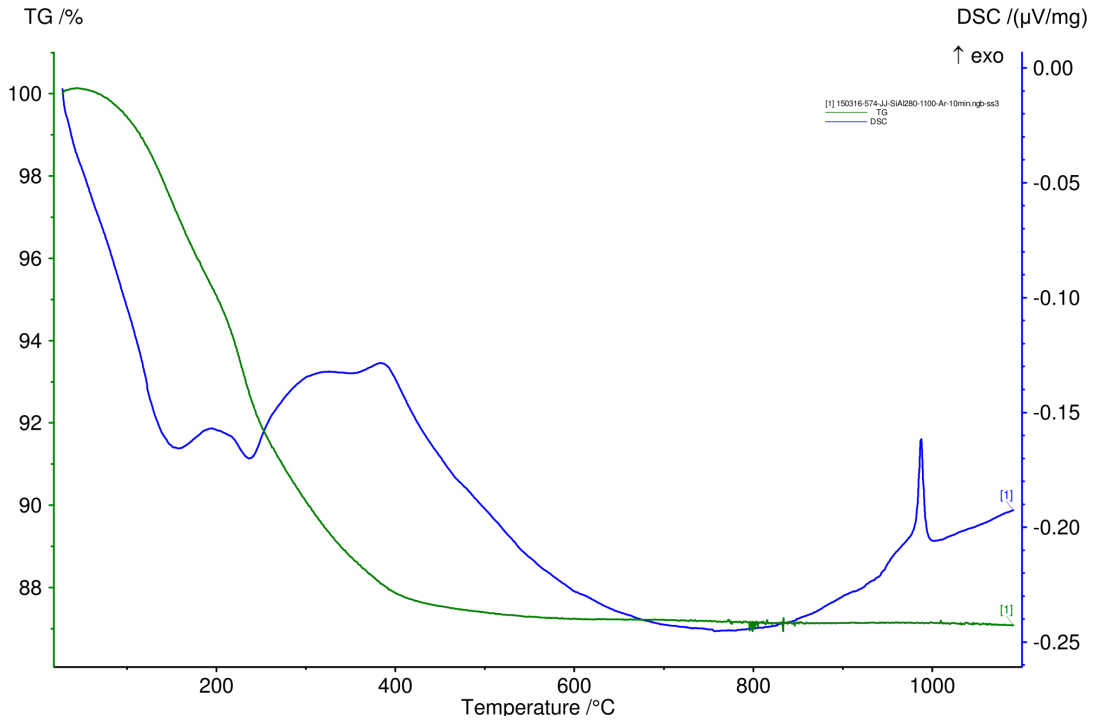

Figure 3-12: Experimental Alumino-silicate sol-gel concentration and crystallization versus the temperatures fitted by Netzsch thermokinetic software. TG: Thermos-gravimetry (green curve), DSC: Differential Scanning Calorimetry (blue curve).

In Figure 3-12, the thermal analysis curves of the coating layer which are related to the performances of Alumino-silicate sol-gel coating on dried solution for given temperatures are shown. The green curve (left axis) is the variation of the coating weight as a function of temperature characterized by Thermos-gravimetry (TG) function of Netzsch. The curve represents the weight of the coating material on the surface which is continuously reducing before 500 °C due to the decomposition process of organics. After 500 °C the curve became flat which means that the sol-gel deposition weight has very little change after this temperature point. The blue curve (right axis) represents the variations of temperature in the sample during the heating process. It shows the endothermic or exothermic reactions for the sample. Before 500 °C, the variation of the curve is the different decompositions and oxidation reactions process. At 988 °C, a sharp peak appears corresponding to the exothermic reaction without any mass loss indicated in TG curve. This is the crystallization point of the sample during the sintering process. Before this temperature, the sol-gel deposition is amorphous with no grain boundaries which could be good propriety for optical application. Therefore, the optimized temperature range should be 500 °C~ 950 °C for a sol-gel deposition. In this thesis, the temperature for sol-gel inner wall coating is set to 600 °C.

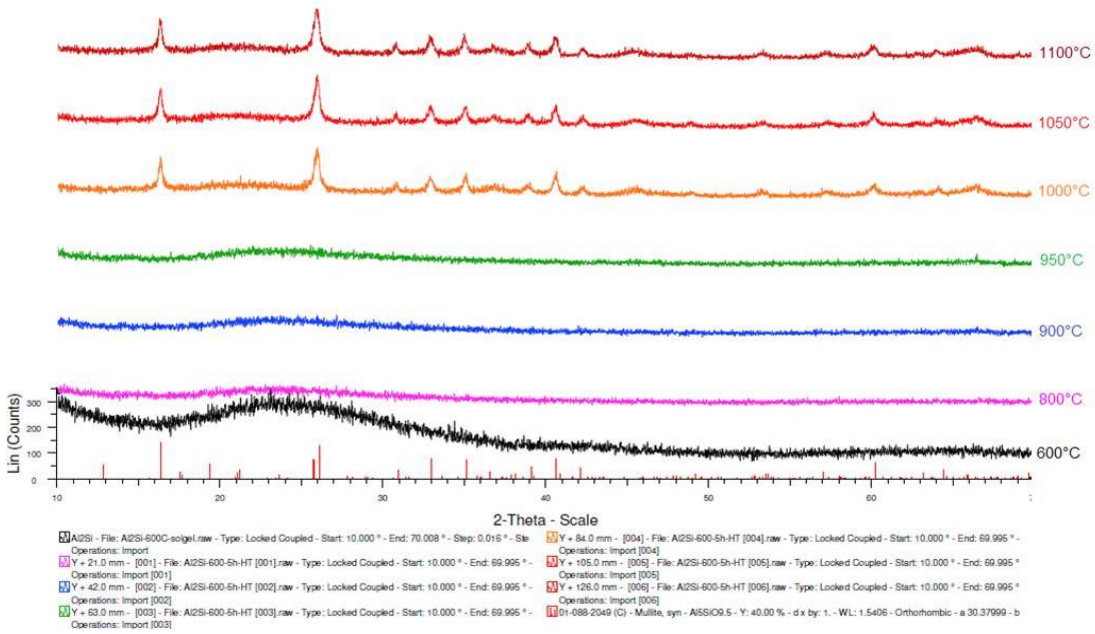

Figure 3-13: Measured of the sol-gel deposition structure by X-ray diffraction function of the temperatures.

The sol-gel deposition layer is also evaluated by X-ray diffraction (XRD) characterization measured at different temperatures. In Figure 3-13, the axis '2-Thera' corresponds to the measured angle, and the axis 'Lin (counts)' is the linear plot of the layer density. The characterization for different temperatures are written at the right of the curves. The variation of the curves should indicate whether the organic component is amorphous (no peaks) or crystalline (peaks). The figure clearly shows that the crystallization (peaks) appears at the temperature 1000 °C which is good agreement with the previous characterization temperature, higher than 988 °C. Otherwise, the position and density of the measured peaks in the fig. 3-13 at high temperature correspond to a mullite phase which is Alumino-silicate. This is coherent with elements used for the coating.

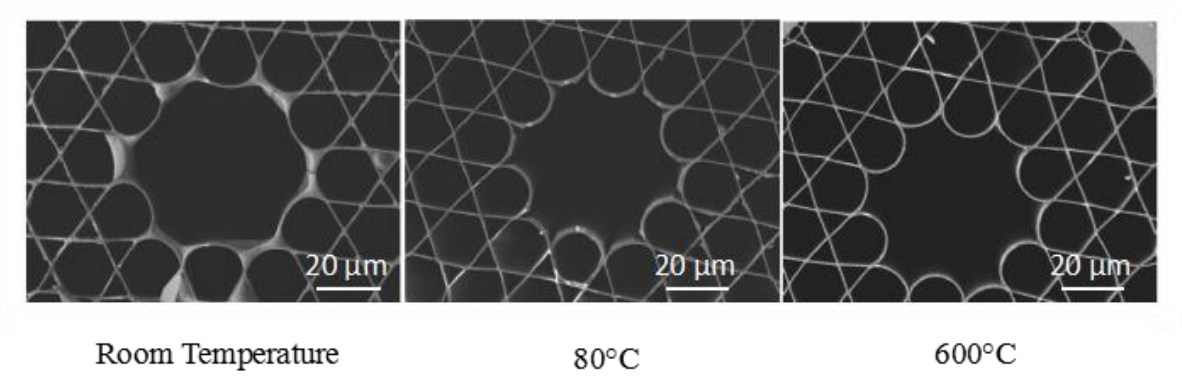

Figure 3-14: SEM images of sol-gel Kagome HC-PCF inner wall coating treated at different temperatures.

Then the sol-gel inner wall coatings made at different heating temperatures in the Kagome HC-PCFs are characterized by SEM technique (Fig. 3-14). Notice that the coating solution is natural dried at room temperature. As indicated by the figure, the coating layer at room temperature is found quite thick and not distributed homogenously. This might cause degradation of the optical guidance properties of the fiber. When the temperature is increased to reach 80 °C, the deposition layer became crudely deposited which is still not suitable. Finally, for temperature of 600 °C, the deposition presents a dense, thick and homogenous layer without crystalline grain. The thickness obtained is measured to be less than 100 nm which is much thinner than the thickness of 400 nm for 80 °C. Further optimizations allow to reach a layer thickness of ~ 30 nm as shown in Fig. 3-15 right.

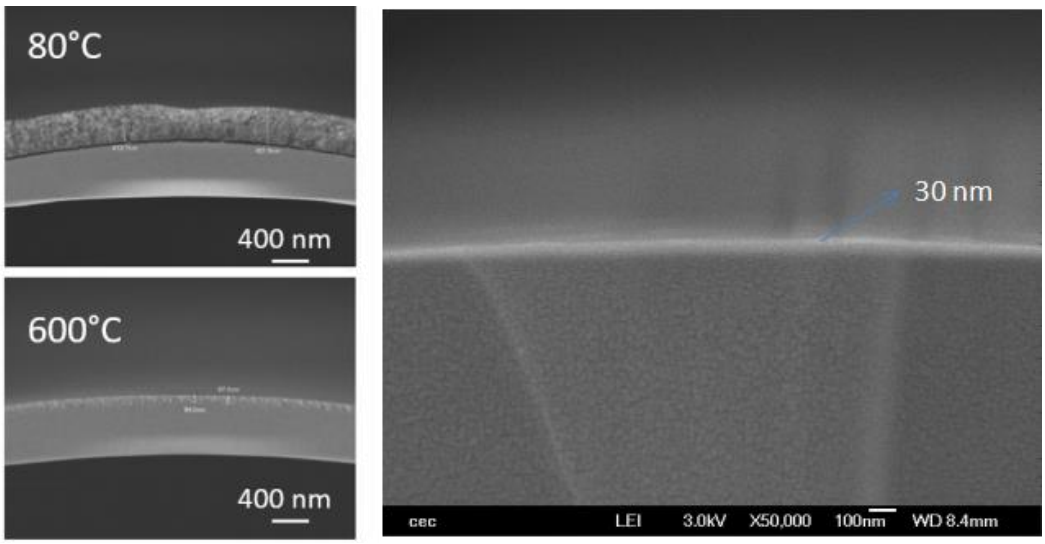

Figure 3-15: SEM images of deposition layer thickness obtained inside the HC-PCFs versus the drying temperature.

Indeed, such thickness values have been obtained by adjusting the sol-gel coating process on pumping and coating solution synthesis. As shown in Fig. 3-16, the SEM images show the coating solution dried at 80 °C (left) and calcined at 600 °C (right) with slow (top) and rapid pumping velocity (bottom). If the coating solution is slowly pumping through Kagome HC-PCF, the solution will be dried or sintered as jam. These 'clusters' from the deposition appear in the middle part of fiber for a 1.5 m long solution filled HC-PCF, resulting in the absence of any optical transmission after the light propagation. When the solution is rapidly pumping through the HC-PCF, these clusters disappeared and the initial optical performances remain unchanged. As expected, the optimized pumping speed not only depends on the volume but also on the geometric of the hollow-core.

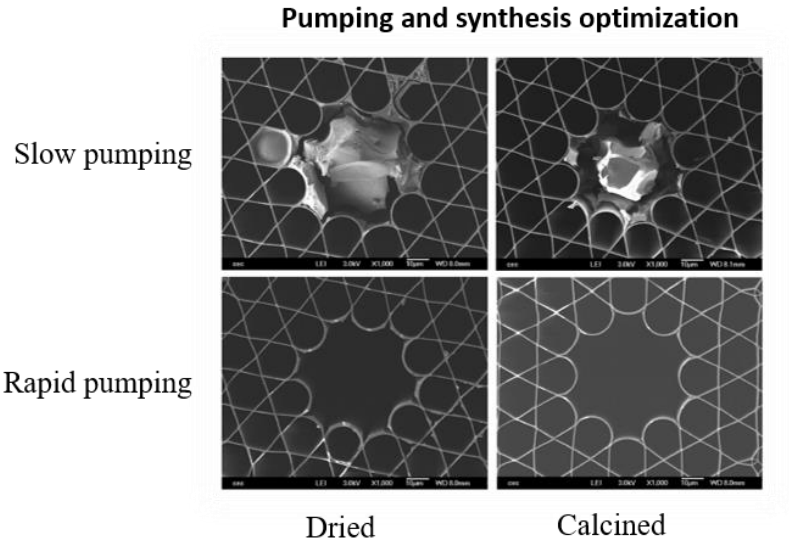

Figure 3-16: SEM images for different pumping velocity and synthesis procedures.

The solution concentration will also influence the coating quality during the last steps. Figure 3-17 shows a zoom on the coating layer obtained for different solution concentrations, C = 0.8 mol.L^{-1} (left) and C = 0.1 mol.L^{-1} (right). For a solution concentration too high, (case of 0.8 mol.L^{-1}), aggregates and cracks are observed at the corner between the arcs of the hollow-core.

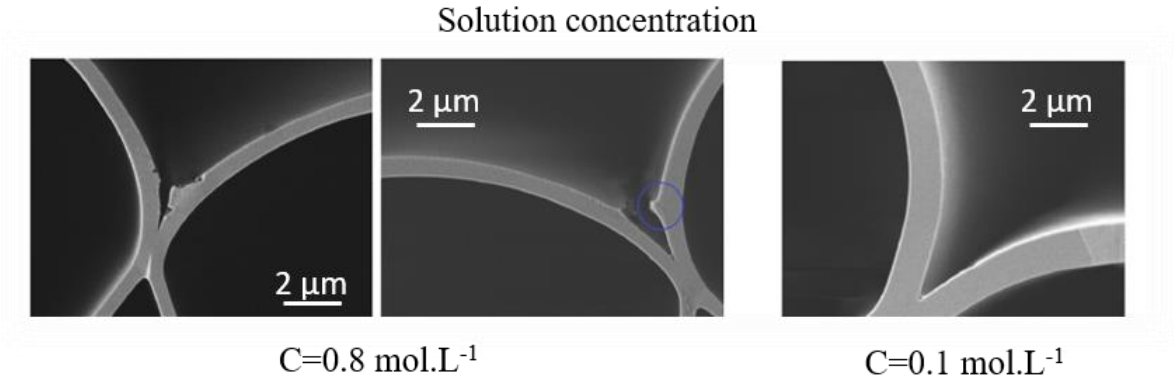

Figure 3-17: SEM images of coating layers made for different solution concentrations of 0.8 mol.L^{-1} and 0.1 mol.L^{-1}.

The success of the anti-relaxation material coating inner core wall surface of HC-PCF is finally optically characterized. A supercontinuum source is coupled into the coated and uncoated Kagome HC-PCF. For comparison, uncoated Kagome HC-PCF with the same physical properties is added as the reference. The modal content is observed by an

InGaAs IR camera, and the transmission spectrum is recorded by an optical spectrum analyzer (OSA). Figure 3-18 presents a typical transmission spectrum for PDMS coated and uncoated Kagome HC-PCF. Similar curves are obtained indicating thin and uniform deposition of the coating. Consequently, there is no coating impact on the transmission at 780 nm which is located on the second transmission band. The difference of light power level is attributed to the condition of light injection. For the following, the measurements of the atomic polarization lifetime which depends on the anti-relaxation material will be presented in the next Chapter 4. Finally, the atom loading challenges and the Rb vapor lifetime in different coated HC-PCF will be presented in the next section.

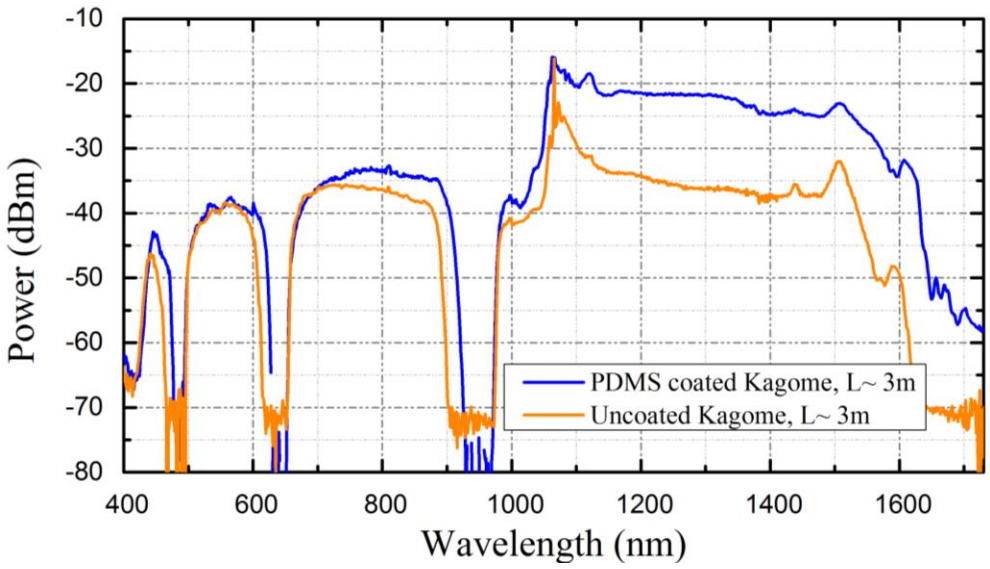

Figure 3-18: Transmission spectrum measured for PDMS coated and uncoated Kagome HC-PCFs.

3.7 Rubidium vapor in sol-gel and PDMS coated Kagome HC-PCF

In this section, the associated challenges of loading atoms into a micro-geometric hollow-core waveguide such as HC-PCF in our case are discussed. The methods that have been used to overcome these challenges (*i.e.* light induced atomic desorption and light induced drift) are presented. Moreover, long Rubidium vapor lifetimes are demonstrated in sol-gel coated Kagome HC-PCF in a comparative study with uncoated fibers.

3.7.1 The challenges of reactive alkali atom loading in micrometric HC-PCF

The issues on alkali atom (^{133}Cs, $^{85/87}$Rb) vapor loading in micro-geometric HC-PCF are detailed in the following. Firstly, alkali atoms provide high reactive properties which required to operate under ultra-high vacuum (UHV) environment. This UHV condition makes the atomic vapor loading into the hollow-core extremely slow and humdrum in molecular free flow regime. Secondly, the geometry of the core size combined with ultra-high operation pressure does not lead an easy loading process into the HC-PCF, *i.e.* for a succeed atom loading it must be flowing towards the core with a small range of solid angles. These factors make the alkali atom loading into hollow dielectric structures extremely challenging. Thirdly, HC-PCF provides large inner core surface to volume ratio which residual OH radicals on the inner core surface react with large quantities of Rb atoms. Moreover, the highly reactive Rb with the surface strongly limits the lifetime of Rb atom inside the HC-PCF.

Hence, the techniques to mitigate these challenges have been researched such as light induced drift (LID) [36][45], and light induced atomic desorption (LIAD) [46]. The LIAD technique has successfully increased Rb vapor densities in PBG fibers, after sufficient surface-light exposure as demonstrated by Gaeta group [49-53]. However, none of these techniques overcomes the issue of the atom-surface physio-chemical interaction in micrometric confined hollow waveguide. Coating the inner wall surface of HC-PCF with anti-relaxation materials should be a good candidate for reducing this physio-chemical interaction. In the following, the discussion of anti-relaxation materials coating for alkali atomic vapor applications is introduced.

3.7.2 Discussion of anti-relaxation materials inner surface coating for alkali metal vapors applications

Previous investigations on macro-cell inner wall surface coating for Cs magneto-optical trapping demonstrated that the coating materials should have low dielectric

constants, low surface absorption energy, low out gassing rates and low reaction ratios [54]. The low surface absorption energy can be expressed by the atom dwell time in thermal equilibrium with the surface,

$$\tau_s = \tau_0 e^{E_a/k_B T}, \tag{3-1}$$

where $\tau_0 \sim 10^{-12}$ s is the elastic collision time, E_a is the surface absorption energy, k_B is the Boltzmann constant and T is the atom temperature. From calculations, the dwell times on different surface are presented in Table 3-3. The table clearly shows that a small difference of surface absorption energy E_a can dramatically change the dwell time over several orders of magnitude. Also, higher dwell time results in less dephasing probability and less light-atom interaction time in the vapor cell.

Table 3-3: Properties of different anti-relaxation coating for comparison.

	Activation Energy E_a (eV)	**Dwell Time (ns) (T=20°C)**	**Outgassing Rate (Torr $cm^{-3}cm^2/s$)**	**Refractive Index**	**Dielectric constant ε_r**
OTS	*0.4±0.03*	*7600*	*$<4\times10^{-7}$*	*1.46*	*2.5[57]*
PDMS	*0.18±0.01[64]*	*1.3*	*10^{-4}*	*1.4*	*2.8[58]*
Aluminosilicate	*0.28±0.04[61]*	*4.4*	*10^{-13}[55]*	*1.54[62,63]*	*4.5[59]*

Choice of a low outgassing and low reaction rate material is a necessity for Alkali atomic vapor application. In addition, low outgassing materials also decrease foreign gas content which can react with Alkali atoms. In this conclusion, octdecyltrichlorosilane (OTS), PDMS and Aluminosilicate were previously identified as suitable materials for atomic vapor applications. From Eq (3-1) the dwell time on aluminosilicate surface is evaluated to ~ 4.4 ns and ~1.3 ns for PDMS surface. From the ref [55], the outgassing rate for aluminosilicate surface can be extremely low with proper baking. The strength of surface interaction such as Van der Waals and electrostatic forces [56] depends on the polarizability of the surface which is related to the dielectric constant of the material. Lower dielectric constant provides a weakened probability. The measured dielectric constant of OTS, PDMS and aluminosilicate are respectively 2.5 [57], 2.8 [58], 4.5 [59]. Additionally, the aluminosilicate sol-gel has been found in ref [60] where the dielectric

constants can achieve values as high as ~5.7 by controlling the porosity and the hydroxyl group content of the sol-gel. In conclusion, considering both physical and chemical properties, aluminosilicate is chosen as the main apparent anti-relaxation material.

3.7.3 Rubidium vapor lifetime in sol-gel coated Kagome HC-PCF

The Kagome HC-PCF inner wall surface has been finally coated with PDMS and sol-gel materials by post-processing technique. The aim of coating materials is to limit the rate of reaction between atom and inner surface of the HC-PCF, thus provide longer atomic vapor lifetime inside the hollow-core. Experimental conditions for the Rb atomic vapor lifetime test inside the HC-PCF is described as following. Several sol-gel coated, PDMS coated and uncoated Kagome HC-PCFs with ~ 8 cm length are inserted into UHV chamber. The Rb atom is released by heating a metal dispenser once the UHV chamber achieve pressure below 5×10^{-8} Torr. Then natural Rb atom loading is processing in molecular free flow during a period of 4 weeks. At the end, the atomic density inside the Kagome HC-PCF reaches n ~ 10^{9} cm^{-3}. The comparison of the Rb absorption line for both ^{87}Rb and ^{85}Rb D_2 contrast in vacuum, uncoated Kagome HC-PCF and sol-gel coated Kagome HC-PCF is shown in Fig. 3-19.

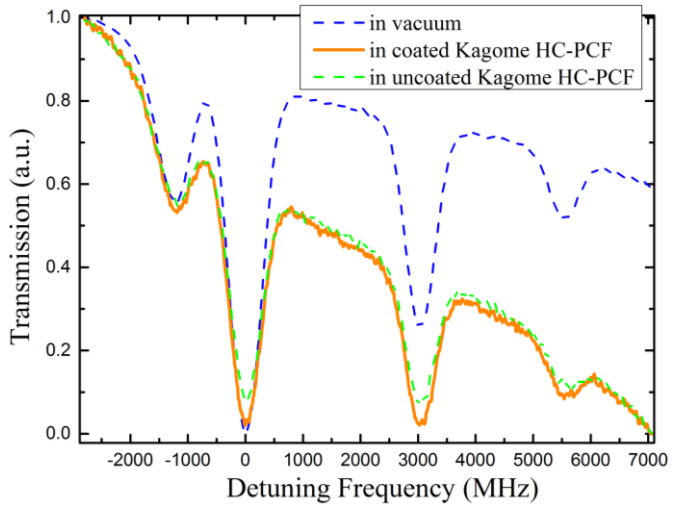

Figure 3-19: Measured Rb D2 absorption lines of Rb vapor contained in Kagome HC-PCFs and vacuum chamber. In vacuum (blue dash line) for reference, in sol-gel coated Kagome HC-PCF (solid orange) and in uncoated Kagome HC-PCF (dash green).

Figure 3-19 confirms that the best contrast of the Rb absorption line is obtained for the sol-gel coated Kagome HC-PCF compared to the uncoated one, which indicate that the coating plays its role to better maintain Rb atoms inside the hollow-core. Next the Rb dispenser is switched off to investigate the Rb lifetime. The guiding beam used for measuring the absorption line is linearly polarized and on resonance $|^{85}Rb\ ^5S_{1/2}\ F=3> \rightarrow |^5P_{3/2}\ F' =1, 2, 3, 4 >$ with operational power ~ 60 nW at wavelength of 780.24 nm. The evolution of the absorption contrast is then recorded over 450 hours for the UHV chamber, the uncoated capillary, the sol-gel coated and uncoated Kagome HC-PCF (fig. 3-20 (a)). The photodetector provides noise equivalent power (NEP) of 2.2 $pW/Hz^{1/2}$ with DC bandwidth 1 MHz and can detect minimum contrast closed to 1%.

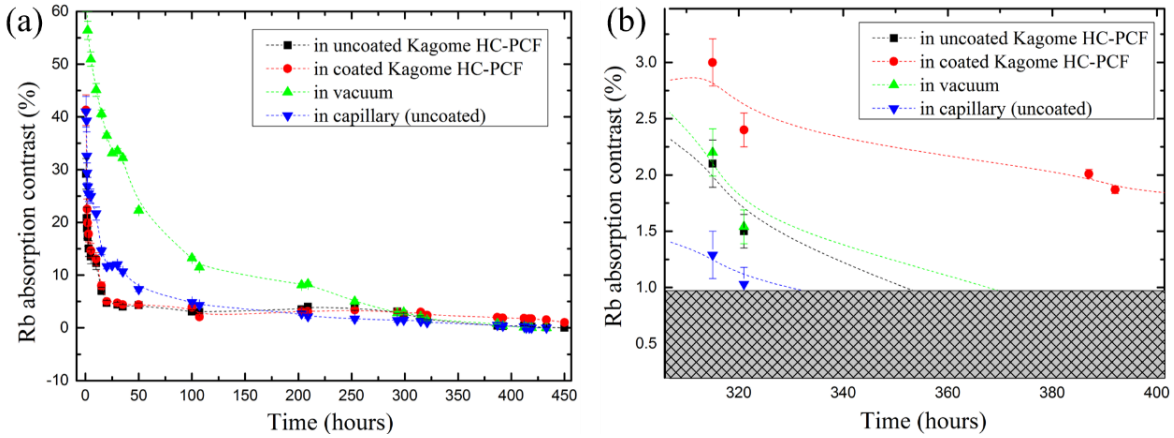

Figure 3-20: (a) Evolution of Rb absorption contrast in vacuum (green dots), uncoated capillary (blue dots), sol-gel coated (red dots) and uncoated Kagome HC-PCF (black dots); (b) Zoom during the last 100 hours.

In the figure 3-20 (a), the absorption contrasts in HC-PCFs are dropping exponentially down to few percent during the first 50 hours. Then, the absorption contrast drops extremely slowly from 6% to 2.5% over 300 hours for sol-gel coated HC-PCF. In comparison, the contrast in the UHV chamber is much stronger than both fibers and capillary over 250 hours but decays faster than fibers and capillary in last 100 hours. This is highlighted in fig. 3-20 (b) where after 400 hours, the Rb absorption contrasts in vacuum, capillary and uncoated HC-PCF drop almost to zero. However, for the case of the sol-gel coated HC-PCF, the contrast is maintained between 2% ~ 3% in the last 100 hours. This indicates that the sol-gel coating reduces the reaction rate of Rb-surface as expected.

3.7.4 The loading atomic density in Rb-filled HC-PCFs

The atomic density for the ground state atomic polarization relaxation time measurement (Chapter 4) in Rb-filled HC-PCFs are shown in the following. The atomic density in HC-PCFs is calculated according to the Beer's law:

$$I(Z) = I_0 e^{-n\sigma(\upsilon)z}, \tag{3-2}$$

where I_0 is the initial light intensity, n is the atomic density, $\sigma(\upsilon)$ is the atomic cross section and z is the media length. The probability $P(\upsilon_z)\mathrm{d}\upsilon_z$ of an atom to absorb the off-resonance light having a velocity in the range from υ_z to $\upsilon_z + \mathrm{d}\upsilon_z$ is expressed by the Maxwellian distribution [65]:

$$\mathrm{P}(\upsilon_z)\mathrm{d}\upsilon_z = \sqrt{\frac{M}{2\pi k_B T}} \exp\left(\frac{-M\upsilon_z^2}{2k_B T}\right) d\upsilon_z \tag{3-3}$$

where M is the atom mass and k_B the Boltzmann constant. This results in a Gaussian curve given by:

$$\mathrm{G}(\upsilon - \upsilon_0) = \frac{2\sqrt{ln2/\pi}}{\Gamma_G} \exp\left(\frac{-4ln2(\upsilon-\upsilon_0)^2}{\Gamma_G^2}\right), \tag{3-4}$$

with a FWHM equal to:

$$\Gamma_G = 2\frac{\upsilon_0}{c}\sqrt{\frac{2k_B T}{M} ln2}, \tag{3-5}$$

The absorbed across section related to the Gaussian curve is:

$$\sigma_G(\upsilon) = \pi r_e c f G(\upsilon - \upsilon_0), \tag{3-6}$$

And the across section on resonance is:

$$\sigma_G(\upsilon) = \frac{2r_e c f\sqrt{\pi ln2}}{\Gamma_G}, \tag{3-7}$$

Here r_e = 2.85×10^{-15} m is the classic electron radius, c is the light velocity, f is the oscillation strength, Γ_G = 566 MHz at the temperature T= 100 ˚C in our experimental

situation [65]. The in-fiber atomic density of Rb atom is increased to ~10^9 cm^{-3} over a period of 30 days which is corresponding optical depth ($OD = -lnT$, where the T is the transmission) is increased to ~2.1 before to be stabilized. For the following relaxation time measurement, the current applied on the Rb getter is switched off to minimize the influence from the Rb source. Otherwise, the Rb atomic density was found to remain steady over the total data collection time < 8 hours.

3.8 Summary

In this chapter, post-processing techniques such as IC HC-PCF tapering, splicing, and sleeve splice are introduced. These techniques can be used to overcome the technical challenges to make the first alkali-vapor photonic microcell. In addition, inner wall surface anti-relaxation materials coating technique to optimize the atomic spectroscopy performance inside the HC-PCF is studied. Especially, Aluminosilicate sol-gel material is found as a potential coating material. Indeed, the experimental measurements demonstrate that Rb atom can be maintained in the coated HC-PCF for greater than 450 hours, due to the reduction of atom-surface reaction by the sol-gel coating. More investigations on the ground state atomic polarization relaxation time to understand the atom-wall collision mechanism and surface potential induced sub-Doppler transparencies are introduced in next two chapters.

3.9 References

[1] F. Benabid, P. J. Roberts, F. Couny, and P. S. Light, “Light and gas confinement in hollow-core photonic crystal fibre based photonic microcells,” J. Eur. Opt. Soc., vol. 4, no. c, pp. 1–9, 2009.

[2] Light, Philip Stephen. "Photonic microcells for quantum optics applications." PhD diss., University Library, 2008.

[3] F. Benabid, F. Couny, J. C. Knight, T. a Birks, and P. S. J. Russell, “Compact, stable and efficient all-fibre gas cells using hollow-core photonic crystal fibres.,” Nature, vol. 434, no. 7032, pp. 488–491, 2005.

[4] P. G. Westergaard, J. W. Thomsen, M. R. Henriksen, M. Michieletto, M. Triches, J. K. Lyngsø, and J. Hald, “Compact, CO_2-stabilized tuneable laser at 205 microns,” Opt. Express, vol. 24, no. 5, p. 4872, 2016.

[5] Fujii, Toshihiro. "Analysis of products from a C 2 H 2/N 2 microwave discharge: new nitrile species." *Chemical physics letters* 313, no. 5 (1999): 733-740.

[6] P. S. Light, J. D. Anstie, F. Benabid, and A. N. Luiten, “Hermetic optical-fiber iodine frequency standard,” Opt. Lett., vol. 40, no. 12, pp. 2703–2706, 2015.

[7] Fsaifes, I., Gilles Feugnet, S. Schwartz, Benoît Debord, Frédéric Gerôme, Georges Humbert, F. Benabid, and Fabien Bretenaker. "Kagome hollow-core photonic crystal fiber resonator for rotation sensing." In *The European Conference on Lasers and Electro-Optics*, p. CH_5_1. Optical Society of America, 2015.

[8] Triches, Marco, Anders Brusch, Jan Hald, Jesper Lægsgaard, and Ole Bang. "Fiber-based portable optical frequency standard for telecommunication." In *Lasers and Electro-Optics (CLEO), 2015 Conference on*, pp. 1-2. IEEE, 2015.

[9] C. Wang, N. V Wheeler, C. Fourcade-Dutin, M. Grogan, T. D. Bradley, B. R. Washburn, F. Benabid, and K. L. Corwin, “Acetylene frequency references in gas-filled

hollow optical fiber and photonic microcells.," Appl. Opt., vol. 52, no. 22, pp. 5430–9, 2013.

[10] P. S. J. Russell, P. Hölzer, W. Chang, A. Abdolvand, and J. C. Travers, "Hollow-core photonic crystal fibres for gas-based nonlinear optics," Nat. Photonics, vol. 8, no. 4, pp. 278–286, 2014.

[11] Z. Wang, F. Yu, W. J. Wadsworth, and J. C. Knight, "Efficient 1.9 μ m emission in H 2 -filled hollow core fiber by pure stimulated vibrational Raman scattering," Laser Phys. Lett., vol. 11, no. 10, p. 105807, 2014.

[12] B. Debord, A. Amsanpally, J. Blondy, F. Gérôme, and F. Benabid, "Low loss Inhibited coupling Hollow-core photonic crystal fiber with ultrabroad Fundamental Band," in Conference on Lasers and Electro-Optics, OSA Technical Digest (2016) (Optical Society of America, 2016), paper STu4P.2.

[13] F. Emaury, C. F. Dutin, C. J. Saraceno, M. Trant, O. H. Heckl, Y. Y. Wang, C. Schriber, F. Gerome, T. Südmeyer, F. Benabid, and U. Keller, "Beam delivery and pulse compression to sub-50 fs of a modelocked thin-disk laser in a gas-filled Kagome-type HC-PCF fiber," Opt. Express, vol. 21, no. 4, pp. 4986–4994, 2013.

[14] M. Azhar, N. Y. Joly, J. C. Travers, and P. S. J. Russell, "Nonlinear optics in Xe-filled hollow-core PCF in high pressure and supercritical regimes," Appl. Phys. B Lasers Opt., vol. 112, no. 4, pp. 457–460, 2013.

[15] Lynch-Klarup, Kyle E., Erin Mondloch, Michael G. Raymer, Fetah Benabid, Frederic Gerome, and Damien Arrestier. "Supercritical-xenon-filled photonic crystal fiber as a Raman-free nonlinear optical medium." In *Frontiers in Optics*, pp. FM4I-2. Optical Society of America, 2012.

[16] A. V. V. Nampoothiri, A. M. Jones, C. Fourcade Dutin, C. Mao, N. Dadashzadeh, B. Baumgart, Y. Wang, M. Alharbi, T. Bradley, N. Campbell, F. Benabid, B. R. Washburn, K. L. Corwin, and W. Rudolph, "Hollow-core Optical Fiber Gas Lasers (HOFGLAS): a review [Invited]," Opt. Mater. Express, vol. 2, no. 7, pp. 948–961, 2012.

[17] P. S. Light, F. Couny, and F. Benabid, “Low insertion-loss (1.8 dB) and vacuum-pressure all-fiber acetylene cell based on hollow-core PCF,” Conf. Lasers Electro-Optics, 2007, CLEO 2007, vol. 2, no. C, pp. 4–5, 2007.

[18] Sprague, Michael R., Duncan G. England, Amir Abdolvand, Joshua Nunn, Xian-Min Jin, W. Steven Kolthammer, Marco Barbieri et al. "Efficient optical pumping and high optical depth in a hollow-core photonic-crystal fibre for a broadband quantum memory." *New Journal of Physics* 15, no. 5 (2013): 055013.

[19] F. Benabid and P. J. Roberts, “Linear and nonlinear optical properties of hollow core photonic crystal fiber,” J. Mod. Opt., vol. 58, no. 2, pp. 87–124, 2011.

[20] Jesper Toft Kristensen, Andreas Houmann, Xiaomin Liu, and Dmitry Turchinovich, "Low-loss polarization-maintaining fusion splicing of single-mode fibers and hollow-core photonic crystal fibers, relevant for monolithic fiber laser pulse compression," Opt. Express 16, 9986-9995 (2008)

[21] B. Debord, F. Gérôme, R. Jamier, C. Boisse-Laporte, P. Leprince, O. Leroy, J.-M. Blondy, and F. Benabid, “First Ignition of an UV Microwave Microplasma in Ar-filled Hollow-Core Photonic Crystal Fibers - OSA Technical Digest (CD),” 37th Eur. Conf. Expo. Opt. Commun., p. Mo.2.LeCervin.5, 2011.

[22] B. Debord et al., "Ultra-Large Core Size Hypocycloid-Shape Inhibited Coupling Kagome Fibers for High-Energy Laser Beam Handling," in Journal of Lightwave Technology, vol. 33, no. 17, pp. 3630-3634, Sept.1, 1 2015.

[23] N. V Wheeler, P. S. Light, F. Couny, and F. Benabid, “Slow and Superluminal Light Pulses in an Acetylene Filled Photonic Mircocell,” J. Light. Technol., vol. 28, no. 6, pp. 870–875, 2010.

[24] F. Couny, P. S. Light, F. Benabid, and P. S. J. Russell, “Electromagnetically induced transparency and saturable absorption in all-fiber devices based on 12C2H2-filled hollow-core photonic crystal fiber,” Opt. Commun., vol. 263, no. 1, pp. 28–31, 2006.

[25] F. Benabid, P. Light, F. Couny, and P. Russell, “Electromagnetically-induced transparency grid in acetylene-filled hollow-core PCF.,” Opt. Express, vol. 13, no. 15, pp. 5694–5703, 2005.

[26] F. Couny, F. Benabid, and P. S. Light, “Subwatt Threshold cw Raman Fiber-Gas Laser Based on H_2-Filled Hollow-Core Photonic Crystal Fiber,” Phys. Rev. Lett., vol. 99, no. October, p. 143903, 2007.

[27] J. D. Mackenzie and E. P. Bescher, “Physical properties of sol-gel coatings,” *J. Sol-Gel Sci. Technol.*, vol. 19, no. 1–3, pp. 23–29, 2000.

[28] K. Knabe, S. Wu, J. Lim, K. a Tillman, P. S. Light, F. Couny, N. Wheeler, R. Thapa, A. M. Jones, J. W. Nicholson, B. R. Washburn, F. Benabid, and K. L. Corwin, “10 kHz accuracy of an optical frequency reference based on (12)C2H2-filled large-core kagome photonic crystal fibers.,” Opt. Express, vol. 17, no. 18, pp. 16017–16026, 2009.

[29] O. H. Heckl, C. R. E. Baer, C. Kränkel, S. V. Marchese, F. Schapper, M. Holler, T. Südmeyer, J. S. Robinson, J. W. G. Tisch, F. Couny, P. Light, F. Benabid, and U. Keller, “High harmonic generation in a gas-filled hollow-core photonic crystal fiber,” Appl. Phys. B Lasers Opt., vol. 97, no. 2, pp. 369–373, 2009.

[30] A. M. Cubillas, J. Hald, and J. C. Petersen, “High resolution spectroscopy of ammonia in a hollow-core fiber.,” Opt. Express, vol. 16, no. 6, pp. 3976–3985, 2008.

[31] Ghosh, Saikat, Amar R. Bhagwat, C. Kyle Renshaw, Shireen Goh, Alexander L. Gaeta, and Brian J. Kirby. "Low-light-level optical interactions with rubidium vapor in a photonic band-gap fiber." *Physical review letters* 97, no. 2 (2006): 023603.

[32] Light, P. S., Fetah Benabid, F. Couny, M. Maric, and A. N. Luiten. "Electromagnetically induced transparency in Rb-filled coated hollow-core photonic crystal fiber." *Optics letters* 32, no. 10 (2007): 1323-1325.

[33] F. Benabid, J. C. Knight, G. Antonopoulos, and P. S. J. Russell, “Stimulated Raman Scattering in Photonic Crystal Fiber,” October, vol. 298, no. October, pp. 2000–2003, 2002.

[34] J. Henningsen, J. Hald, and J. C. Peterson, “Saturated absorption in acetylene and hydrogen cyanide in hollow-core photonic bandgap fibers.,” Opt. Express, vol. 13, no. 26, pp. 10475–10482, 2005.

[35] D. C. . Vasconcelos, J. A. . Carvalho, M. Mantel, and W. . Vasconcelos, “Corrosion resistance of stainless steel coated with sol–gel silica,” *J. Non. Cryst. Solids*, vol. 273, no. 1–3, pp. 135–139, 2000.

[36] Gel’Mukhanov, F. Kh, and A. M. Shalagin. "Light-induced diffusion of gases." JETP Lett 29.12 (1979): 711-713.

[37] B. Debord, 1 M. Alharbi, 1, 2 T. Bradley, 1, 2 C. Fourcade-Dutin, 1 Y.Y. Wang, 1 L. Vincetti, 3 F. Gérôme, 1 and F. Benabid1 and 1, “Hypocycloid-shaped hollow-core photonic crystal fiber Part I: Arc curvature effect on confinement loss,” Opt. Express, vol. 21, no. 23, pp. 28597–21, 2013.

[38] M. Alharbi, T. Bradley, B. Debord, C. Fourcade-Dutin, D. Ghosh, L. Vincetti, F. Gérôme, and F. Benabid, “Hypocycloid-shaped hollow-core photonic crystal fiber Part II: cladding effect on confinement and bend loss.,” Opt. Express, vol. 21, no. 23, pp. 28609–16, 2013.

[39] N. V Wheeler, M. D. W. Grogan, P. S. Light, F. Couny, T. A. Birks, and F. Benabid, “Large-core acetylene-filled photonic microcells made by tapering a hollow-core photonic crystal fiber,” vol. 35, no. 11, pp. 1875–1877, 2010.

[40] X. Zheng, B. Debord, L. Vincetti, B. Beaudou, F. Gérôme, and F. Benabid, “Fusion splice between tapered inhibited coupling hypocycloid-core Kagome fiber and SMF,” Opt. Express, vol. 24, no. 13, p. 14642, 2016.

[41] J.D.Love;W.M.Henry;W.J.Stewart;R.J.Black;S.Lacroix;F.Gonthier, “Part 1 : Adiabaticity criteria,” IEE Proceedings-J, vol. 138, no. 5, 1991.

[42] Timothy A.Birks;YouweiW.Li, “The Shape of Fiber Tapers,” J. Light. Technol., vol. 10, no. 4, 1992.

[43] L. Vincetti, B. Debord, M. Alharbi, and F. Benabid, “Kagome hollow-core photonic crystal fiber,” CLEO US 2015, vol. 1, no. c, pp. 15–16, 2015.

[44] C. Wang, T. Bradley, Y. Wang, K. L. Corwin, F. Gérôme, and F. Benabid, “Angle splice of large-core kagome hollow-core photonic crystal fiber for gas-filled microcells - OSA Technical Digest (online),” Cleo 2013, p. CM3I.1, 2013.

[45] Antsygin, V. D., et al. "Light-induced diffusion of sodium vapor." JETP LETTERS 30.5 (1979): 243-245.

[46] Meucci, M., et al. "Light-induced atom desorption." EPL (Europhysics Letters) 25.9 (1994): 639.

[47] A. Mata, A. J. Fleischman, and S. Roy, “Characterization of polydimethylsiloxane (PDMS) properties for biomedical micro/nanosystems.,” Biomed. Microdevices, vol. 7, no. 4, pp. 281–293, 2005.

[48] M. J. Kasprowicz, T. Dohnalik, L. Jozefowski, K. Rubahn, and H. G. Rubahn, “Diffusion of rubidium atoms in PDMS thin films,” Chem. Phys. Lett., vol. 391, no. 1–3, pp. 191–194, 2004.

[49] Bhagwat, Amar R., et al. "On-demand all-optical generation of controlled Rb-vapor densities in photonic-band-gap fibers." Physical Review A 79.6 (2009): 063809.

[50] Slepkov, Aaron D., et al. "Spectroscopy of Rb atoms in hollow-core fibers." Physical Review A 81.5 (2010): 053825.

[51] Slepkov, Aaron D., et al. "Generation of large alkali vapor densities inside bare hollow-core photonic band-gap fibers." Optics express 16(23) (2008): 18976-18983.

[52] Londero, Pablo, et al. "Ultralow-power four-wave mixing with Rb in a hollow-core photonic band-gap fiber." Physical review letters 103(4) (2009): 043602.

[53] Venkataraman, Vivek, et al. "All-optical modulation of four-wave mixing in an Rb-filled photonic bandgap fiber." Optics letters 35.13 (2010): 2287-2289.

[54] Stephens, M., R. Rhodes, and C. Wieman. "Study of wall coatings for vapor-cell laser traps." Journal of applied physics 76.6 (1994): 3479-3488.

[55] Redhead, P. A. "The ultimate vacuum." Vacuum 53.1-2 (1999): 137-149.

[56] Zaremba, Eugene, and Walter Kohn. "Van der Waals interaction between an atom and a solid surface." Physical Review B 13.6 (1976): 2270.

[57] Di, Chong-an, et al. "Effect of dielectric layers on device stability of pentacene-based field-effect transistors." Physical Chemistry Chemical Physics 11.33 (2009): 7268-7273.

[58] Kuo, Alex CM. "Poly (dimethylsiloxane)." Polymer data handbook (1999): 411-435.

[59] Teiserskis, Arunas, et al. "Investigation of alumina–silica films deposited by pulsed injection metal–organic chemical vapour deposition." Thin solid films 515.4 (2006): 1830-1834.

[60] Teiserskis, Arunas, et al. "Investigation of alumina–silica films deposited by pulsed injection metal–organic chemical vapour deposition." Thin solid films 515.4 (2006): 1830-1834.

[61] Giuntini JC, Douillard JM, Maurin G, Devautour-Vinot S, Nicolas a., Henn F. Aluminosilicate surface energy and its evolution upon adsorption using dielectric relaxation spectroscopy. Chemical Physics Letters. 2006 May; 423(1-3):71–5.

[62] Farrell RA, Neu JT. Refractive Index of Several Glasses as a Function of Wavelength and Temperature. Journal of the Optical Society of America. 1969; 59(6):774–6.

[63] Benatsou M, Capoen B, Bouazaoui M. Structural and Optical Properties of Sol-Gel Derived Aluminosilicate Planar Waveguides Doped with Er 3 Ions. 1998; 533:529–33.

[64] Arslanov V V, Ogarev VA. Kinetics of the fusion of drops of polydimethylsiloxane on solid surfaces. Izvestiya Akademi Nauk SSSR. 1974 ;(8):1795–9.

[65] Seltzer, Scott Jeffrey. *Developments in alkali-metal atomic magnetometry*. Princeton University, 2008.

Chapter 4

Ground-state atomic polarization relaxation measurements in Rb filled HC-PCF with different core inner-surfaces

In this chapter, we present experimental results on the relaxation dynamic of rubidium ground state polarization relaxation. The experimental protocol relies on monitoring the magneto-optical rotation of the atoms in the dark. Based on this technique, relaxation time of Rb inside HC-PCF with different core inner-wall surfaces and under different magnetic field amplitude, pump power levels have been measured. The results demonstrate that the measured polarization relaxation is dominant by the dwell time of the adsorbed atoms and that the polarized atoms are primarily formed by slow atoms. Finally, we used this technique to deduce the dwell time for bare silica surface, ceramic coating and PDMS coating.

4.1 Introduction

The early work on atom-filled HC-PCF [1] [2] and in ARROW waveguides [3][4][5] have shown that sub-Doppler spectral lines from electromagnetically induced transparency or saturated absorption spectroscopy have their linewidth limited by transit time or by collision with the core inner-wall, even in the presence of anti-relaxation coating.

Furthermore, considering the HC-PCF specific modal properties, the guided mode field diameter d_m is very close to the fiber geometrical diameter d_f which make it difficult to discriminate the optical spectral-line broadening due to the transit-time $\tau_{tt} = (2/\pi)d_m/v$ [6] from that due to the atom-wall collision $\tau_w = (v/A)(2/\sqrt{\pi})/v$ [7]. This expression is reduced to $\tau_w = (\sqrt{\pi}/2)d_f/v$ for a cylinder geometriy. Here, v, A and V are the atoms average velocity, hollow-core cross section and core quasi-cylinder volume respectively.

Finally, the large surface-to-volume ratio of the fiber core along the vicinity of the atoms to the surface raise a question on the role of atom-surface effect on the profile of the absorption and other spectral lines and on the dephasing of an excited optical coherence. Indeed, the transit time τ_{tt} is extremely short (< 100 ns for a 50 µm core diameter HC-PCF) which is the main limitation of the spectral broadening in atoms-confined HC-PCF [8], even when operated with low power levels and large frequency detuning. In this case, only slow atoms can complete a Rabi transition cycle before collision with the inner wall surface. Second, the atoms close to the inner wall surface which are trapped on the surface for sometimes (dwell time) in the range of $\tau_{tt} \sim 80\ ns$ - $55\ \mu s$ [9][10] due to the physical-chemical adsorption processes [11][12] must be taken into account.

In consequence, detailed investigations on spectroscopy measurements of atom-light interaction in HC-PCF is required. In this chapter we report on magneto-optical spectroscopy (MOS) of Rb-loaded IC Kagome HC-PCF in which the ground state atomic polarization relaxation dynamics are experimentally and theoretically investigated. The results show that the ground state atomic polarization relaxation time τ_1 can be up to two fold longer than dwell time τ_{dw} and 20 times longer that transit time τ_{tt}. A Monte-Carlo simulations results show that the polarization relaxation time is dominantly set by the

dwell time and the transit-time of the slow polarized atoms. Secondly, we used the fact that the speed of the slow polarized atom can be controlled by the pump laser power to measure the dwell time of three core inner-surfaces of Kagome HC-PCF: silica uncoated surface, PDMS coated surface and ceramic coated surface.

The chapter is structured as follows. Section 4.2 reviews the basics of magneto-optical mechanism and its effect on a laser probe polarization. Section 4.3 describes the experimental set-up and the measurement protocol of the probe polarization rotation relaxation. The section also reports on how the relaxation time due to transit time, atom-wall collision and dwell time are deduced from the optical rotation relaxation. Section 4.4 presents experimental results related to the dwell time on different surfaces with investigations on the pump power and the detuning frequency.

4.2 Linear magneto-optical effect

Anti-relaxation materials have been investigated by utilizing multifarious methods. For example, the investigation of hyperfine resonances in Tetracontane ($C_{40}H_{82}$) coated vapor cells filled with ^{87}Rb atom has been reported by Robinson *et al.* [13]. Extreme narrow hyperfine resonances with full width at half maximum (FWHM) of 10.6 Hz was demonstrated in such tetracontane coated vapor cell. The first investigation on the relaxation time of atomic polarization was described by Franzen *et al.* using optical pumping probe method in a Rb-buff gas mixed anti-relaxation coated vapor cells [14]. Franzen technique consists of optical pumping Rb atoms by using circular polarization light beam. The pump beam is suddenly shut off for a short time interval by a mechanical shutter. In this interval, the relaxation takes place and causes polarized Rb atoms to lose their polarization through atom-atom and atom-surface collisions. In 2005, Graf *et al.* [15] proposed a modification of this technique to measure the longitudinal relaxation time of Alkali filled vapor cells with buffer gas and paraffin inner wall coating. The modified Franzen technique consists in initially optical pumping the atoms into a spin oriented state and then abruptly shutting off the pump laser and measuring (while keeping the pump off)

the linearly polarized probe optical rotation exponential decay, from which the atomic polarization relaxation rate can be deduced. Indeed, under optical pumping, the population of the Zeeman degenerate ground states can be placed into a single Zeeman level or a well-defined combination of them, thus acquiring orientation and alignment along the axis of light propagation. Alignment can be understood as Zeeman sub-level population distribution which relates to zero magnetic angular momentum. On the other hand, the orientation corresponds to Zeeman sub-level population distribution which is total non-zero magnetic angular momentum. This atomic ground magnetic-state can be generated by a circular polarized pump. Furthermore, it impinges a polarization rotation on a linearly polarized probe laser beam. The optical rotation is generated by circular birefringence phase shift between two circular components of the light as it propagates in an atomic medium. This effect can be written by decomposing a linearly polarized beam into two circularly polarized light, left one, (σ^+), and right one, (σ^-) [16] and considering their respective refractive indices $n_\pm$. Consequently, the optical rotation of a linearly polarized light is directly related to the phase shift of σ^+ and σ^-, and thus the optical-rotation is given by the difference between the real parts of n_+ and n_-.

To illustrate this effect, the simple case of a two a level atom gives the following expressions of the refractive indices [17]:

$$n_-(v) = 1 + 2\left(\frac{3}{4}\rho\left(-\frac{1}{2}\right) + \frac{1}{4}\rho(+1/2)\right)\left(\frac{nr_e c^2 f_{D2}}{4v_0}\right) Im(V(v - v_0)) \qquad (4\text{-}1a)$$

$$n_+(v) = 1 + 2\left(\frac{1}{4}\rho\left(-\frac{1}{2}\right) + \frac{3}{4}\rho(+1/2)\right)\left(\frac{nr_e c^2 f_{D2}}{4v_0}\right) Im(V(v - v_0)) \qquad (4\text{-}1b)$$

where ρ(-1/2), ρ(+1/2) are the ground state population of spin down and spin up identities, V(υ-υ0) is the Voigt distribution of the atomic absorption, n is the atomic density, r_e is the classical electron radius, c is the light speed, f_{D2} is the D_2 absorption line oscillation strength and υ_0 is the transition frequency. Figure 4-1 shows the near-resonance spectra of $n_\pm$ (Fig 4-1(a) and (c)) and their associated optical rotation (Fig 4-1(b) and (d)) for the case of Rb polarization orientation and alignment respectively. One can see that in both cases of the atomic polarization, a strong optical rotation takes place near resonance.

The strength and the frequency at which the optical rotation is maximum depends on the nature of the atomic polarization.

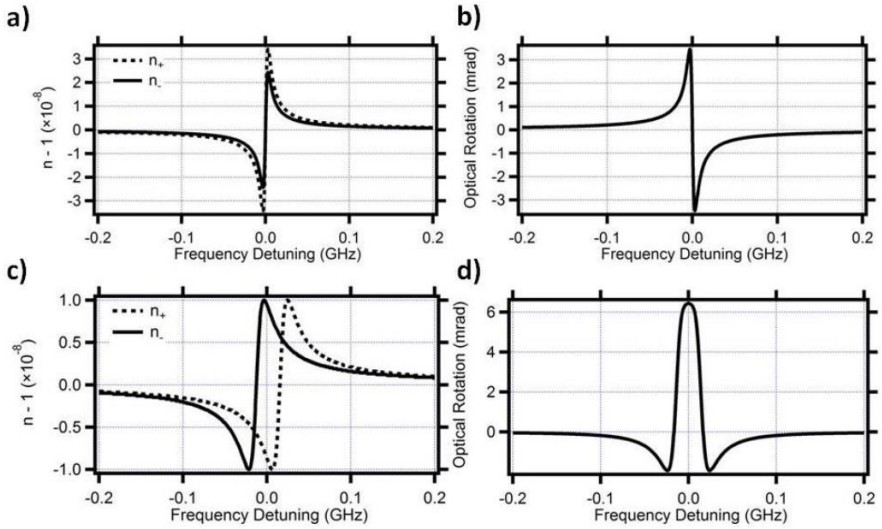

Figure 4-1: a) Refractive index $n_{\pm}$ varies near atomic resonance due to orientation in hyperfine structure of ^{85}Rb at atomic density $n = 10^{12}$ cm^{-3}, b) optical rotation due to difference in $n_{\pm}$ from c) variation of refractive index $n_{\pm}$ near atomic resonance due to alignment d) optical rotation due to difference $n_{\pm}$ [24].

What noteworthy for our experiment is that the ground state polarization relaxation can be monitored by observing the rate at which the probe rotated polarization comes back to its initial polarization. In turn, the ground state polarization relaxes at a rate given by the dephasing rate of collisional mechanisms that can be identified. Five different types of collision mechanisms contribute to atomic polarization relaxation: i) electron randomization collisions with the inner surface, ii) spin exchange collisions between atoms, iii) homogenous relaxation due to the reservoir effect, iv) transit time of the polarized atom across the guided laser beam and v) the dwell time of the polarized atoms at the wall without dephasing.

For the case of HC-PCF, given the Rb small density (see Chapter 3) and the small fiber-core diameter the spin exchange collision can be ignored. Also, the reservoir effect can also be suppressed thanks to the small conductance of HC-PCF and by shutting-off the Rb suspensor. As such the relaxation times that will be considered are those: (1) atom-wall collision (τ_w), (2) transit time (τ_{tt}), and dwell time of the atoms at the surface (τ_{dw}). In the

next section, the ground state atomic polarization relaxation time measurement is introduced.

4.3 Ground state atomic polarization relaxation time measurement experimental set-up

4.3.1 Experimental set-up and atomic polarization relaxation measurement

The experimental set-up for probing atomic polarization state of Rb vapour loaded in HC-PCF is schematically illustrated in Fig. 4-3 (a). For that the laser beam is linearly polarized from an external cavity diode laser (ECDL Toptica DL100) and is split into two beams using a polarizing beam splitter cube. One beam is high power beam (600 nW) with circular polarization after passing through a quarter waveplate and set as pump beam. The second one is a low power probe beam (60 nW) with linear polarization. The pump beam is chopped at a frequency of 500 Hz and is set at 500 MHz blue-detuned from the ^{85}Rb D_2 absorption line ($^5S_{1/2,}$ F=3→$^5P_{3/2,}$ F'=2, 3, 4). The atomic transitions for ^{85}Rb, D_2 lines are illustrated in Fig. 4-2.

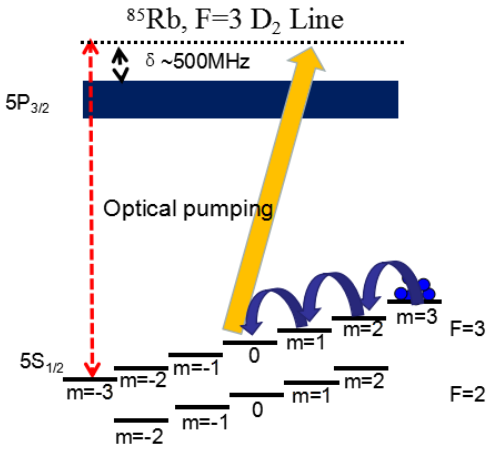

Figure 4-2: Transition scheme of ^{85}Rb, F=3 D_2 absorption line, with optical pumping process and atomic population thermal contribution due to the wall collision.

Next the two beams are recombined through a non-polarizing beam splitter (NPBS) cube and coupled into the HC-PCF under test contained in the UHV chamber. Then the output is split into two linear polarization components and are detected by using a large-area balanced amplified photodetectors to measure the polarization rotation. The Zeeman sub-level degeneracy is lifted by applying a DC magnetic field (< 65 Gs) along the guidance axis of the optical fiber using a solenoid wound around the vacuum chamber.

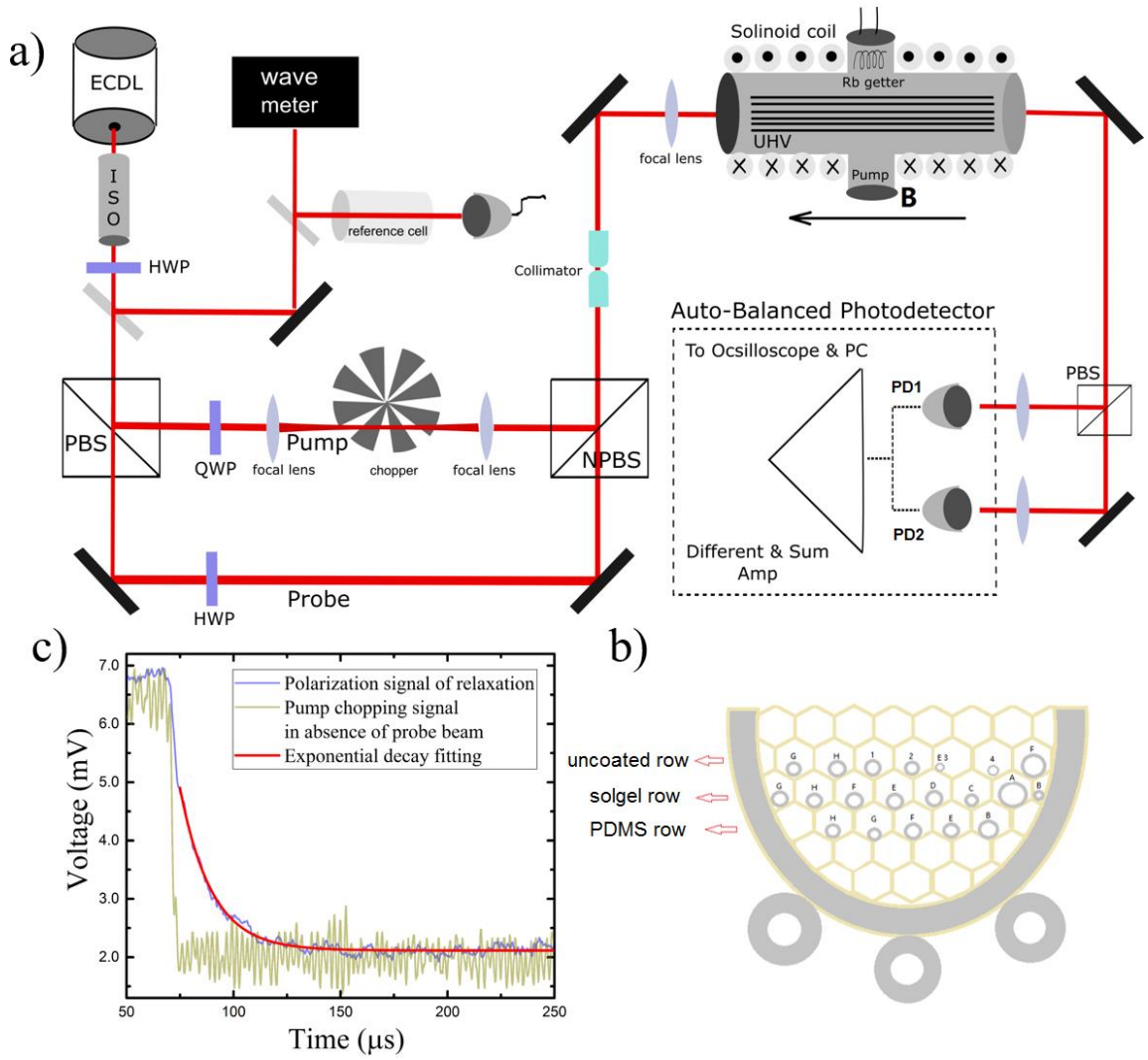

Figure 4-3: (a) Experimental set-up for probing atomic polarization state of Rb vapor loaded in HC-PCFs. ISO: isolator; PD: photodetector; PBS: polarizing beam-splitter, NPBS: non-polarizing beam-splitter. HWP: half waveplate, and QWP: quarter waveplate. (b) System maintaining PDMS, sol-gel coated and uncoated HC-PCFs in the UHV chamber. (c) Chopping decay and probe beam polarization rotation signal.

The fiber set under test consists of four hypocycloidal-like core-shaped Kagome HC-PCF with different contour curvature values and radii. The physical properties and optical performances of the fibers are detailed in the Chapter 2 section 2.8.2 and are plotted in Fig. 4.4 as a reminder. All these fibers have been fabricated to present low loss attenuation around 780 nm ranging between 70 to 350 dB/km. For each, 8 cm-long pieces have been prepared with PDMS and sol-gel coating fibers as described in Chapter 3 section 3.6. The fibers are then positioned into the UHV as shown in Fig. 4-3 (b). The loading of natural Rb vapor into the HC-PCF consists of pumping the UHV chamber by a Turbo-pump until ~ $3*10^{-8}$ Torr and then heating a commercial Rb dispenser (SAES Rb/NF/6.4/17/FT-10). Notice that when the Rb getter is switch on, the vacuum pressure is increased to $8*10^{-8}$ Torr. Also, to enhance the in-fiber atom density which is limited by the fiber geometry, the UHV chamber is maintained at 100 ˚C during all our experiments. The Rb atom in-fiber loading has been tested for a rough period of 4 weeks which time varies depends on the core radius of Kagome HC-PCFs [18].

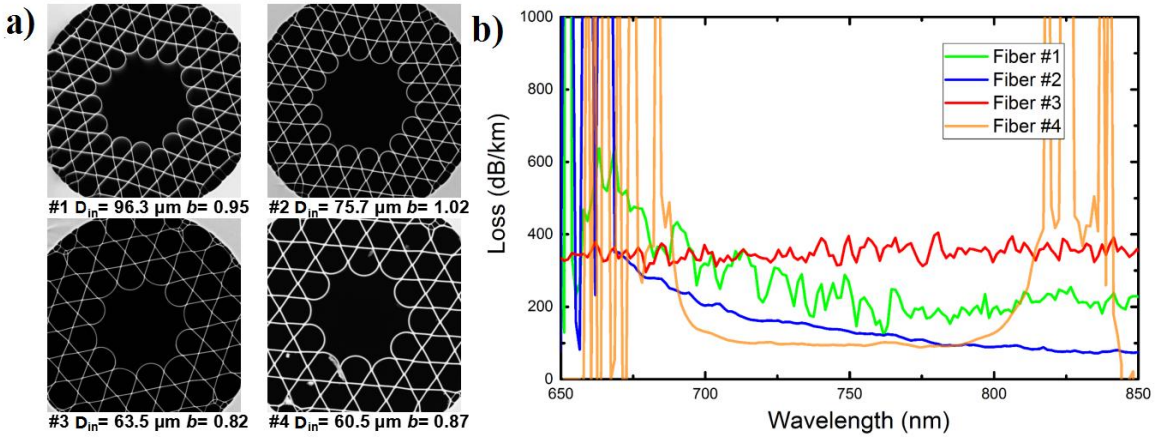

Figure 4-4: Remind of the IC Kagome fibers used for ground state atomic polarization investigation. (a) SEM images of the four fibers differing by core contour, cell defect and radii. (b) Corresponding transmission spectrum in the region of interest.

The brown curve in Figure 4-3 (c) shows the chopper modulated probe in the absence of pump beam. The trace shows a fall and rise time of ~ 500 ns. The latter represents the temporal resolution of out experimental set-up. In other word, the set-up cannot resolve any dynamic faster than 500 ns. When the pump is on and its intensity is

modulated between an on-state (power is at its maximum) and an off-state (power is nil), optical pumping occurs during the time when the pump is at its on-state, and thus an atomic polarization is generated as mentioned in section 4-2. During the pump off-state, the recorded signal from the polarimeter is given by:

$$\Phi = \frac{P_1 - P_2}{2(P_1 + P_2)}, \tag{4-2}$$

The recorded signal given by Equation (4-2) is directly related to the polarization angle of probe beam. Here, P1 and P2 are the detected signals from the two channels of the auto-balanced photodetector: P1 and P2 are the power of the two orthogonal polarization components split by a polarizing beam splitter (PBS). Both measures pass through an electronic circuit of summing and difference amplifier. Therefore, the rotational signal can be obtained by timely comparing the sum and the difference of two polarization components. Figure 4-3(c) presents also the temporal trace (blue curve) of the detected signal Φ. The trace shows a typical negative exponential decay as illustrated by the fit trace (red curve), and consequently can be written in the following form:

$$\Phi = Ae^{-t/\tau_\varphi} + \Phi_0 \, . \tag{4-3}$$

Here, τ_φ is the decay time of the probe polarization rotation A and Φ_0 are fitting constants. The decay time of the probe polarization rotation τ_φ was found to be in the range of 10-50 μs, which is much larger than the transit time due to the chopper.

Now, we explore the physical mechanisms that contribute to τ_φ. As mentioned above, the atomic polarization is deduced from the measured optical polarization rotation. This in turn is determined by the spin state of the atom. In order to extract the relaxation of the electronic spin relaxation, which is the quantity that is related to transit and collisional dephasing times, one needs to eliminate the contribution of the nuclear spin contribution to the optical rotation decay. This can be done by simply recalling that the electronic spin relaxation time τ_1 is related to τ_φ by the equality $\tau_1^{-1} = \tau_\varphi^{-1}/18$ [19]. Here the factor 18 is the calculated ratio between the state change probability in the electron spin and atom total spin after a single collision [18].

Table 4-1: Atomic density, physical properties of different Rb loaded in Kagome HC-PCFs.

N°	Uncoated n [cm^{-3}]	Ceramic coated n [cm^{-3}]	PDMS coated n [cm^{-3}]	R_{in}/R_{out} [µm]	b	τ_{tt} [µs]	τ_w [µs]
#1	6.91×10^{8}	1.3×10^{9}	3.73×10^{9}	48.2/57.9	0.95	0.16	0.32
#2	1.04×10^{9}	1.09×10^{9}	2.45×10^{9}	37.8/46.2	1.02	0.12	0.25
#3	6.51×10^{8}	6.58×10^{8}	7.8×10^{8}	31.8/37.7	0.82	0.11	0.21
#4	7.62×10^{8}	1.54×10^{9}	2.36×10^{9}	30.3/35.7	0.87	0.10	0.20

Table 4-2: Measured τ_φ and associated τ_1 for the different Kagome HC-PCF under test.

Fiber N°	τ_φ [µs]	τ_1 [µs]
#1 uncoated	12.51	0.695
#1 Ceramic coated	14.59	0.811
#1 PDMS coated	17.35	0.964
#2 uncoated	12.53	0.696
#2 Ceramic coated	14.11	0.784
#2 PDMS coated	16.68	0.926
#3 uncoated	11.17	0.620
#3 Ceramic coated	13.87	0.771
#3 PDMS coated	15.16	0.842
#4 uncoated	12.62	0.701
#4 Ceramic coated	14.20	0.789
#4 PDMS coated	16.08	0.893

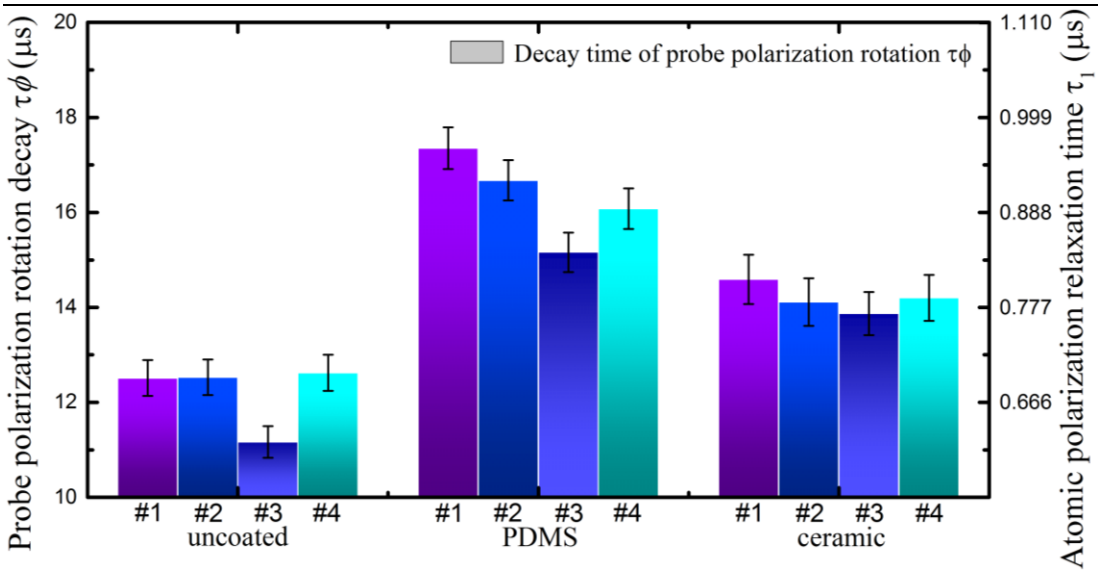

Figure 4-5: Measured optical rotation relaxation time for different HC-PCF and classified by core inner wall surface materials.

Consequently, one can directly relate the measured relaxation time of the probe polarization rotation signal $\varphi(t)$ to the electronic spin relaxation time as:

$$\Phi = Ae^{-t/18\,\tau_1} + \Phi_0\,. \tag{4-4}$$

The table 4-1 lists the measured atomic density *n* along with the physical integrities of Kagome HC-PCFs (*i.e.* the curvature parameter *b*, the inner and outer core radius) and the calculated transit time τ_{tt}, and the atom-wall collision τ_w (see formulas in section 4.1). From the table, we can extract several remarks. The fibers under test exhibit core diameters that range from ~96 μm to ~60 μm, allowing to explore by comparison the effect of the transit time and atom-wall collisions. For comparable experimental conditions, and after 4 weeks of loading process, the Rb atomic densities were found to the following inequalities $n_{PDMS} > n_{ceramic} > n_{uncoated}$. Furthermore, for fibers with the same core surface material, the density is on average the same within a standard deviation in the range of 1-2×10^8 cm^{-3}. Finally, as state before the relaxation timescales for the transit-time and atom-wall collision are only a few hundreds of ns. This corresponds to stronger surface absorption energy results on longer atom confinement time (see atom loading procedures in Chapter 3).

Table 4-2 lists the measured decay time of the probe polarization rotation τ_φ for different HC-PCFs geometry with different inner wall coating surfaces and the associated ground-state atomic polarization τ_1. In PDMS coated HC-PCFs, the decay time of the probe polarization rotation τ_φ presents the longest value for different geometry core sizes, respectively ~17.35 μs for PDMS fiber #1, ~16.68 μs for PDMS fiber #2, ~15.16 μs for PDMS fiber #3 and ~16.08 μs for PDMS fiber #4. On the other hand, the uncoated HC-PCFs have the shortest decay time of polarization rotation, reaching ~12.51 μs for uncoated fiber #1, ~12.53 μs for uncoated fiber #2, ~11.71 μs for uncoated fiber #3, ~12.62 μs for uncoated fiber #4. Finally, the ceramic coated HC-PCFs have been found to be in between. The effect of the surface materials on the optical rotation relaxation is noticeable in Fig. 4-5. Further experimental results, data processing and analysis related to the effect of the surface material on the ground state polarization relaxation will be discussed in the

section 4.4.1. In the following, the discussions of the deduced transit time and dwell time will be introduced.

4.3.2 Transit time and dwell time deduction

Among the striking features on the results summarized in tables 4-1 & 2 is the fact that the ground state electronic spin relaxation time (τ_1 ~ 1 μs) is much larger than the atom-wall collision time (τ_w ~ 200 ns) and the transit time (τ_{tt} ~100 ns) of thermal atoms inside HC-PCF. Below, we review the different relaxation mechanisms that contribute to the electron spin relaxation time τ_1 and the differences that the HC-PCF configuration bring to the conventional picture.

Following Graf *et al.* formalism (see equation (7) in [15]), the time-dependence of the probe beam polarization rotation $\varphi(t)$ mainly due to the relaxation of the atomic polarization form as:

$$\varphi(t) = \alpha_f e^{-\gamma_f t} + \alpha_s e^{-\gamma_s t} + \varphi_{dc}, \tag{4-5}$$

where γ_f and γ_s are the faster and slower relaxation rate, α_f and α_s are the amplitudes of the fast and slow relaxing exponential, φ_{dc} is the DC rotation from linear Faraday effect. The quantities γ_f and γ_s are related to the different ground state polarization relaxation mechanisms and are given for the case of Rb by (equations (2)-(6) of [15]):

$$\gamma_{f,s} = \gamma_u + \frac{1}{108}\left(57\gamma_{er} + 38\gamma_{se} \pm \sqrt{2601\gamma_{er}^2 + 3684\gamma_{er}\gamma_{se} + 1444\gamma_{se}^2}\right). \tag{4-6}$$

Here, the relaxation rates are: (1) γ_{er} is the rate of electron randomization of atom-wall collision; (2) γ_{se} is the rate of spin-exchange for atom-atom collision and (3) γ_u for reservoir effect. Furthermore, we recall that α_f and α_s are opposite in sign, and thus the negative exponential that is fitted from the measured trace is limited to the slow decay component of $\varphi(t)$ (*i.e.* $\varphi(t) \approx \alpha_s e^{-\gamma_s t} + \varphi_{dc}$) when the taken experimental data at times are longer than 5 μs.

In our experiment, the Rb atom-atom spin exchange collision γ_{ex} is ignored because of the low atomic density ($n < 10^{10}$ cm^{-3}) reached in the fiber even when operated at 100 ˚C. The Rb-Rb collisional relaxation time is $\gamma_{ex} = 1/\tau_{ex}$ ($\tau_{ex} = 1/(n\sigma_{ex}v) \approx 180\ ms$) which corresponds to several orders of magnitude larger value than the atom-wall collision. Furthermore, because of the small fiber core size the reservoir effect is also ignored. Consequently, we have $\gamma_s = \frac{\gamma_{er}}{18}$, and retrieve our relation between the optical rotation relaxation time and the electronic spin relaxation time. In other word, the relaxation time of the probe polarization rotation signal $\varphi(t)$ corresponds dominantly to the rate electron spin randomization.

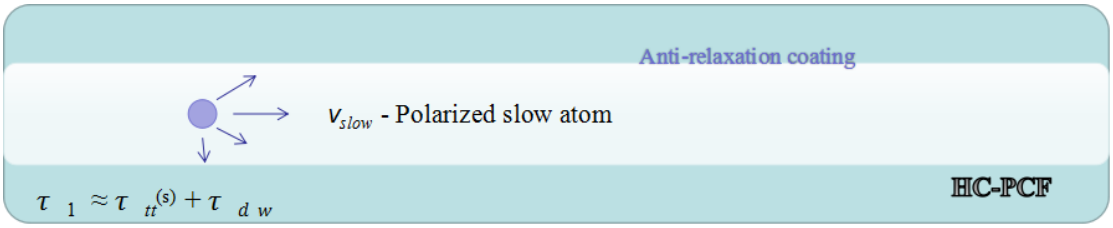

Figure 4-6: Illustration of the dynamic of atomic flying and collision in the HC-PCF.

Furthermore, Bradley *et al.* [20] showed that the relaxation dynamics of ground state-polarized atoms follows a specific sequence and is strongly influenced by transit time and dwell time on the surface. Figure 4-6 shows schematically the sequence and the main timescales. In this dynamics the polarized atoms are those with much smaller velocity because of the short transit time relative to the optical pumping rate. As a result when the pump laser is switch off, the polarized atoms transit with time duration $\tau_{tt}^{(s)}$ longer than thermal one. These atoms will then dwell at the wall surface for a time equal to τ_{dw} before fully thermalizing upon collision with the fiber core wall surface. In turn, the electron spin relaxation time can be written as $\tau_1 \approx \tau_{tt}^{(s)} + \tau_{dw}$. Below, we give a more quantitative and detailed account of this dynamics.

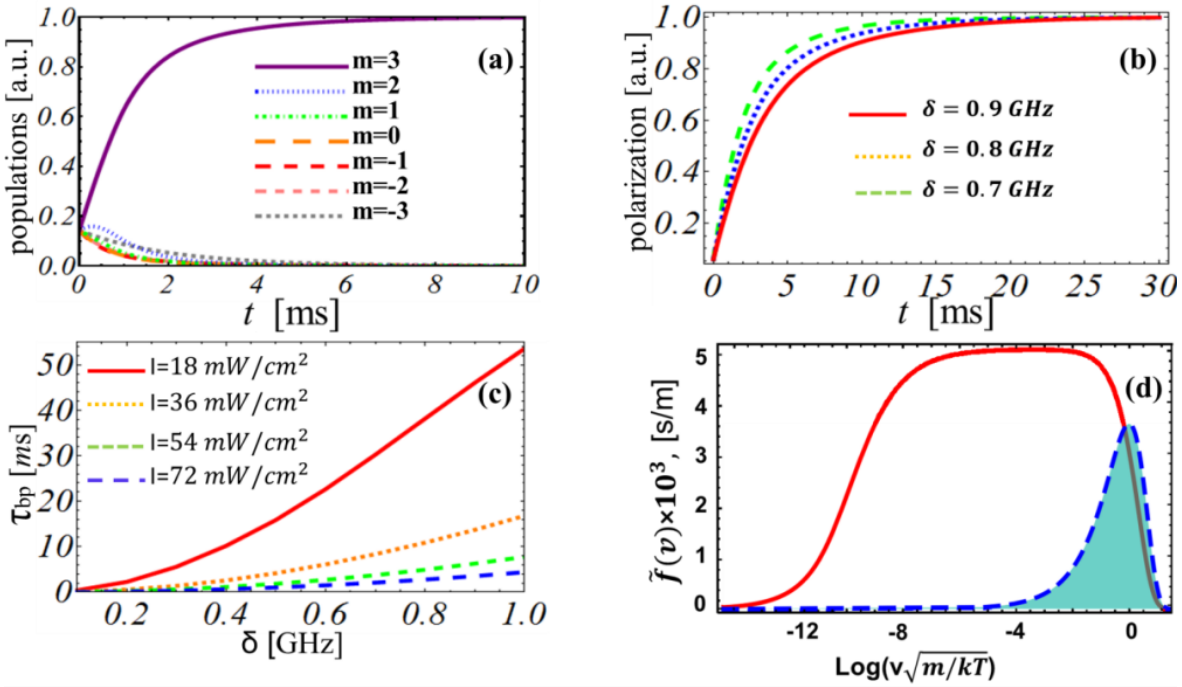

Figure 4-7: Numerical simulations for (a) Seven Zeeman sublevels population evolution in the presence of optical pumping process in fiber #1. (b) Atom polarization lifetime evolution with pump laser intensity of 18 mW/cm^2 and detuning of 700 MHz (solid red curve), 800 MHz (dotted orange curve) and 900 MHz (dashed green curve). (c) Population build-up time versus the pump frequency detuning with the intensity of 18 mW/cm^2 (solid red curve), 36 mW/cm^2 (dashed orange curve), 54 mW/cm^2 (dashed green curve), 72 mW/cm^2 (dashed blue curve). (d) The effective transverse speed probability density function for the polarized atoms (red curve). For comparison the Rb thermal Maxwell-Boltzmann distribution is shown (blue filled curve) (from reference [20]).

Fig. 4-7 (a) shows the time evolution of the Zeeman level populations of the ground state under the action of a pumping laser. One note that the atomic population is found to be completely optical pumped to the steady state of Zeeman sublevel |F = 3, m = +3⟩ after certain build-up time τ_{bp}. Consequently, the optical pumping induced population loading of the state |F = 3, m = +3⟩ is $\propto (1 - e^{-\frac{t}{\tau_{bp}}})$, in consistency with the numerical results shown in Fig. 4-7(a). This build-up time depends on both the pump laser intensity and frequency detuning from F = 3→ F'. Fig. 4-7 (b) shows the numerical calculations on how the pump laser intensity and detuning affects the built-up time. These results are consistent with the scaling law $1/\tau_{bp} \sim I/\delta^2$ [21]. In order to have an estimate of this building time range in a HC-PCF configuration, it is noteworthy recalling that in a fiber with 50 μm core diameter, for a pump power of only 173 nw- *i.e.* intensity of 18 mW/cm^2, and a detuning of 500

MHz, the numerical results show that the associated τ_{bp} was found to ~2 ms. which is more than three orders of magnitude larger than transit-time τ_{tt}. This means that even with very low pump-power levels and large frequency detuning (in Fig.4-7(b)), only the atoms that are sufficiently slow can complete one Rabi-cycle before the atom-wall surface interaction. In other words, only the transversal slow atoms participate in the polarization (in Figure. 4.6).

The average velocity of these slow polarized atoms can be deduced from the velocity distribution of the polarized atom shown in the red curve of Fig. 4-7(d) for the case of an intensity of 18 mW/cm^2. In the figure, this distribution of polarized atom transverse velocity in Kagome HC-PCF is plotted for comparison with the Maxwellian distribution (blue curve). The result shows that average velocity of the polarized atoms is ~20 times smaller than thermal velocity of Rubidium. As such that transit time is 20 larger than τ_{tt}. In conclusion, in HC-PCF configuration, which contrasts with its very short transit-time and atom-surface collisions for thermal atoms, the main mechanisms contributing in the atomic polarization relaxation are set first by the polarized slow atom time of fly (transit time of slow atom), and then by the dwell time on the core inner-wall surface.

Such specific scenario has been corroborated using Monte Carlo simulation [20] to trace the trajectory of polarized atoms. The results are summarized in Fig. 4-8 showing a good agreement between the measured and the calculated relaxation time τ_1. The calculated τ_{tt} and τ_{dw} are also plotted in Fig.4-8 for comparison. The results demonstrate that the atomic polarization relaxation time τ_1 is significantly longer than the one of thermal Rb. The value found for τ_{dw} of 0.7 μs agrees with the measured one in [11]. Consequently, the rate of electron spin randomization in HC-PCF configuration can be approximated to $\tau_1 \approx \tau_{tt}^{(s)} + \tau_{dw}$ as introduced above.

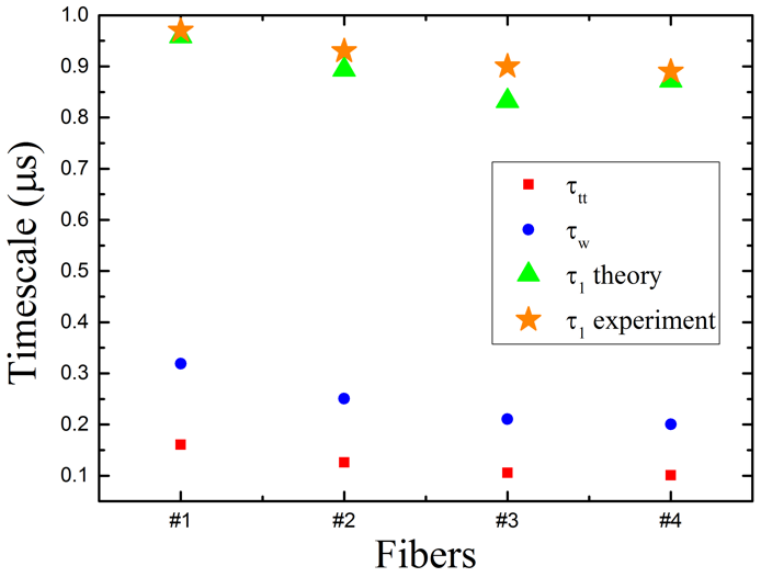

Figure 4-8: Monte-Carlo simulation calculated (green triangles) and measured (orange stars) τ_1. For atom-wall relaxation time for the tested four fibers. The theoretical thermal atom transit time τ_{tt} (red) and dwell time τ_{dw} (blue) are also indicated.

So our purpose in the following is to investigate how the anti-relaxation coating improve physico-chemical absorption, to distinguish transit time broadening from the atom-wall collision broadening, and understand how to optimize the beam power and detuning frequency.

In the following section, we explore theses finding to analyse our results summarised in tables 4-1 and 4-2 and Fig. 4-5. In particular, we report on an experimental means to deduce un-ambiguously the dwell time for the different fiber-core wall surfaces.

4.4 Measurements on dwell time and discussion

4.4.1 Investigations on different coated Kagome HC-PCFs

Figure 4-9 summarizes the measured polarization rotation relaxation τ_φ and its associated electronic spin randomization relaxation time τ_1 (solid lines and symbols) for the 12 pieces of HC-PCFs under test (see Table 4-2). Furthermore, the figure shows the calculated τ_φ (open symbols and dashed lines) using the Monte-Carlo simulations and the

calculation of the polarized atom average velocity mentioned above. The results show very good agreement between the measured and the calculated τ_φ for all the tested fibers, corroborating thus the relxation sequence mentioned above [20]. Furthermore, the results show a noticeable effect of the fiber core surface material on the relaxation time.

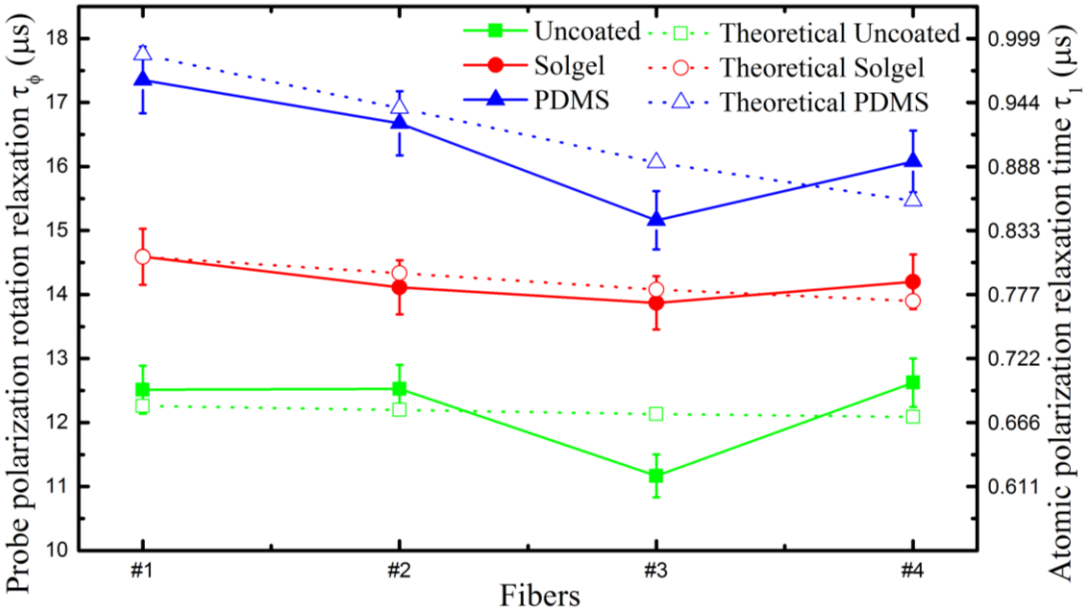

Figure 4-9: Experimental systematic study of polarization rotation relaxation time based on different Kagome fiber inner core sizes and curvature *b* parameters. The dashed curve represents the simulation results.

The electronic spin relxation, τ_1, was found to be faster for the uncoated HC-PCF (*i.e.* silica surface) with $\tau_1 \sim 0.7\ \mu s$, then for the aluminosilica-ceramic coated surface (sol-gel) with $\tau_1 \sim 0.8\ \mu s$, and finally the PDMS with $\tau_1 \sim 1\ \mu s$. Despite the scarce and varying data on the dwell time available in the existing literature, the found order in τ_1 between the different surfaces is consistent with the fact that the adsorption activation energy follows $E_{a\_(PDMS)} > E_{a\_(Solgel)} > E_{a\_(silicate)}$ (see Chapter 3) as reported in [22][23]. Indeed, because the atomic polarization relaxation is set by the transit time of slow atoms and the dwell time of atoms at the surface on one hand, and because the transit time of slow atoms is the same for each HC-PCF on the other hand, the differences in the relaxation time τ_1 for each HC-PCF design is due to the dwell times.

Furthermore, and as expected [25], the results show that the relxation time decreases with the fiber label order (*i.e.* from fiber #1 to fiber #4), which is set by a decreasing order of the fiber inner diameter (Table 4-1). However, the small difference in the slop in τ_1 with the fiber label order between the three surfaces remains unexplained, and could be due to difference in the deposited coating layer.

4.4.2 Dwell time deduction

In this section, we will explore the fact that one can control the resulted average velocity of the polarized atom with the laser intensity to deduce the dwell time by increasing the laser intensity and thus decreasing the transit time of the polarized atoms to that of thermal one.

The basic idea of this approach stem from the fact that in a very fast transit time, the contribution of the fast atoms in optical pumping can be greatly reduced by operating at a laser intensity that is $\Omega_R \ll \tau_{tt}^{-1}$ or increased for higher laser intensity [27]. Following the formalism In [27], we define the transverse velocity $v_t^m = d_m \tau_{tt}^{-1}$ as the borderline slow atoms (*i.e.* those which are in the collisional regime) and the fact ones (*i.e.* those which are in free flight). Because the fast free-flying atoms contribution to the pumping scales as $(\Omega_R \tau_{tt})^4$ [27], one can increase their contribution to the final state of the polarized atoms by simply increasing the laser power to a level were the transit time is much shorter than the dwell time. The above is clearly corroborated by the asymptotic behavior of the curves in Figure 4-10 showing our measurement of τ_1 with laser pump power for the different fiber core surfaces.

Figure 4-10 results were obtained using the same expertimental set-up described earlier. The laser beam is 500 MHz blue detuned to the resonance of D2 absorption lines of ^{85}Rb ($^5S_{1/2}$, F=3→$^5P_{3/2}$, F'=1, 2, 3, 4) and coupled to the fiber noted #1 (19-cell defect with inner core size D_{in} = 96.3 μm and curvature parameter b = 0.95). The probe beam is set to a linear polarization with power of 60 nW, whereas the pump beam power can varied from 300 nW to 5 μW chopped at 500 Hz frequency. The magnetic field is maintained constant at 25 Gs. Notice that, our experimental setup cannot distinguish the optical rotation at

power as low as pW level because of the limited sensitivity of our detection. The figure shows the polarization rotation relaxation time in function of the pump beam power in different coated fibers. The error bars represent the measurement uncertainty deduced from the standard deviation of several measurements.

The evolution of τ_φ, or equivalently τ_1, with the pump power shows a hyperbolic decrease before assymptotocally converging to a time constant. The latter depends on the surface material of the HC-PCF core and was found to be the measured atom polarization relaxation time after ~30 times bounds off are τ_1 (PDMS) ~ 785 ns ± 50 ns, τ_1 (sol-gel) ~ 755 ns ± 50, τ_1 (uncoated) ~ 725 ns ± 50 ns. Substructing the contribution of the transit time, which is equal to 160 ns for such geometry of this fiber, we find dwell time of 630 ns ± 50 ns, 600 ns ± 50, 560 ns ± 50 ns for the PMDS coating, ceramic coating and silica glass surface respectively.

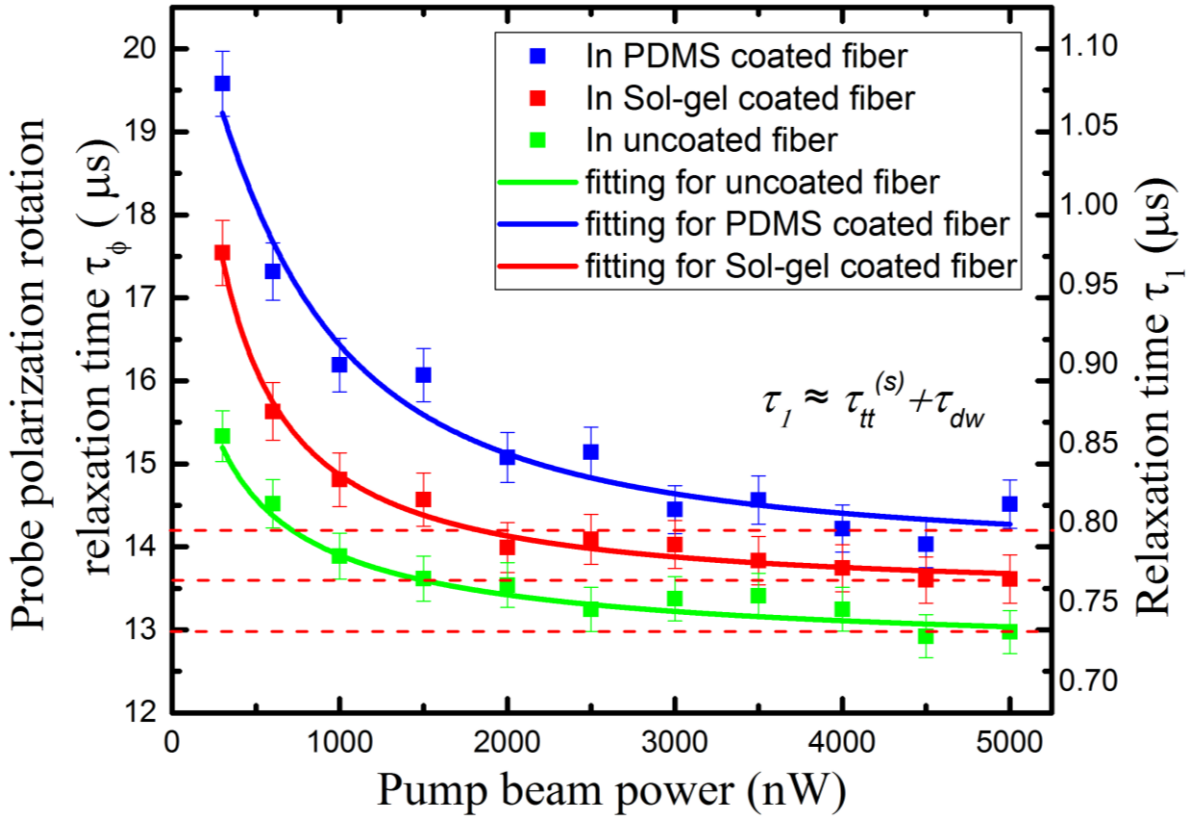

Figure 4-10: Relaxation time pump beam power dependency in different coated Kagome fibers. The dwell time for each surface materials are backstairs obtained when the pump beam is saturated.

The dwell time values found above are consistent with the most recent dwell time measurement using evanescent wave technique [28], where a dwell time of 530 ns was found for Rb atoms on OTS coated pyrex surface. Furthermore, and unlike the technique reported in [28], our reported technique allows measurements of dwell time *in situ* is relative to the device or component under test. This would be very useful in experiments were there is need to measure dwell time in real conditions of the experiment.

4.4.3 Detuning frequency dependence

The above results showed how we one can generate atoms with polarized ground state and control their velocity or quatum state through optical pumping with an appropriate laser excitation. Moreoever, the results indicate how these atoms confer to the atom filled HC-PCF with Farady rotation and magnetometry capabilities. Finally, we have also seen the dominant dephasing mechanisms behind that atom relaxation times. In this section, we explore, as a prove of concept, the effect of a polarized atomic photonic device on a laser probe, with the aim to further our understanding on the relaxation dynamic of polarized atoms insided HC-PCF, but also to inveistage its use as a compact Faraday rotator or as magnetometer.

For this, we explore the optical rotation of a probe laser in a continuousely optical pumped Rb atoms insided a HC-PCF. This is undertaken by assessing its relaxation time using the same experimental protocol as that of section 4.3.1. The difference is that the probe laser has no longer the same frequency and is swept over the D2 transition of ^{85}Rb.

Figure 4-11 shows the experimental set-up and conditions. The set-up is the same as the one of Fig. 4-3, with the different that we use two lasers. A frequency tuned and linearaly polarized laser beam is emitted from a tunable ECDL (from a NewFocus Tunable Diode Laser (Model TBL-7113) is used as the probe beam. The probe frequency tuning spans from -1500 MHz to 5500 MHz relatirve to the resonance ^{85}Rb D2 absorption line ($^5S_{1/2}$ F=3→$^5P_{3/2}$ F'=2, 3, 4). The power of probe beam is set ~ 60 nW.

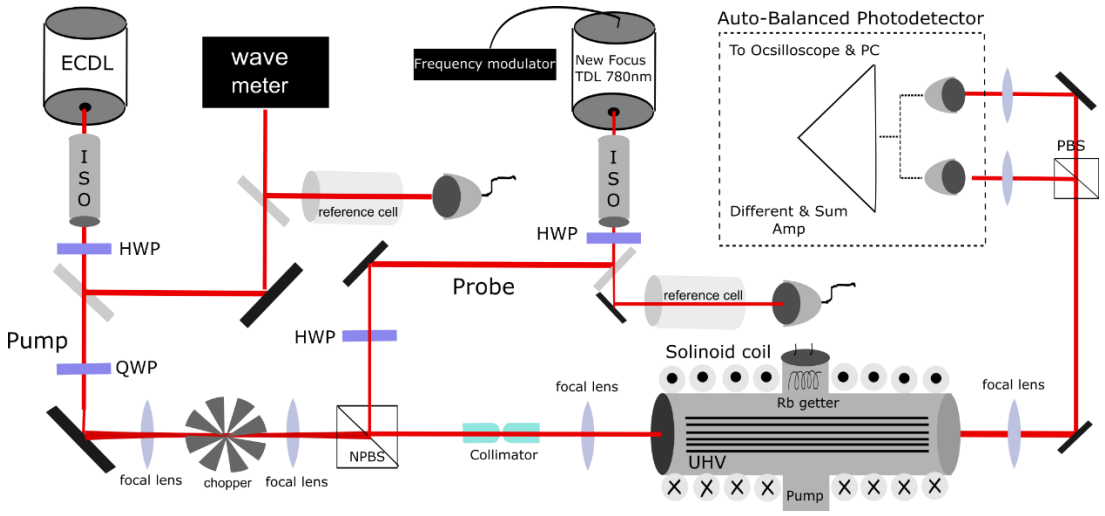

Figure 4-11: Experimental setup for measuring the atomic polarization relaxation by using different input lasers. ISO: isolator; PD: photodetector; PBS: polarizing beam-splitter, NPBS: non-polarizing beam-splitter. HWP: half waveplate, and QWP: quarter wavelplate.

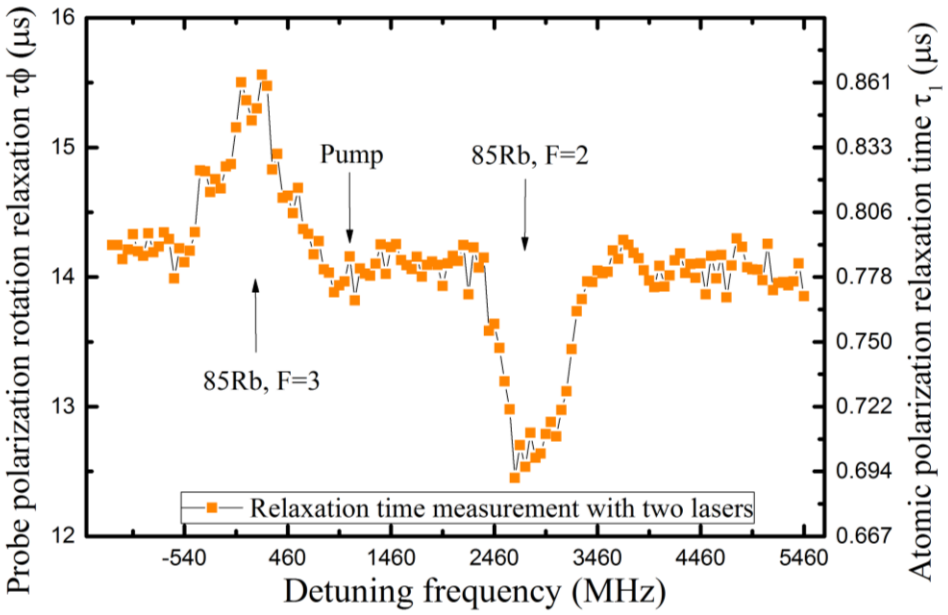

Figure 4-12: Polarization rotation relaxation time of detuning frequency dependency of probe beam with fixed pump blue detuning 800 MHz off resonance to the ^{85}Rb, F=3. The probe beam detuning in the range of 7 GHz which cover all four absorption lines.

The second laser corresponds to the circularly polarized pump beam. It is emitted from another ECDL (Toptica DL100). The pump frequency is set 800 MHz blue-detuned

from the resonance ^{85}Rb D2 line $|^5S_{1/2}, F=3\rangle \rightarrow |^5P_{3/2}, F'\rangle$. The pump beam is chopped with an optical chopper at a frequency of 500 Hz. The pump beam power is 600 nW which is less than the power required to reach saturated intensity for the core diameter of the fiber under test. The fiber used is solgel coated fiber #1 (see fiber information in section 4.4a), and to which both probe and pumps are coupled after being combined beam. The longitudinal DC magnetic field was set ~ 25 G. For each probe frequency setting, the probe beam polarization rotation relaxation is then measured using the protocole described earlier.

Figure 4-12 shows the measured probe optical rotation with frequency. A polarization relaxation time maximum appeared at the resonance of the transition ^{85}Rb, F=3→ F', and the minimum at the resonance of ^{85}Rb, F=2→ F'. The maximum was found to be around 15.5 μs, which is larger by 0.97 μs compared to the configuration when the pump and probe have the same frequency. The minimum was found to be 12.2 μs, which 2.14 μs faster than the configuration when the pump and the probe have the same frequency. Outside the two resonances, the relaxation rate is approximately constant and equal to 14 μs. The difference in τ_φ between the two resonances was attributed to the difference in the dipole strength of the two transition, and hence to the difference in the contribution to τ_φ of the transit time of the slow polarized atoms at each resonance frequency.

Recalling that increasing τ_φ can be obtained by decreasing the pump beam power and/or decreasing the detuning to increase the transit time of the slow polarized atoms by optically pumping the slowest ones, one deduce from the results shown in Fig. 4-12, that Rb-filled HC-PCF can be used as a Faraday rotator over a significant spectral range. Furthermore, there results can be further exploited to measure how dwell time of Rb atoms at different surface evolve with frequency.

These results are extremely useful for our longterm objective to develop stand-alone all-fiber alkali vapor photonic microcells.

4.5 Summary

This chapter introduced experimental and theoretical investigation of the ground state atomic polarization relaxation time in the micrometer scaled core of several Kagome HC-PCF. The experiment was based on measuring the probe magneto-optical rotation relxation rate via a modified Franzen method. The dynamic of this optical rotation was theoretically assessed by solving the Bloch equations and deducing the ground state steady-state under optical pumping, and by using Monte-Carlo simulation to trace the trajectory of polarized atoms before the full depolarization.

The results show that the relxation of the polarized atoms go the following sequence. The polarized atoms, which happen to be very slow because of the faster transit-time of thermal atoms relative the optical pumping rate, go through a free fly until for a time equal $\tau_{tt}^{(s)} = (v_t/v_p)\tau_{tt}$, which is longer a factor given by the ratio between the thermal velocity, v_t, and average velocity of the polarized atom, v_p. Then, when these atoms arrive near the fiber core surface, they spend a certain time (a dwell time) before deplorizing via collision with the wall. This sequence leads to the following conclusion. The relaxation of the electronic spin of polarized atoms inside a HC-PCF are set by the transit time of the slow atoms and the dwell time at the core inner wall surface. This scenario has been corroborated with several HC-PCF having different core diameters and difference core inner-surface materials.

We used the above polarization relaxation time measurement protocol and the fact that we can set the polarized atom velocity v_p by varying the pump laser power to deduce the dwell time of the three fiber-core inner surfaces. We found that the dwell time were 630 ns ± 50 ns, 600 ns ± 50, 560 ns ± 50 ns for the PDMS coating, ceramic coating and silica glass surface respectively, which are consistent with recently measured dwell times.

4.6 Reference

[1] S. Ghosh, A. R. Bhagwat, C. K. Renshaw, S. Goh, A. L. Gaeta, and B. J. Kirby, "Low-Light-Level Optical Interactions with Rubidium Vapor in a Photonic Band-Gap Fiber," vol. 23603, no. July, pp. 1–4, 2006.

[2] P. S. Light, F. Benabid, F. Couny, M. Maric, and A. N. Luiten, "Electromagnetically induced transparency in Rb-filled coated hollow-core photonic crystal fiber," vol. 32, no. 10, pp. 1323–1325, 2007.

[3] W. Yang, D. B. Conkey, B. Wu, D. Yin, A. R. Hawkins, and H. Schmidt, "Atomic spectroscopy on a chip," *Nat. Photonics*, vol. 1, no. 6, pp. 331–335, 2007.

[4] M. R. Sprague, D. G. England, A. Abdolvand, J. Nunn, X. Jin, W. S. Kolthammer, B. Rigal, P. S. Michelberger, F. M. Tessa, P. S. Russell, and I. A. Walmsley, "E cient optical pumping and high optical depth in a hollow-core photonic-crystal fibre for a broadband quantum memory arXiv : 1212 . 0396v1 [quant-ph] 3 Dec 2012," 2012.

[5] J. Nunn, N. K. Langford, W. S. Kolthammer, T. F. M. Champion, M. R. Sprague, P. S. Michelberger, X.-M. Jin, D. G. England, and I. A. Walmsley, "Towards scalable photonics via quantum storage," vol. 8636, p. 863612, 2013.

[6] W. Demtroder, *Laser Spectroscopy, Vol. 2: Experimental Techniques*. 2008.

[7] M. Danos and S. Geschwind, "Broadening of microwave absorption lines due to wall collisions," *Phys. Rev.*, vol. 91, no. 5, pp. 1159–1162, 1953.

[8] C.J.Borde, "Saturated absorption line shape: Calculation of the transit-time broadening by a perturbation approach," vol. 14, no. l, 1976.

[9] Torralbo-Campo, Lara, Graham D. Bruce, Giuseppe Smirne, and Donatella Cassettari. "Light-induced atomic desorption in a compact system for ultracold atoms." *Scientific reports* 5 (2015).

[10] A. Hatakeyama, M. Wilde, and K. Fukutani, "Classification of Light-Induced Desorption of Alkali Atoms in Glass Cells Used in Atomic Physics Experiments," *e-Journal Surf. Sci. Nanotechnol.*, vol. 4, no. January, pp. 63–68, 2006.

[11] K. F. Zhao, M. Schaden, and Z. Wu, "Method for measuring the Dwell time of spin-polarized Rb atoms on coated Pyrex glass surfaces using light shift," *Phys. Rev. Lett.*, vol. 103, no. 7, pp. 1–4, 2009.

[12] T. D. Bradley, J. Jouin, J. J. McFerran, P. Thomas, F. Gerome, and F. Benabid, "Extended duration of rubidium vapor in aluminosilicate ceramic coated hypocycloidal core Kagome HC-PCF," *J. Light. Technol.*, vol. 32, no. 14, pp. 2486–2491, 2014.

[13] H. G. Robinson and C. E. Johnson, "Narrow 87Rb hyperfine-structure resonances in an evacuated wall-coated cell," *Appl. Phys. Lett.*, vol. 40, no. 9, pp. 771–773, 1982.

[14] W.Franzen, "Spin Relaxation of Optically Aligned Rubidium Vapor, Franzen.pdf." 1959.

[15] M. T. Graf, D. F. Kimball, S. M. Rochester, K. Kerner, C. Wong, D. Budker, E. B. Alexandrov, M. V. Balabas, and V. V. Yashchuk, "Relaxation of atomic polarization in paraffin-coated cesium vapor cells," *Phys. Rev. A - At. Mol. Opt. Phys.*, vol. 72, no. 2, 2005.

[16] D.Budker, *Optical Magnetometry*. 2013.

[17] S. J. Seltzer, "Developments in Alkali-Metal Atomic Magnetometry," 2008.

[18] T. D. Bradley, Y. Wang, M. Alharbi, B. Debord, C. Fourcade-Dutin, B. Beaudou, F. Gerome, and F. Benabid, "Optical Properties of Low Loss (70dB/km) Hypocycloid-CoreKagome Hollow Core Photonic Crystal Fiber for Rb and Cs BasedOptical Applications," *J. Light. Technol.*, vol. 31, no. 16, pp. 2752–2755, 2013.

[19] M. T. Graf, D. F. Kimball, S. M. Rochester, K. Kerner, C. Wong, D. Budker, E. B. Alexandrov, and M. V Balabas, "Relaxation of atomic polarization in paraffin-coated cesium vapor cells," pp. 25–28, 2005.

[20] Bradley, Thomas D., Ekaterina Ilinova, J. J. McFerran, Jenny Jouin, Benoît Debord, Meshaal Alharbi, Philippe Thomas, Frédéric Gérôme, and F. Benabid. "Ground-state atomic polarization relaxation-time measurement of Rb filled hypocycloidal core-shaped Kagome HC-PCF." *Journal of Physics B: Atomic, Molecular and Optical Physics* 49, no. 18 (2016): 185401.

[21] M.Tanaka, "Depolarization of optically pumped sodium atoms by wall surfaces," vol. 41, no. 3, 1990.

[22] V. V. Arslanov and V. A. Ogarev, "Kinetics of the fusion of drops of polydimethylsiloxane on solid surfaces," *Bull. Acad. Sci. USSR Div. Chem. Sci.*, vol. 23, no. 8, pp. 1716–1719, 1974.

[23] J. C. Giuntini, J. M. Douillard, G. Maurin, S. Devautour-Vinot, A. Nicolas, and F. Henn, "Aluminosilicate surface energy and its evolution upon adsorption using dielectric relaxation spectroscopy," *Chem. Phys. Lett.*, vol. 423, no. 1–3, pp. 71–75, 2006.

[24] D. Budker, D. F. Kimball, S. M. Rochester, V. V Yashchuk, and M. Zolotorev, "Sensitive magnetometry based on nonlinear magneto-optical rotation," vol. 62, pp. 1–7, 2000.

[25] A. Franz, "Relaxation at Cell Walls in Optical-Pumping Experiments," vol. 6, no. x, 1972.

[26] Bradley, Thomas. "Atomic vapours filled hollow core photonic crystal fibre for magneto-optical spectroscopy." PhD diss., University of Bath, 2014.

[27] Chardonnet, Ch, F. Guernet, G. Charton, and Ch J. Bordé. "Ultrahigh-resolution saturation spectroscopy using slow molecules in an external cell." *Applied Physics B: Lasers and Optics* 59, no. 3 (1994): 333-343.

[28] Zhao, K. F., M. Schaden, and Z. Wu. "Method for measuring the dwell time of spin-polarized Rb atoms on coated pyrex glass surfaces using light shift." *Physical review letters* 103, no. 7 (2009): 073201.

Chapter 5

Atom-surface Van der Waals potential induced sub-Doppler transparencies in Rb vapor filled Kagome HC-PCF

This chapter introduces Rb-surface interaction induced sub-Doppler transparencies observed in the absorption spectrum of Rb-confined vapor inside a Kagome HC-PCF. Unlike with saturated absorption or electromagnetically induced transparency, the sub-Doppler lines are generated with a single forward propagating laser beam. The chapter reports on how these sub-Doppler transparencies change with magnetic field, laser power and polarization for three different core inner-wall surfaces. Then, the results are compared with those of a theoretical model, which considers the adsorbed atom trapped in a Van-der-Waal potential, and shows that sub-Doppler transparencies can occurs via optical pumping between the translational energy levels of the adatoms inside the potential. The comparison between the theoretical model and the experimental results show a qualitative consistency and paves the way for a novel spectroscopy based on atoms in HC-PCF.

5.1 Introduction

In the previous chapter we have seen that the dwell time of the atoms on the fiber core inner surface plays a significant role in the relaxation dynamics. In particular, because the small core diameter, and thus the very short transit time (typically in the range of 100-200 ns), the dwell time-scale, found to be ~1 μs, becomes the longest relaxation time. Furthermore, in deducing the dwell time in our measurement protocol, the surface so far was considered only as a mechanical barrier for the atoms inside the fiber-core, and the dwell time was implemented phenomenologically. This picture doesn't of course take into account the nature of the atom-surface interaction, nor the energy structure change of the adsorbed atoms, or adatoms, relative to the "free flying" atoms. The results of Chapter 4 showed that in order to assess properly the atomic dynamic of the in-fiber atoms, the atom-surface has to be modeled more accurately. This is particularly true when we recall that the fraction of the adatoms can be extremely large. Indeed, writing the total number of the atoms inside the fiber core in the following manner [3]:

$$n_{tot} = n_v \left(1 + \frac{v_{th} A}{4\,V} \tau_0 e^{E_a/kT}\right), \tag{5-1}$$

where the v_{th} is the thermal velocity of atoms, A is the inner surface area of the vapor cell, V is the volume of the vapor cell and n_v is the number of the atoms in the vapor cell. The ratio of the adatoms density over the total atom density is equal to $n_{ad}/n \sim \langle \tau_{ad} \rangle \bar{v}$, and can be very large as shown in Fig. 5-1. Here, $\bar{v}$ is the mean speed of Rb and $\langle \tau_{ad} \rangle$ is adsorption time given by $\langle \tau_{ad} \rangle = \tau_0 e^{E_a/kT}$ [1]–[3]. The quantity E_a is adsorption activation energy. Figure 5-1 plots the fraction n_{ad}/n with E_a for two very different values of τ_0. This is justified because of the inconsistent reported values for silica surface of τ_0, which is stated to range from 10^{-14}s to 10^{-9}s [4], and of E_a, which can be as low as 0.1 eV and as high as 0.7 eV (see Table 5-1). The first is $\tau_0 = 10^{-12} s$, and is the most often used value is the early literature [3], and the second $\tau_0 = 10^{-9} s$, which corresponds to most recent measurement reported in [1], and in which E_a was also measured to be 0.19 eV (symbol in Fig. 5-1). Furthermore, for each τ_0, we plot n_{ad}/n for two different temperatures: room temperature and $T = 370\,K$, which is the typical value in our

experimental conditions. According to the Fig. 5-1 results, and if one takes the experimental values represented in circle symbols, the fraction of the adatoms ranges between 50% and 90%. Such a fraction is sufficiently large to not ignore the atom-surface interaction and to explore its effect on the atom dynamics in particular in the relaxation time scale.

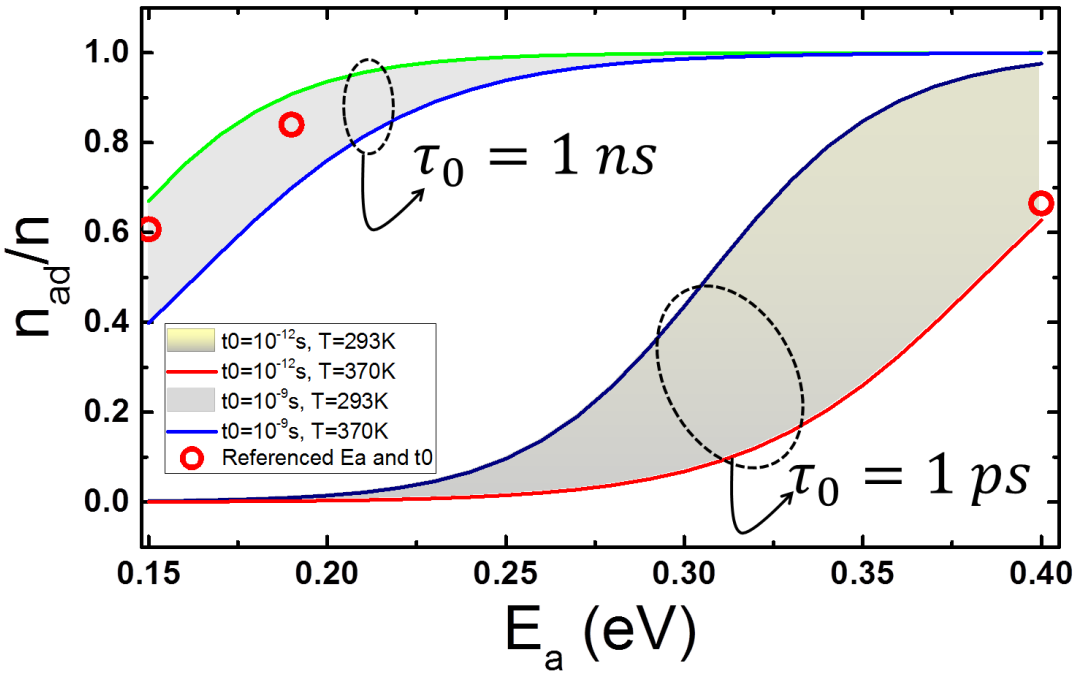

Figure 5-1: The adatoms fraction for the case of room temperature of 293 K (red and blue curves) and T = 370 K (dark blue and green curves) and for $\boldsymbol{\tau_0 = 1\ ps}$ (red and dark blue curves) and $\boldsymbol{\tau_0 = 1\ ns}$ (blue and green curves). The symbols correspond to $\boldsymbol{n_{ad}/n}$ deduced from $\boldsymbol{\tau_0}$ and $\boldsymbol{E_a}$ found references [3], [19] and [20].

Surface	Atoms	E_a (eV)	τ_0	Reference
Uncoated pyrex	Cs	0.53	$1.4 \pm 0.6*10^{-3}$ s	[3]
Dry film OTS pyrex	Cs	0.44	$4.5*10^{-5}$ s	[3]
Sapphire	Cs	0.43±0.01	< 160 µs	[3]
Silica	Cs	0.66	-	[21]
OTS pyrex	^{87}Rb	0.19±0.03	0.53± 0.03 µs	[19]
OTS pyrex	^{87}Rb, 72 ℃	0.15	0.9±0.1 µs	[20]
Paraffin coated pyrex	^{87}Rb, 72 ℃	0.15	1.8±0.2 µs	[20]

Table 5-1: Values of E_a and τ_0 reported in the literature for different atoms and surfaces.

In this chapter, we show another mechanism that is correlated to atom-surface effect by reporting on the observation of sub-Doppler transparencies in a configuration where the transmission spectrum of a single laser beam through Rb-filled HC-PCF exhibits sub-Doppler transparencies. This configuration contrasts from both saturated absorption spectroscopy (SAS) and electromagnetically induced transparency (EIT) configurations. Indeed, while in SAS, a counter-propagating probe beam is required to monitor the pump saturated transition, in our case the observed transparencies donnot rely on two counter-beam scheme. Similarly, in EIT, two lasers are tuned to two transitions of a lambda, ladder or V schemes, while our configuration is observed with a single laser frequency. Furthermore, our experimental and theoretical results indicate that the transparencies results from optical pumping between translational energy levels of the adatoms trapped in the atom-surface potential.

The chapter is structured as follows. Section 5.2 reviews the basics of atom-surface potential with an emphasis on the glass-atom interaction in a hollow-core configuration. We give a qualitative description of the energy level structure of the Rb along the transverse dimension of the fiber-core, and the additional translational energy levels of the adatoms and their shift relative the free flying atoms. Section 5.3 covers the description of the experimental set-up and the sub-Doppler transparencies. Here, we start by reviewing the previous preliminary observation of such sub-Doppler features reported in Bradley doctoral thesis [5] and the different attempts to explain their physical origin. Then, we will present several measurements protocols that have being undertaken to assess how the observed sub-Doppler lines evolve with the magnetic field, the laser power and polarization, the temperature and the surface material. In this work, an emphasis was put on exploring a possible correlation between the observed sub-Doppler transparencies and the atom-surface interaction. We thus confront the experimental results to a theoretical model that calculates the optical pumping between loosely bound translational levels from trapped atoms in a Lennard-Jones-shaped potential. Finally, we discuss the consistency of the observed sub-Doppler lines with the theoretical models and list the future work to undertake for further confirmation of this atom-surface potential related spectroscopy.

5.2 Atom-surface effects

The effect of atom-surface interaction on the atomic transitions has always been of interest in applications such as frequency metrology and in fundamental physics such as the quantum electrodynamics interaction of atom with the electromagnetic vacuum through Casimir force [6]. In recent years, and with the progress made in nano- and micro-photonics, the topic of atom-surface dynamics has regained a renewed and timely attention. For example, long-range atom-surface interaction, such as Casimir-Polder effect [7] is becoming highly relevant for nano- and micro-photonic components like HC-PCF [8], [9], which, as seen in Chapter 4, exhibits a large surface-to-volume and a close vicinity of the atom to the core inner-wall surface.

The atom-surface interaction takes several forms, from an elastic collision whereby an atom bounces back with no change to its quantum state to adsorption whereby the atom is trapped on the surface for a given laps of time. The physical mechanisms entailed in atom-surface are also of different nature, and can be split into two categories-depending on the surface bonds involved: physisorption and chemisorption. In the case of physisorption, the surface bond results from the Van-der-Waals (VdW) force between the atom and the surface, the energy range for such an atom-surface interaction is less than 0.1 eV (*i.e.* 152 THz). In chemisorption, the atoms and the surface substrate create a true chemical bond, thus changing the chemical structure of the surface. Here the required energy level range is between 1 and 10 eV (*i.e.* 1.52 - 15.2 PHz). For our experimental conditions, the atom-surface interaction is of physisorption nature.

5.2.1 Atomic dipole near a flat surface

Near a flat surface, the atom-surface interaction is often presented by Lennard-Jones (LJ) potential. This is often deduced empirically and combines the attractive and repulsive potential in the interaction [10]. One form of LJ potential is the so called 6-12 potential version of Mie potential (*i.e.* with $n = 12$ and $m = 6$) [10]:

$$U_{LJ}{}^{(1)}(r) = 4\epsilon\left[\left(\frac{\sigma}{r}\right)^{n} - \left(\frac{\sigma}{r}\right)^{m}\right] \tag{5-2}$$

Here, the first term accounts for the repulsive potential and the second for the attractive potential. The quantity r is the distance between the atom and the surface. σ is the distance at which the potential is nil, and is also related to position where the potential is minimum and is given $r_{min} = \sigma e^{-\frac{\ln(m)+\ln(n)}{m-n}}$. The black curve in Figure 5-2 shows the shape for the Lennard Jones 12-6 potential. Here we have taken the values reported for rubidium-perfect metal interactions $\epsilon = 58.6\,THz$ and $\sigma = 0.45\,nm$ [11] and multiplied ϵ by $(n^2-1)(n^2+1)^{-1}$ to correct for the fact that the surface is made of silica with a refractive index n. Based on these values one observe that the potential minimum occurs at r_0 ~ 0.5 nm away from the surface and corresponds to a potential depth of 60 THz. Figure 5-2 also illustrates the potential values for different distance ranges from the surface wall. For the 6-12 the potential reaches close to zero values for r > 100 nm, and contrasts with other commonly used VdW potential. Among the most common expressions to represent the atom-surface potential is the one written below [12] :

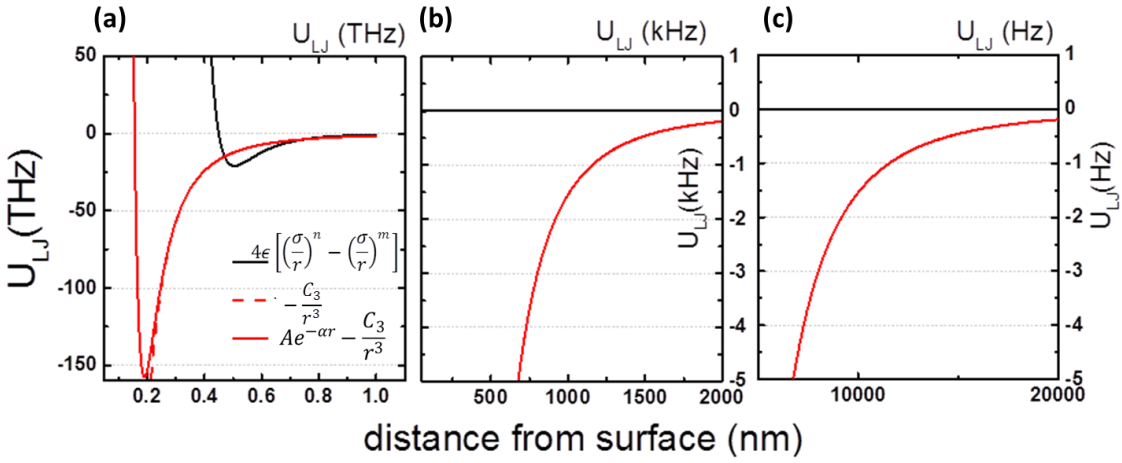

Figure 5-2: Surface-atom potential for the case of Rb ground state and for different ranges of the atom-surface distance. The black curve corresponds to 6-12 type potential (equation 5-1) with the parameters taken from reference [11]. The red curve corresponds to the potential of equation 5-3 with the parameters taken from reference [14].

$$U_{LJ}{}^{(2)}(r) = Ae^{-\alpha r} - \frac{C_3}{r^3} \tag{5-3}$$

Here, the short range (*i.e.* atom-surface distance < 1 nm from the surface wall) repulsion is approximated by a negative exponential function, where the parameters A and α determine the height and range, respectively, of the repulsion. The term $-\frac{C_3}{r^3}$ represents the long-range (> 1 nm) VdW attraction potential. Here, C_3 is the VdW coefficient. In this potential's expression we ignore the Casimir-Polder potential evolution from r^{-3} length scale law to r^{-4}, as it was recently shown that the experimental data fits well with the VdW scale of r^{-3} [13]. The red curve in Fig. 5-2 shows profile of this potential for the values of C_3, A and α being respectively equal 1.53 THz nm^3, 1.6×10^6 THz and 53 nm^{-1}. These value correspond to Rb-silica interaction for the case of the atom ground state [14]. For comparison, the VdW asymptote term of $-\frac{C_3}{r^3}$ is plotted in the red dashed line, and which shows that both expression are very close for r > 1 nm. On the other hand, this potential strongly differs from the 6-12 potential. For example, the depth $U_{LJ}{}^{(2)}(r)$ reaches over 150 THz whilst $U_{LJ}{}^{(1)}(r)$ is only 20 THz deep. Furthermore, the minimum of $U_{LJ}{}^{(2)}(r)$ is around $r_0 \sim 0.2$ nm and is closer that of $U_{LJ}{}^{(1)}(r)$ is ~ 0.5 nm. This example illustrates the difficulty in rigorously determining the exact profile of $U_{LJ}(r)$, especially at short range. Indeed, whilst the long range profile and the VdW coefficient C_3 are sufficiently well documented [13], the potential parameters for atom-surface distances below 1 nm remain very scarce, and a conclusive theoretical model is yet to be developed. This situation casts a large uncertainty on location of the potential minimum and depth as illustrated in Fig.5-2. For the following of this chapter, we take $U_{LJ}{}^{(2)}(r)$ as a representative profile for atom-surface interactions because of its long range accuracy, and we consider the repulsive part of the potential as a qualitative conjecture. Moreover, in considering the case of atom-surface interaction inside HC-PCF, we make the following assumptions. We approximate the core-contour to a flat semi-infinite dielectric surface. This means that we ignore the geometrical factor and the nanometric thickness of the fiber silica web that affects the atom-surface potential [6]. Second, we ignore the surface roughness, which height is typically less than 1 nm [15]. We also ignore local clustering of

atoms or time evolution of the surface due to processes such as adsorption/desorption. Finally, we ignore the dispersive nature of C_3 and deduce its value from atom-perfect mirror ${C_3}^{(mirror)}$ using the following identity:

$$C_3 = \frac{n^2-1}{n^2+1} {C_3}^{(mirror)}. \tag{5-4}$$

Using the above assumptions, the following section addresses the additional potentials that rubidium atoms confined in the core of a HC-PCF experience.

5.2.2 Atomic dipole inside a hollow-core PCF

In the case of a vapor filled HC-PCF, the atoms are surrounded by the core inner-wall. The surface of the latter can be made by either pure silica glass or by a layer of coating. In our case, we investigated two coating materials; PDMS and sol-gel based ceramic (see Chapter 3). Furthermore, in a typical atom-optical configuration with HC-PCF, the atoms are excited with a guided laser beam, which mode is HE_{11}. Consequently, and ignoring surface roughness or approximating the core contour to that of a cylinder, the total potential the atoms experience can be written in the following form:

$$U_{tot}(r) = U_{light}(r) + {U_{LJ}}^{(2)}(r) \tag{5-5}$$

The first term $U_{light}(r)$ in the right hand side of the equation corresponds to optical dipole potential, or Stark shift. Near a resonance with an angular frequency ω_0, the expression of the optical dipole potential can be written as $U_{light}(r) = \frac{\pi c^2 \Gamma}{2 {\omega_0}^3} \wp \frac{I(r)}{\Delta}$. Here, the quantity $\wp$ is a function dependent of the light polarization and the transition states, Δ is the frequency detuning of the laser frequency from that of the considered transition. In the case of rubidium D2 line, it is more practical to deduce $U_{light}(r)$ from the values of the static scalar polarizability α_0 and tensor polarizability α_2 using the expressions $U_{ligh}(r) = \frac{1}{2} E^2 \left(\alpha_0 - \alpha_2 \mathrm{F}(J)\right)$, and where $\mathrm{F}(J)$ is a function of the electronic angular moment J. A quick calculation of $U_{light}(r)$ with our typical experimental parameters (fiber core

diameters and laser powers) shows that the induced frequency shift is well below Hz-level. Consequently, we will ignore this effect in our consideration, and limiting thus the additional potential to the in-fiber atoms to that of the atom-surface one.

In the case of an atom inside the fiber core, it will see a radial potential from both any opposite surfaces of the fiber core, which is written below:

$$U_{tot}(r) \approx {U_{LJ}}^{(2)}(r) + {U_{LJ}}^{(2)}(D_f - r). \tag{5-6}$$

Figure 5-3 shows this potential profile along a radial axis of a 30 μm radius HC-PCF with a cylindrical core-contour and for ground and excited states of the D2 transition of ^{85}Rb. Examination of the potential at the center and near wall of the fiber core shows that frequency shift of both states is negligible for atoms which distance from the wall is larger than 5 μm. For these atoms the potential depth and the transition shift remain less than 100 Hz.

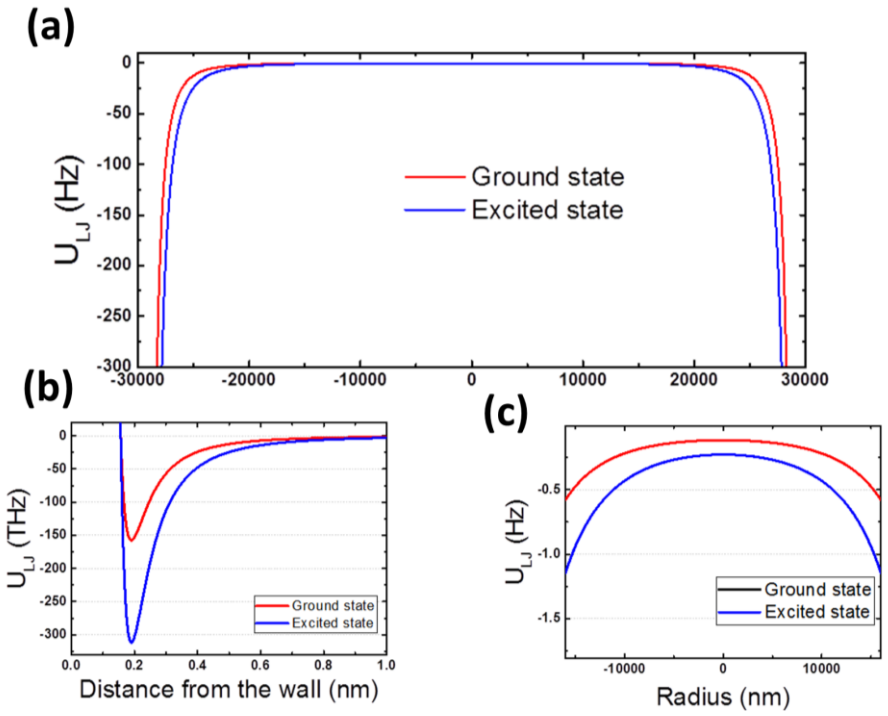

Figure 5-3: Surface-atom potential profile as experienced by a Rb atomic inside and a 60 μm diameter core of HC-PCF for the D2 transition ground (red curve) and excited state (blue curve).

5.3 Experimental results of single beam generated sub-Doppler features

5.3.1 Historical context of the observation of sub-Doppler line in HC-PCF excited with a single laser beam.

Figure 5-4 shows a summary of the early observation sub-Doppler transparencies in HC-PCF excited with a single laser beam [5]. The results show two transparency lines observed in Rb vapour confined in Kagome HC-PCF within the Doppler broadened ^{85}Rb $^5S_{1/2}$ F=3→$^5P_{3/2}$ F'=2,3,4 absorption line. The lines exhibit a height in the range of 1-4%, their frequency spacing ranges between 30 and 40 MHz (Fig. 5-4(b)) and present comparable linewidths, with a FWHM in the range of 15 and 25 MHz (Fig. 5-4(c)). Comparison of the properties of these lines with existing work on SAS in Rb vapor cells demonstrates remarkable resemblances. However , the occurrence of such features are unusual as only a single circularly polarized beam from a frequency scanned ECDL is used to generate them, which contrasts with those generated via EIT, CPT or SAS, and in which pump and probe laser beam configuration is required. Consequently, the generated sub-Doppler line in this configuration indicates a new physical mechanism. Two theoretical models attempting to explain this occurrence of such spectral lines have been investigated. The first one relies on the possibility of a non-uniform distribution of Rb vapor along the propagation axis of the HC-PCF. The atomic vapor distribution along the HC-PCF is most likely to be parabolic because of the molecular free flow loading from the open fiber ends, and exhibit localized Rb clusters [16]. This non uniform atom distribution will have an associated variation in refractive index along the fiber length. Such a variation in index gives rise to a possibly sufficiently strong scattering signal that couples back to the fiber core in both directions. This in turn creates an SAS type pump probe laser beam configuration. Such a possibility was not conclusive because of the too small index contrast that was found to enable measurable signal from the fiber core back-coupled light from the scattering. The second theoretical model which is being worked on is based upon a Faraday rotation induced Bragg grating in the Rb vapour confined in the Kagome HC-

PCF. In Kagome HC-PCF the birefringence beat length is on the order of several meters, estimated from theoretical modelling. This model stems from the experimental observation of a modulation with applied magnetic field in a transmitted signal. However, the modulation depth was too small to draw any conclusive statement.

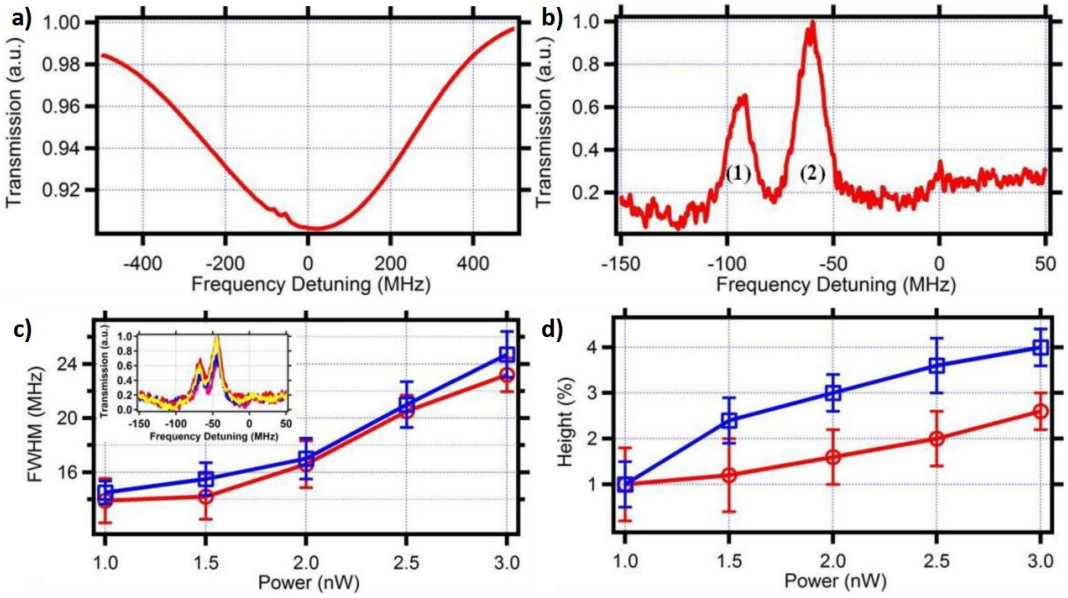

Figure 5-4: The sub-Doppler features are generated by a circular polarization laser beam in Rb-filled capillary. The magnetic field is 5.5 G and the beam power is ~ 2000 µW with beam waist of 1.5 mm. The Doppler feature is at ^{85}Rb, F=3 D2 absorption line. (From[5])

In order to further investigate the origin of these spectral lines, we precede with a more systematic study by investigating the sub-Doppler transparency features as a function of laser power, applied magnetic field and input polarization in Rb filled in HC-PCF with different surface materials, with an attention to find out any correlation with atom-surface interactions.

In the following section, we present the experimental observation of single laser beam generated sub-Doppler transparencies in Rb-filled capillary and Kagome HC-PCFs. The sub-Doppler transparencies of F=3 → F' absorption line evolution with input laser power and polarization and the magnetic field strength were undertaken. In each measurement, the polarization of the transmitted laser is considered. Finally, we compare these sub-Doppler lines for different temperature and different surface materials.

5.3.2 Sample Preparation and Experimental setup

Figure 5-5 shows the schematic of the experimental set-up. A single laser beam, emitted from an fine-tunable external cavity diode laser (ECDL) at wavelengths near 780 nm and whose polarization is controlled by a quarter waveplate, is coupled to a high vacuum chamber harbored HC-PCF. The laser power is typically in the range micro-Watts. The fiber transmitted laser beam is monitored by a homemade polarimeter. The polarimeter consists of a PBS, two auto-balanced photodetectors and an electronic operational amplifier. The latter provides four signals: two signals, $P_{\parallel}$ and $P_{\perp}$, corresponding the two orthogonally polarized laser beams from the PBS, one signal proportional to the total fiber output power, $P_{\parallel}+P_{\perp}$, and a last signal corresponding to the ellipticity of the fiber output laser, $P_{\parallel} - P_{\perp}$.

The Rb filled HC-PCF under-test is one from a set of 12 fibers. These fibers are 8 cm long mounted in the holes of glass tube with a honey comb structure. For each fiber deign type, we have three samples, two of which we coated their inner core surface with PDMS using the process described in Chapter 3.

Once the fibers inserted into the vacuum chamber, we release the Rb so to load the fibers via diffusion during ~ 4 weeks whilst an Ion pump evacuating continuously. Once the atom density achieves ~ 10^9 cm^{-3} we start the experiments. A longitudinal magnetic field, which can be varied to a maximum of 65 G, is applied to Rb-filled HC-PCF by coiling around the UHV chamber with solenoid coil.

For reference and comparison, part of the laser beam is concurrently sent to a macroscopic cell and its transmission spectrum is continuously monitored. Furthermore, the transmission of the laser through a ~ 600 μm hole of the honey combs glass tube was also measured.

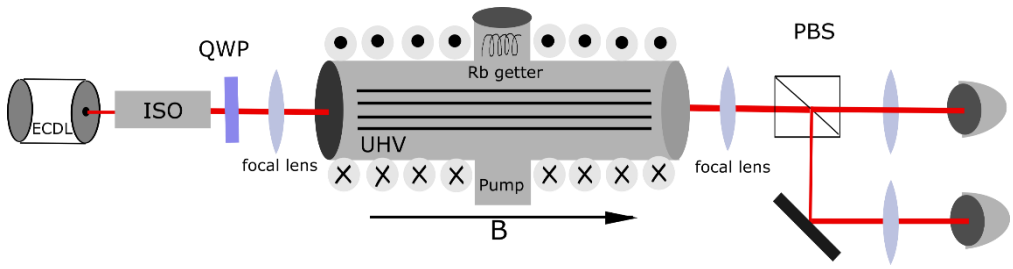

Figure 5-5: Experimental setup for sing laser beam generated sub-Doppler transparencies. ISO: isolator, ECDL: external cavity diode laser, QWP: quarter waveplate, PBS: polarization beam splitter.

5.3.3 Experimental results

Figure 5-6 shows the typical recorded ~ 6 GHz span spectra by the polarimeter when it is impinged by a HC-PCF output laser whose frequency is swept near the absorption spectrum for ^{85}Rb and ^{87}Rb D2 lines. The HC-PCF is a Kagome HC-PCF with core diameter D_{in}/D_{out} = 61.7 μm/73.3 μm, and a curvature *b* parameter of 0.83. The atom density was measured to be ~ 8×10^{10} /cm^3. The fiber corresponds to the HC-PCF labeled fiber #3 in chapter 3. The guided laser is circularly polarized and has a power of 150 μW, and with no the magnetic field (here, the wiring has been unplugged to avoid any residual field).

The spectra correspond to the transmission from a macroscopic reference cell (Fig. 5-6(a)), and to the different polarimeter channels for three types of fiber core inner-surface. The red curves correspond to uncoated silica wall surface, the blue curves to PDMS coated core inner wall and the green curves to the ceramic (sol-gel) coated inner surface.

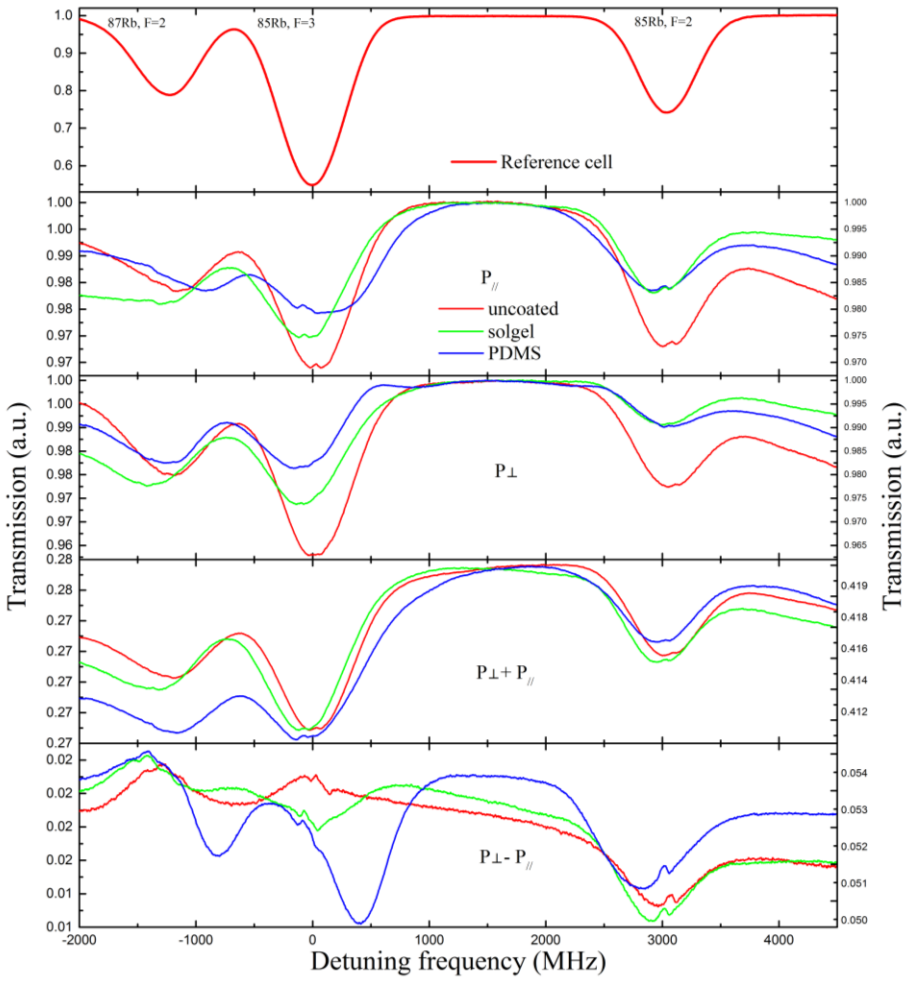

Figure 5-6: Typical spectra. Absorption spectrum from a macroscopic cell (reference cell) (a). The fiber transmitted spectrum of the polarized power $\boldsymbol{P}_{\parallel}$ along one of the PBS axis (b), of the polarized power $\boldsymbol{P}_{\perp}$ along the second PBS axis (c), of total power $\boldsymbol{P}_{\parallel} + \boldsymbol{P}_{\perp}$ ((c), and of the difference $\boldsymbol{P}_{\parallel} - \boldsymbol{P}_{\perp}$. The spectra were obtained from the same HC-PCF but with different core inner-surface. The red curves correspond to an uncoated silica inner-surface, the green curves to sol-gel ceramic coated surface and the blue curves to the PDMS coated surface. The spectra were recorded with 0 G DC magnetic field, 150 μW laser power. The laser is circularly polarized, and the temperature was 100 Celsius.

In accordance with the results reported in [5], the spectra of $P_{\parallel}+P_{\perp}$ (Fig. 5-6(d)), $P_{\parallel}$ (Fig. 5-6(b)), and $P_{\perp}$(Fig. 5-6(c)), all show in the Doppler broaden absorption lines of the D2 transition, sub-Doppler lines (SDL), despite the magnetic field was set to 0 G. This means that the observed SDL are not related to the magnetic field induced light polarization modulation [17]. The SDL were observed for the three types of surface materials. Furthermore, the spectra show some differences. The first difference is spectral

location of the ^{85}Rb D2 absorption lines, where it is easy to note a frequency shift between the absorption lines for the different fiber-core surfaces. We recall that the 3 fibers are identical and the spectra obtained using the same laser parameters, thus this shift is surface material related. The difference in spectra between the different fiber-core surfaces is more apparent in the $P_{\parallel} - P_{\perp}$spectrum. The latter results from the atom related optical rotation effect as the fiber birefringence is negligible (the calculated birefringence for this fiber was found to be over several meters). A further analysis of the effect of the surface on the SDL is provided in one of the flowing sections below.

In the following section we explore their dependence with the input laser polarization.

5.3.3.1 Input laser Polarization dependence

Figures 5-7(a) and (b), show the spectra of $P_{\parallel}$ and $P_{\perp}$ when the input laser polarization is varied. This was achieved by rotating a quarter wave plate from 0˚ to 90˚ (In our convention, the 0˚ corresponds to q circular polarization entering the fiber, and thus the 90° correspond to the circular polarization with the opposite handedness as the one at 0°). The rest of the experimental conditions are the same as for the one listed above. Except that the DC magnetic field was set ~ 45 Gauss.

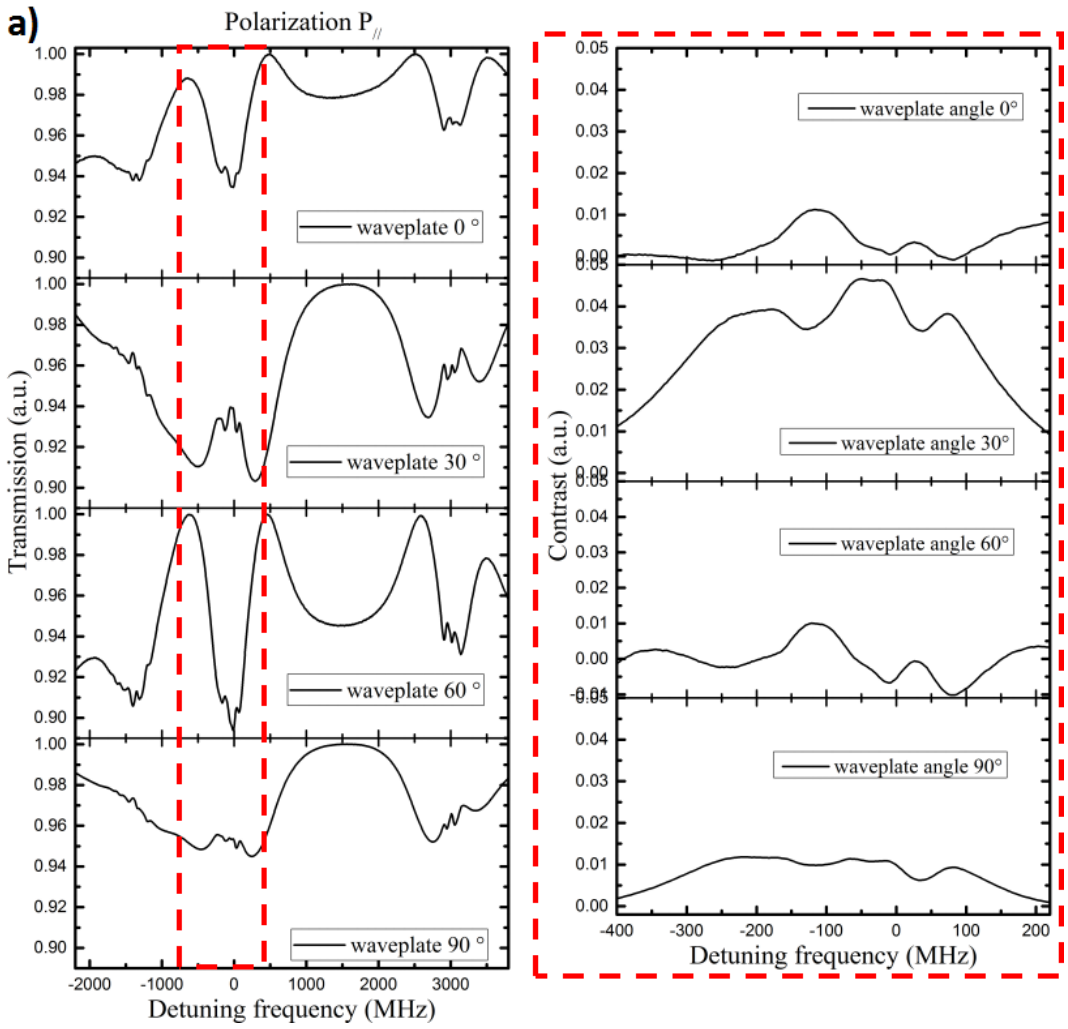

Figure 5-7: (a) $P_{//}$ spectral evolution of ^{85}Rb-filled HC-PCF D2 absorption lines (left column), and a zoom in at the SDL of the F=3→F' Doppler line. Here, the DC magnetic field is 45 G, beam power ~ 150 μW, temperature: 100 ˚C.

The results show that for both polarization axes, the SDL strongly depend on the input polarization in their spectral structure and location. Depending on the ellipticity of the input laser, the SDL show three comparable peaks or one dominant peak. Figure 5-8 summarizes the frequency shift and its height with the input laser polarization for both PBD polarization output ports.

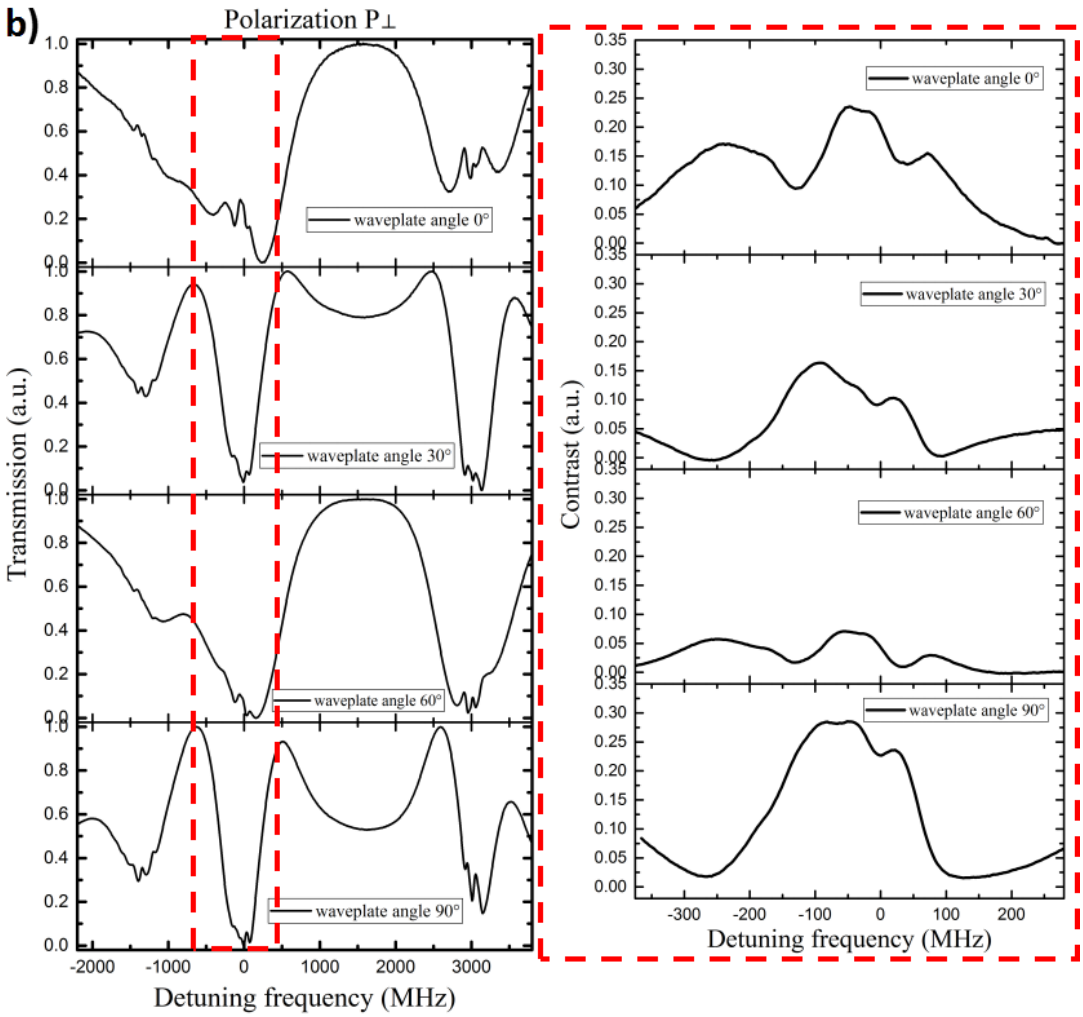

Figure 5-7: (b) $P_{\perp}$ spectral evolution of ^{85} Rb-filled HC-PCF D2 absorption lines (left column), and a zoom in at the SDL of the F=3→F' Doppler line. Here, the DC magnetic field is 45 G, beam power ~ 150 μW, temperature: 100 ˚C.

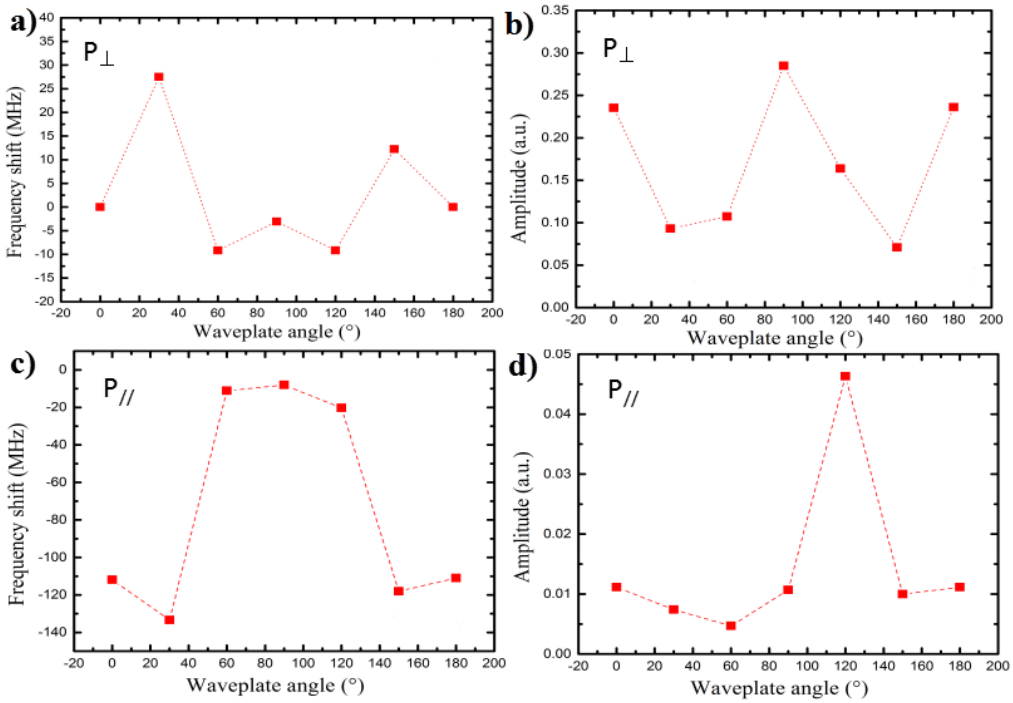

Figure 5-8: Frequency shifts and variations of amplitude of sub-Doppler feature on ^{85}Rb, F=3 line, as the waveplate angle is varying. (a) & (b) for the polarization component $P_{\perp}$ and (c) & (d) for the polarization component $P_{//}$.

In the next section, the SDL dependence on the input beam operational power is explored.

5.3.3.2 Input laser Power dependence

As shown in Figure 5-9(a) and (b), the absorption spectra of recorded polarization components $P_{\parallel}$ and $P_{\perp}$ is varied as the input beam power increasing. The input beam power is operated from 50 μW to 300 μW by rotating a variable neutral density filter (Thorlabs NDC-100). Notice two points here: One is the sub-Doppler features cannot be distinguished from Doppler lines when the input operational beam is < 10 μW. Second one is the coupling efficiency is ~ 17 % by comparing the measured output/input power levels. Actually, the beam is traversed several optical components (one focal lens, one reflective metal mirror, viewport of vacuum chamber) and then is coupled into the Rb-loaded HC-

PCFs laying in vacuum chamber. The coupling from out of vacuum chamber to in-vacuum HC-PCF is challenge to get high coupling efficiency even the guiding of single mode is confirmed by view the near field at the output through a camera (Coherent LaserCam-HR). The rest of the experimental conditions are the same as the above experiments.

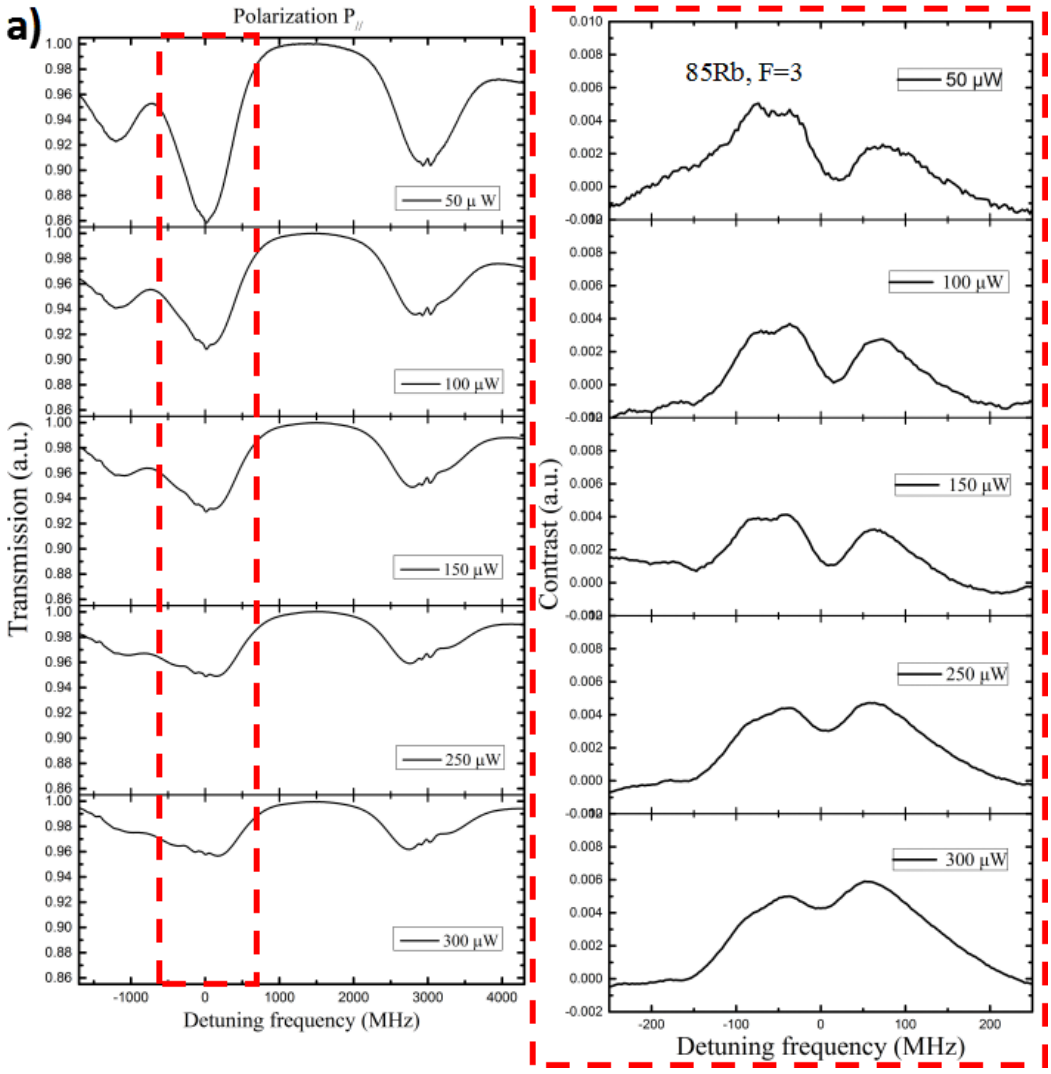

Figure 5-9: (a) Polarization component $P_{//}$ spectral evolution of ^{85}Rb-filled HC-PCF D2 absorption lines (left column), and a zoom in at the SDL of the F=3→ F' Doppler line. Here, the DC magnetic field is 45 G, beam power is varied from 50 μW to 300 μW, temperature: 100 ˚C.

The figures show that for both polarization components, the contrasts of the Doppler absorption lines are dropping as the operational power increasing, and the sub-Doppler features are varying as well.

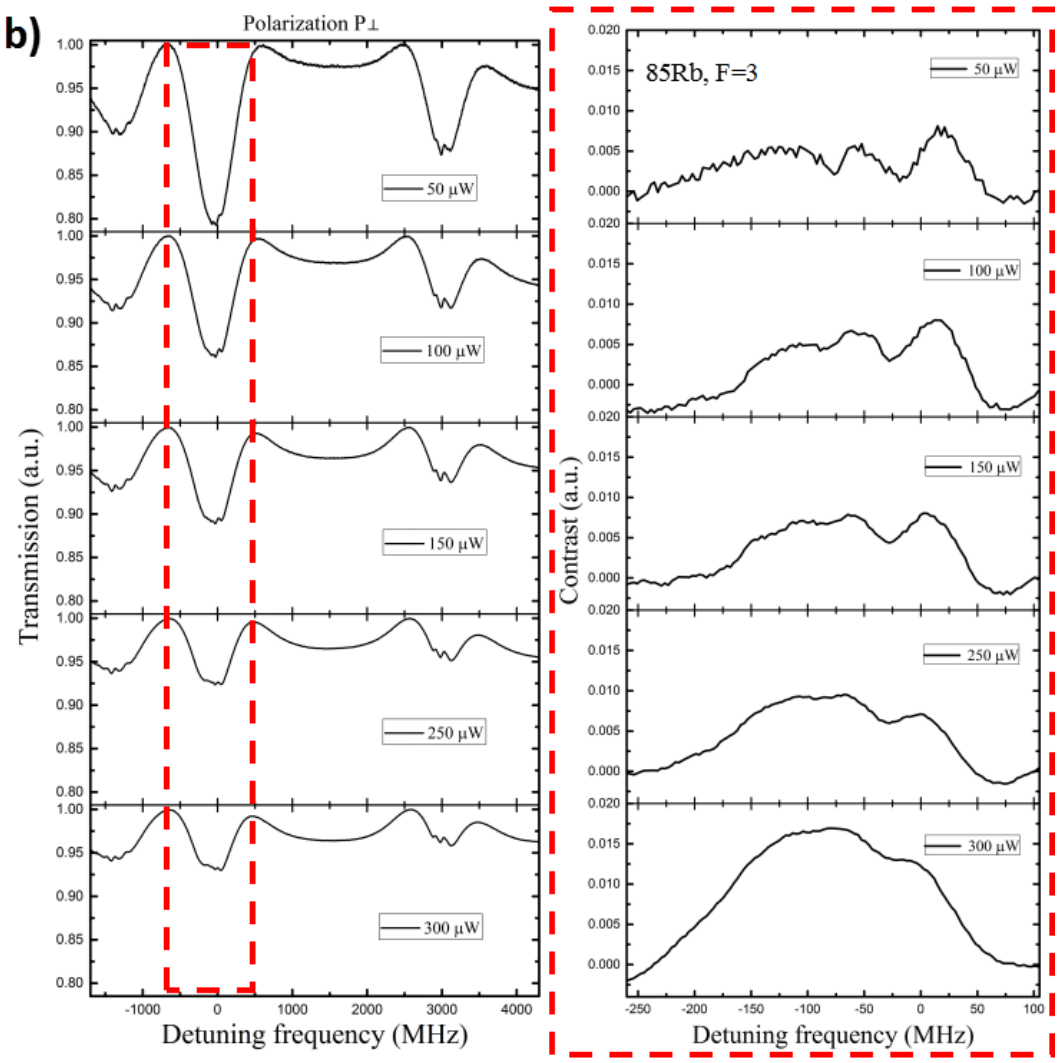

Figure 5-9: (b) Polarization component $P_{\perp}$ spectral evolution of ^{85}Rb-filled HC-PCF D2 absorption lines (left column), and a zoom in at the SDL of the F=3 → F' Doppler line. Here, the DC magnetic field is 45 G, beam power is varied from 50 µW to 300 µW, temperature: 100 ˚C.

Examples of sub-Doppler features of ^{85}Rb, F=3 → F' Doppler line are shown in right column of Fig.5-9(a) & (b). The increased beam power results on the enhancement of amplitude and frequency shifts of SNL. The summarized contrasts and frequency shifts of one of SDL (right one in figures) are plotted in Figure 5-10 with the beam power varying, for different polarization components $P_{\perp}$ (Fig. 5-10(a) & (b)) and Fig. 5-10(c) & (d) for component $P_{//}$. The frequency shifts of SDL for $P_{\perp}$ are changed from ~ 3 MHz to ~ 12 MHz when the beam power is increased from 100 µW to 300 µW (in Fig. 5-10(a)). And

the frequency shifts of SDL are inversely changed from ~ 6 MHz to ~24 MHz for polarization $P_{//}$ with the same power operational range. The frequency shift of 0MHz corresponds to the frequency center at 50 μW operational power.

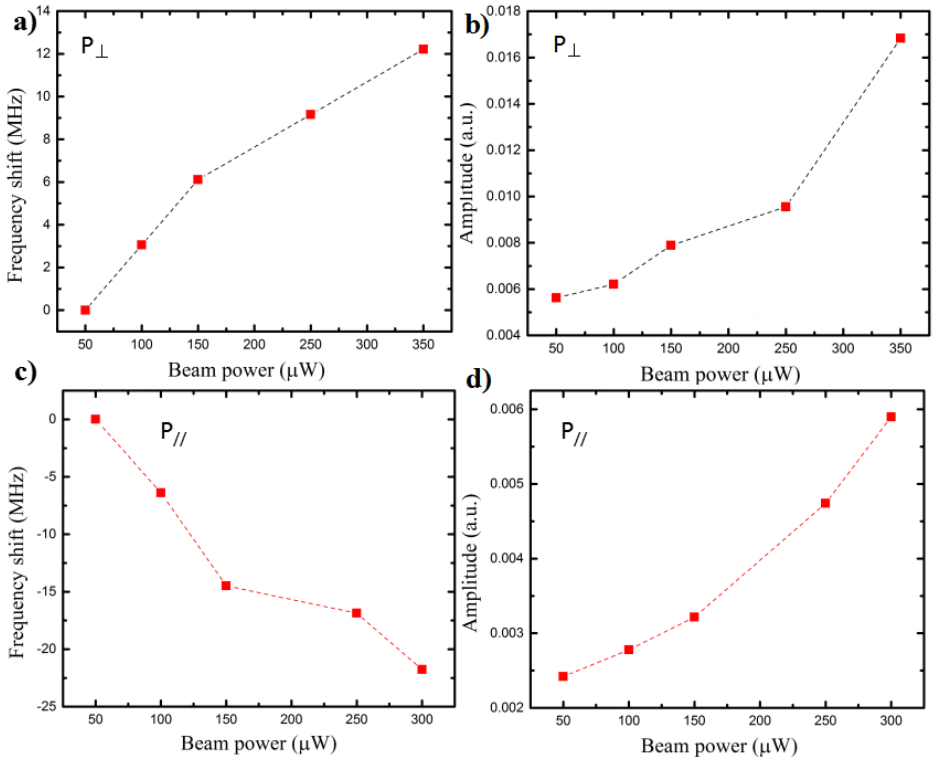

Figure 5-10: Show the frequency shifts and the enhancement of amplitudes of SDL on ^{85}Rb, F=3 line, as the operational power increasing. (a) & (b) for the polarization component $P_{\perp}$ and (c) & (d) for component $P_{//}$.

More investigations of magnetic field dependence for SDL are shown in the following section.

5.3.3.3 DC magnetic field dependence

Furthermore, the DC magnetic field dependence of SDL are investigated and the results are plotted in Figure 5-11(a) & (b). The magnetic field varies from 0 Gauss to 45 Gauss by changing the applied current through the solenoid coil which the calibration of the corresponded Ampere-Gauss has been done before the coil mounted around the

vacuum cell. Otherwise, the negative sign in figures for magnetic force means the direction of magnetic field is counter-propagated with the laser beam. Other experimental parameters such as beam polarization, beam power and temperature are same as the previous experiments.

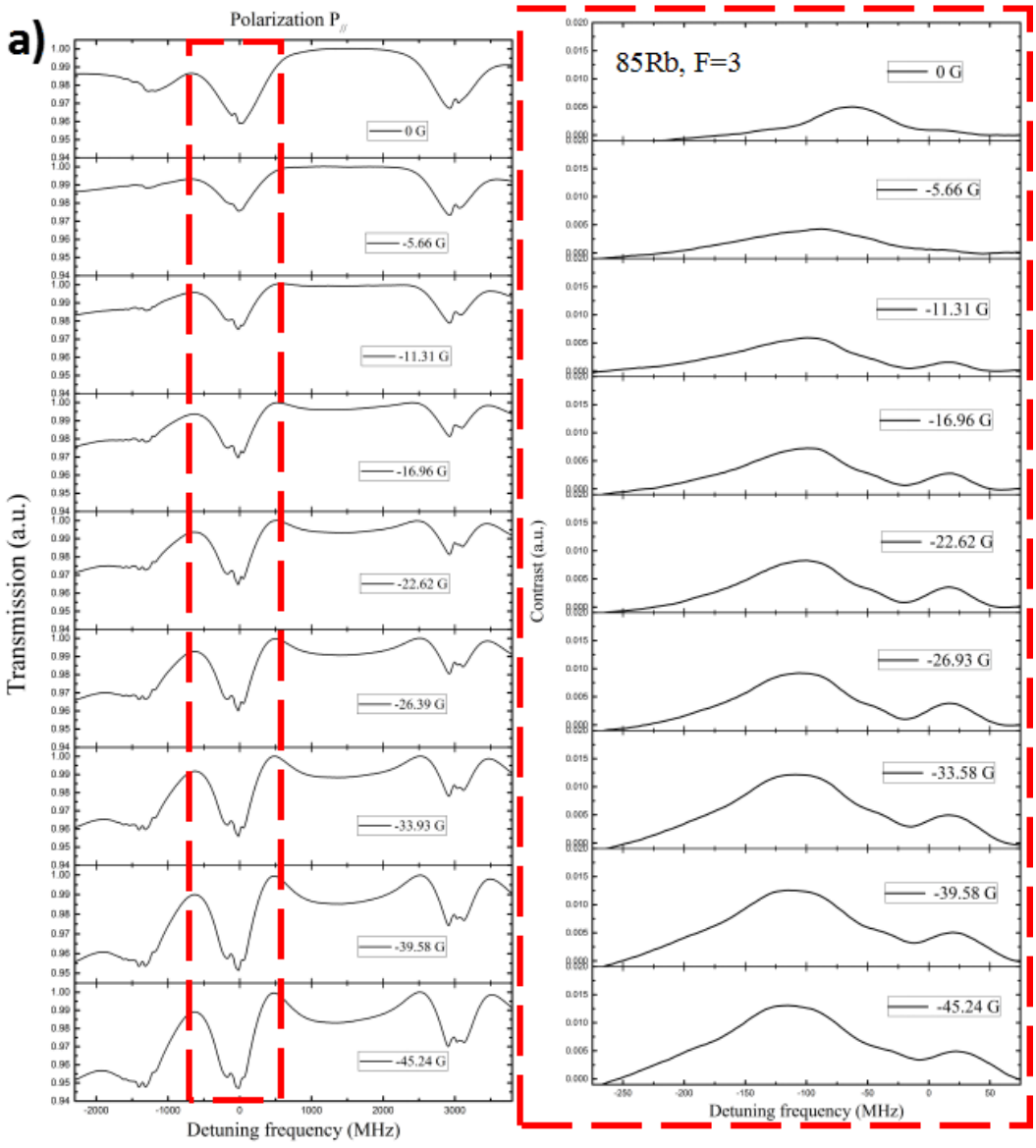

Figure 5-11: (a) Polarization component $P_{//}$ spectral evolution of ^{85}Rb-filled HC-PCF D2 absorption lines (left column), and a zoom in at the SDL of the F=3→ F' Doppler line as the magnetic field increasing. Here, the magnetic field varies from 0 Gauss to 45 Gauss, laser beam is circular polarization with 150 μW operational power, temperature: 100 ˚C.

For both polarization components, the contrasts of the Doppler absorption lines are increasing as the magnetic force augmenting except with the 0 G magnetic field (Figure 5-11a) &b)). The figures also show the related SDL highly depends on the magnetic force in the frequency shift and amplitude. More details of SDL on magnetic field dependency are plotted in Fig. 5-12.

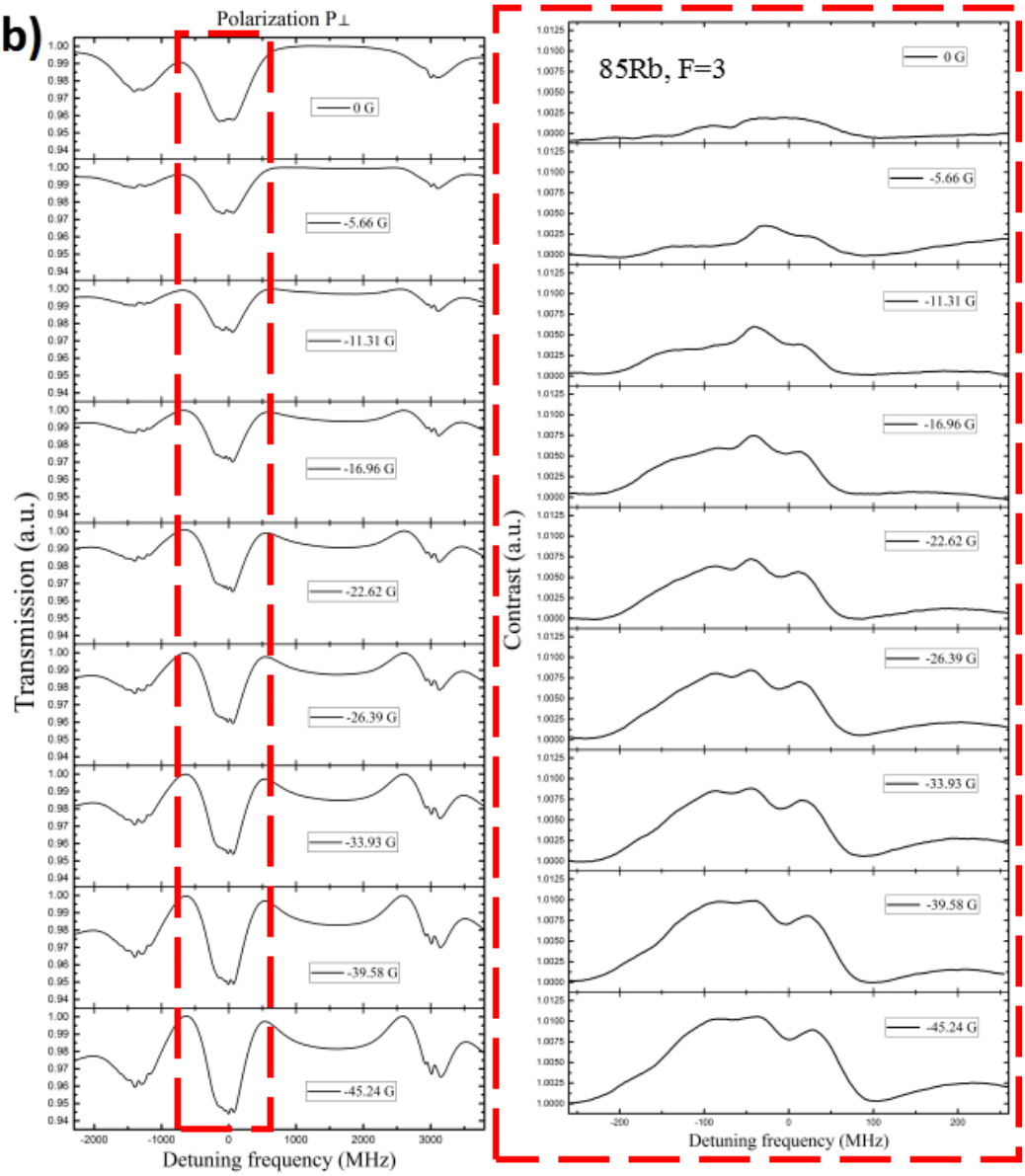

Figure 5-11: (b) Polarization component $P_{\perp}$ spectral evolution of ^{85}Rb-filled HC-PCF D2 absorption lines (left column), and a zoom in at the SDL of the F=3→ F' Doppler line as the magnetic field increasing. Here, the magnetic field varies from 0 Gauss to 45 Gauss, laser beam is circular polarization with 150 μW operational power, temperature: 100 ˚C.

As shown in right column of Figure 5-12, the sub-Doppler features of ^{85}Rb, F=3 → F' have frequency shifts of 12 MHz in maximum for polarization axe $P_{\perp}$ (fig.5-12(b)), and a range of ~ 27 MHz to 58 MHz when the magnetic field changed from 5 G to 45G (fig.5-

12(d)). The amplitudes of SDL are quasi-linearly increasing for both polarization axes as the magnetic field augmenting. Furthermore, there is no Zeeman splitting appeared when applying the magnetic field.

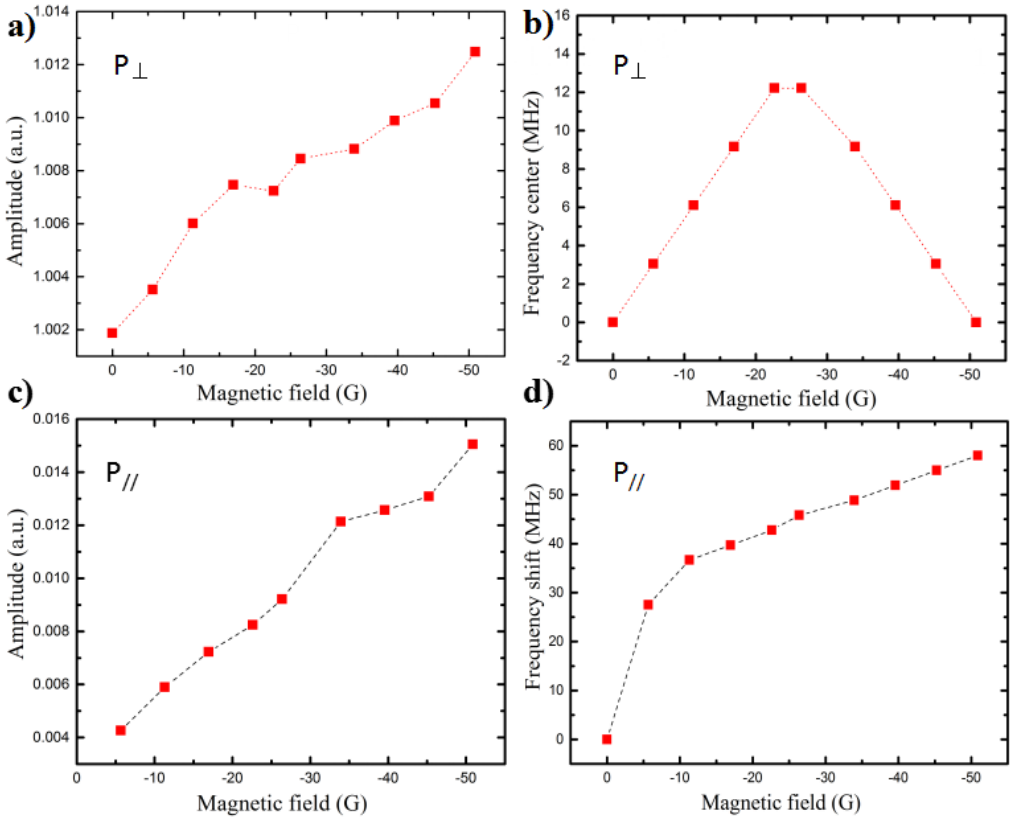

Figure 5-12: Show the frequency shifts and the enhancement of amplitudes of SDL on ^{85}Rb, F=3 line, as the magnetic field increasing. (a) & (b) for the polarization component $P_{\perp}$ and (c) & (d) for component $P_{//}$.

Above all, the investigations focused on with one direction of magnetic field which negative sign is the counter-propagated direction with the laser beam, and the positive sign is the co-propagated direction along the fiber axis. In the following, we also give the comparison of SDL spectra between two contrary directions of magnetic field. Figure 5-13 show the Doppler absorption lines (in a) & b)) and the SDLs (in c)-h)) for polarization component $P_{//}$ as the magnetic field positive or negative increasing. All spectra in left column show the variations as the positive magnetic field changing, and the spectra in right column are for the negative magnetic field. In the first row of Figure 5-13 clearly show

main phenomena of the Doppler narrowing (a)) and broadening (b)) which results from the magnetic field increasing.

In parallel, the contrasts of resident SDL of all Doppler lines are dropping as the positive magnetic field increasing (in left column), and are enhanced as the negative magnetic field augmenting (in right column). Meanwhile, the frequency shifts of SDL are contrary with different magnetic field directions, blue shifts for positive magnetic field and red shifts for negative field. Otherwise, we observed the same phenomena as previous section shown that there is no Zeeman splitting between 0 G magnetic field and applied magnetic field. More observations of frequency shifts on different surface materials and with different temperatures are presented soon.

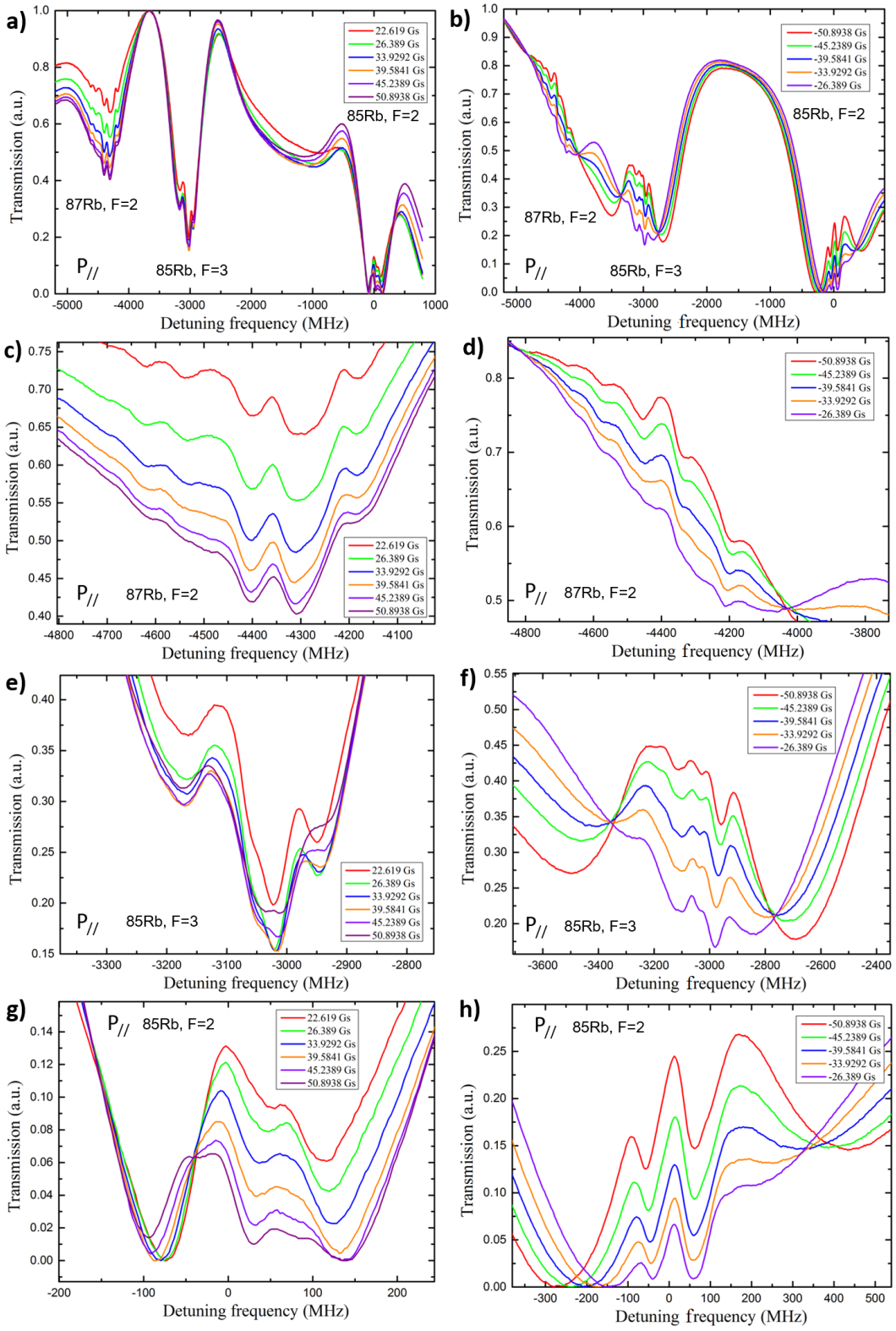

Figure 5-13: Magnetic field dependence of SDL with different magnetic field directions. Spectra in left column are the variations of absorption lines with positive magnetic field, b) with negative magnetic field. And the residential SDLs in the Doppler lines ^{87}Rb, F=2 c) & d), ^{85}Rb, F=3 e) & f), ^{85}Rb, F=2 g) & h). All spectra are the polarization component $P_{//}$ evolution.

5.3.4 Surface material effect and temperature effect on the sub-Doppler lines

Here, the guiding samples for surface effect investigations are uncoated and sol-gel Kagome HC-PCF of fiber #3. The guiding laser is a circular polarization beam with operational power 200 μW. The applied magnetic field is ~ 25G at temperature 100 Celsius. Figure 5-14a) show the sub-Doppler features of ^{85}Rb, F=2 Doppler line in different coated Kagome HC-PCFs, blue curve is sol-gel coated fiber and red curve is uncoated fiber. The results show the frequency shift for different inner wall surface. The measured shift between ceramic coated fiber and the uncoated fiber was found to be ~29.5 MHz in these experimental conditions.

The temperature effect on the sub-Doppler lines are shown in Figure 5-14b). Blue curve is the SNL evolution at the temperature 37 Celsius, red curve is the SDL spectra at the temperature of 100 Celsius. Mention here, the temperature 37 Celsius is different from room temperature due to the supplementary heat from magnetic coil. Clearly observed the frequency shift between different temperature conditions.

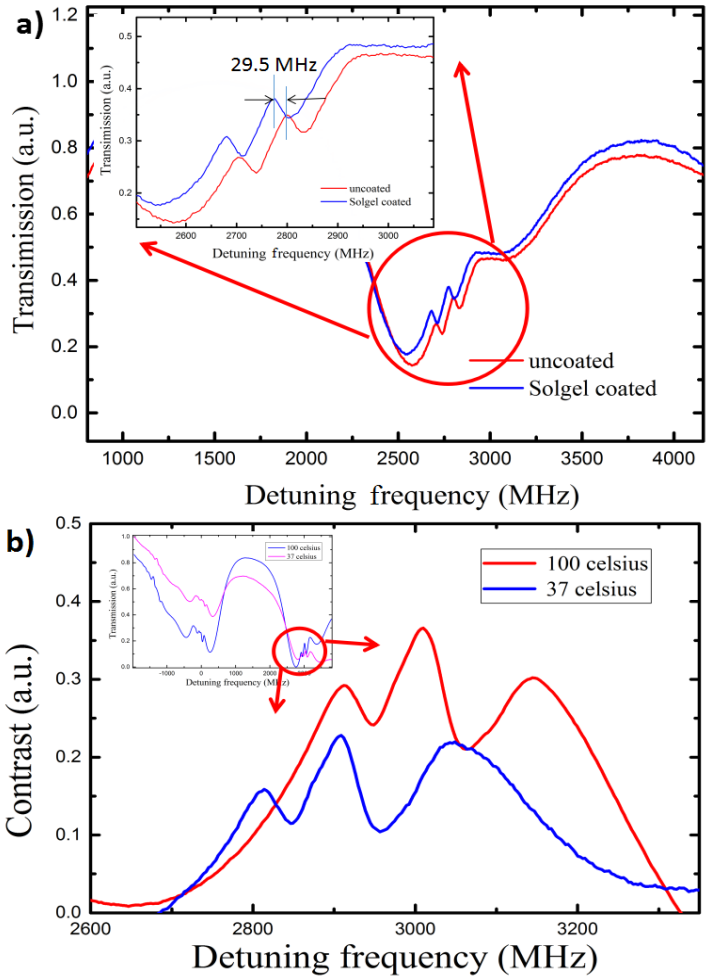

Figure 5-14: Show the evolutions of SDL on different surface materials (a), and with different temperatures (b).

5.4 Optical pumping from adsorbed atoms

In this section, we explore a possible model to explain the observed SDL. The model entails the specific atom-surface dynamic in HC-PCF described in Chapter 4, and the above observed correlation between the surface material and the spectral locations of the SDL. According to this model, we claim that the sub-Doppler lines result from optical pumping between high-order translational states of Rb atoms trapped in the atom-surface VdW potential described in equation 5-3 (see Section 5.2).

Figure 5-15(a) shows schematically the energy structure of Rb atoms near the surface that is produced by the VdW interaction between the atoms and the fiber-core inner surface. We have seen in Section 5.2 that the minima of these potentials occur at a distance from the surface of less than 1 nm, and that potential depth is extremely deep (~100 THz level) at this short range. Given our experimental conditions, the atoms at this short range are not relevant. Indeed, the possible dipole transitions between the associated vibrational states are far shifted from our operational spectral range. Secondly, the light at this distance from the surface strongly drop compared to that at the core center (typically of one consider on the HE_{11} fiber core mode, the fractional power near the core inner surface is less than 10^{-5}).

However, if one consider the high order weakly-bounded vibrational states, their frequency spacing and shift from the free atom frequency can range between a few 100s of MHz and 10s of MHz [18], is qualitatively consistent with our experimental values. Secondly, the wavefuntions of these trapped atoms exhibits a spatial extent as large as a few 100s of nanometers [18], which renders the cross section between these atoms and the guided laser field no longer negligible.

Using the formalism of Fam Le Kien et al. [18] and their potential parameters[14] we calculated the eigenfrequency of these states. Figure 5-15(b) shows the energy levels of the atom translational states for both the ground state $|^5S_{1/2}\, F = 3, \nu s\rangle$ and the excited state $|^5P_{3/2}F' = 2,3,\ \nu' p\rangle$ of ^{85}Rb atoms in the case of the surface is made uncoated silica glass material, and for translational state orders ν and ν' between 275 and 280. Using the results of [18] (Fig.5-2) , the spatial extent of these atomic translational states ranges between 50-100nm.

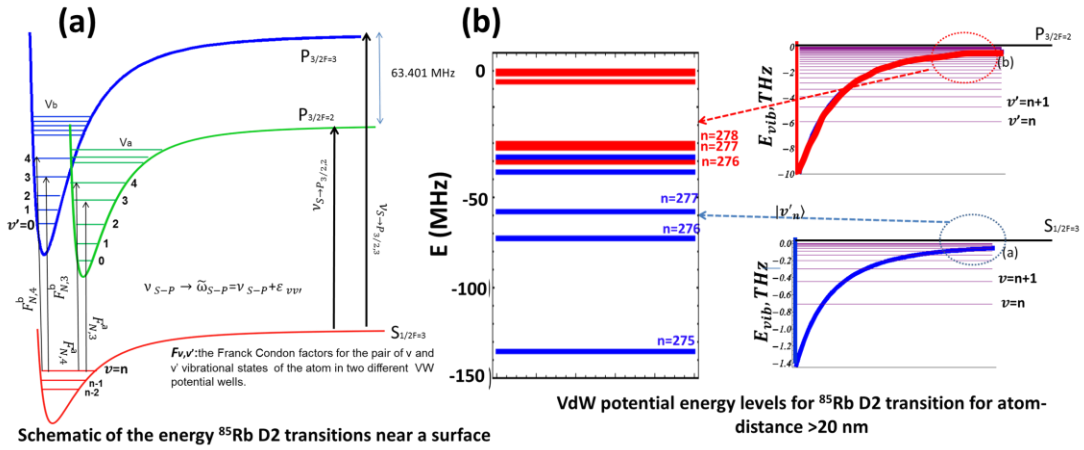

Figure 5-15: (a) Schematic representation of the energy level of VdW potential for Rb atoms at the surface for the D2 line transition, showing the atom-wall interaction mediated energy exchange between the different vibrational levels of the atom in the ground state and the excited state of ^{85}Rb D2 transitions. (b) Calculated VdW potential vibrational states energy levels and ranges for orders *n* between 275 and 280.

In order to gather further evidence on the origin of the observed SDL, we have calculated the laser frequency dependence of normalized pumping rate of the double transition $|^5S_{1/2}\ F\ =\ 3,\nu\rangle \rightarrow |^5P_{3/2}\ F'=2,3,\nu'\rangle \rightarrow |^5S_{1/2}\ F\ =\ 3,\nu''\rangle$ for several values of r_0-the distance of the potential minimum from the surface. Here, we considered the weakly-bound vibrational states $|\nu\rangle$ such that $|\varepsilon_{free}-\varepsilon_\nu|<1$ GHz. with ε_{free} being state energy of the unbound free flying atom, and applied the Born-Oppenheimer approximation to deduce the rate of transition $|SF,\nu\rangle \rightarrow |PF',\nu'\rangle$.

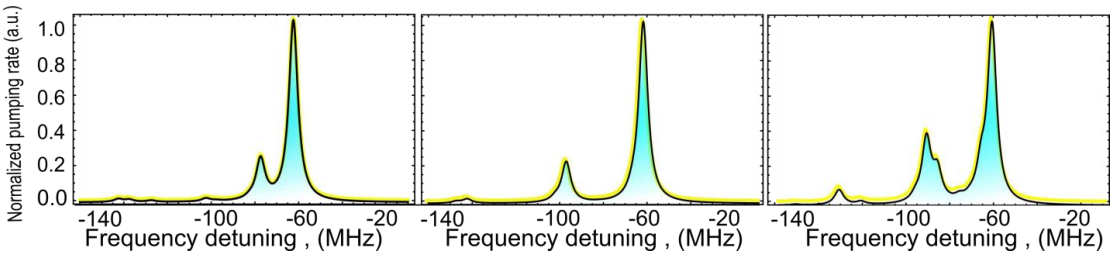

Figure 5-16: The laser frequency dependence of normalized pumping rate $|^5S_{1/2}\, F = 3,\nu s\rangle \rightarrow |^5P_{3/2}\, F'=2,3,\nu p\rangle \rightarrow |^5S_{1/2}\, F = 3,\nu s'\rangle$ for several values of parameter r_0. Left: r_0=0.2 nm, center: r_0=0.6 nm, right: r_0=1.4 nm.

Figure 5-16 plots the results of calculated of pumping rate for different r_0. The results show that at a red-shifted frequency-range of 140-20 MHz from that of $|^5S_{1/2}\, F = 3,\nu\rangle \rightarrow |^5P_{3/2}\, F'=2,3,\nu'\rangle$, the pumping rate shows resonances which height and frequency spacing that depends on the potential minimum position. The frequency position of these resonances, their number and the frequency-spacing is in a qualitative agreement with the experimental results presented above.

5.5 Conclusion

In conclusion, the Sub-Doppler transparencies have been for the first time experimentally observed within the Doppler broaden absorption lines of D2 transition of Rb vapor loaded in HC-PCF. The evolution of these SDL have experimentally explored with varying input laser power and polarization, DC magnetic field and fiber core inner-surface materials.

Based on a theoretical model involving the description of the atom-surface VdW potential, the analysis of the spectrum of the observed features shows that those can originate from the optical pumping of the wall trapped atoms in to an off resonant $|^5S_{1/2}F = 2\rangle$ state. This model requires further work to corroborate that the observed SDL are indeed related to trapped atoms with the atom-surface potential

The present results shed a new light on the atomic dynamic inside HC-PCF, and will certainly be useful in designing Rb PMC for atom optics applications.

5.6 References

[1] K. Zhao, M. Schaden, and Z. Wu, "Method for Measuring the Dwell Time of Spin-Polarized Rb Atoms on Coated Pyrex Glass Surfaces Using Light Shift," *Phys. Rev. Lett.*, vol. 103, no. 7, p. 73201, Aug. 2009.

[2] K. F. Zhao, E. Ulanski, M. Schaden, and Z. Wu, "Dwell Time Measurement of Wall Collisions of Spin Polarized Rb Atoms on Antirelaxation Coatings," *J. Phys. Conf. Ser.*, vol. 388, no. 1, p. 12046, Nov. 2012.

[3] M. Stephens, R. Rhodes, and C. Wieman, "Study of wall coatings for vapor-cell laser traps," *J. Appl. Phys.*, vol. 76, no. 6, pp. 3479–3488, Sep. 1994.

[4] A. Hatakeyama, M. Wilde, and K. Fukutani, "Classification of Light-Induced Desorption of Alkali Atoms in Glass Cells Used in Atomic Physics Experiments," *Eur. J. Surf. Sci. Nanotechnol.*, vol. 4, no. cond-mat/0512451, pp. 63–68, 2005.

[5] E. Ilinova, T. Bradley, X. Zheng, B. Debord, F. Gerome, and F. Benabid, "Atom-surface Van der Waals potential induced sub-Doppler transparencies in Rb vapor filled Kagome HC-PCF," in *2016 Conference on Lasers and Electro-Optics, CLEO 2016*, 2016.

[6] D. Bloch and M. Ducloy, "Atom-wall interaction," *Adv. At. Mol. Opt. Phys.*, vol. 50, pp. 91–154, 2005.

[7] R. Marani, L. Cognet, V. Savalli, N. Westbrook, C. I. Westbrook, and A. Aspect, "Using atomic interference to probe atom-surface interactions," *Phys. Rev. A*, vol. 61, no. 5, p. 53402, 2000.

[8] S. Okaba, T. Takano, F. Benabid, T. Bradley, L. Vincetti, Z. Maizelis, V. Yampol'skii, F. Nori, and H. Katori, "Lamb-Dicke spectroscopy of atoms in a hollow-core photonic crystal fibre," *Nat. Commun.*, vol. 5, no. May, p. 4096, 2014.

[9] J. I. Cirac and H. J. Kimble, "Quantum optics, what next?," *Nat Phot.*, vol. 11, no. 1, pp. 18–20, Jan. 2017.

[10] J. N. Israelachvili, *Intermolecular and surface forces*. Academic press, 2015.

[11] R. D. Mountain and . S. W. H., "Molecular Dynamics Study of Liquid Rubidium and the Lennard--Jones Fluid.," *J. Res. Natl. Bur. Stand.*, vol. 48.6, pp. 439–446, 1979.

[12] E. G. Lima, M. Chevrollier, O. Di Lorenzo, P. C. Segundo, and M. Oriá, "Long-range atom-surface bound states," *Phys. Rev. A*, vol. 62, no. 1, p. 13410, Jun. 2000.

[13] A. Laliotis, T. P. de Silans, I. Maurin, M. Ducloy, and D. Bloch, "Casimir–Polder interactions in the presence of thermally excited surface modes," *Nat. Commun.*, vol. 5, p. 4364, Jul. 2014.

[14] F. Le Kien and K. Hakuta, "Spontaneous radiative decay of translational levels of an atom near a dielectric surface," *Phys. Rev. A*, vol. 75, no. 1, p. 13423, Jan. 2007.

[15] P. Roberts, F. Couny, H. Sabert, B. Mangan, D. Williams, L. Farr, M. Mason, a Tomlinson, T. Birks, J. Knight, and P. St J Russell, "Ultimate low loss of hollow-core photonic crystal fibres.," *Opt. Express*, vol. 13, no. 1, pp. 236–44, Jan. 2005.

[16] A. D. Slepkov, A. R. Bhagwat, V. Venkataraman, P. Londero, and A. L. Gaeta, "Spectroscopy of Rb atoms in hollow-core fibers," *Phys. Rev. A*, vol. 81, no. 5, p. 53825, May 2010.

[17] D. Suter, *The physics of laser-atom interactions.* Cambridge University Press., 1997.

[18] F. Le Kien, S. Dutta Gupta, and K. Hakuta, "Phonon-mediated decay of an atom in a surface-induced potential," *Phys. Rev. A*, vol. 75, no. 6, p. 62904, Jun. 2007.

[19] Zhao, K., and Z. Wu. "Hyperfine Polarization and Its Normal Gradient Coefficient of R b 87 Atoms in the Vicinity (~ 10− 5 c m) of Coated and Uncoated Pyrex Glass Surfaces." *Physical review letters* 91, no. 11 (2003): 113003.

[20] E. Ulanski and Z. Wu, "Measurement of dwell times of spin polarized rubidium atoms on octadecyltrichlorosilane- and paraffin-coated surfaces," *Appl. Phys. Lett.*, vol. 98, no. 20, pp. 20–22, 2011.

[21] A. Hatakeyama, M. Wilde, and K. Fukutani, "Classification of Light-Induced Desorption of Alkali Atoms in Glass Cells Used in Atomic Physics Experiments," *e-Journal Surf. Sci. Nanotechnol.*, vol. 4, no. January, pp. 63–68, 2006.

Conclusion and future work

This manuscript reported on several results toward the development of alkali-vapor photonic microcell (PMC), which is a stand-alone optical fiber consisting with a length of hollow-core photonic crystal fiber (PMC) filled with the vapor and sealed at both end to another solid fiber with low insertion loss.

In this work we used Rb atoms, and motivated our choice of Inhibited-Coupling guiding HC-PCF for: (i) its ultra-low loss at 780 nm, which represents now the state-of-art, and broadband transmission, which allows multi-frequency laser excitation of the confined atoms. (ii) its relatively large core diameter, which reduces the difficulty of the Rb loading process and decrease the collision with the core inner wall, and (iii) its modal content, which allows single mode excitation.

Several Inhibited-Coupling guiding Kagome HC-PCF have been designed and fabricated for this purpose. The fibers exhibited different core diameter to assess their effect on the Rb spectroscopy response ant its amenability in post-processing the fiber. The fibers have been optically characterized post-processed for different aims. The process chain that has been used comprises HC-PCF tapering, splicing, in-fiber gas handling, fiber core inner-wall coating and of course vapor loading. Based on this process chain we developed fiber-core inner-wall coated with PDMS and ceramic. The results show that the ceramic coated HC-PCFs exhibit much longer Rb life time inside the fiber which is paramount milestone in making stand-alone alkali-vapor PMCs. Furthermore, we have explored several techniques to splice Kagome HC-PCF to conventional all-solid optical fibers, such as splicing tapered Kagome HC-PCF, sleeve-based splicing. The latter is justified to prevent any reactivity of Rb during the necessary heating during the splicing process.

In this work, we have also investigated the atom polarization relaxation of the ground state of Rb filled HC-PCF. The results in HC-PCF with different surface materials show that the dwell time of the atoms near the core inner surface is among the longest relaxation time

because of the extremely short transit time. Furthermore, because of the short transit time, the atom polarization is dominantly generated by the slow atoms, creating thus a magneto-optical spectroscopy dynamics that contrasts with conventional configuration. We explored this specific relaxation dynamics to measure the dwell time for silica surface, PDMS and ceramic coatings. These results could be exploited *in situ* characterization of surface coating of atomic vapor filled HC-PCF and future atom PMCs. Finally, we reported on a new sub-Doppler transparency lines that we have attributed to atom-surface potential.

Whilst the achieved results during this doctoral work represent important milestones toward the development of Rb-PMC, there are several work remain to undertake in the future before a successful assembly of the PMC and their implementation in atom optical applications.

Among the immediate work that can be done is to splice Rb-loaded HC-PCF. The ceramic coating allows a long lifetime of the Rb inside the fiber core with no reactivity or aging, and the splicing using the sleeving technique could enable splicing with no heating the confined Rb, which could damaging to its chemical integrity. Other Rb loading technique could also be envisaged such as side-hole drilling of the HC-PCF. In the GPPMM, set-up is already under development to make holes on the side of the fiber that are sufficiently large and that cause little transmission loss. This endeavor is taken in parallel with a continuous improvement in HC-PCF design and fabrication for atom optics applications.

On the other hand, the results shown in chapter 4 and chapter 5 illustrated the distinctive properties of atom dynamic inside the core of HC-PCF, which strongly differs from the existing macroscopic vapor cells. The results call for further experimental and investigation on the atom-surface interactions in this in-fiber configuration. Among the necessary future work is to corroborate our technique of dwell-time measurements, and to exploit it in generating coherent magneto-optical effects with polarized atoms. Finally, the origin of the observed sub-Doppler lines are still to be fully understood. A future work that must be immediately undertaken is to finish the construction of a more rigorous theoretical model, with a full description of the atom-surface VdW potential.

Publications list

Journal articles peer reviewed: (+2 articles under writing)

1. Zheng, Ximeng, Benoît Debord, Luca Vincetti, Benoît Beaudou, Frédéric Gérôme, and Fetah Benabid. "Fusion splice between tapered inhibited coupling hypocycloid-core Kagome fiber and SMF." *Optics express* 24, no. 13 (2016): 14642-14647.

Conference papers peer reviewed:

1. Ximeng Zheng, Benoît Debord, Jenny Jouin, Philippe Thomas, Frédéric Gérôme, and Fetah Benabid, "Single laser-beam generated sub-Doppler transparencies in Rb-filled Kagome HC-PCF", CLEO Europe 2017, paper CH-7.6.

2. Ximeng Zheng, Benoît Debord, Frédéric Gérôme, Fetah Benabid, 'Observation d'un nouveau type de transparences sub-doppler au sein d'une fibre creuse kagome remplie de rb' , conférence JNOG, 2017, paper 199.

3. Ximeng Zheng, Jenny Jouin, Ekatarina Ilinova, Benoît Debord, Philippe Thomas, Frédéric Gérôme, and Fetah Benabid, "Ground-state population relaxation dynamics of polarized Rb atoms in Kagome HC-PCF", CLEO US 2016, paper SM2H.8.

4. Ekaterina Ilinova, Tom Bradley, Ximeng Zheng, Benoît Debord, Frédéric Gérôme, and Fetah Benabid, "Atom-surface Van der Waals potential induced sub-Doppler transparencies in Rb vapor filled Kagome HC-PCF", CLEO US 2016, paper SM2H.7.

5. Ximeng Zheng, Benoît Debord, Meshaal Alharbi, Luca Vincetti, Frédéric Gérôme, and Fetah Benabid, "Splicing Tapered Inhibited-coupling Hypocycloid-core Kagome Fiber to SMF Fibers", CLEO US 2015, paper STu1N.1

Post-traitement de fibre et spectroscopie atomique pour le développement de vapeur atomique en microcellules photoniques

Cette thèse concerne la spectroscopie atomique pour le développement de microcellules photoniques à base de vapeur atomique alcaline (PMC). Le travail est motivé par reproduire les performances remarquables obtenues dans les domaines des références de fréquences et de l'optique cohérente en environnement laboratoire et à les transférer dans des dispositifs très compacts et autonomes accessibles à une communauté scientifique plus large ou à un marché commercial. Dans notre cas, ces futurs composants seront basés sur une fibre à cristal photonique à coeur creux (HC-PCF) remplie d'un matériau en phase gazeuse pour former la PMC et se distingue par une longueur d'interaction ultra longue associée à des dimensions modales transverses micrométriques. Cependant, cette échelle micrométrique du coeur creux de la fibre contenant les atomes soulève plusieurs défis techniques et scientifiques. Parmi les défis techniques, nous énumérons le développement d'un processus efficace pour le chargement d'atomes dans une telle fibre optique, la suppression ou l'atténuation de la réactivité physio-chimique des atomes (c'est-à-dire le rubidium) avec la surface interne silice entourant le coeur de la fibre, etc... En parallèle, le rapport large surface / volume du coeur de la fibre soulève des questions comme la dynamique de relaxation de la cohérence et la nature et l'effet de l'interaction atome-surface. Ainsi, les travaux de thèse reposent sur l'utilisation de revêtements spécifiques de la surface interne du coeur de la fibre avec différents matériaux pour atténuer ces réactions physico-chimiques, sur l'amincissement des larges coeurs creux des HC-PCF Kagomé à couplage inhibé et sur une technique de soudure qui garantit de faibles pertes d'insertion et l'absence de réactivité avec les atomes. Parallèlement, la thèse rapporte un ensemble d'expériences de spectroscopie pour évaluer la dynamique de relaxation des atomes à l'intérieur des HC-PCF et l'observation de nouvelles transparences sous-Doppler.

Mots-clés : Post-traitement de fibre, Anti-relaxation, Sous-Doppler, Couplage inhibé

Fiber post-processing and atomic spectroscopy for the development of atomic-vapour photonic microcell

This thesis reported on atomic spectroscopy for the development of alkaline atomic vapor photonic microcell (PMC). The work is motivated by reproducing the outstanding laboratory environment based performances achieved in the fields of frequency standard and coherent optics in highly compact and stand-alone devices that can be accessible to a wider scientific community or to a commercial market. In our case these future devices will be based a Hollow-core photonic crystal fiber (HC-PCF) filled with a gas phase material to form a PMC, and outstands with an ultra-long long interaction length and micrometric modal area. However, the micrometric scale of the fiber core harboring the atoms raises several technical and scientific challenges. Among the technical challenges, we list the development of efficient process for atom loading inside long hollow fiber with small core diameter, the suppression or mitigation of physio-chemical reactivity of the atoms (*i.e.* Rubidium) with the fiber core inner-surface silica etc. In parallel, the large surface-to-volume ratio of the fiber-core raises questions like the coherence relaxation dynamics and the nature and effect of the atom-surface interaction. The thesis reports on fiber-core inner surface coating with different materials to mitigate the physio-chemical reactions of the confined atoms with the surface, on tapering large core inhibited coupling Kagome HC-PCF, and splicing technique that ensures low splice loss and no atomic reactivity during the splicing process. In parallel, the thesis reports on a set of spectroscopy experiments to assess the relaxation dynamics of atoms inside HC-PCF and to report on novel sub-Doppler transparencies.

Keywords : Fiber post-processing, Anti-relaxation, Sub-Doppler, Inhibited coupling